



UNIVERSIDAD NACIONAL AUTÓNOMA DE MÉXICO
POSGRADO EN CIENCIAS DE LA TIERRA
CENTRO DE GEOCIENCIAS

Paleogeographic reconstruction of the Early-Middle Jurassic of Oaxaca, Mexico

TESIS

**QUE PARA OPTAR POR EL GRADO DE:
MAESTRO EN CIENCIAS DE LA TIERRA**

Presenta:

Diego Alberto Osorio Afanador

Tutor de tesis:

Dr. Roberto Stanley Molina Garza
Centro de Geociencias

Comité tutor:

Dr. Harald Böhnelt

Dr. Timothy Lawton

POSGRADO EN CIENCIAS DE LA TIERRA

Santiago de Querétaro, Querétaro, México

Noviembre, 2019



Universidad Nacional
Autónoma de México

Dirección General de Bibliotecas de la UNAM

Biblioteca Central



UNAM – Dirección General de Bibliotecas
Tesis Digitales
Restricciones de uso

DERECHOS RESERVADOS ©
PROHIBIDA SU REPRODUCCIÓN TOTAL O PARCIAL

Todo el material contenido en esta tesis esta protegido por la Ley Federal del Derecho de Autor (LFDA) de los Estados Unidos Mexicanos (México).

El uso de imágenes, fragmentos de videos, y demás material que sea objeto de protección de los derechos de autor, será exclusivamente para fines educativos e informativos y deberá citar la fuente donde la obtuvo mencionando el autor o autores. Cualquier uso distinto como el lucro, reproducción, edición o modificación, será perseguido y sancionado por el respectivo titular de los Derechos de Autor.

Declaro conocer el Código de Ética de la Universidad Nacional Autónoma de México, plasmado en la Legislación Universitaria. Con base en las definiciones de integridad y honestidad ahí especificadas, aseguro mediante mi firma al calce que el presente trabajo es original y enteramente de mi autoría. Todas las citas de, o referencias a la obra de otros autores aparecen debida y adecuadamente señaladas, así como acreditadas mediante los recursos editoriales convencionales.

Diego A. Osorio A.

Agradezco a mi papá y a mi mamá que siempre me han apoyado

Agradezco a Roberto Molina por el apoyo recibido durante la realización de mi maestría

Agradezco los miembros de mi comité Harald y Timothy por el apoyo y los aportes que encaminaron el proyecto

Agradezco a los revisores John Geissmann, Harald Bohnel, Yam Zul Ocampo y Martín Guerrero por las sugerencias que mejoraron de manera notable el manuscrito final

Agradezco a Paola y Daniel por acompañarme a campo

Agradezco Giovanni y Danielle de la USP por ayudarme en el laboratorio

Agradezco a los investigadores del CGEO por todo el conocimiento que me transmitieron

Agradezco a los técnicos de los laboratorios de paleomagnetismo y magnetismo de rocas, petrografía, laminación y de fluidos corticales del CGEO por su apoyo en la adquisición de datos

Agradezco a mis amigos y compañeros del CGEO por la compañía y el apoyo que me brindaron durante mi estadía en Querétaro

Index

1. Introduction.....	11
1.1 Objectives and work hypothesis	12
2. Framework	15
2.1 Jurassic Tectonic Framework.....	15
2.2 Regional Geological Framework.....	17
2.2.1 Olinalá Basin	19
2.2.2 Otlaltepec Basin.....	20
2.2.3 Ayuquila Basin	20
2.3 Local Geologic Framework.....	21
2.4 Bibliographic review on Tlaxiaco’s Basin Stratigraphy.....	23
2.4.1 Historical perspective.....	23
2.4.2 Stratigraphy	24
3. Paleomagnetic methods and results.....	32
3.1 Methods.....	32
3.2 Results.....	34
3.2.1 Field observations	35
3.2.2 Microscopy	37
3.2.4 Rock Magnetism.....	43
3.2.5 Paleomagnetism.....	52
4. Stratigraphy, sedimentology and petrography: methods and results.....	63
4.1 Methods.....	63
4.1 Stratigraphy and facies description.....	66
4.2 Petrography and provenance	69
5. Discussion	76
5.1 Magnetic mineralogy	76
5.2 Paleomagnetic directions and paleopoles	78
5.2.1 Comparison with other results from the Mixteca terrane.....	86
5.3 Facies and environment	91
5.3.1 Lithofacies distribution	93
5.3.2 Architectural elements	95
5.3.3 Fluvial style	96
5.4 Petrography	98
5.5 Arc and continental paleogeography	101
5.6 Pangea.....	103
6. Conclusions.....	105
References.....	108
Appendix 1.....	126
Appendix 2.....	164
Appendix 3.....	174
Appendix 4.....	207
Appendix 5.....	213

List of figures

Figure 2-1. Paleogeographic reconstruction of continental masses in western equatorial Pangea during the Early Jurassic.....	17
Figure 2-2. Geographic and geologic locations discussed in the text.	19
Figure 2-3. Stratigraphic correlation of the regional study area, and geographic reconstruction for the Lower – Middle Jurassic.....	21
Figure 2-4. Local geology, stratigraphy and basin reconstruction for the Mesozoic.....	23
Figure 3-1. Hysteresis parameters used in this study to characterize the magnetic mineralogy of the analyzed rocks.	34
Figure 3-2. Sites sampled in San Juan Diquiyú area for paleomagnetic study.	36
Figure 3-3. Field photos of Diquiyú unit outcrops.....	37
Figure 3-4. Photomicrographs showing the most important petrographic features of the sampled Diquiyú unit rocks.	39
Figure 3-5. Photomicrographs showing the most important petrographic features in reflected light of the sampled Diquiyú unit.	42
Figure 3-6. Scanning electron microscope (SEM) photomicrographs of the sites sampled in the Diquiyú unit.....	43
Figure 3-7. Isothermal remanent magnetism (IRM) acquisition and backfield demagnetization plots for all analyzed sites.	45
Figure 3-8. Isothermal remanent magnetization (IRM) acquisition curve and modeled results using linear acquisition plot (LAP) and gradient acquisition plot (GAP) after Kruiver et al. (2001).	49
Figure 3-9. Representative hysteresis loops of analyzed samples.	52
Figure 3-10. Day plot comparing the principal hysteresis ratios	52
Figure 3-11. Examples of orthogonal demagnetization diagrams for the samples analyzed in this study (Zijderveld, 1967).	55
Figure 3-12. Orthogonal demagnetization diagrams and equal area projection of sample directions from clasts of a conglomerate bed overlying the lavas from the Diquiyú unit.	56
Figure 3-13. DC plot obtained for Diquiyú unit sites.....	57
Figure 3-14. Equal are projections of site mean directions and mean paleomagnetic direction for magnetization components A and B.....	58
Figure 4-1. Condensed stratigraphic column of Rosario Nuevos’s creek succession.....	66
Figure 4-2. Outcrop characteristics and facies of Prieto conglomerate.	68
Figure 4-3. Outcrop characteristics and facies of the transition between Prieto conglomerate and Cualac conglomerate.....	69
Figure 4-4. Outcrop characteristics and facies of Cualac conglomerate. Up in the figure represents up-section in the field.....	71
Figure 4-5. Photomicrographs representative of: A) Zorrillo Formation, B) Cualac conglomerate, C) Transition between Prieto and Cualac conglomerates, and D) Prieto conglomerate.....	73
Figure 4-6. Classification and tectonic discrimination diagrams.....	74
Figure 4-7. Ternary diagrams using lithic parameters.	75
Figure 5-1. VGP distribution for the sites collected in the Diquiyú unit.).	80

Figure 5-2. Comparison between Diquiyú unit pole and selected poles from the reference APWP of Torsvik et al., 2012.	81
Figure 5-3. Declination comparison between selected Lower and Middle Jurassic poles and reference APWP's.	88
Figure 5-4. Paleolatitudinal comparison between selected Lower and Middle Jurassic poles and reference APWP's.	91
Figure 5-5. Different nomenclatures for the succession outcropping in Rosario Nuevo creek.	93
Figure 5-6. Stratigraphic relationships and basin interpretation for Rosario Formation, Prieto conglomerate member and Cualac conglomerate.	93
Figure 5-7. Two possible river system configurations for the Rosario Formation and for the Prieto conglomerate member of the Rosario Formation.	97
Figure 5-8. Paleogeographic reconstruction of continental masses in western equatorial Pangea during the Early Jurassic.....	104

List of tables

Table 3-1. Components used to model the IRM acquisition curve of selected samples, according to Kruiver <i>et al.</i> (2001).....	47
Table 3-2. Hysteresis parameters for Diquiyú unit samples	50
Table 3-3 Paleomagnetic results for Diquiyú Unit. 59	
Table 4-1 Facies codes used for the classification of the analyzed succession.	63
Table 4-2. Codes and recalculation parameters used for the sandstone petrographic analysis.	64
Table 4-3. Recalculated compositional parameters obtained for Prieto conglomerate, Cualac conglomerate, and Zorrillo Formation.....	72
Table 5-1. Rotation and translation estimates between Diquiyú unit direction and reference directions for the North American Plate.	81
Table 5-2. Rotation and translation estimates between Zorrillo Formation (Modified from Böhnel, 1999).....	85
Table 5-3. Data from selected sites used for the construction of figures 5.3 and 5.4.	87
Table 5-4. Rotation and flattening parameters for selected sites related to Nazas arc. 90	
Table 5-5. Architectural element classification and interpretation	95

Abstract

In order to clarify the overlap problem between southern Mexico and northern Colombia that is common in most Pangea reconstructions, and also to assess continuity of the Nazas continental arc (which extended from northern North America to southern South America), I conducted a multi-technique approach to reconstruct the paleogeography of southern Mexico (Oaxaca) and to infer some tectonic implications related to drainage patterns and evolution and to continental block kinematics. The area selected as best for assessing these problems is located in the northern part of Oaxaca State in southern Mexico, namely the Tlaxiaco Basin. The Diquiyú Anticlinorium crops out at the northern edge of this basin and exposes Lower Jurassic andesitic lava flows followed by a Lower-Middle Jurassic sedimentary succession typical of continental to transitional environments capped at the top by Middle-Upper Jurassic limestones. I chose the lava flows at the base of the succession (Diquiyú unit) for the paleomagnetic study in order to avoid inclination shallowing effects. I determined the magnetic mineralogy with rock magnetic experiments and extracted the characteristic remanent magnetization (ChRM) using standard stepwise demagnetization techniques. Conformable over the Diquiyú unit lavas there are volcanic conglomerates (Prieto conglomerate member of the Rosario Formation) that slowly grade to quartzitic conglomerates and sandstones at the top (Cualac conglomerate). To determine the tectonic and climatic influences on the deposition of these units I described the principal textural and compositional features of the succession, also sampled sandstones for petrologic analysis, and measured paleocurrent orientations using the direction of clast imbrication in the volcanic conglomerates and the cross-stratification in the quartzitic conglomerates and sandstones.

The natural remanent magnetism (NRM) is generally multivectorial or bi-vectorial. The characteristic remanent magnetization of the andesites and dacites of the Diquiyú unit is of primary nature, and resides chiefly in magnetite and hematite. The characteristic magnetization of dual polarity passes conglomerate and fold tests, and points in tilt corrected coordinates towards the ENE with shallow inclinations (Dec: 82.8°, Inc: -1.4 °, k: 11.25, α_{95} : 9.4, N: 23). This result when compared with published reference

paleopoles of the North American Craton is interpreted to reflect clockwise rotation of at least 80° since the Early Jurassic but prior to the Cretaceous. The discordant paleomagnetic direction in rocks of the Diquiyú unit can be interpreted in two ways depending on the selected reference poles. The first is a northern translation of southern Mexico relative to the North American Plate, and the second is a stationary position of southern Mexico blocks, traveling together with North American Plate. This second option seems more plausible as lately other paleomagnetic studies have reached similar conclusions. The petrologic attributes together with some published geochemical analysis allow classifying lavas of the Diquiyú unit as a volcanic arc product.

The analysis of the overlying clastic succession showed that braided and wandering rivers with high gravel content were responsible for eroding, transporting and depositing the sediment in a basin close to the source area. An evolving compositional pattern was identified and interpreted as the complete unroofing of local sources (continental arc lavas) succeeded by more distal sources eroding metamorphic crustal complexes in a wider basin. Humid conditions prevailed during the deposition of the Prieto conglomerate member of the Rosario Formation and Cualac conglomerate. Paleocurrent data obtained from clast imbrication orientations consistently point towards the SW, and when back rotated on the basis of paleomagnetic data point to the SE. The characteristics of lavas and detrital rocks allow proposing an extensional intra-arc setting, in which the major faults controlling the location of source-basin areas were oriented parallel to the arc, which is SW – NE, as this direction is perpendicular to the paleocurrents. According to these data we can conclude that the overlap between southern Mexico and northern South America can be solved by dividing this region into blocks whose relative positions can be accommodated according to the paleomagnetic data. We also conclude that the Nazas arc extended throughout almost all these blocks.

1. Introduction

Almost all the recent literature on Jurassic rocks in Mexico claims Pangea as the accepted paleogeographic framework (Morán-Zenteno *et al.*, 1993; Martini & Ortega-Gutiérrez, 2016; Zepeda-Martínez *et al.*, 2018; Ocampo-Díaz *et al.*, 2019). In doing this, these studies call on models that try to reconcile the continent shapes, structural trends in geologic provinces, facies and faunal distributions, and paleomagnetic directions. An A-type Pangea configuration, similar to the proposed by Wegener, seems to reconcile the data at least until the Late Triassic (Domeier *et al.*, 2012). An additional requirement for western equatorial Pangea reconstructions is the required closure the Gulf of Mexico during the Ouachita collision (Pindell & Dewey, 1982). An A-type reconstruction produces, however, significant overlap between southern North America (southern Mexico) and northern South America (northern Colombia) (Pindell & Dewey, 1982; Anderson & Schmidt, 1983; Lottes & Rowley, 1990).

Another common reference in the literature is the recurrent proposal of competing rift and/or arc settings as the processes responsible for the modification of the crust and the generation of Jurassic rock successions in the western equatorial border of Pangea (Mexico, Colombia). Three scenarios have been proposed: a unique continental arc developing intra-arc and back-arc basins (Lawton & Molina-Garza, 2014; Zuluaga *et al.*, 2015), a regional segmented rift basin development (Cediel *et al.*, 2003), or a combined arc-rift model (Dickinson & Lawton, 2001; Martini & Ortega-Gutiérrez, 2016). However, little *consensus* has been reached concerning the extent of each setting processes.

The most accepted hypothesis to solve the overlap between continental crust in Mexico and Colombia in western equatorial Pangea involves displacing some of the Mexican blocks (*e.g.*, Caborca, Oaxaquia, Tampico) to the NW (Anderson & Schmidt, 1983). Yet no conclusive evidence has been found to prove the existence of faults able to move the Mexican blocks, nor has a definite paleomagnetic study demonstrated their paleo-latitudinal displacement to reach their present position. Other models have solved the

overlap problem by placing some blocks actually located in Colombia (*e.g.*, Sierra Nevada de Santa Marta, Central Cordillera) at more southern latitudes than their present position (Bayona *et al.*, 2006; 2010). But these models also fail to demonstrate the existence of the faults responsible for their subsequent latitudinal movement, and the paleomagnetic database supporting the model is weak.

Jurassic volcanic and sedimentary successions cropping out in the Mixteca Terrane of southern Mexico offer good quality material to assess the problems postulated here, as is the region where the continental overlap in proposed western equatorial Pangea reconstruction occurs. Although some paleomagnetic studies have been repeated, it appears that none of them have successfully isolated a primary Jurassic remanence (Molina-Garza *et al.*, 2003a), and although sedimentary studies have been published, their databases and conclusions are objectively inconclusive (*e.g.*, Zepeda-Martínez *et al.*, 2018). In this study, I carry out a paleomagnetic study of the Sinemurian-Pliensbachian Diquiyú volcanic succession (U-Pb, Durán-Aguilar, 2014), together with a rock magnetic study in order to understand the nature of the remanence. I also describe in detail the Toarcian-Bathonian (U-Pb, Durán-Aguilar, 2014; Zepeda-Martínez *et al.*, 2018) sedimentary succession overlying the Diquiyú unit (Prieto conglomerate member of the Rosario Formation and Cualac conglomerate) to interpret the effect of tectonism and/or climate in the development of its sedimentary features.

1.1 Objectives and work hypothesis

The main objectives of this research are:

Conduct a paleomagnetic sampling and analysis of the Lower Jurassic Diquiyú volcanic sequence along and across the Diquiyú Anticlinorium

Measure, describe, sample and interpret a complete stratigraphic section of the Prieto conglomerate member of the Rosario Formation and Cualac conglomerate cropping out along Rosario Nuevo Creek south of Tezoatlán, Oaxaca.

From these two main objectives, specific research plans include:

Describe petrographically and with rock magnetism techniques the rocks of the Diquiyú unit in order to assess its magnetic mineralogy

Isolate a ChRM direction from the samples of the Diquiyú unit using standard demagnetization techniques

Use the conglomerate and fold tests to assess the primary nature of the ChRM

Obtain a paleolatitude and relative rotation with respect to the North America reference of the sampled area, also, obtain rotation and translation estimates of the sampled region by comparing the obtained direction with reference paleomagnetic directions of the North American craton

Define a paleocurrent direction for the sedimentary successions by measuring different sedimentary structures, and correct this direction with the rotation estimate obtained from the paleomagnetic study

Define the depositional environment of the sedimentary units by facies analysis

Describe and interpret the petrographic evolution of the sedimentary successions

Using the facies analysis, petrography and paleocurrents assess the provenance and the tectonic environment in which the sedimentary successions were deposited

Infer climatic conditions and their regional extent during the deposition of the sedimentary units and compare these conditions with the paleolatitudinal estimate obtained from the paleomagnetic analysis

Reconcile the data collected in a paleogeographic model and compare it with the existent in the literature

My central hypothesis is that paleomagnetism is a useful approach to obtain paleolatitudinal estimates, and that sedimentary rocks are excellent climatic and tectonic recorders; thus, I believe that the paleomagnetic-sedimentologic study of the Diquiyú unit and overlying Jurassic strata will lead to conclusive evidence for postulating a paleolatitudinal position of the Mixteca Terrane during the initial phases of Pangea breakup. This result will help to reassess the reconstructions of western equatorial Pangea during the Early-Middle Jurassic by placing southern Mexico in an appropriate latitudinal position; in this sense I believe that the requirement for a relative displacement between the Mixteca Terrane and North America craton during the Jurassic would be discarded.

2. Framework

2.1 Jurassic Tectonic Framework

The Early Jurassic was marked by the initial breakup of Pangea through opening of the central Atlantic (McHone, 2000; Labails *et al.*, 2010). Mexican continental terranes were located in the western equatorial part of this supercontinent, and were subjected to the stress effects of east-directed subduction (Dickinson & Lawton, 2001; Lawton & Molina-Garza, 2014) and the NW-SE separation of the North American and South American plates (Pindell & Kennan, 2009). These processes initiated with the formation and/or reactivation of series of normal faults that exposed crustal basement blocks, and whose erosion products filled the adjacent basins (Michalzik, 1991; Morán-Zenteno *et al.*, 1993; Barboza-Gudiño *et al.*, 2010; Rubio-Cisneros & Lawton, 2011; Zepeda-Martínez *et al.*, 2018) (Figure 2.1).

The Lower Jurassic volcanic rocks cropping along and across Mexico (*e.g.*, northeastern Durango, Huizachal-Peregrina uplift, Real de Catorce area in central Mexico, Olinalá Basin, west-central Chiapas) have been interpreted as the result of the continental Nazas volcanic arc (Bartolini *et al.*, 2003; Barboza-Gudiño *et al.*, 2008; Godínez-Urban *et al.*, 2011a; Lawton & Molina-Garza, 2014) or as localized eruptions influenced by a combined arc-rift tectonic setting (Martini & Ortega-Gutiérrez, 2016). A stratigraphic inspection of these basins suggests that the action of backarc-intraarc extensional settings evolved to pure rift settings (Godínez-Urban *et al.*, 2011a; Rubio-Cisneros & Lawton, 2011). The Jurassic successions of the Huizachal-Peregrina uplift and Chiapas region change gradually from arc-related volcanic rocks interbedded with volcanoclastic and epiclastic deposits in an arc like fashion, to continental epiclastic deposits that slowly evolve to marine related rocks as common for rift related successions (Gawthorpe & Leeder, 2000). The marine incursion from the Atlantic Ocean into the Gulf of Mexico started in the Callovian, predating anticlockwise rotation of Maya Block (Molina-Garza *et al.*, 1992; Goldhammer, 1999; Goldhammer & Johnson, 2001). Nevertheless, some basins record marine deposition at earlier times (*e.g.*, Bajocian Taberna Formation in

Tlaxiaco Basin, Morán-Zenteno *et al.*, 1993; Huayacocotla Formation in Huayacocotla uplift and in San Luis Potosí state, Ochoa-Camarillo *et al.*, 1998; Ocampo-Díaz *et al.*, 2019) representing a probable incursion from the Pacific Ocean (Cantu-Chapa, 1998) or an earlier Thethian connection with southern Mexican basins (Gómez-Álvarez *et al.*, 2012 in Vite del Ángel, 2014).

Earlier paleomagnetic studies of Jurassic strata in the Mixteca region (Morán-Zenteno *et al.*, 1988; Ortega-Guerrero & Urrutia-Fucugauchi, 1993; Böhnell, 1999) have proposed latitudinal displacements of southern Mexican terranes from a northward position compared with its present day position. Inferred displacement occurred since at least the Middle Jurassic, as the obtained paleolatitudes for these rocks are higher than expected for the North American craton. These interpretations have been used by other authors (Martini & Ortega-Gutiérrez, 2016; Zepeda-Martínez *et al.*, 2018) to propose a solution to the geometric problem derived from reconstructions of Jurassic western Pangea, such as the overlap between north and South America described above. This translation would have stopped in Albian times, as southern Mexican Cretaceous paleolatitudes coincide with North American cratonic ones (Böhnell, 1999). Molina-Garza *et al.* (2003a) have proposed instead that paleomagnetic data recovered from Jurassic strata in the Mixteca region reflect widespread remagnetization during the Late Cretaceous, based on the similarity between the observed directions in Jurassic strata and the Late Cretaceous reference and also the absence of field tests for the age of the magnetizations in the studies by Morán-Zenteno *et al.* (1988) and Ortega-Guerrero & Urrutia-Fucugauchi (1993).

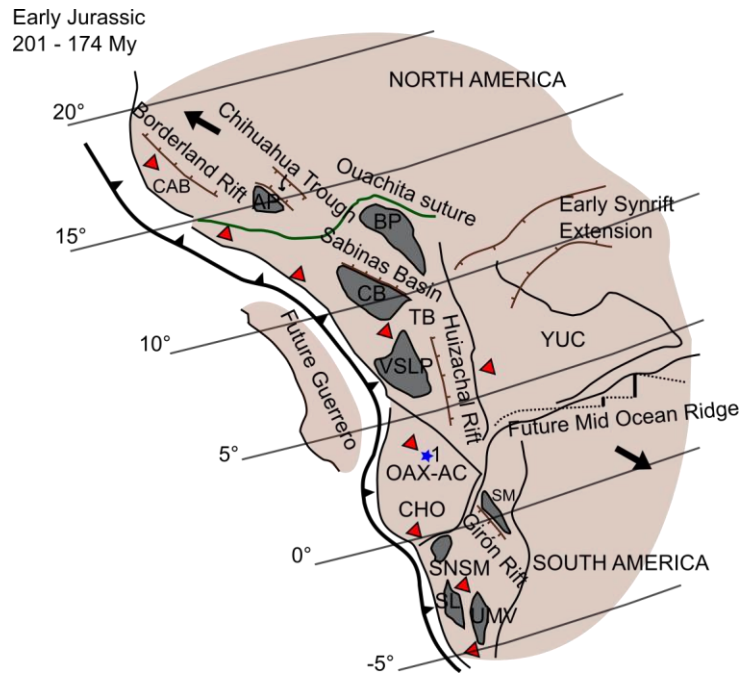


Figure 2-1. Paleogeographic reconstruction of continental masses in western equatorial Pangea during the Early Jurassic. This figure adjusts to a Pangea-A reconstruction and shows complete closure between all the continental blocks. Grey shaded polygons represent Paleozoic or older continental blocks; red triangles represent Nazas continental arc possible extension; black arrows indicate the separation direction between North and South American plates; blue star with 1 label indicates Diquiyú area studied here. CAB- Caborca Block; TB- Tampico Block; YUC- Yucatan Block; OAX-AC- Oaxaca-Acatlán block; CHO- Chortis Block; AP- Aldama Platform; BP- Burro Platform; CB- Coahuila Block; VSLP- Valles San Luis Platform; SM – Santander Massif; SNSM – Sierra Nevada de Santa Marta Massif; SL – San Lucas Range; UMV – Upper Magdalena Valley. Figure provided by Roberto Molina-Garza and based on Pindell (1985), paleolatitudes from Torsvik et al. (2012). Southern paleolatitudes for Colombian continental blocks (SNSM, SL, and UMV) are according to Bayona et al. (2006, 2010).

2.2 Regional Geological Framework

The Mexican territory has been subdivided in different terranes according to geologic characteristics including basement age, lithology, structure and evolution (Figure 2.2) that differentiate each terrane from the adjacent terranes (Campa & Coney, 1983; Sedlock *et al.*, 1993). Terranes are also delimited by crustal-scale discontinuities. Six different terranes have been proposed for southern Mexico (Guerrero Terrane, Mixteca Terrane, Oaxaca Terrane, Cuicateco Terrane, Xolapa Terrane and Maya Terrane). The juxtaposition of different geologic domains has been interpreted as result of a protracted rifting-subduction-accretion history of allochthonous and para-autochthonous oceanic and

continental crustal fragments since the Mesoproterozoic era (Sedlock *et al.*, 1993; Ortega-Gutiérrez *et al.*, 1994; Fitz-Díaz *et al.*, 2018).

The Mixteca Terrane is limited to the east by the Oaxaca Terrane, to the south by the Xolapa Terrane, to the west by the Guerrero Terrane and to the north is apparently buried under the Trans Mexican Volcanic Belt or under Cenozoic strata. In the eastern, southern and western limits there are regional scale faults (*e.g.* Caltepec Fault, Chacalapa Fault, Papalutla Fault respectively). The Caltepec Fault zone has been interpreted as the remnant of the accretion between the Mixteca and Oaxaca Terranes (Elías-Herrera *et al.*, 2005). The crystalline basement in the Mixteca Terrane is the Acatlán Complex (Ortega-Gutiérrez, 1978), composed of Paleozoic metasedimentary and metaigneous rocks of different metamorphic grades and disposed in a complex structural setting. Overlying this metamorphic complex are upper Paleozoic sedimentary rocks such as the marine facies of the Permian Olinalá – Los Arcos Formation (Corona-Esquivel, 1981) and the Tecomate Formation (Sánchez-Zavala *et al.*, 2004). The Matzitz Formation, of similar age but with continental facies, has been mapped as overlying both the Acatlán and Oaxacan complexes. East of the Mixteca Terrane, the Oaxaca Complex is the Grenvillian aged crystalline basement of the Oaxaca Terrane. These terranes are juxtaposed along Caltepec Fault Zone. The Jurassic successions in the Mixteca Terrane crop out along the axis of major structures as in the Tlaxiaco and Olinalá basins, and on homoclinal folds as in Otlaltepec and Ayuquila Basins (Figure 2.2) and, despite their geographical truncation, share facies trends representing continental conditions slowly and non-synchronously evolving to marine conditions (Morán-Zenteno *et al.*, 1993) (Figure 2.3).

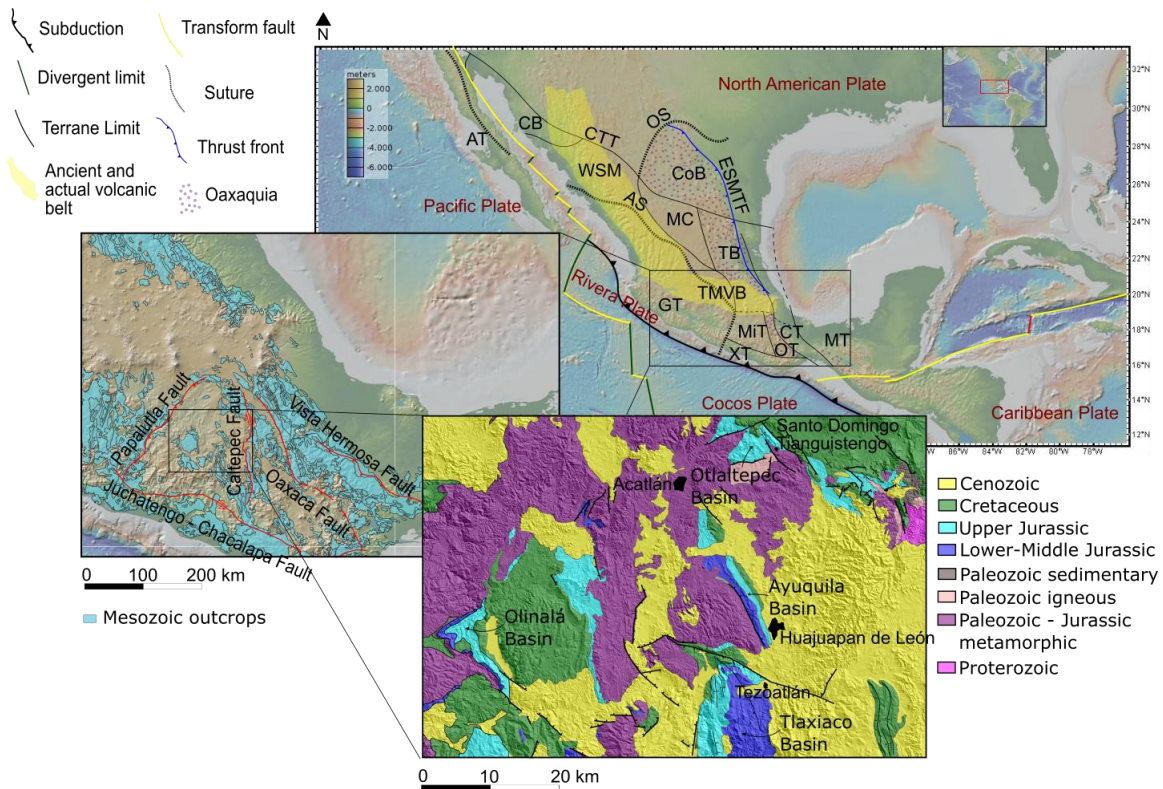


Figure 2-2. Geographic and geologic locations discussed in the text. AT- Alisitos Terrane; CB- Caborca Block; CTT – Coahuila-Tamaulipas Transform; WSM- Western Sierra Madre; CoB – Coahuila Block; MC – Mesa Central; TB – Tampico Block; TMVB – Trans Mexican Volcanic Belt; GT – Guerrero Terrane; MiT- Mixteca Terrane; XT- Xolapa Terrane; OT – Oaxaca Terrane; CT- Cuicateco Terrane; MT – Maya Terrane; AS – Arperos Suture; OS – Ouachita Suture; ESMTF – Eastern Sierra Madre thrust front. Terrane limits from Sedlock *et al.* (1993) and Dickinson & Lawton (2001). Mesozoic outcrop distribution from Instituto Nacional de Estadística y Geografía (INEGI). Geology modified from charts E14-5 Cuernavaca, E14-6 Orizaba, E14-8 Chilpancingo, and E14-9 Oaxaca from Servicio Geológico Mexicano.

2.2.1 Olinalá Basin

The Olinalá Basin is located in the eastern part of Guerrero State in the northwest corner of Mixteca Terrane. Corona-Esquivel (1981) recognized and described the Los Arcos Formation and Las Lluvias ignimbrite, exposed along the flanks of folded strata near Olinalá; upper Paleozoic and Jurassic ages are given to these sequences respectively. The Los Arcos Formation is about 600 m thick and rests unconformably over the Acatlán Complex. The 50 - 80 m thick Las Lluvias ignimbrite U-Pb dated between 179-168 My (Campa-Uranga *et al.*, 2004) lies over Los Arcos Formation in unconformity. The 30 - 200 m thick Cualac conglomerate (*sensu* Erben, 1956) was discordantly deposited over Acatlán Complex, Los Arcos Formation, and over Las Lluvias ignimbrite, being the most

widely exposed unit in the area. The Tecocoyunca Group (*sensu* Erben, 1956) rests conformably over Cualac conglomerate (Corona-Esquivel, 1981).

2.2.2 Otlaltepec Basin

Located in southern Puebla State in the northern part of Mixteca Terrane, the Otlaltepec Basin was first described by Ortega-Guerrero (1989) who named the units in this sequence, from base to top: Piedra Hueca, Otlaltepec and Magdalena informal units. They have been assigned to the Lower-Middle Jurassic based on fossil flora and U-Pb detrital zircons (Martini *et al.*, 2016). The Mesozoic sequence in Otlaltepec Basin near Santo Domingo Tianguistengo has an estimated thickness of ~2,500 m, overlying Acatlán Complex and Totoltepec stock (Permian) (Morán-Zenteno *et al.*, 1993) (Figure 2.3). The sedimentary environment and provenance of these successions has been interpreted by Martini *et al.* (2016) as the result of rivers denudating first Oaxacan and Acatlán complexes during Piedra Hueca Formation deposition, followed by the unroofing of Totoltepec stock which provided detritus for the Otlaltepec Formation. Martini *et al.* (2016) relate this change in provenance to the exhuming effect of normal faults (*e.g.* Matanza Fault).

2.2.3 Ayuquila Basin

In the work of Morán-Zenteno *et al.* (1993) the Ayuquila Basin succession starts with Tecamazúchil Formation overlying Acatlán Complex. Recently, Campos-Madrigal *et al.* (2013) divided and described three units as La Mora, Ayuquila, and Tecamazúchil formations. The conglomeratic La Mora Formation of inferred Triassic age (Campos-Madrigal *et al.*, 2013; Silva-Romo *et al.*, 2015) is the basal unit of the Mesozoic succession resting over the Acatlán Complex. Following La Mora Formation, the Ayuquila and Tecamazúchil formations, of similar lithologic characteristics but separated by an angular unconformity represent the deposition of rivers and local lakes during the Middle Jurassic (Campos-Madrigal *et al.*, 2013). Climatic variations from arid to humid

have been interpreted for these rocks. Correlation with Piedra Hueca and Otlaltepec formations in the Otlaltepec Basin has been proposed (Campos-Madrigal *et al.*, 2013). The faults that juxtapose Jurassic sedimentary units against the Acatlán Complex (Texcalapa Fault, El Sabino Fault) have been interpreted as being active during Middle Jurassic time when these units were being deposited, and the adjacent Ayú Complex was being exhumed (Campos-Madrigal *et al.*, 2013). A depositional contact between La Mora Formation and Acatlán Complex is evident 10 km west of Petlalcingo.

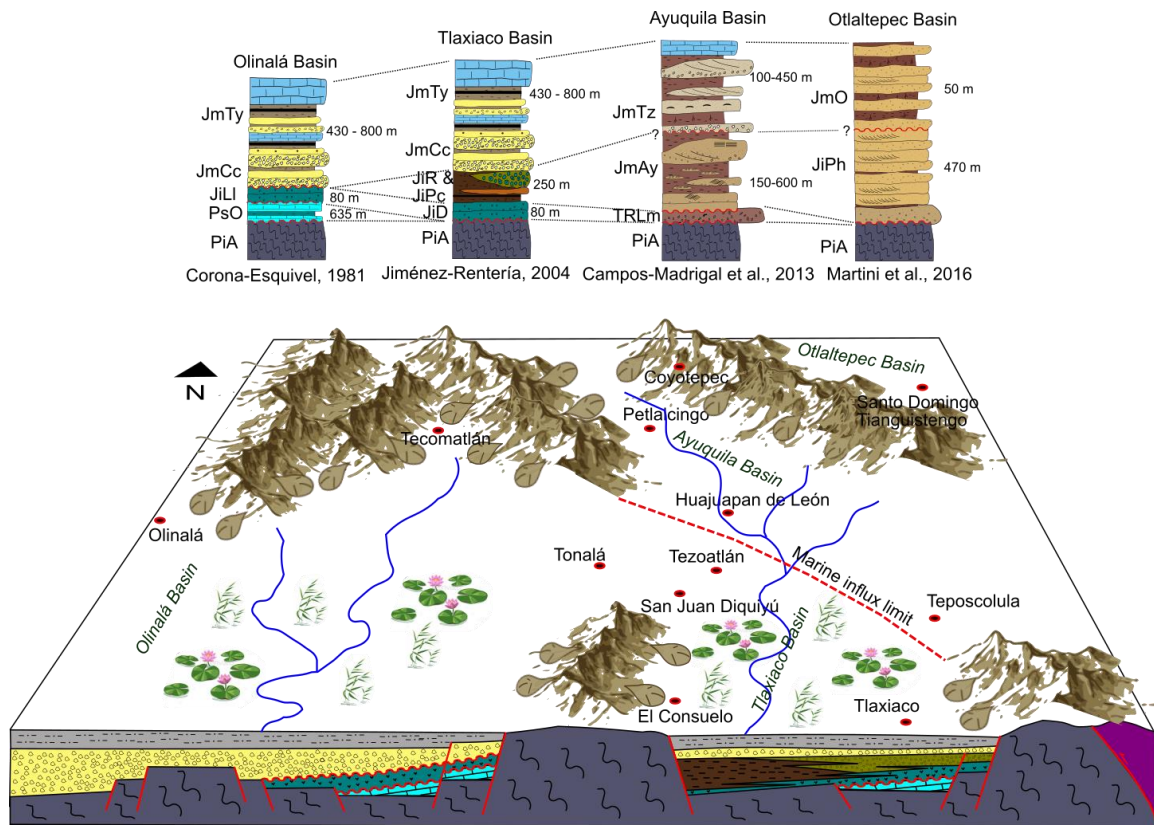


Figure 2-3. Stratigraphic correlation of the regional study area, and geographic reconstruction for the Lower – Middle Jurassic. Notice that during Middle Jurassic only the Olinalá and Tlaxiaco basins received marine influence, different from Ayuquila and Otlaltepec basins where rivers dominated. Modified from Morán-Zenteno *et al.* (1993). Pia – Acatlán Complex; PzO – Olinalá Formation; JiLl – Las Lluvias ignimbrite; JmCc – Cualac conglomerate; JmTy – Tecocoyunca Group; JiD – Diquiyú unit; JiPc – Prieto conglomerate; JiR – Rosario Formation; TRLm – La Mora Formation; JmAy – Ayuquila Formation; JmTz – Tezomazúchil Formation; JiPh – Piedra Hueca Formation; JmO – Otlaltepec Formation.

2.3 Local Geologic Framework

In the Diquiyú Anticlinorium (Erben, 1956) (Figure 2.4), an asymmetric fold trending NNW – SSE (Morán-Zenteno *et al.*, 1993), there are good exposures of the volcanic and sedimentary succession that constitutes the Tlaxiaco Basin (Alencaster, 1964). In the core of this fold, the axis of which curves towards the west at the trace of the Salado Fault, a series of andesitic-dacitic volcanic flows interbedded with ignimbrites and autobreccias is exposed (Ochotorena, 1981). Approximately 70 m has been described in drill cores in which the contact with the underlying Acatlán Complex is reported (Ochotorena, 1981). The age of this unit has been proposed as Early Jurassic based on U-Pb dating (Durán-Aguilar, 2014) although with arguable evidence. The 70 m thick Rosario Formation (*sensu* Jiménez-Rentería, 2004) consists of a succession of mudstone and sandstone with interbedded coal; this unit grades laterally and vertically to the 67 m thick Prieto conglomerate (*sensu* Jiménez-Rentería, 2004) constituted by clast-supported andesitic-clast conglomerate interbedded with fine to coarse sandstone and mudstone with abundant plant fossils. These two units have been grouped in Consuelo Group (Jiménez-Rentería, 2004), the age of which has been determined as Lower Jurassic using palynomorphs and U-Pb detrital geochronology (Jiménez-Rentería, 2004; Zepeda-Martínez, 2017). Cualac conglomerate (*sensu* Erben, 1956) overlies transitionally the Consuelo Group and, according Alencaster (1964) and Jiménez-Rentería (2004), constitutes the base of Tecocoyunca Group. The Cualac conglomerate is 30 to 90 m thick, and the unit is composed by clast-supported quartzitic-metamorphic conglomerates and sandstones with occasional mudstones and coal. It has been assigned to the Early Jurassic by palynomorphs (Jiménez-Rentería, 2004), and to the Middle Jurassic by U-Pb detrital geochronology (Durán-Aguilar, 2014). The overlying rocks are, in ascending order, the Zorrillo, Taberna, Simón, Otatera and Yucuñuti formations, that together sum to a thickness of about 500 m and could represent varying cycles of progradation (Zorrillo and Simon formations) and retrogradation (Taberna, Otatera, Yucuñuti formations) of a coastline (Vite del Ángel, 2014). The units of the Tecocoyunca Group (*sensu* Erben, 1956) are assigned to the Middle Jurassic (Alencaster, 1964; Morán-Zenteno *et al.*, 1993, Jiménez-Rentería, 2004). The Tecocoyunca Group (*sensu* Jiménez-Rentería, 2004) and similar aged (Middle Jurassic) rocks (Ayuquila Formation, Tecomazúchil Formation, and Otlaltepec Formation) crop out in a wide region inside Mixteca Terrane; on the other

hand, the Consuelo Group, of assigned Early Jurassic age, crop out in a restricted area only in Tlaxiaco Basin.

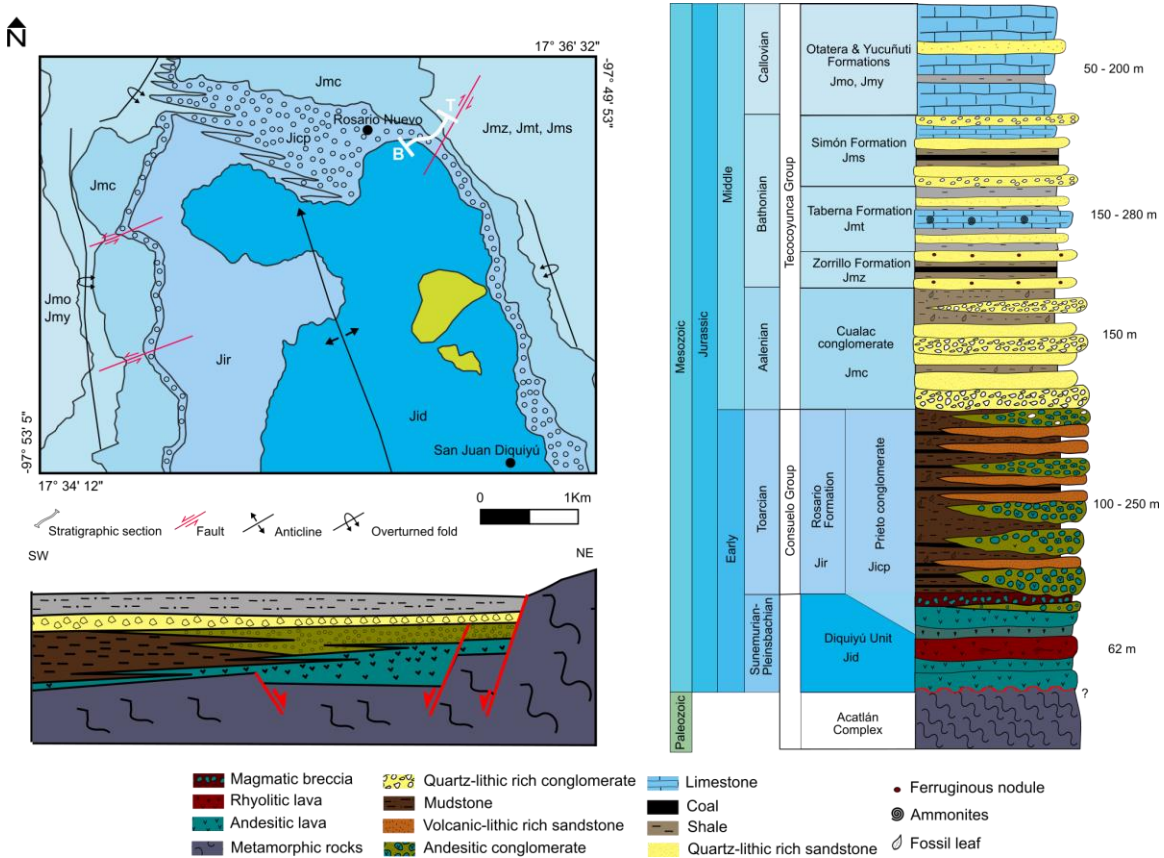


Figure 2-4. Local geology, stratigraphy and basin reconstruction for the Mesozoic. Notice the intertonguing relation between Rosario Formation and Prieto conglomerate Member, also between these two units and the underlying Diquiyú unit, this implies a synchronous deposition of the three rock units. Modified from Jiménez-Rentería (2004).

2.4 Bibliographic review on Tlaxiaco's Basin Stratigraphy

2.4.1 Historical perspective

Since the end of the 1800's, the Tlaxiaco Basin has been the focus of interest, with Ramírez (1882) as the first study, focused in coal exploration (In Vite del Ángel, 2014). Birkinbine (1911) made the first cartography and established a coarse stratigraphy (In Alencaster, 1964). The study by Wieland (1914) is the base of paleobotanic studies in the

Tlaxiaco Basin, and although a lot amount of research on this subject has been made during the the decades from 1940 to 1980 none of them has yet accomplished on assigning a precise age to the succession (Jiménez-Rentería, 2004). The most precise stratigraphic age determined in this basin was Burckhardt's (1927) Middle Jurassic age assigned to the Taberna Formation based on the study of ammonites. Erben (1956), based on biostratigraphic data, established the most widely used stratigraphic framework of the region (Figure 2.4); nevertheless, recently Rueda-Gaxiola (2009) made a different stratigraphic proposition based on detailed petrography and sedimentologic work in the outcrops of the Rosario Nuevo (Jiménez-Rentería, 2004; Vite del Ángel, 2014). This subdivision will be discussed in this work.

2.4.2 Stratigraphy

Acatlán Complex

The rocks composing the Acatlán Complex have an areal extent of about 10.000 km². The record of these units encompasses at least three orogenic cycles of ocean closure (Iapetus, Rheic and Paleo-Pacific, Ortega-Gutiérrez *et al.*, 2018) dated as Late Ordovician - Middle Devonian, Late Devonian - Mississippian, and early Permian. These metamorphosed sediments, volcanic rocks, and intrusions of at least three different cycles of rifting-subduction. These events generated different rocks (Esperanza Granitoids, Xayacatlán Formation, Cosoltepec Formation, and Tecomate Formation) whose stratigraphic and structural relationships are not fully understood (Ortega-Gutiérrez, 1978; Keppie *et al.*, 2006). The Esperanza Granitoids are recognizable for their augengneiss and augenschist texture; the main minerals that compose this metaigneous rock are quartz, potassic feldspar and plagioclase. The Xayacatlán Formation, notable for eclogitic facies metamorphism, consists mainly of metagabbros, metabasalts and serpentinites with of chlorite, calcite, epidote and tremolite; related to these rocks there are greenschists and amphibolites (Ortega-Gutiérrez, 1978). Esperanza Granitoids and Xayacatlán Formation both comprise the Piaxtla Suite; these are interpreted as peri-Gondwanan continental and oceanic crust formed by felsic and mafic plutonism

generated by anatexis of continental crust (interpreted by some as similar to the Oaxaca Complex) and melting of lithospheric mantle, and sedimentation derived probably from the Oaxacan Complex; this assemblage was later subducted during Late Ordovician - Middle Devonian to reach eclogite facies metamorphism (Ortega-Gutiérrez *et al.*, 2018). The presence of 600 to 500 Ma inherited zircons in Esperanza Granitoids, which do not have equivalents neither in Oaxaquia nor in Laurentia, indicates provenance from intraplate sources in NE Gondwana and some older from the Amazonian Craton (Teixeira *et al.*, 1989; Ortega-Gutiérrez *et al.*, 2018). The Cosoltepec Formation is the most extensive metamorphic unit exposed in southern Mexico and is composed of phyllites and quartzites with some quartz veins and possible fragments of oceanic crust (pillow basalts, serpentinites). It has a pre-Devonian protolith age (Ortega-Gutiérrez, 1978; Ortega-Gutiérrez *et al.*, 2018). In the northern edge of Tlaxiaco basin adjacent to the Salado Fault there are metapelites and metapsammites with parallel foliation and quartz veins crossing it pertaining to Cosoltepec Formation; clasts of this nature are abundant in the Cualac conglomerate (Zepeda-Martínez, 2017); these are the actual nearest exposures of crystalline basement to the Tlaxiaco Basin. The youngest rocks of the basement are the Upper Carboniferous - lower Permian Tecomate Formation, of low metamorphic grade, and the similar aged Cozahuico and Totoltepec plutons; the ~275 Ma Cozahuico pluton was emplaced in the suture between the Acatlán and Oaxacan complexes (Ortega-Gutiérrez *et al.*, 2018).

Diquiyú unit

Ochoterena (1981) provides numerous descriptions of the Diquiyú unit in outcrop and in wells; he reported andesites, basalts and rhyolites, with amygdaloidal and fluidal structures, banded sometimes, and slightly metamorphosed some of them, also showing serpentinitization, epidotization, breccia development and cataclasis in some places. Zepeda-Martínez (2017) suggested greenschist facies metamorphism for the Diquiyú unit. Also, Zepeda-Martínez (2017) described magmatic folds, autobreccias and devitrification structures. The possible contact between Diquiyú unit and Acatlán Complex has been described by Ochoterena (1981) NW of San Juan Diquiyú along Santa

Catarina creek; also, Silva-Romo *et al.* (2015) reports Diquiyú unit resting over the Triassic La Mora Formation in the Ayuquila Basin. Although the upper contact of Diquiyú unit with Consuelo Group has been described as erosional (González-Torres, 1989; Durán-Aguilar, 2014), faulted (Jiménez-Rentería, 2004), and conformable (Zepeda-Martínez, 2017), in some wells reported in Cortés-Obregón *et al.* (1957) Ochoterena (1981) recognizes the presence of rocks of Diquiyú unit directly under Cualac conglomerate. González-Torres (1989) reports interbedding of the Diquiyú unit with the Consuelo Group rocks representing probable synchronous vulcanism and sedimentation. This interpretation is supported by the pepperites reported by Durán-Aguilar (2014) at the top of this unit. Most authors (Morán-Zenteno *et al.*, 1993; Jiménez-Rentería, 2004) have assigned a pre-Toarcian age for this unit, based on its position under Toarcian Rosario Formation age according to Erben (1956). A 197 - 184 My U-Pb date reported by Durán-Aguilar (2014) places Diquiyú unit in the Sinemurian-Pliensbachian stages. Nevertheless, this age, as discussed by Zepeda-Martínez (2017) is arguably imprecise due to its large uncertainty (less than 5% of ages and more than 15% discordance). Zepeda-Martínez (2017) obtained an age pattern from detrital zircons in Diquiyú unit rocks with Early Jurassic, Permian, Neoproterozoic, Mesoproterozoic ages and older isolated grains; these patterns show the crystallization age of the Diquiyú volcanic rocks (Early Jurassic) to inheritance from Permian Granites (Totoltepec stock, Cozahuico Granite), sedimentary successions (Matzitzi and Olinalá formations), and older basement rocks.

Consuelo Group (*sensu* Jiménez-Rentería, 2004)

Although Durán-Aguilar (2014) considered the subdivision of Consuelo Group between Rosario Formation and Prieto conglomerate as cartographically complicated and unnecessary due to the small areal extension of Prieto conglomerate, the present author considers this subdivision to be of use, at least for the stratigraphic discussion and the paleogeographic interpretation. In this sense the Consuelo Group will be considered, for now, as composed of the Rosario Formation in the lower part and Prieto conglomerate in the upper part.

Rosario Formation (*sensu* Jiménez-Rentería, 2004)

Ochoterena (1981) described this unit as composed of mudstone, siltstone, coal and sandstone with some conglomeratic lenses composed of igneous clasts of different rock types. This author mentioned the continental affinity of the Rosario Formation and excluded any possibility of marine influence in its deposit. Jiménez-Rentería (2004), in contrast, mentions the possible influence of marine deposits in Rosario Formation due to the presence of certain specific marine microfossils; this author also mentions the presence of a metavolcanic clast with a limestone included making possible the presence of older calcareous rocks such as in Olinalá Basin (Corona-Esquivel, 1981). According to Jiménez-Rentería (2004) the thickness of the Rosario Formation increases to the WSW, from 71 m in Rosario Nuevo locality to 137 m in El Consuelo; nevertheless, in this last locality the thickness may be repeated due to faulting. An interesting feature of this unit is its intertonguing relationship with the Prieto conglomerate (Jiménez-Rentería, 2004). The tongues of Prieto conglomerate increase in thickness and grain size towards the east of the Diquiyú Anticlinorium and upsection (Figure 2.4) making the thickest Rosario Formation outcrops appear in the western part of the Diquiyú Anticlinorium (Jiménez-Rentería, 2004). Another interesting feature of this unit and the overlying Prieto conglomerate is the abundant presence of plant and wood fossils up to meters in size. Zepeda-Martínez *et al.* (2018) reported the presence of synsedimentary faults and intraformational unconformities that could have been developed in a tectonically active basin. The most accepted age for this unit has been Early Jurassic (Toarcian-Aalenian, Erben, 1956), obtained by stratigraphic position; nevertheless, and because this unit is synchronic with Prieto conglomerate, the age of both units would be the same, Sinemurian in the sense of Jiménez-Rentería (2004) or Toarcian according Zepeda-Martínez *et al.* (2018).

Prieto conglomerate (*sensu* Jiménez-Rentería, 2004)

Jiménez-Rentería (2004) proposed the section exposed in Encinar de Castro hill, near Rancho Juárez (Figure 2.4), as a possible Prieto conglomerate formation type section. Unfortunately, this publication does not have validity to propose a formal unit. In this locality the intertonguing relationships with Rosario Formation are exposed. In the Rosario Nuevo locality, the Prieto conglomerate rests directly over the Diquiyú unit in fault contact (Jiménez-Rentería, 2004) or a conformable contact (Zepeda-Martínez *et al.*, 2018); there, the Rosario Formation does not crop out. The Prieto conglomerate varies in thickness from 67 m near Rosario Nuevo to 344 m near El Consuelo (Jiménez-Rentería, 2004); the thickness at El Consuelo (Figure 2.3) can result from repetition due to faulting. An observation by Jiménez-Rentería (2004) is the decrease in clast content of this to the west, accompanied by an increase in mudstones in the Rosario Formation. The upper contact with the Cualac conglomerate is described as erosional (Rancho Juarez locality, Figure 2.4), faulted (Rosario Nuevo Creek according to Jiménez-Rentería (2004)) or transitional (Rosario Nuevo Creek according Zepeda-Martínez *et al.* (2018)). The age of this unit has been inferred as Sinemurian by Jiménez-Rentería (2004) using palynomorphs and Toarcian by Zepeda-Martínez *et al.* (2018) using detrital U-Pb geochronology (179.4 ± 3.0 Ma, although they call this unit Rosario Formation), Permian-Triassic, Panafrican and Grenvillian zircon grains were also reported.

Durán-Aguilar (2014) reports that the base and middle parts of this unit contain Gci (lithofacies classification *sensu* Miall, 2006, see Table 4.1) interpreted as the result of high-energy and high-density flows which produced erosional bases and gave as a result lobular conglomeratic bodies. Gcm are the lithofacies that this author describes with most interest, and interprets this as the result of avalanches near active volcanic zones; and, together with Gt the author interprets these deposits as channel bedforms shaped by the energy of the traction currents and whose variations in grain size and textural organization are the result of flow energy variations. Although the author describes for the top of the Prieto conglomerate fluvial related lithofacies Gp, Gt he points out the influence of gravity related debris and density flows, but doesn't present any lithofacial evidence that can be interpreted as a definite result of those processes; the distribution of facies is interpreted as the result of bar migration in a fluvial environment.

Zepeda-Martínez (2017) described 150 m of the Prieto conglomerate their Rosario Formation to be composed of mainly conglomerates with clasts of the same composition as the Diquiyú unit. The principal lithofacies reported is coarse horizontal laminated conglomerates with imbrication features; this is interpreted by the author as longitudinal dune migration inside river channels. This author reports matrix-supported conglomerates, clast-supported inverse graded conglomerates and clast-supported massive conglomerates, all of which are interpreted as representing debris and density flows. Interbedded with this lithofacies are fine sandstones and siltstones with plane-parallel lamination that the author interprets as related to flooding events and filling of abandoned channels. The paleocurrents reported by this author and by Zepeda-Martínez *et al.* (2018) are towards the NW and NE quadrants. Zepeda-Martínez *et al.* (2018) interpret this unit as the proximal part of an alluvial fan.

Tecocoyunca Group (*sensu* Jiménez-Rentería, 2004)

Jiménez-Rentería (2004) cites previous observations made by Alencaster (1964) concerning the great lithologic and mineralogic variation between Rosario Formation and Prieto conglomerate with Cualac conglomerate, and proposes the inclusion of the latter in the base of Tecocoyunca Group. The present author considers this as appropriate, not only because of the marked contrast between Cualac conglomerate and the underlying units, but also because of the similarity between this unit and the overlying succession.

Cualac conglomerate (*sensu* Jiménez-Rentería, 2004)

Erben (1956) assigned the name of the Cualac conglomerate, although before it had been recognized in the Olinalá and Ayuquila basins and named differently (Jiménez-Rentería, 2004). Alluding to the low presence of conglomerates *sensu-stricto* in this unit, Jiménez-Rentería (2004) proposes the name Cualac quartzitic formation due to the ubiquitous presence of quartz clasts, and proposed the outcrops along Rosario Nuevo Creek as a paratype section. Recently, Zepeda-Martínez *et al.* (2018) renamed this unit as Cualac Formation, but did not discuss a type section. This unit has local thickness variations

from 30 m in Rosario Nuevo to 90 m in El Consuelo. Ochoterena (1981) discussed the possibility of an arid climate during Cualac conglomerate deposition revealed by the absence of secondary clay minerals.

Ochoterena (1981) proposed an interfingering relationship between Rosario Formation (*sensu* Erben, 1956) and Cualac conglomerate, assigning the same age to both units, and explaining this configuration as a result of coastline changes and local erosion windows (Diquiyú type volcanism only present in a small area). Thus, based on Erben (1956), Ochoterena (1981) assigned a Toarcian-Aalenian age to both Rosario Formation and Cualac conglomerate. The age of this unit before U-Pb dating detrital zircons became available was based on paleobotanical information. Jiménez-Rentería (2004) made a review of previous work on this issue, and concluded that only the articles published by Silva-Pineda (1970, 1984) deal with the plant fossils of the Cualac conglomerate. A Toarcian-Aalenian age is proposed, but this range of ages is uncertain because the geochronologic range of the fossils is wide. Jiménez-Rentería (2004), based on palynomorphs, determined an age range between the Pliensbachian and Aalenian. The MDA (maximum depositional age) obtained by Durán-Aguilar (2014) of 166.67 ± 9 Ma place the Cualac conglomerate in the Bathonian stage in the Middle Jurassic. This age obtained from a silty arenite, also shows a Silurian peak and a Grenvillian Mesoproterozoic grain population. Durán-Aguilar (2014) based on the MDA proposes this unit as a lateral facies change of lower Tecocoyunca Group (Zorillo, Taberna, Simón formations *sensu* Erben (1956)) resulting from a W towards E channel migration in fluvial systems. Zepeda-Martínez *et al.* (2018) also conducted U-Pb dating of two samples within this unit and obtained peaks mainly of Grenvillian, Panafrican, Ordovician - Carboniferous, Permian - Triassic and Lower Jurassic ages. These peaks can be well correlated at least in with the Cosoltepec Formation of the Acatlán Complex. An MDA obtained for a single sample is 183.9 ± 6.2 Ma, slightly older than the underlying Prieto conglomerate.

At least five authors have described the lithofacies in this unit obtaining similar conclusions. Morán-Zenteno *et al.* (1993) reported plant remains. Described a lenticular

geometry that thins out laterally, and propose that proximal alluvial fans developed in extension during deposition. Jiménez-Rentería (2004) differentiates two intervals and describes the lower as composed of conglomeratic and coarse grained sandstones, and the upper one with predominance of medium-fine sandstones and mudrocks. The author interpreted the succession as formed by the action of meandering rivers in the lower part, and braided rivers in the upper part. Durán-Aguilar (2014) described the base of the Cualac conglomerate and relate the lithofacies to the fill of active and abandoned channels by migrating anastomosed streams; one lithofacies (Gmg) due to its matrix supported state could represent local gravity density flows or flash-floods. The author proposed a NW-SE paleocurrent direction. Vite del Ángel (2014) described the upper 78 m of Cualac conglomerate in which he found cross-bedded conglomerates, sandstones, siltstones, and mudstones with plant fossils; the author interpreted these rocks as being deposited by a braided river. According to De Anda Garcia (2008) these rocks show a SW paleocurrent direction and carry sediment eroded from the Oaxacan Complex. Zepeda-Martínez *et al.* (2018) measured 96 m of this unit, in which they described several lithofacies associated with the processes of bar migration inside fluvial channels of braided nature and filling of abandoned channels. These lithofacies are: conglomerate with planar and concave cross lamination, sandstones with planar cross lamination and ripples, and fine sandstones and siltstones with plane-parallel stratification. These authors interpret the middle part of an alluvial fan or a braided river system.

I do not include here a detailed description of the overlying Tecocoyunca Group units because of their low significance to this study.

3. Paleomagnetic methods and results

3.1 Methods

This research involved paleomagnetism and stratigraphic-petrologic analysis. The paleomagnetic approach initiated with an eight days field campaign. Twenty one sites in Jurassic aged rocks were sampled, nine with a portable drill core and 12 with oriented hand samples, chosen for the difficulty of drilling these sites in the field. Site locations are shown in Figure 3.1. All localities correspond to rocks in the Diquiyú unit (andesites, basaltic andesites, dacites, and minor rhyolites), each locality represents a single lava flow, and the petrologic characteristics were described using standard petrographic principles (Streckeisen, 1980; McPhie *et al.*, 1993; MacKenzie *et al.*, 1982). From each locality a minimum of 7 cores were drilled and oriented *in situ* with magnetic compass (corrected for +4 declination according to NOAA) and with sun compass (direction calculated using SUNUSGS software). The orientation used was the media between magnetic and sun compass measurements. From each core a minimum of one and a maximum of three specimens (2.5 cm diameter, 2.1 cm height) were obtained. A total of 227 specimens were subjected to AFD (Alternating Field Demagnetization, 62 specimens), THD (Thermal Demagnetization, 134 specimens), and mixed (31 specimens) procedures. For this we used an AGICO LDA-3A alternating field demagnetizer, one degausser system of alternating fields (600), and an ASC Scientific TD-48SC furnace. The demagnetization steps were independent in each specimen according to pilot studies used to infer their magnetic mineralogy; the softer fractions (titano-magnetite or magnetite dominated) were demagnetized using AFD in incremental steps of 5 mT until reaching 50 mT, then in steps of 10 mT up to 90 mT; some samples were subjected to alternating fields of up to 160 mT. The specimens with harder magnetic fractions (SD-PSD magnetite, hematite dominated) were treated with THD in incremental steps of different values using the smaller increments (10°C) in the range between 400 °C - 580 °C (titanomagnetite-magnetite unblocking temperature ranges).

The measurement of the NRM after each demagnetizing step was made on an AGICO JR6 magnetometer (111 specimens) located in the Paleomagnetism and Rock Magnetism Laboratory of the Centro de Geociencias (CGEO) of the Universidad Nacional Autónoma de México (UNAM), and on a 2G Enterprises Superconducting Rock Magnetometer 755-4K (116 specimens) located in the Paleomagnetism Laboratory of the Instituto de Astronomía y Geofísica (IAG) of the Universidade de Sao Paulo (USP). In order to characterize the magnetic mineralogy, an IRM (Isothermal Remanent Magnetization) acquisition curve was obtained for one specimen for each site applying pulses from 10 to 3000 mT; we used a MMPM-10 Pulse Magnetizer, and measured each step in the JR6 magnetometer. DC demagnetization or backfield curves were determined for each specimen. For acquisition of hysteresis loops we used a Princeton Measurements Corp. Micromag 2900 Alternating Gradient Magnetometer (AGM) for samples from 15 sites; all the rock magnetic experiments were made on CGEO facilities.

The results from the demagnetization experiments were inspected and analyzed using the AGICO Remasoft 3.0 software (Chadima & Hrouda, 2006); this software displays the demagnetization behavior using Zijderveld diagrams (Zijderveld, 1967). With visual analysis the user selects the demagnetization ranges that better define each component; and, with principal component analysis (Kirschvink, 1980) the declination, inclination and a precision estimate called MAD (Maximum Angular Deviation) were calculated for each component. Only the components with MAD lower than 12° were used for site mean calculations, although in site DDP13 MAD values lower than 15° were considered. The site mean calculations were obtained using Fisher statistics (Fisher, 1953) whose results provide the best estimate of the precision parameter k , and the confidence interval of the mean α_{95} ; only the site means with $k > 10$ and $\alpha_{95} < 20^\circ$ were considered for VGP calculations. A double structural correction was applied to all sites; the first one considers the shallow dip of the Cenozoic lava flows overlying the anticline that expose the Diquiyú unit, and the second one considers the dip of the sampled strata. For the final calculations we included sites reported in Molina-Garza *et al.* (2014).

The IRM acquisition curves were modeled using methods described by Kruiver (2001), which are based on the coercivity spectra of each sample. The hysteresis parameters H_c , M_{rs} and M_s were obtained directly from the hysteresis loop, whilst the parameter H^{**cr} was calculated using the Ascending-Descending loops vs. applied field (Figure 3.1). H^{**cr} is the value of the field necessary to reduce the ascending-descending difference to the half of the maximum value (Tauxe, 2005). The description of each site's magnetic mineralogy was detailed with reflected petrography analysis using an Olympus BX-RLA2 reflected light brightfield/darkfield illuminator using the 10X and 50X ocular magnifications. The oxide textures were better described with SEM (scanning electron microscope) analysis in a magnification scale from x100 to x20000; using a SEM model TM-1000 of Hitachi and housed in the CGEO. Finally, an Oxford energy dispersive X-ray spectroscopy (EDS) coupled to the SEM was used for a qualitative view of the elemental composition of the magnetic minerals; it was set to a voltage of 15kV and collected from 500 to 1200 counts per spot analyzed. The spot size is generally 50 nm wide and has 1 mm of penetration.

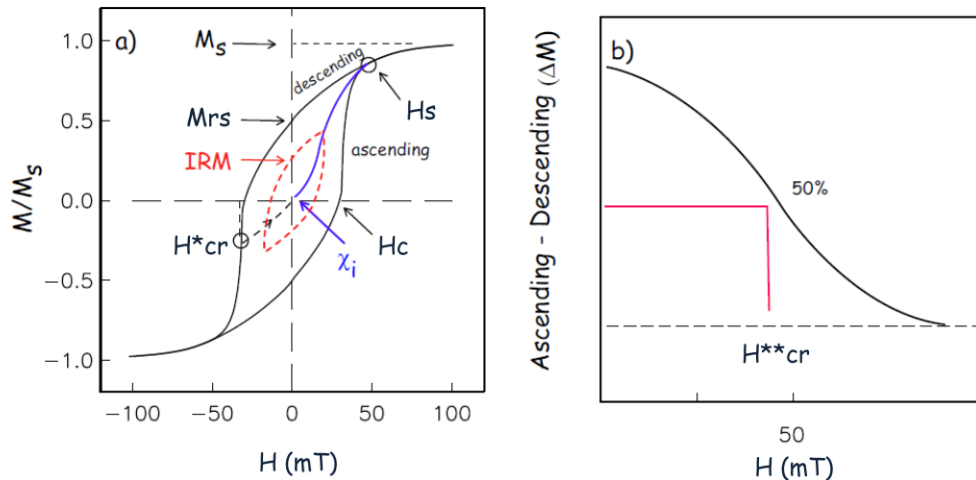


Figure 3-1. Hysteresis parameters used in this study to characterize the magnetic mineralogy of the analyzed rocks. Modified from Tauxe (2005)

3.2 Results

3.2.1 Field observations

A series of volcanic rocks with different characteristics crops out in the core of the Diquiyú Anticlinorium. Individual site descriptions, hand sample characteristics and petrography are included in Appendix 1. Sites DDP03, DDP04, DDP05, and DDP06 (Figure 3.2) are similar, and correspond to blue aphanitic volcanic rocks, likely andesite, forming a succession of at least 100 m (Figure 3.3 A, B); at the top of this succession a brownish blue rock with brecciated character is present, this can be an auto-breccia or an aa type lava. Sites DDP11, DDP12 and DDP14 crop out in more isolated patches, and have a brownish-red color (Figure 3.3 C); many of these isolated outcrops are crossed by numerous quartz and calcite veins.

Sites DDP13, DDP15 and DDP16 were sampled along the western flank of the Diquiyú Anticlinorium. Site DDP15 corresponds to an auto-breccia constituted by andesite fragments in a small outcrop; nevertheless, its structural position below Rosario Formation was clear. On the other hand, the structural position of DDP13 could not be determined due to its isolation and lack of contacts. The relationship of site DDP16 with Diquiyú unit volcanism its ambiguous, it is interbedded with Rosario Formation mudstones developing a thin layer of green clay (Figure 3.3 E) that is interpreted as a baked contact; this observation suggests that site DDP16 may be a sill-like intrusion, post-dating Diquiyú unit.

Sites DDP17, DDP18, DDP19, DDP20 and DDP22 were all sampled on a section of andesites interbedded with rhyolites (Figure 3.3 F); volcanic breccias composed of an andesitic-rhyolitic matrix with andesite fragments of various sizes are interbedded in this section (Figure 3.3 G,H).

The paleomagnetic sampling focused on aphanitic volcanic rocks whose flow surfaces were measurable in the field. This was possible at all localities except in DDP14 (Figure 3.3 D); in this case the attitude of the closest lava flow was measured.

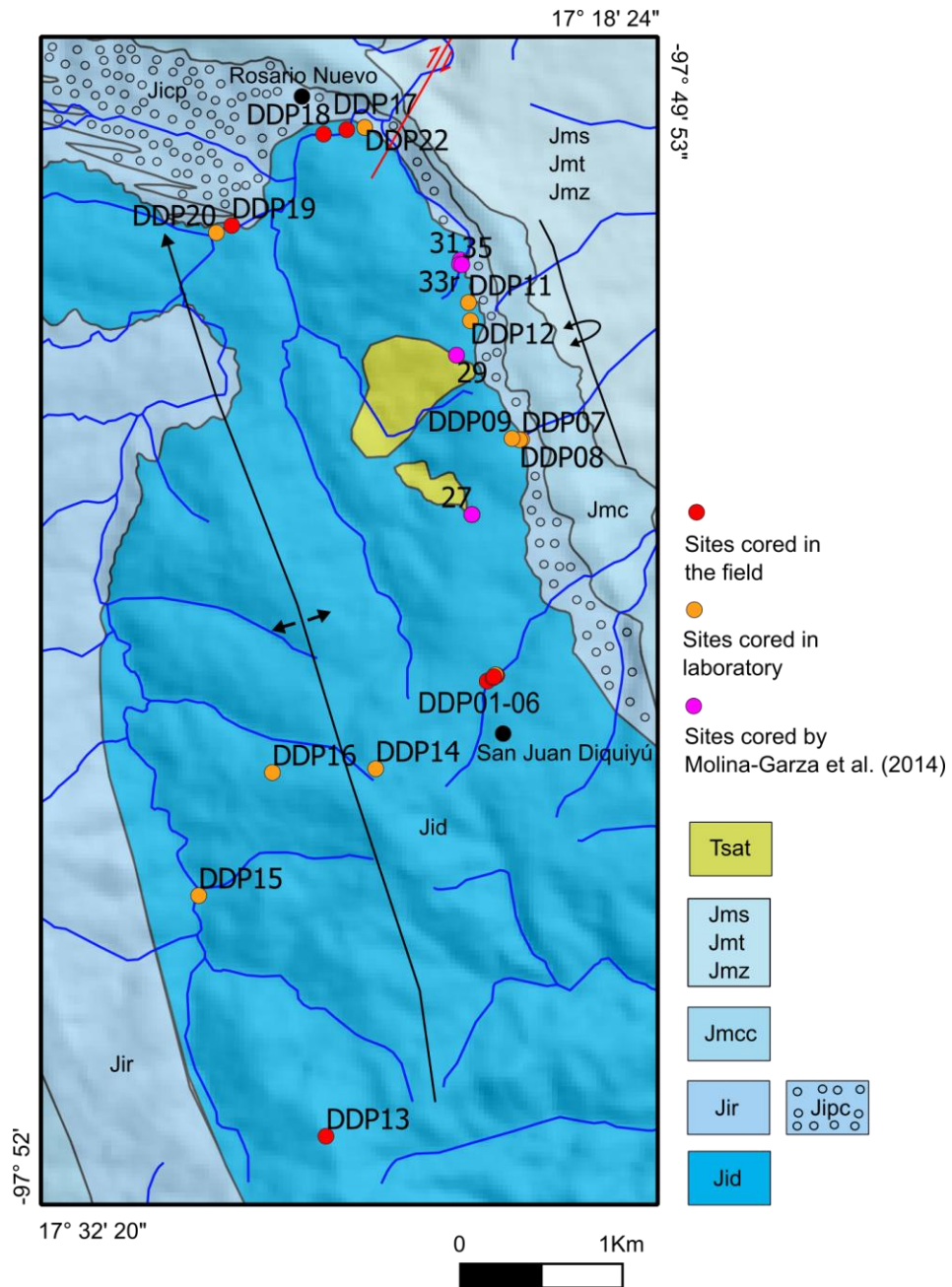


Figure 3-2. Sites sampled in San Juan Diquiyú area for paleomagnetic study. Labels as in figure 1.4.



Figure 3-3. Field photos of Diquiyú unit outcrops. A, B) Laminated andesites, different from A, B contains rocks with brecciated character; C, D) Andesites and vitrophyres crossed by hematite and calcite veins, also, an alteration coating covers the surface of the outcrops; E) Sill like andesitic intrusion of site DDP16, the volcanic rock has a porphyritic texture and develops a baked contact with the surrounding mudstones; F) Laminated andesites and rhyolites; G, H) Andesitic auto-breccia, fragments of vesicular andesite are included inside an andesitic-rhyolitic matrix which also develops folding.

3.2.2 Microscopy

Petrography

All the sites analyzed in this study show similar characteristics under the microscope, and these are described in Appendix 1. The rock type is principally andesitic with variable contents of phenocrysts and matrix. The principal constituent of almost all the samples is plagioclase, present both as a matrix (0.01 mm – 0.1 mm) and as phenocrysts (0.5 mm – 1 mm). Sites DDP02, DDP09, DDP13, DDP17, DDP18, DDP19, DDP20, and DDP22 are composed almost exclusively of plagioclase; in some of these sites a marked pilotaxitic texture is observable (Figure 3.4 D, G, H). A typical form in which plagioclase occurs is as phenocrysts floating in the matrix. This is observed in almost all the samples (Figure 3.4 A-E, G), and could represent a pre-eruptive phase of crystal growth; often these phenocrysts have a secondary alteration to sericite but the rocks are not metamorphic.

Sites DDP01, DDP04, DDP07, and DDP08 have the highest content of a cryptocrystalline aggregate of quartz and feldspar (Figure 3.4 A–C); this aggregate is interpreted as devitrified glass and is the principal constituent of sites DDP01, DDP07, and DDP08, and a secondary component of sites DDP03, DDP04, DDP06 and DDP12 where the crystalline phase is predominant; nevertheless, all the sites have this aggregate as part of their matrix in different percentages. Sites DDP01, DDP07 and DDP08 have a mesoscopic and microscopic banded structure marked principally by the variation of crystal size (Figure 3.4 C).

A third primary component is ferromagnesian silicate minerals (*e.g.* hornblende, pyroxene, biotite), these minerals are present in low (<5%) percentage; but due to their replacement by opaque minerals their properties could not be described. Some secondary features, such as amygdales filled with quartz-chlorite-calcite are common in several sites, but of great visual importance in sites DDP01, DDP09 and DDP11; opaque minerals border the outer parts of these vesicles (Figure 3.4 A, E). Sites DDP17 and DDP18 have voids filled with calcite. Quartz, calcite and hematite veins are ubiquitous (Figure 3.4 C). DDP15 is a singular site, is composed of angular rock fragments with all the previous described characteristics (Figure 3.4 H).

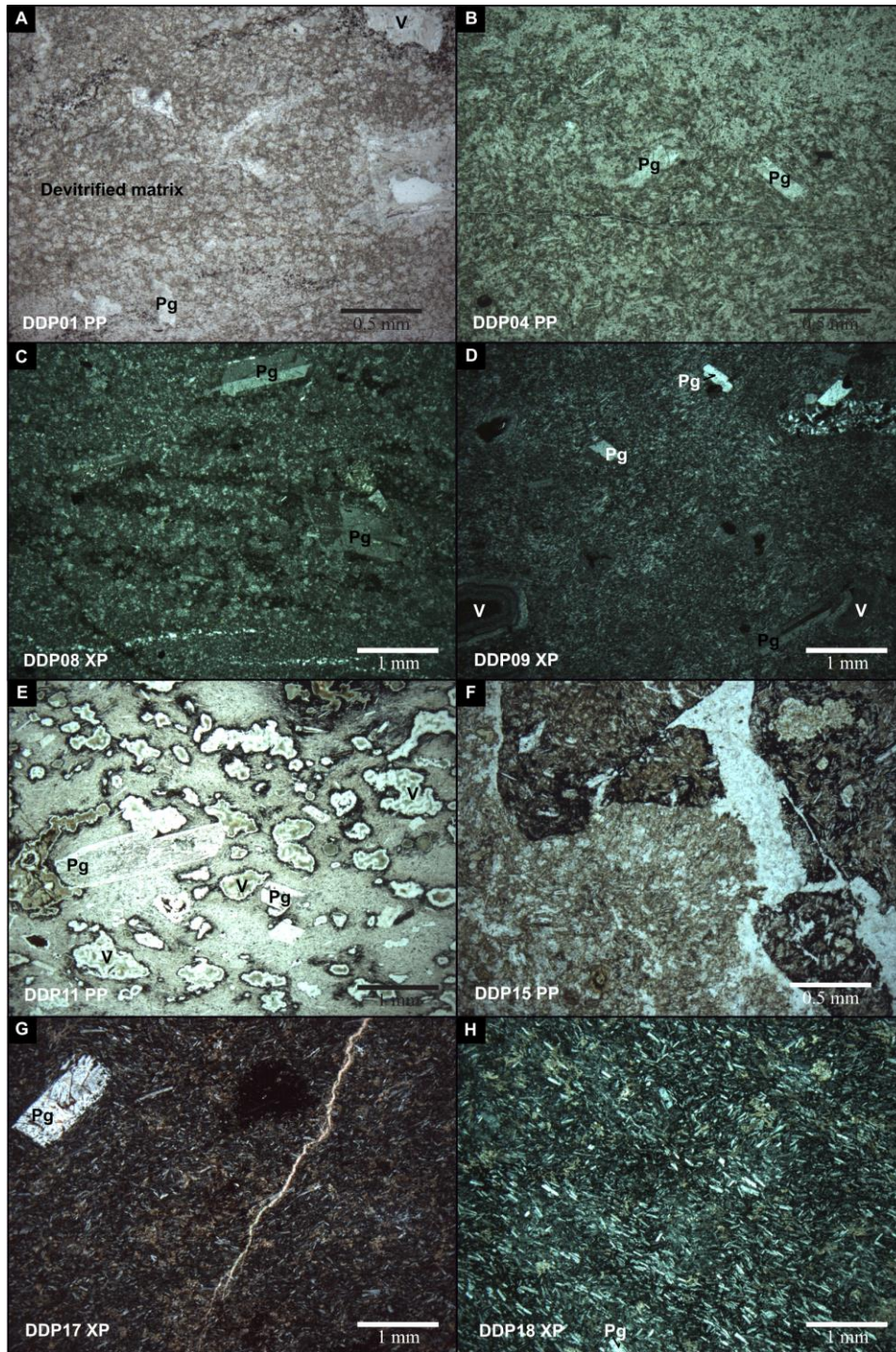


Figure 3-4. Photomicrographs showing the most important petrographic features of the sampled Diquiyú unit rocks. Pg – Plagioclase, V – Vesicle. A) Extrusive rocks composed primarily by a quartz-feldspar matrix with saccharoid texture; B) Andesite with intermediate content of devitrified matrix; C) Banded vitrophyre with plagioclase phenocrysts; D) Andesite with vesicles and plagioclase phenocrysts; E) Andesite fully crossed by chlorite filled vesicles; F) Auto-breccia composed of andesitic rock fragments cemented by quartz; G – H) Andesites composed by plagioclase with marked pilotaxitic texture.

Reflected light petrography

Diquiyú unit samples contain opaque minerals showing different oxidation stages (Watkins & Haggerty, 1967). The most abundant mineral observed at all sites is magnetite, and it is present as subhedral to anhedral crystals dispersed in the plagioclase matrix of the andesites as well as inside some ferromagnesian grains (*e.g.* DDP03, 06). Samples for sites as DDP03, DDP06 (and DDP04, DDP05) show magnetite as the only ferrimagnetic phase, appearing as subhedral crystals of various size ranges, from $<10\ \mu\text{m}$ to $\sim 0.2\ \text{mm}$ (Figure 3.5 B). Images and descriptions of reflected light microphotographs are provided in Appendix 1. Most crystals described in this section are larger than $100\ \mu\text{m}$, so they don't contribute significantly to the NRM; nevertheless, the optical properties of finer crystals are difficult to describe using normal petrographic microscopes, so, I infer that some of the characteristics of the larger crystals may be present in the finer ones, which contribute largely to the NRM. Some of the larger magnetite crystals develop a maghemitic coating, resulting of low temperature oxidation, and hence, are of secondary origin. All the other sites are composed of both magnetite and hematite as magnetic minerals present, and from other Fe oxide phases as ilmenite and martite (Figure 3.5).

In the largest crystals it is possible to recognize complex intergrowth patterns. For instance, a primary intergrowth of magnetite and ilmenite is observed in DDP11 (Figure 3.5 E), while an intergrowth between ilmenite and hematite is shown by sites DDP08 and DDP09 (Figure 3.5 C, D). Other sites DDP14, DDP18, and DDP20 show intergrowth textures of magnetite-ilmenite-hematite in variables degrees, this texture reflects a higher degree of high temperature oxidation. The highest degree of this type of oxidation, common in igneous eruptive rocks (Watkins & Haggerty, 1967), is observed in sample DDP18 where a hematite-rutile intergrowth is developed (Figure 3.5 G). All these textures may be the exsolution products of an original titanomagnetite. Finally, some needle-shape crystals of hematite are ubiquitous in sites DDP01, DDP09, DDP11, DDP14 and DDP20 (Figure 3.5 D, E, H); the hematite needles are distributed across the matrix, bordering magnetite-ilmenite crystals, as well as in veins. Restricted hematitic patches are common in DDP14 (Figure 3.5 F).

Scanning electronic microscope (SEM)

SEM observations allow a refinement of petrographic observations due to the higher spatial resolution, and together with the EDS qualitative compositional assessment, grant a better classification of the magnetic mineralogy. Images and descriptions of SEM images are detailed in Appendix 1. Magnetite shows different shapes from euhedral (Figure 3.6 A, H), subhedral (Figure 3.6 G) to anhedral (Figure 3.6 F), and a wide range of sizes from less than 5 μm in diameter (Figure 3.6 C, E, G) to crystals bigger than 300 μm (Figure 3.6 H). The EDS spectrum show that the number of counts detected in the energy intervals relatable to Ti atoms vary from 0% to 40%, this fact classifies most crystals as titanomagnetites (See Appendix 1). The mode of occurrence of titanomagnetite is mainly as dispersed crystals in the matrix, but they also occur as inclusions in ferromagnesian silicate grains (Figure 3.6 C).

Ilmenite is found both as isolated crystals of probable primary origin (Figure 3.6 G) and as lamellae coexisting with hematite and rutile (Figure 3.6 D, E). Hematite occurs in two ways, the first and most common is as needle shape crystals dispersed throughout the matrix and bordering other crystals (Figure 3.6 B, E) and as lamellae growing together with ilmenite and rutile (Figure 3.6 D, E). Rutile is the Ti richest fraction and is present in the hematite-rich sites (DDP08, DDP09, DDP11, DDP12, DDP14, DDP18, and DDP20) as inclusions in the largest ilmenite-hematite crystals.

Although these microscopic techniques are the most direct means to observe the magnetic mineralogy of the sites, they are size-biased as one can only observe crystals as small as $\sim 1 \mu\text{m}$; the magnetic minerals able to carry a remanence for geologic time periods are of nanometric scale (for the magnetite-ulvospinel series), so, other techniques are needed to describe the properties at these scales.

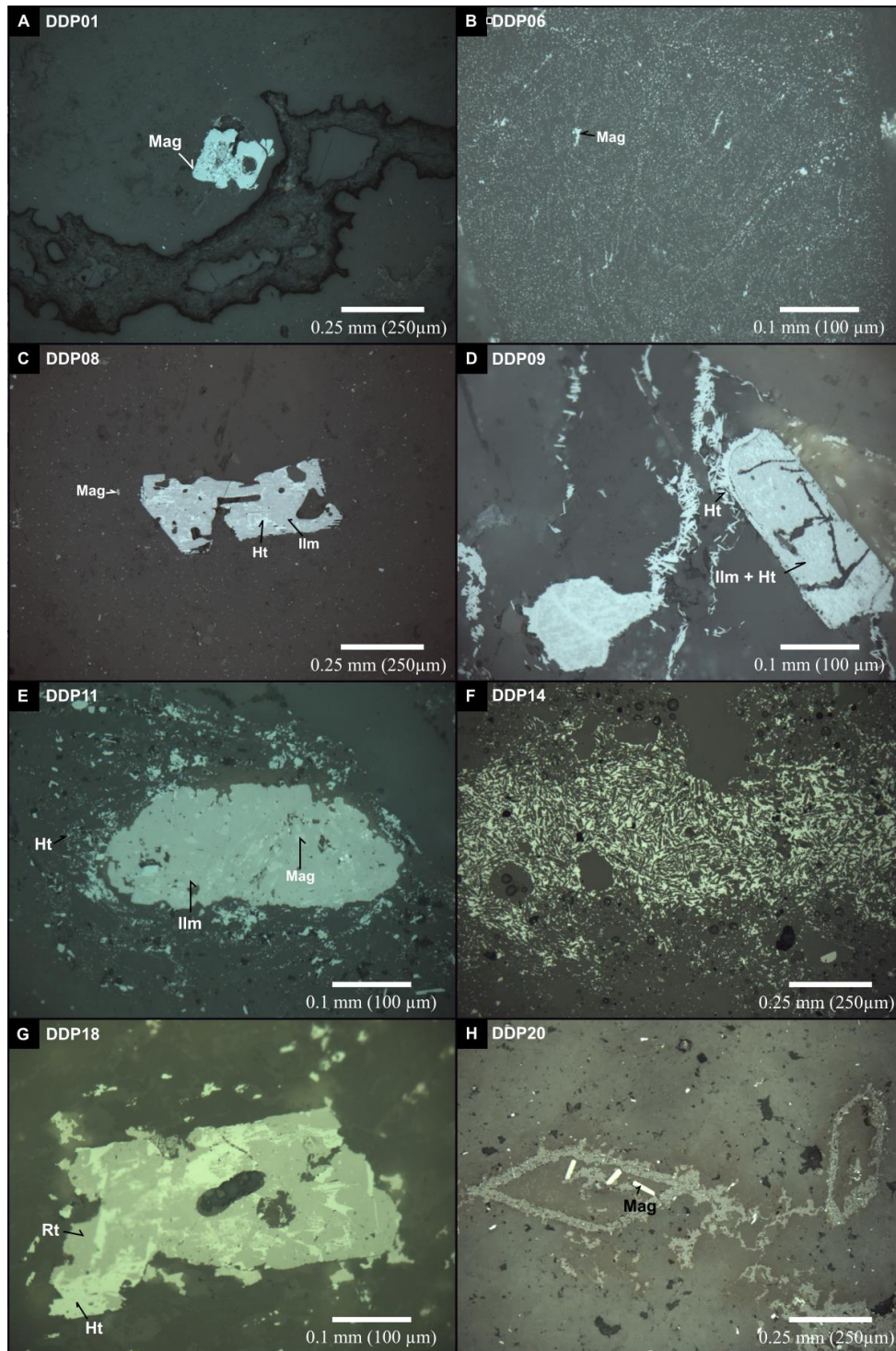


Figure 3-5. Photomicrographs showing the most important petrographic features in reflected light of the sampled Diquiyú unit. Mag – Magnetite; Ilm – Ilmenite; Ht – Hematite; Rt – Rutile.

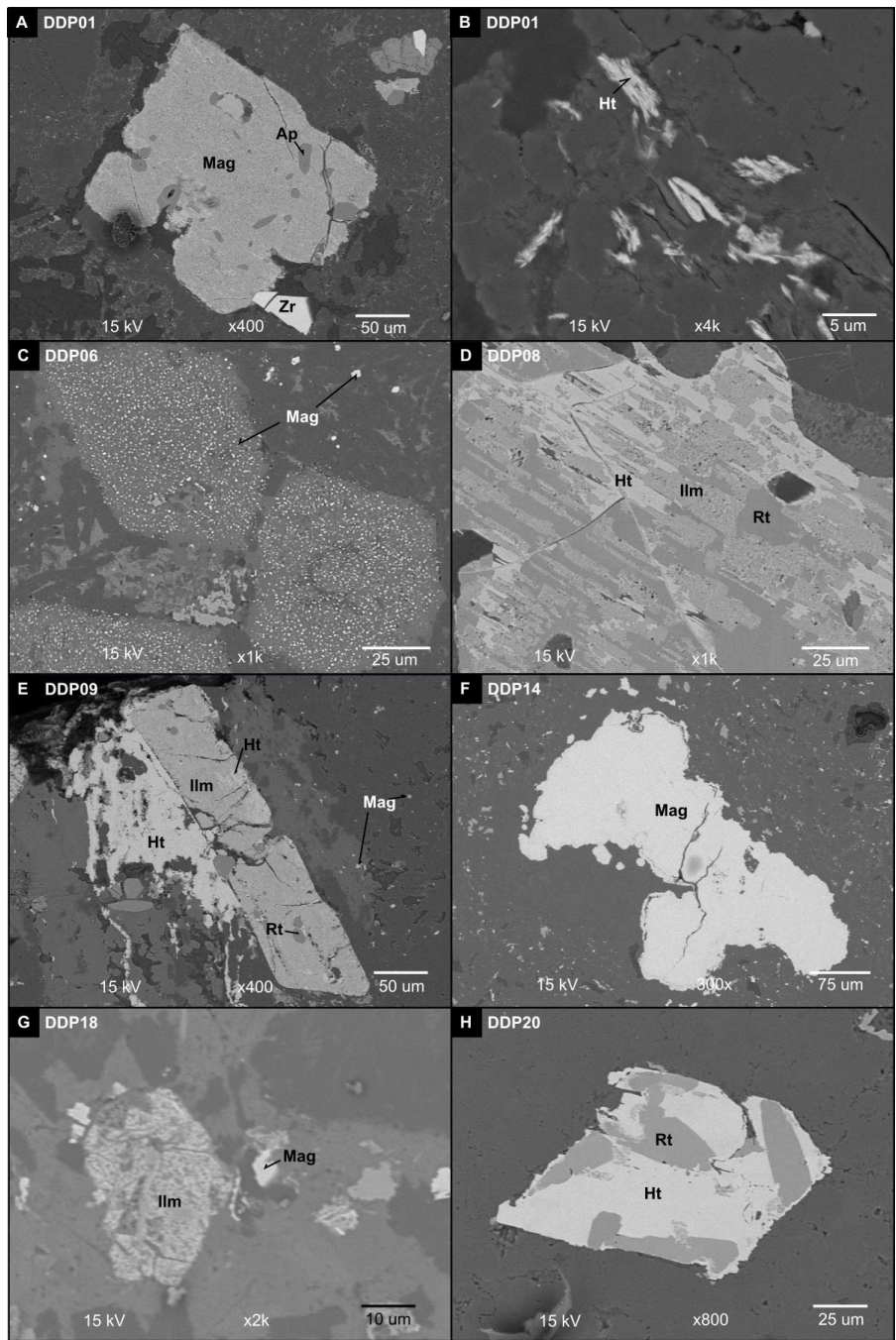


Figure 3-6. Scanning electron microscope (SEM) photomicrographs of the sites sampled in the Diquiyú unit. Mag – Magnetite; Ilm – Ilmenite; Ht – Hematite; Rt – Rutile; Ap – Apatite; Zr – Zircon.

3.2.4 Rock Magnetism

Isothermal remanent magnetism (IRM)

In the following section the IRM results are presented (Figure 3.7), together with an interpretation of different coercivity components (Table 2.1, Figure 3.8), according to the method of Kruiver *et al.* (2001). Additional results are presented in Appendix 2.

Sites DDP02, DDP03, DDP05, DDP06, DDP13, and DDP15 reach saturation at ~0.3 T or less showing an abrupt increase in magnetization in low fields. In backfield IRM experiments, the curves never crossed the horizontal scale; instead the IRM increase after the curve reaches values close to zero (*e.g.*, sample 01CZ in figure 3.7). In backfield demagnetization curves, sites DDP02, DDP03, DDP05, DDP06, DDP13, and DDP15 reach close to zero magnetization values at ~100 mT or less. Sites DDP07 and DDP08 show similar behavior but they reach saturation at lower fields (~200 mT). Site DDP09 does not reach saturation at 0.5T and site DDP11 at ~2 T. Sites DDP12, DDP14, DDP18, and DDP20 do not reach full saturation after applying a field of 3 T, and during backfield demagnetization they reach close to zero values at 100 mT- 300 mT. DDP16 is far from reaching saturation at 3 T, and appears to reach zero values during backfield at ~500 mT.

The samples were modeled with two to four components (Figure 3.8). Low coercivity components contribute the most to the IRM. These are components with a $B_{1/2}$ of about 18 to 80 mT. In some samples only low coercivity components (<80 mT) are present (DDP02, DDP08), but generally low coercivity components make about 30 to 50 % of the IRM. In DDP16 the contribution from low coercivity phases is minor (~10%). High coercivity components (>100 mT) are present in nearly all samples, but very high coercivities (>300 mT) are observed in a handful of samples (*e.g.*, DDP01, DDP11, DDP12, DDP14, DDP16, DDP18, DDP19, and DDP20). In DDP13 the contribution from very high coercivity components is minor (~5%), but in others it makes about 15 to 50% (Table 3.1). This suggests that hematite is a relevant ferromagnetic phase in a number of samples. DDP11, DDP14, and DDP18 show components with coercivities >1000 mT attributed to Goethite, this mineral phase may be present as a result of weathering.

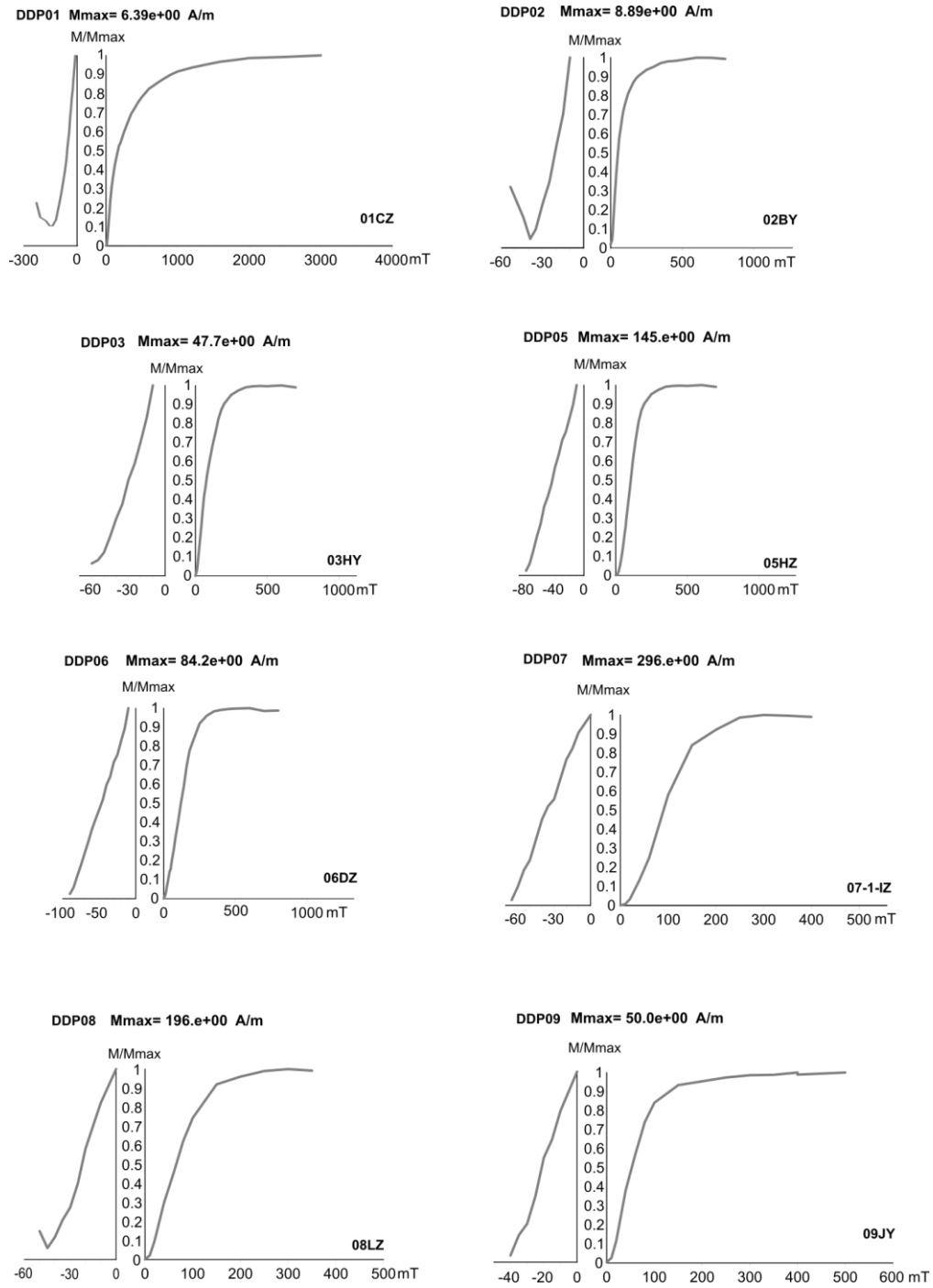


Figure 3-7. Isothermal remanent magnetism (IRM) acquisition and backfield demagnetization plots for all analyzed sites, normalized to the maximum value of IRM.

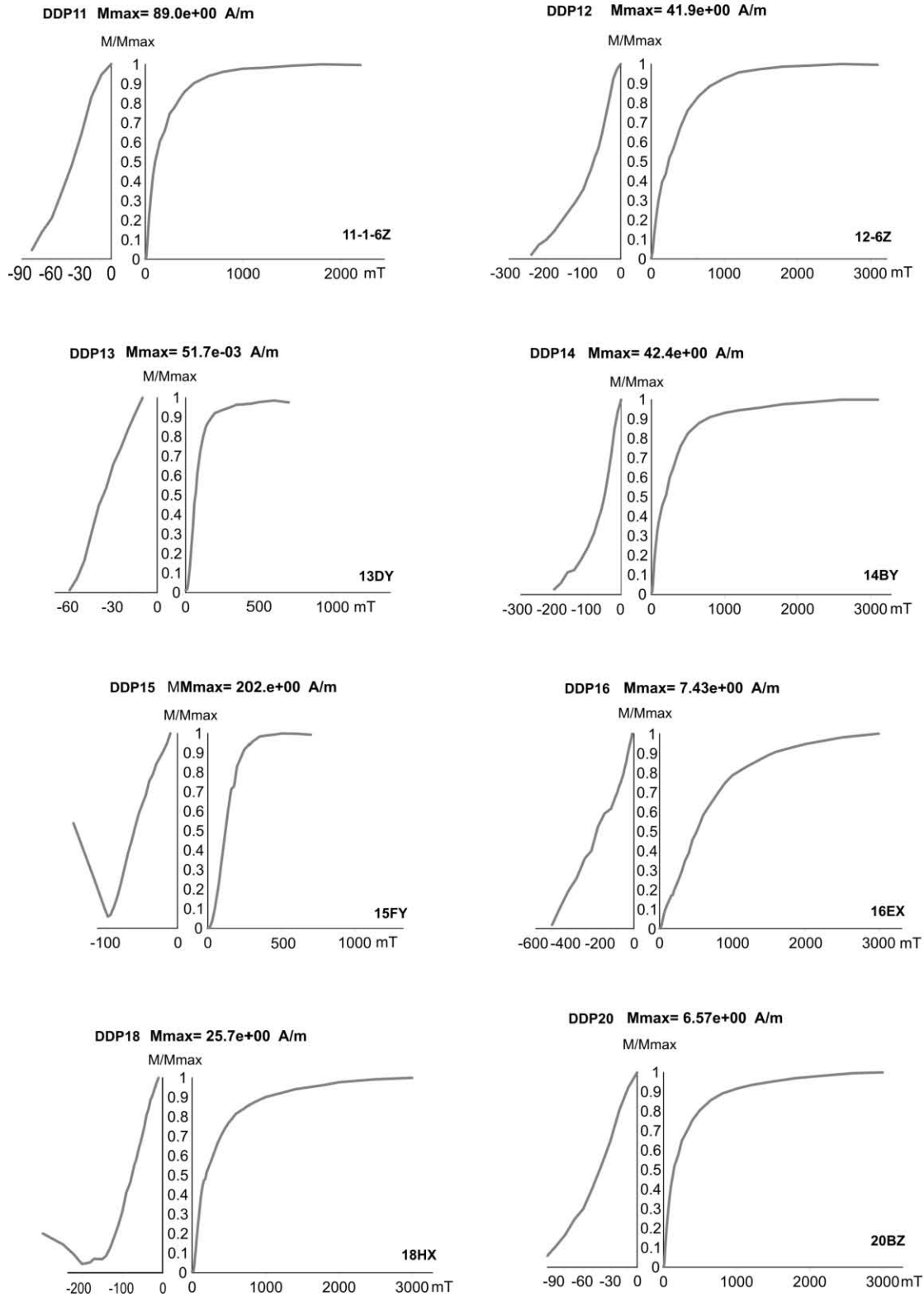


Figure 3.7 continued. Isothermal remanent magnetism (IRM) acquisition and backfield demagnetization plots for all analyzed sites, normalized to the maximum value of IRM.

Table 3-1. Components used to model the IRM acquisition curve of selected samples, according to Kruiver *et al.* (2001). The S-ratio is calculated by the classical formula $-\text{IRM}_{-0.3\text{T}}/\text{IRM}_{1\text{T}}$ (Only for site DDP16 the formula $1-\text{IRM}_{-0.3\text{T}}/\text{IRM}_{1\text{T}}/2$ by Bloemendal *et al.* (1992) is used) if no magnetic interaction occurs and the hysteresis loop is closed from 300 mT on, then the S-ratio correspond to $2*(\text{IRM}_{+0.3\text{T}}/\text{IRM}_{1\text{T}}) - 1$ (Kruiver *et al.*, 2001).

Sample	Component	Contribution (%)	SIRM (A/m)	log(B1/2) (mT)	B1/2 (mT)	DP (mT)	S-ratio
DDP01	1	47.7	3.1	1.8	63.1	0.36	0.433
	2	10.8	0.7	2.42	263	0.31	
	3	41.5	2.7	2.72	524.8	0.39	
DDP02	1	100	8.87	1.71	51.3	0.43	0.928
DDP03	1	67.7	32.5	1.7	50.1	0.39	0.945
	2	32.3	15.5	2.12	131.8	0.2	
DDP05	1	33.1	48	1.85	70.8	0.35	0.960
	2	66.9	97	2.05	112.2	0.19	
DDP06	1	21.3	18	1.5	31.6	0.37	0.921
	2	78.7	66.5	2.13	134.9	0.21	
DDP07	1	38.6	115	1.76	57.5	0.34	0.980
	2	61.4	183	2.02	104.7	0.18	
DDP08	1	35.2	70	1.5	31.6	0.35	0.990
	2	64.8	129	1.9	79.4	0.23	
DDP09	1	18.6	9.5	1.3	20	0.28	0.936
	2	70.6	36	1.74	55	0.24	
	3	10.8	5.5	2.3	199.5	0.45	
DDP11	1	12.3	11	1.37	23.4	0.24	0.604
	2	50.4	45	1.82	66.1	0.3	
	3	35.3	31.5	2.51	323.6	0.26	
	4	2	1.8	3.13	1349	0.09	
DDP12	1	14.2	6	1.5	31.6	0.3	0.221
	2	28.9	12.2	1.95	89.1	0.26	
	3	42.7	18	2.57	371.5	0.2	
	4	14.2	6	3	1000	0.21	
DDP13	1	9.3	0.0048	1.4	25.1	0.4	0.911
	2	84.9	0.044	1.82	66.1	0.26	
	3	5.8	0.003	2.6	398.1	0.22	
DDP14	1	61	26	1.86	72.4	0.46	0.403
	2	28.2	12	2.55	354.8	0.16	
	3	10.8	4.6	3.1	1258.9	0.22	
DDP15	1	43.9	90	1.99	97.7	0.39	0.899

	2	56.1	115	2.1	125.9	0.17	
DDP16	1	8	0.6	1.67	46.8	0.33	0.382
	2	6.6	0.5	1.9	79.4	0.22	
	3	85.4	6.42	2.8	631	0.34	
DDP18	1	16.5	4.3	1.67	46.8	0.32	0.390
	2	34.6	9	1.97	93.3	0.19	
	3	34.6	9	2.58	380.2	0.2	
	4	14.2	3.7	3.15	1412.5	0.2	
DDP19	1	84.7	11.6	1.74	55	0.26	0.826
	2	5.8	0.8	2.58	380.2	0.14	
	3	9.5	1.3	3.05	1122	0.4	
DDP20	1	25.5	1.7	1.5	31.6	0.35	0.522
	2	37.5	2.5	2.1	125.9	0.34	
	3	31.5	2.1	2.62	416.9	0.36	
	4	5.4	0.36	3.25	1778.3	0.21	

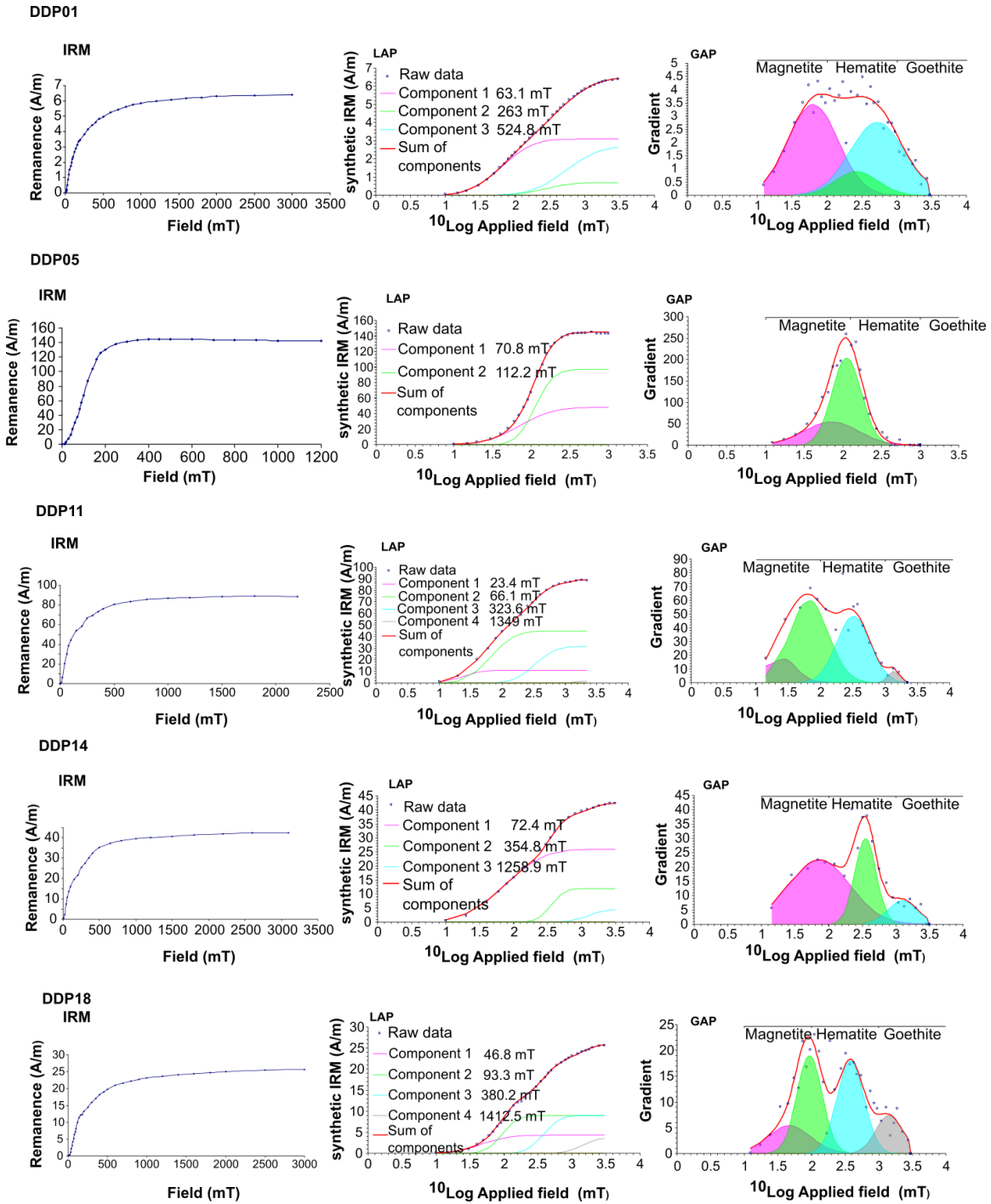


Figure 3-8. Isothermal remanent magnetization (IRM) acquisition curve and modeled results using linear acquisition plot (LAP) and gradient acquisition plot (GAP) after Kruiver et al. (2001). Blue squares represent raw data, purple, green, and blue lines and polygons represent the different interpreted components. $B_{1/2}$ values are indicated in the LAP diagram for each component. Interpreted magnetic minerals in GAP after Abrajvitch et al. (2009).

Hysteresis parameters

Hysteresis loops together with hysteresis ratios (H_{cr}/H_c , M_{rs}/M_s) are widely used as proxies for discriminating different magnetic phases and grain sizes; these data are presented in this section. A summary of hysteresis parameters is shown in Table 3.2. The loops vary from pot-bellied to wasp-waisted (Figure 3.9).

The samples analyzed (Table 3.2, Figure 3.10) have typical hysteresis ratios in the pseudo-single domain range, with relatively high M_{rs}/M_s ratios greater than 0.2, but these ratios are low in DDP06 and DDP09. H_{cr}/H_c ratios are high, but this is likely caused by the presence of hematite.

Table 3-2. Hysteresis parameters for Diquiyú unit samples

Sample	M_{rs} (Am ²)	M_s (Am ²)	H_{cr} (H^{**}_{cr}) (mT)	H_c (mT)	M_{rs}/M_s	H_{cr}/H_c
DDP04	0.5858	3.274	126	23.16	0.178925	5.440415
DDP05	0.7362	5.243	135	18.71	0.140416	7.215393
DDP06	0.257	3.19	145	10.6	0.080564	13.67925
DDP07	2.03	8.17	75.3	26.6	0.24847	2.830827
DDP08	1.02	4.12	70.2	23.8	0.247573	2.94958
DDP09	0.1582	1.458	40	7.91	0.108505	5.05689
DDP11	0.3975	1.703	49.7	20.84	0.233412	2.384837
DDP12	0.1865	0.6473	97	29.93	0.28812	3.240895
DDP14	0.2074	0.9133	89	19.46	0.227089	4.573484
DDP15	0.575	1.758	90.3	40.35	0.327076	2.237918
DDP17	0.05436	0.2221	49.7	22.31	0.244755	2.227701
DDP18	0.06128	0.2316	80.3	39.13	0.264594	2.052134
DDP19	0.05044	0.1901	19.5	17.82	0.265334	1.094276
DDP20	0.05289	0.2387	115	35.54	0.221575	3.235791

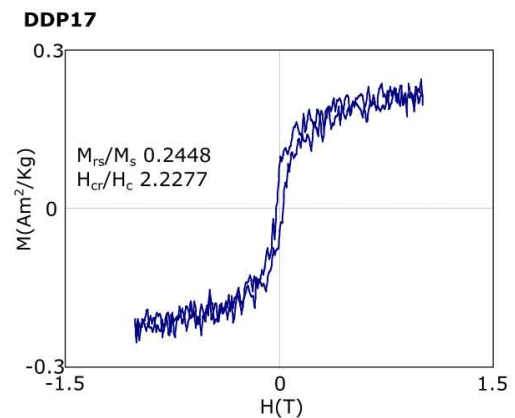
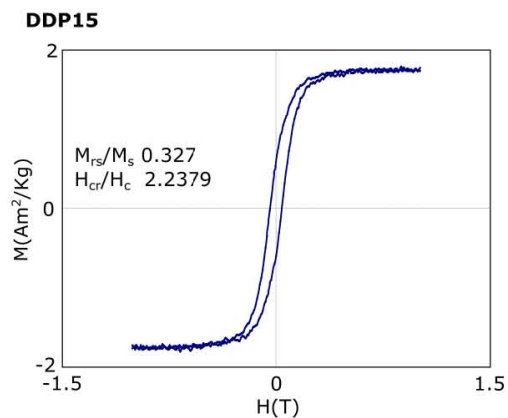
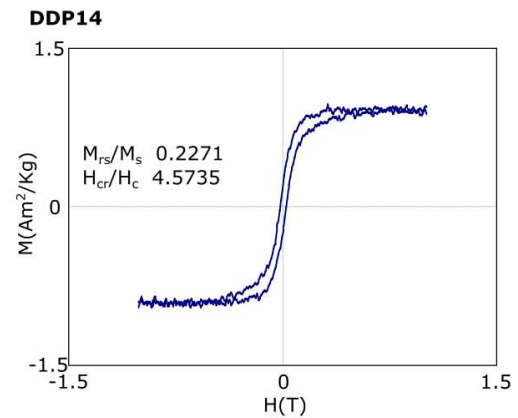
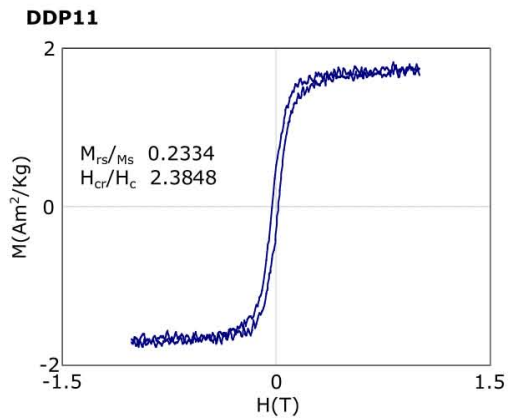
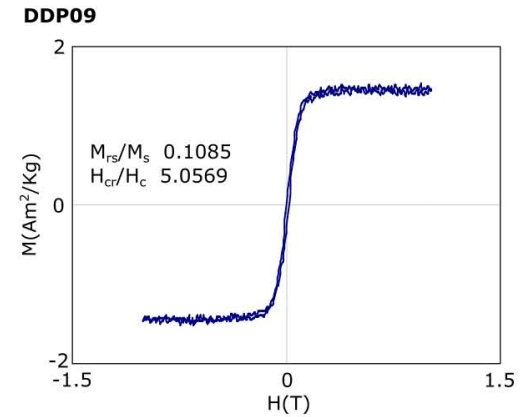
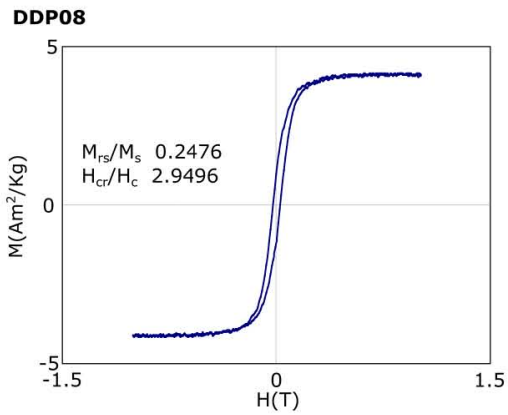
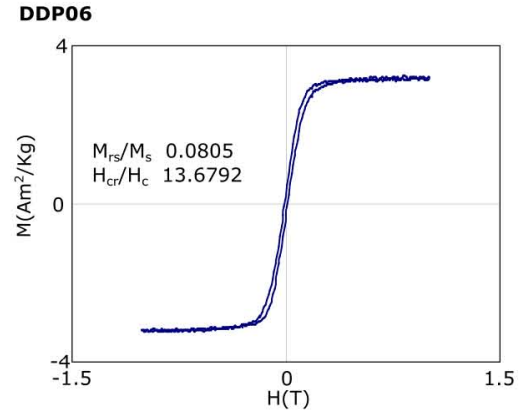
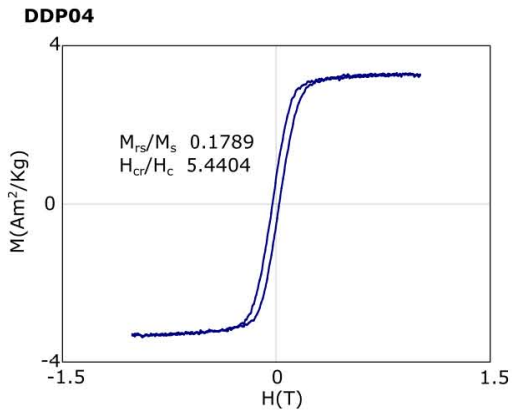


Figure 3-9. Representative hysteresis loops of analyzed samples. Characteristic parameter ratios (remanence ratio M_{rs}/M_s ; coercivity ratio H_{cr}/H_c) are presented. M_{rs} – saturation remanence; M_s – saturation magnetization; H_c – bulk coercive field; H_{cr} – remanent coercive force.

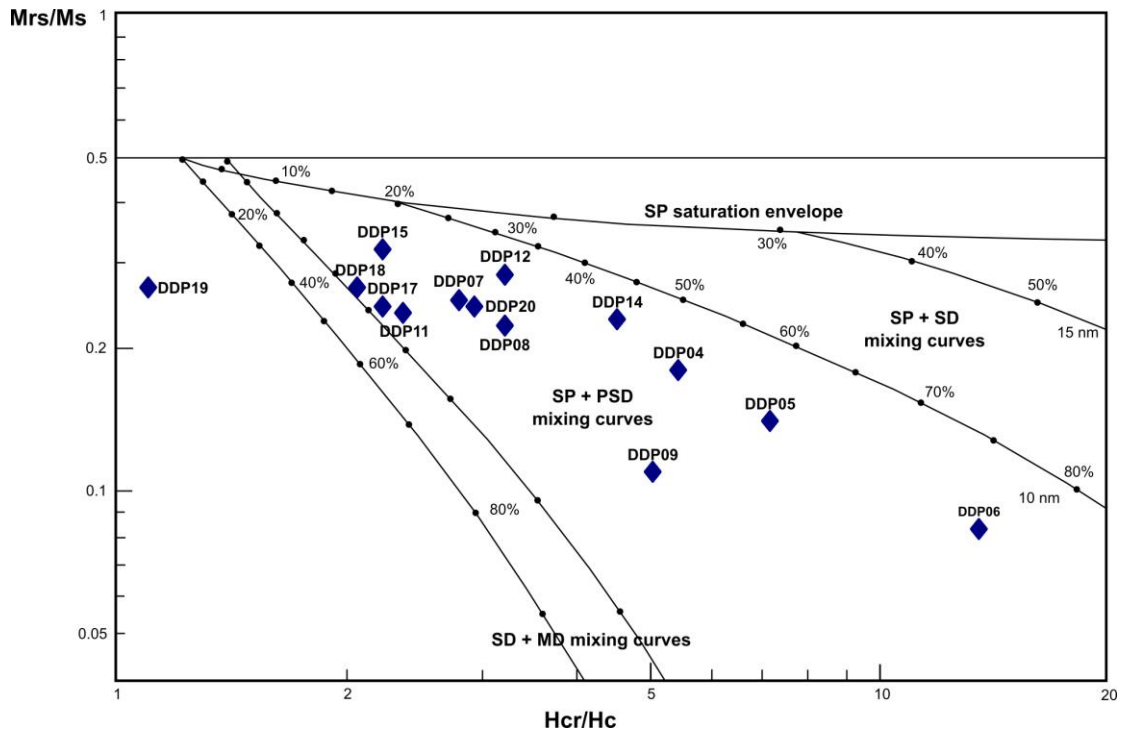


Figure 3-10. Day plot comparing the principal hysteresis ratios, after Dunlop (2002). SD – single domain; MD – multidomain; PSD – pseudo single domain; SP – super paramagnetic.

3.2.5 Paleomagnetism

Zijderveld diagrams

The magnetization in rocks sampled in the Diquiyú unit is complex, as some samples present multivectorial behavior, but most of the samples are bi-vectorial and some of them are univectorial (see Appendix 3 for descriptions and examples for each site). Typically, a linear stable decay to origin is observed in most of the samples after removing a low coercivity-laboratory unblocking temperature A component. Only localities DDP04 and DDP14 show univectorial behavior (Figure 3.11 F) after applying both alternating field demagnetization (AFD) and thermal demagnetization (THD); however, the directions differ in that the DDP04 yields a direction to the north with

intermediate positive inclinations (Figure A3-4) and DDP14 yields magnetizations to the SW with shallow positive inclinations (Figure 3.11 F).

A bi-vectorial behavior is the most commonly observed, and is characteristic of sixteen of twenty localities. The high coercivity or high unblocking temperature component is recognized as component B. DDP01 shows a north directed component between 5 mT to 40 mT that changes to a NW directed component when thermal demagnetization is applied (Figure 3.11 A). The main decrease in the intensity of the magnetization is observed between 400°C and 500°C (Figure A3-1). DDP03 and DDP06 show similar paths characterized by an N-NNE directed soft A component that changes to a ENE B component after 400°C, which shows shallow positive inclinations. The biggest drop in intensity of magnetization for the high laboratory unblocking temperature B component occurs between 500 and 570°C (Figure 3.11 B). DDP05, on the other hand, shows a clear division between the “soft” and the “hard” component (Figure A3-5). The soft component, traceable in ranges of 3mT to 45mT and 100°C up to 180°C, is north directed with shallow inclinations; the hard component is traceable from 230°C up to 580°C and is directed to the SE-NW with steep negative inclinations. The highest decrease in magnetization intensity occurs between 270°C and 360°C (Figure A3-5). Similar to DDP05, DDP07 and DDP08 show a clear division between the two components. In DDP07 the low temperature component points towards the north at temperatures lower than 500°C and the “hard” B component is WNW directed with steep negative inclination and is defined at higher laboratory temperatures between 500 and 595 °C (Figure 3.11 D). The most significant drops in the intensity of magnetization occur between 0°C - 100°C for the low temperature A component and between 500°C - 580°C for the high temperature B component (Figure 3.11 D). DDP11 and DDP12 also show two demagnetization paths with inflexions at 500°C. The low unblocking temperature A component points towards the NNW to NNE with positive inclinations, and the high unblocking temperature B component aims to the west - southwest with steep negative inclinations (Figure 3.11 E, Figures A3-11, 12). An abrupt decrease in the intensity of magnetization occurs between 530°C and 580°C, but the maximum unblocking temperature is 680 °C.

Sites DDP17, DDP18, DDP19, and DDP22 show similar demagnetization behavior upon both AFD and THD techniques. A soft component is identified between 100°C and 500°C or between 5 mT and 30 mT. It is N-NE directed with positive intermediate inclinations (Figure 3.11 G); after 500°C or 30 mT the demagnetization trajectory is a linear decay to the origin. The high temperature (or coercivity) component is SW directed and of negative/shallow inclination (Figure 3.11 G). Sites DDP13, DDP15, and DDP16 show bi-vectorial demagnetization paths; the soft component identified in alternating fields of 5 mT up to 60 mT and temperatures between 90°C and 380°C points towards the N-NNE with positive intermediate inclinations (Figures A3-13, 15 and 16). The hard component of these sites is less well developed, for it does not show stable linear decay to the origin or presents a high scatter at the within site level (Figures A3-13, 15 and 16). For site DDP13, we excluded from the site mean calculation samples that appear partially contaminated by the low coercivity component. For site DDP16, the “hard” or B component is statistically valuable, and points towards the NNE with intermediate positive inclinations (Figure A3-16). For DDP15 the high coercivity component is unresolved.

Multicomponent magnetizations are present only at sites DDP09 and DDP20 (Figure 3.11 C, Figure A3-20). In DDP09 a significant drop in intensity of magnetization occurs in the lowest alternating field and laboratory temperature intervals (2.5 mT – 10 mT, 90°C - 350°C), and the magnetization removed is WNW directed with steep positive inclination. An intermediate component is present in a range that does not affect the intensity of magnetization (15 mT – 35 mT, 350°C - 500°C) showing a SW direction with positive inclinations; the hardest component is SW directed and appears when the highest alternating fields (40 mT – 160 mT), or laboratory temperatures (500°C – 620°C) are applied (Figure 3.11 C). DDP20 only demagnetizes by THD although both the low and intermediate temperature components are highly scattered and no statistically meaningful site mean can be obtained. Nonetheless, the hard (high unblocking temperature) component traceable from 580°C up to 700 °C yield good results pointing towards the SSW with negative inclinations.

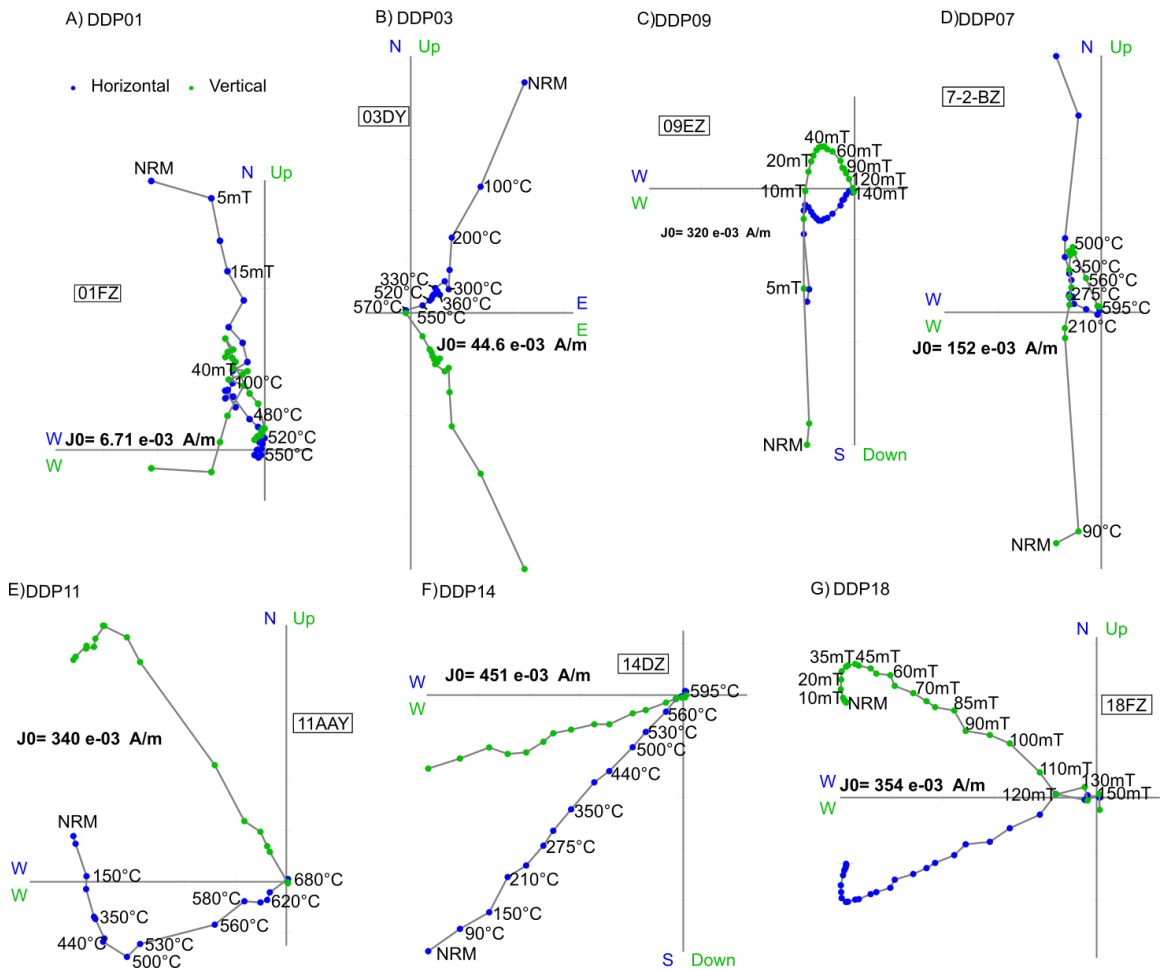


Figure 3-11. Examples of orthogonal demagnetization diagrams for the samples analyzed in this study (Zijderveld, 1967). All the graphics are in geographic coordinates.

Field tests

In order to assess the primary character of the interpreted ChRM's, two field tests were performed: a conglomerate test and a DC test (direction-correction tilt test of Enkin, 2003). The conglomerate test was made with andesite clasts of the base of the Prieto conglomerate, which overlies/conformably the Diquiyú unit, just above sites DDP17, DDP18 and DDP22. The andesitic clasts are similar to the andesite lavas below and we infer that the Prieto conglomerate is composed by clasts eroded from the Diquiyú unit. Most of the demagnetization paths resulting from AFD and THD techniques of the conglomerate clasts show univectorial behavior, although one or two samples show a

second component randomized before 7.5 mT pointing northward (Figure 3.12) and interpreted as a viscous component. The characteristic remanence interpreted for 12 clasts show a stable endpoint behavior and a range of coercivities between 7.8 mT and 160 mT and of blocking temperatures between 500°C and 595°C; the resulting directions are dispersed, although three to four clusters are indicated (Figure 3.12 D). This is interpreted as evidence of remanence acquisition before erosion and deposition; therefore, a qualitative conglomerate test is positive.

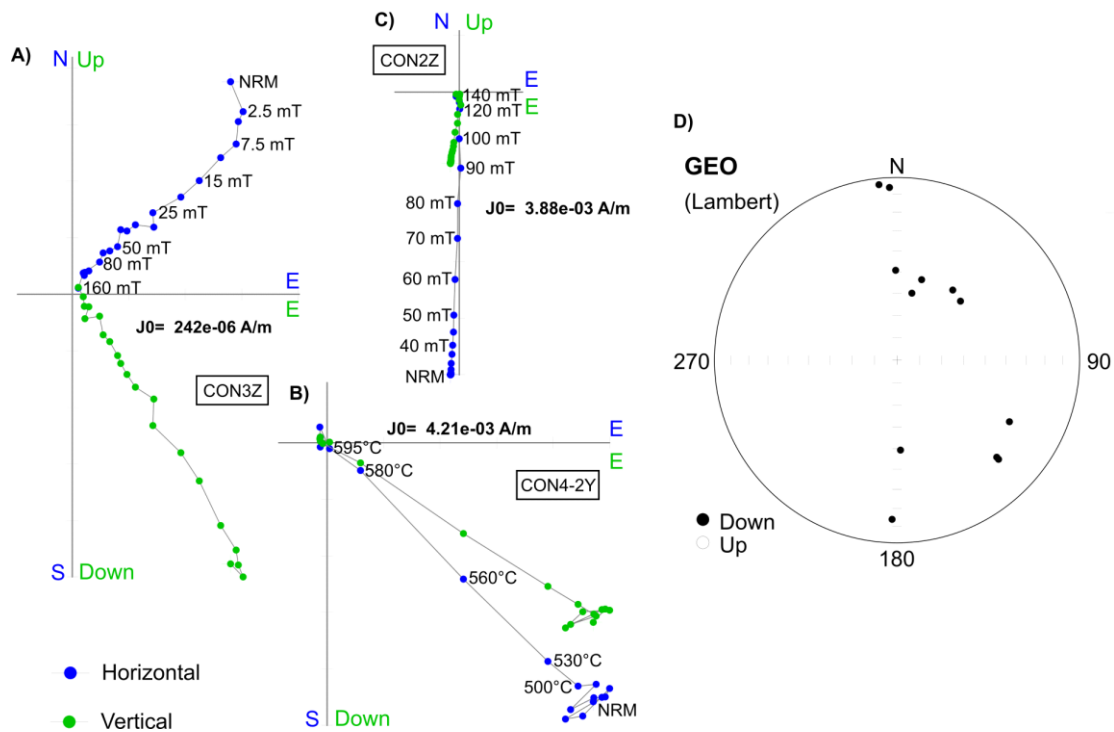


Figure 3-12. Orthogonal demagnetization diagrams and equal area projection of sample directions from clasts of a conglomerate bed overlying the lavas from the Diquiyú unit.

For the DC-test (Enkin, 2003) sites DDP02, DDP13, DDP15, and DDP22 were excluded due to the large α_{95} ($>20^\circ$); site DDP16 was excluded due to its uncertain field relationships, it appears to be younger than the rest of the collection. The DC-test was performed using the site means of 15 sites (Figure 3.13, Table 3.3) whose azimuth and dip variation is 182° and 41° respectively, which is an optimal variation for the test (Enkin, 2003). The test supposes the best data grouping with an unfolding of $124\% \pm 50\%$, meaning that the test is positive.

Data provided by Molina-Garza *et al.* (2014) collected in Diquiyú unit localities near to the sites sampled here were used to calculate the mean paleomagnetic direction and pole for the Diquiyú unit (Table 3.3) and to perform the reversal test by McFadden & McElhinney (1990). The test gave as a critical angle between the normal and reverse directions a value of 23.36° and an observed angle of 16.43° ; this classifies the test as $R_c(10^\circ < \gamma_c < 20^\circ)$. Both positive conglomerate and DC tests allow interpreting the characteristic magnetization (B component) isolated for 14 sites of Diquiyú unit as primary, and the R_c reversal test supports the primary nature of the magnetization, and allows us to infer a possibly successful sampling of the paleosecular variation.

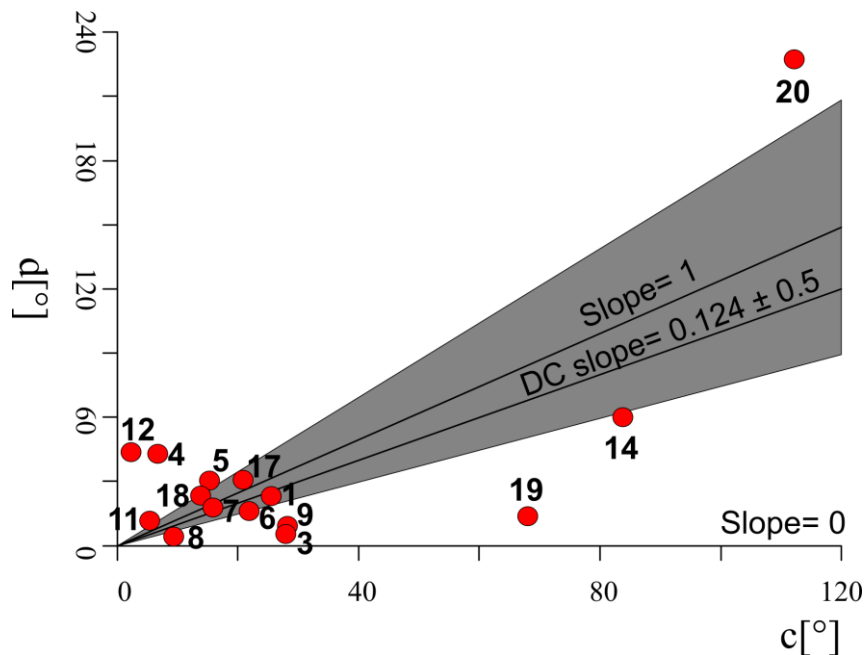


Figure 3-13. DC plot obtained for Diquiyú unit sites, the DC slope is not significantly different from 1 but significantly different from 0, meaning a pre-tilting remanence acquisition; c is the angular distance between the geographic mean direction and back-corrected stratigraphic site mean direction, d is the angular distance from the geographic mean to the intersection between the great circle that forms the geographic mean and back-corrected stratigraphic site means and the perpendicular great circle which goes through each site geographic mean.

For the calculation of the mean paleomagnetic direction for the B component a total of 23 site means were used (14 from this study and 9 from Molina-Garza *et al.* 2016). The sites were plotted in geographic coordinates (Figure 3.14 A). Afterwards, a double structural correction was performed in order to first restore the anticline plunge and second to unfold the beds (Figure 3.14 B). The mean direction was calculated using the site means

transposed to the same quadrant (See discussion on polarity of the magnetization on the next section) (Figure 3.14 C); the resultant direction (Dec: 82.8°, Inc: -1.4°, α_{95} : 9.4; k : 11.25) represents the vector of the thermoremanent magnetization preserved by the andesites of Lower Jurassic Diquiyú unit. An overprinted magnetization (A component, Figure 3.13 D) was also calculated (Dec: 12.4; Inc: 44.5, α_{95} : 13, k : 11.13) and could represent overprinting acquired during times after the Early Jurassic. The direction is consistent with acquisition of a recent viscous remanence (VRM).

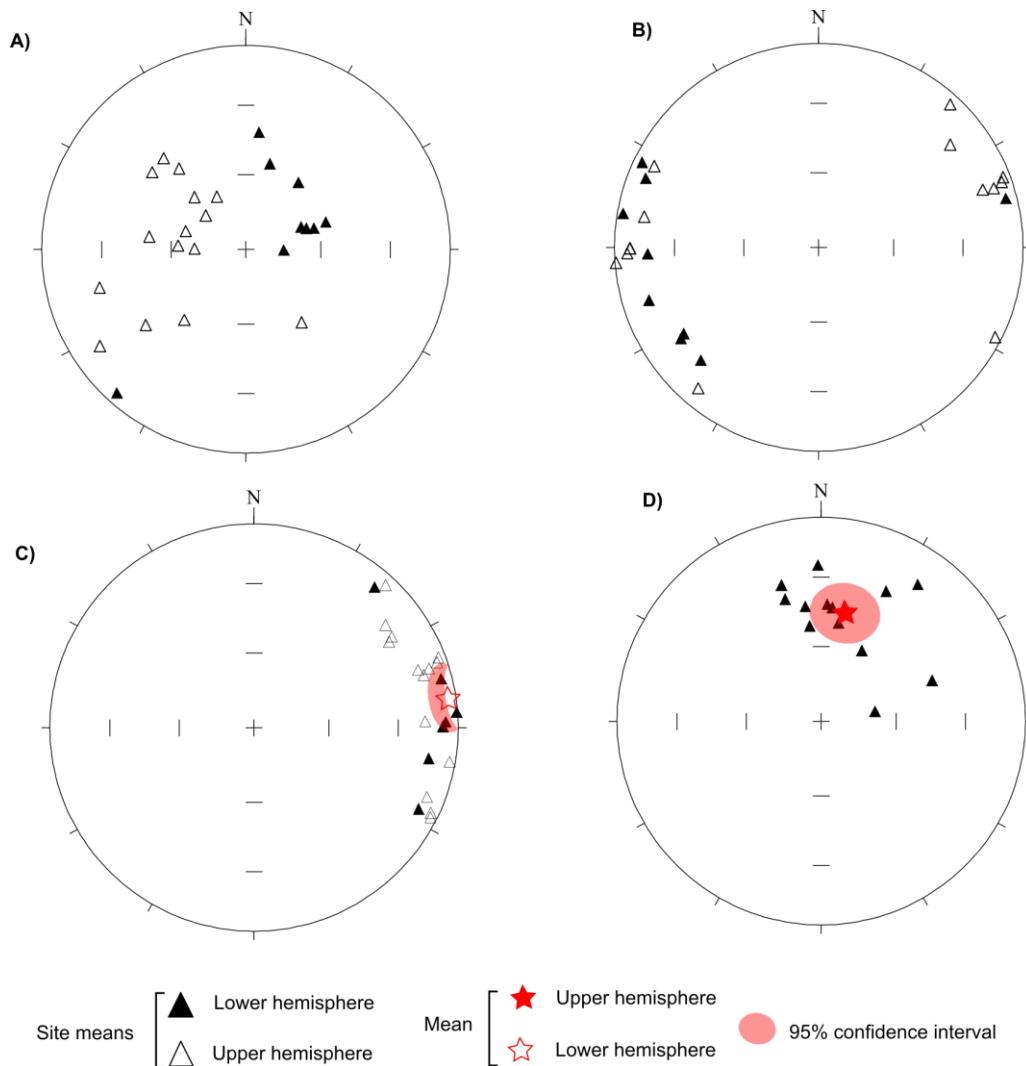


Figure 3-14. Equal are projections of site mean directions and mean paleomagnetic direction for magnetization components A and B. A) B component in geographic coordinates; B) B component in stratigraphic coordinates; C) Transposed B component and mean paleomagnetic direction for Diquiyú Unit; D) A component plots and associated estimation of mean direction.

Table 3-3 Paleomagnetic results for Diquiyú Unit. Dp – dip direction; N – total specimens per site; n – specimens with isolated component; Dec – Declination; Inc – Inclination.

Site	Unit	Latitude	Longitude	Dd/dip	n/N	AF/Thermal	<i>In situ</i>		Tilt corrected		a95	k	Comp.	VGP Lat	VGP Long
							Dec.	Inc.	Dec.	Inc.					
DDP01	Diquiyú Unit	17°34'07,5''	-97°50'28,8''	76/70	6/10	300 °C - 625 °C	315.4	-60.6	285.40	-3.60	19.9	12.3	B	14.09636613	165.640872
DDP02	Diquiyú Unit	17°34'10,5''	-97°50'28,5''	78/54	3/8	5 mT - 590 °C	53.5	41.7	58.1	-17.8	9.2	181.7	B	-26.71653228	192.370127
DDP03	Diquiyú Unit	17°34'11,2''	-97°50'27,3''	72/72	5/7	3 mT - 60 mT; 375 °C - 570 °C	38	55.7	57.4	-10.9	7.2	115.11	B	-28.83842449	188.964002
DDP04#	Diquiyú Unit	17°34'11,7''	-97°50'26,5''	59/42	8/12	5 mT - 90 mT; 100 °C - 430 °C	6.4	41.8	23.2	11.1	11.5	24.34	B	-64.36148072	197.188038
DDP05	Diquiyú Unit	17°34'11,8''	-97°50'26,8''	79/60	5/10	230 °C - 580 °C	331.2	-65.9	287.3	-20.4	7	118.8	B	12.91692922	156.533161
DDP06	Diquiyú Unit	17°34'11,4''	-97°50'27,1''	74/66	7/10	100 °C - 570 °C	15.6	54.1	47.8	2.8	10.8	31.94	B	-40.35886205	185.776539
DDP07	Diquiyú Unit	17°35'01,0''	-97°50'21,3''	74/60	8/8	440 °C - 610 °C	286.7	-64.8	270.8	-8.2	2.5	511.29	B	-0.483281021	167.99071
DDP08	Diquiyú Unit	17°35'00,9''	-97°50'21,7''	94/55	5/6	400 °C - 620 °C	270.7	-69.5	277.2	-14.5	4.9	248	B	4.574171866	162.935746
DDP09	Diquiyú Unit	17°35'01,2''	-97°50'23,3''	83/74	8/14	40 mT - 160 mT; 500 °C - 660 °C	221.2	-52.1	243.6	12.9	5.2	112.95	B	-22.75168116	187.367863
DDP11	Diquiyú Unit	17°35'29,6''	-97°50'32,4''	93/48	9/12	360 °C - 700 °C	273.1	-62.8	276.6	-14.8	6.5	63.28	B	3.958626563	162.970374
DDP12	Diquiyú Unit	17°35'25,8''	-97°50'32,0''	85/45	6/8	400 °C - 700 °C	318.9	-48	301.9	-14.4	11.2	36.5	B	27.46114782	153.778419
DDP13****	Diquiyú Unit	17°32'35,4''	-97°51'02,2''	226/24	3/8	15 mT - 160 mT	246.4	65.7	237	42.5	17.9	48.72	B		

DDP14#	Diqiyú Unit	17°33'52,2''	-97°50'51,8''	275/45	8/10	90 °C - 650 °C	221.9	6	214.4	-18	4.4	156.63	B	-55.57404706	181.599916
DDP15*	Diqiyú Unit	17°33'25,7''	-97°51'28,8''	274/64	5/6	60 mT - 90 mT	334.8	39.3	311.7	-3.5	34.9	5.75	B		
DDP16**	Diqiyú Unit	17°33'51,4''	-97°51'13,4''	259/35	7/8	380 °C - 590 °C	15	41.4	337.8	46.9	6.1	98.03	B		
DDP17	Diqiyú Unit	17°36'6,2''	-97°50'54,1''	37/30	9/16	15 mT - 160 mT; 480 °C - 580 °C	236.5	-15.3	236.2	13	4.7	122.5	B	-29.47712372	190.664605
DDP18	Diqiyú Unit	17°36'04,8''	-97°51'02,7''	47/36	7/10	35 mT - 160 mT; 510 °C - 570 °C	250	-28.4	247.6	5.2	4.4	186.52	B	-20.43282039	181.88359
DDP18	Diqiyú Unit	17°36'04,8''	-97°51'02,7''	47/36	5/10	>570°C	69.5	29.3	67	-4.4	6.6	160.45	B'	-21.13323316	181.696837
DDP19#	Diqiyú Unit	17°35'45,7''	-97°51'21,9''	313/50	8/13	20 mT - 160 mT; 525 °C - 660 °C	232.9	-38.4	191.6	-30.2	7.9	50.16	B	-78.81920658	177.467842
DDP20	Diqiyú Unit	17°35'44,2''	-97°51'25,1''	264/70	8/9	580 °C - 700 °C	142.7	-52.9	110.4	1.3	8.1	47.48	B	19.19671442	165.07654
DDP22*	Diqiyú Unit	17°36'6,2''	-97°50'54,1''	37/30	5/5	15 mT - 80 mT	226.2	-18.5	225.8	11.2	25.1	10.26	B		
25***	Diqiyú Unit	17°34'45,39''	-97°50'31,7''	70/70	5		67.8	66.2	69.1	-3.8	5.6	185.1		-19.26065642	180.638746
26***	Diqiyú Unit	17°34'45,39''	-97°50'31,7''	70/70	6		70.7	64.5	70.3	-5.5	3.7	331.9		-17.84584722	181.068095
27***	Diqiyú Unit	17°34'45,39''	-97°50'31,7''	70/70	3		90.9	75	75.3	5.9	7.5	270.3		-14.90220631	173.773304
28***	Diqiyú Unit	17°34'45,39''	-97°50'31,7''	70/70	5		72.6	61.4	71.3	-10.6	12.2	40.4		-16.03191197	183.263318
29***	Diqiyú Unit	17°35'18,62''	-97°50'34,9''	70/70	8		277.5	-50.6	267.9	15.4	5.9	88.6		0.379515671	180.264392

	Unit														
30***	Diquiyú Unit	17°35'18.62"	-97°50'34.9"	70/70	5		310.1	-69	268.3	-8.7	8.5	81.2		-2.937667958	168.495171
31***	Diquiyú Unit	17°35'38.56"	-97°50'34.1"	70/70	5		309.5	-40.3	291.8	8.2	6.5	138.9		22.01215979	169.470329
33r***	Diquiyú Unit	17°35'37.65"	-97°50'34.3"	70/70	5		318	-39.6	295.8	3.1	7.6	102.9		25.01797324	165.458375
35***	Diquiyú Unit	17°35'37.50"	-97°50'33.8"	70/70	6		71	56	70.6	-14	12.6	29.1		-16.0692857	185.24223
Mean					23				82.8	-1.4	9.4	11.25		Paleolatitude= -0.7	
								Normal	69.5	-5.9	10.9	20.43	n=10		
								Reverse	273.3	-2.2	12.5	11.9	n=13		
								Paleopole	175°E	6.6°S	8.7	13.1	n=23		
RO (Böhnel, 1999)	Zorrillo Formation			47/58	15		231.6	-51.9	230.4	6	5.9	42.8			
Overprint															
DDP01	Diquiyu unit	17°34'07,5''	-97°50'28.8"	76/70	5/10	5 mT - 30 mT	343.7	31			7.3	111.02	A		
DDP02****	Diquiyu unit	17°34'10,5''	- 97°50'28,5''	78/54	7/8	5 mT - 20 mT; 100 °C - 530 °C	109.7	-57.7			16.8	13.84	A		
DDP03	Diquiyu unit	17°34'11,2''	-97°50'27,3"	72/72	5/6	5 mT - 90 mT; 90 °C - 350 °C	3	42			10	56.69	A		
DDP05****	Diquiyu unit	17°34'11,8''	- 97°50'26,8''	79/60	6/10	0 °C - 180 °C	1.6	5.5			11	38.02	A		

DDP07	Diquiyu unit	17°35'01,0''	-97°50'21,3''	74/60	8/8	90 °C - 500 °C	353.2	51.1			5.6	97.32	A		
DDP08	Diquiyu unit	17°35'00,9''	-97°50'21,7''	94/55	5/6	150 °C - 440 °C	343.5	37.6			7.7	99.84	A		
DDP09****	Diquiyu unit	17°35'01,2''	-97°50'23,3''	83/74	8/14	2.5 mT - 10 mT; 90 °C - 500 °C	153.7	67.9			12.6	20.37	A		
DDP11	Diquiyu unit	17°35'29,6''	-97°50'32,4''	93/48	10/14	90 °C - 530 °C	29.7	57.2			10.3	22.75	A		
DDP12	Diquiyu unit	17°35'25,8''	-97°50'32,0''	85/45	5/6	90 °C - 530 °C	26.5	29.5			6.1	156.4	A		
DDP13	Diquiyu unit	17°32'35,4''	-97°51'02,2''	226/24	9/17	2.5 mT - 60 mT	352.1	42.5			8.4	38.66	A		
DDP15	Diquiyu unit	17°33'25,7''	-97°51'28,8''	274/64	6/10	5 mT - 90 mT	358.7	24.4			4.8	195.71	A		
DDP16	Diquiyu unit	17°33'51,4''	-97°51'13,4''	259/35	7/8	90 °C - 380 °C	35.2	19			5.8	109.08	A		
DDP17	Diquiyu unit	17°36'6,2''	-97°50'54,1''	37/30	7/10	2.5 mT - 30 mT; 100 °C - 410 °C	9.9	49.5			8.4	52.82	A		
DDP18	Diquiyu unit	17°36'04,8''	-97°51'02,7''	47/36	5/9	2.5 mT - 25 mT; 100 °C - 480 °C	5.5	43.3			8.7	77.64	A		
DDP19	Diquiyu unit	17°35'45,7''	-97°51'21,9''	313/50	6/9	2.5 mT - 20 mT; 100 °C - 525 °C	69.8	41.7			16.4	17.54	A		
DDP20	Diquiyu unit	17°35'44,2''	-97°51'25,1''	264/70	7/12	90 °C - 650 °C	79.5	68.2			12	26.46	A		
DDP22*	Diquiyu unit	17°36'6,2''	-97°50'54,1''	37/30	4/6	5 mT - 20 mT; 100 °C - 400 °C	348	40.1			22.5	17.6	A		
Mean					13		12.4	44.5			13	11.13			

*a95 > 20

** not used for ambiguous field relationships

*** sites reported by Molina-Garza *et al.* (2016)

**** not used for in calculation

s # sites excluded by a 45 cutoff

4. Stratigraphy, sedimentology and petrography: methods and results

4.1 Methods

The stratigraphic-petrologic approach involved a ten day field trip focused of the bed by bed measurement and description of the sedimentary succession that crops out along Rosario Nuevo creek, using a 1.5 m Jacob Staff. I compiled geometric, textural, compositional and paleocurrent data (Figure 4.1; Appendix 4). Thirteen medium to coarse sandstone samples were taken for microscopic petrography analysis (See Appendix 4 for sample location). Facies codes by Miall (2006, Table 4.1) were used for the facies classification of the sedimentary succession. The textural descriptions (grain size, roundness, sphericity, contacts) were made following Folk (1974). A 200-400 point count was made for each thin section following the Gazzi-Dickinson method (Ingersoll *et al.*, 1984) and using the criteria exposed on table 4.2. The number of counts were subjected to the quality of the thin section; nevertheless, the estimated percentages by volume of minerals would only have errors between 2 to 7% in 2σ (Van der Plas & Tobi, 1965). The results were plotted on classification triangles (Folk, 1974; Garzanti, 2016) and on tectonic discrimination triangles (Dickinson & Suczek, 1979; Dickinson, 1985).

Table 4-1 Facies codes used for the classification of the analyzed succession. Modified from Miall (2006).

Facies code	Description
Gmm	Matrix-supported, massive conglomerate
Gmg	Matrix-supported conglomerate with inverse to normal grading
Gci	Clast-supported conglomerate with inverse grading
Gcm	Clast-supported massive conglomerate
Gh	Clast-supported, crudely bedded conglomerate with imbrication
Gt	Trough cross-bedded conglomerate
Gp	Planar cross-bedded conglomerate
St	Trough cross-bedded fine to very coarse or pebbly sandstone
Sp	Planar cross-bedded fine to very coarse or pebbly sandstone
Sr	Ripple cross-laminated fine to very coarse sandstone

Sh	Horizontally laminated fine to very coarse or pebbly sandstone
Sl	Low-angle cross-bedded fine to very coarse or pebbly sandstone
Fl	Horizontally laminated sandstone, siltstone and/or claystone

Table 4-2. Codes and recalculation parameters used for the sandstone petrographic analysis. Modified from Dickinson (1979)

Symbol	Definition	Recalculated parameters
Qm	Monocrystalline quartz	$QtFL\%Qt = 100Qt/(Qt+F+L)$
Qpq	Polycrystalline quartz	$QtFL\%F = 100F/(Qt+F+L)$
Qc	Chert	$QtFL\%L = 100L/(Qt+F+L)$
K	Potassium feldspar	$QmFLt\%Qm = 100Qm/(Qm+F+Lt)$
P	Plagioclase feldspar	$QmFLt\%F = 100F/(Qm+F+Lt)$
Lvf	Felsitic volcanic lithic grains	$QmFLt\%Lt = 100Lt/(Qm+F+Lt)$
Lvl	Lathwork volcanic lithic grains	$LmLvLs\%Lm = 100Lm/(Lm+Lv+Ls)$
Lvm	Microclitic volcanic lithic grains	$LmLvLs\%Lv = 100Lv/(Lm+Lv+Ls)$
Lvt	Tufaceous and vitric volcanic lithic grains	$LmLvLs\%Ls = 100Ls/(Lm+Lv+Ls)$
Lm	Metamorphic grains	$QpLvLs\%Qp = 100Qp/(Qp+Lv+Ls)$
Ls	Sedimentary grains	$QpLvLs\%Lv = 100Lv/(Qp+Lv+Ls)$
Qt	Total quartzose grains (=Qm+Qpq+Qc)	$QpLvLs\%Ls = 100Ls/(Qp+Lv+Ls)$
F	Total feldspar (=K+P)	
Lv	Total volcanic grains (=Lvf+Lvl+Lvm+Lvt)	
L	Total unstable lithic grains (=Lm+Lv+Ls)	
Qp	Total polycrystalline quartz (=Qpq+Qc)	
Lt	Total lithic grains (=L+Qp)	

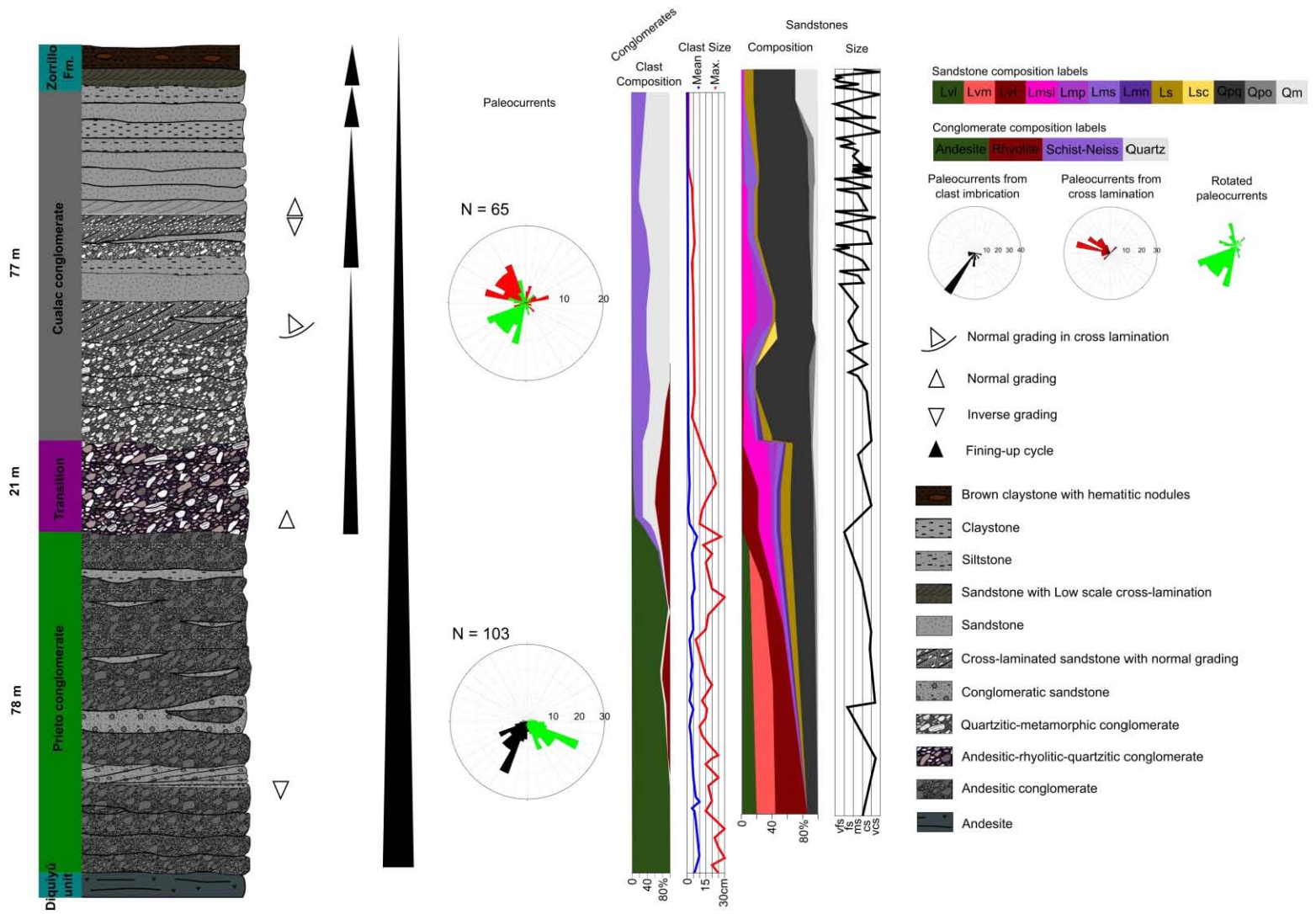


Figure 4-1. Condensed stratigraphic column of Rosario Nuevos's creek succession. Cross-stratification and normal and inverse grading are indicated. Fining-upward cycles are indicated both within formations and together configuring a big upward-fining cycle. The change in composition of clasts in conglomerates and in grains in sandstones can be depicted from diagrams located to the right of the figure, also, both with and without back corrected paleocurrents are depicted.

4.1 Stratigraphy and facies description

The base of Prieto conglomerate rests conformable over the Diquiyú unit. The first 17 m of the succession (see Appendix 4 for the complete drawing of the succession) are composed by lenticular clast-supported conglomeratic beds up to 2 m thick; the clasts are of exclusive andesitic composition and show imbrication (Figure 4.2 H). The contact between beds is erosive, no lamination was detected but a coarse gradation is observed (Figure 4.2 G). These beds classify as Gcm lithofacies. The remaining succession pertaining to the Prieto conglomerate consist of conglomeratic clast-supported beds with crude horizontal bedding (Figure 4.2, A, B, E), occasionally with sandstone lenses parallel to bedding. These bedforms classify as Gh lithofacies. A 1 m sandstone-mudstone (plant fossil-rich) interval (Figure 4.2 F) is detected at ~ 30 m from the base, classified as Sh and Fl lithofacies. A pack of cross-bedded sandstones was detected at ~60 m from the base, resembling lateral accretion geometry (Figure 4.2 D); nevertheless, the restricted lateral extent of the outcrop doesn't allow a certain classification. The clast composition in these conglomerates is uniformly andesitic, with a minor increase in rhyolite and quartz clasts in the middle-upper part of the succession (Figure 4.1). Some fossil leaves and tree trunks replaced by silica were detected (Figure 4.2 C). A total of 78 m were measured for the Prieto conglomerate succession. The paleocurrent directions measured from imbrication features have a radial orientation pattern that consistently point towards the SW (Figure 4.1), and to the SE when back rotated according to the paleomagnetic results.

The 21 m transitional interval between Prieto conglomerate and Cualac conglomerate has a relatively high content of metamorphic and rhyolitic clasts, which give a purple color to the matrix (Figures 4.3 E-F). The first meters are matrix-supported, and classify as Gmm lithofacies. After this interval, Gh facies reappear, with some Sh and St interbedded

(Figure 4.3 C-D), and present an up-dip increase in metamorphic and quartz clast content (Figure 4.1; Appendix 4).

The base of the Cualac conglomerate is marked by the appearance of a Gt bed rich in quartz pebbles (Figure 4.3 A) in which imbrication was measured (Figure 4.3 B) with a NE direction (Figure A4-3). After this point, the succession is constituted by conglomeratic, sandy-conglomeratic and sandy beds with lenticular shape (Figure 4.4 E-F). It presents curved and trough cross-stratification (Figure 4.4 C, E, G, H), planar cross-stratification, both within individual beds at lamina scale (Figure 4.4 F), together with inverse (Figure 4.4 C) and normal grading. The conglomeratic (Gt, Gh) beds are the predominant in the succession; nevertheless, in some fining-up intervals, more common up-section, St, Sh, and Fl facies interbedded with ~5 cm coal beds are predominant (Figure 4.4 D-E).

A commonly observed characteristic is the presence of ~10 cm thick conglomeratic lenses inside trough cross-bedded sandstones (Figure 4.4 E), and also the inclined normal grading structure present on beds with Gt and St facies. The measurements from cross-stratification structures indicate a paleocurrent flow to the NW and to the SW when paleomagnetically back rotated (Figure 4.1). The thickness measured for Cualac conglomerate is 77m. The conglomerates of Cualac conglomerate contain quartz and metamorphic pebbles, with a mean diameter of 1 to 5cm, different from the andesitic clasts of Prieto conglomerate which have mean diameter of 5 to 10 cm, reaching diameters of ~30 cm.

The contact with the overlying Zorrillo Formation is transitional, and can be placed where the sandstone-mudstone proportion dominates over conglomerates, that become thin and scarce up-section (Figure A4-6). The Zorrillo Formation presents bioturbated mudstones and shales (Figure 4.4 A), sandstones with ripple structures, (Figure 4.4 B) and coal beds of 50 cm to 1 m.

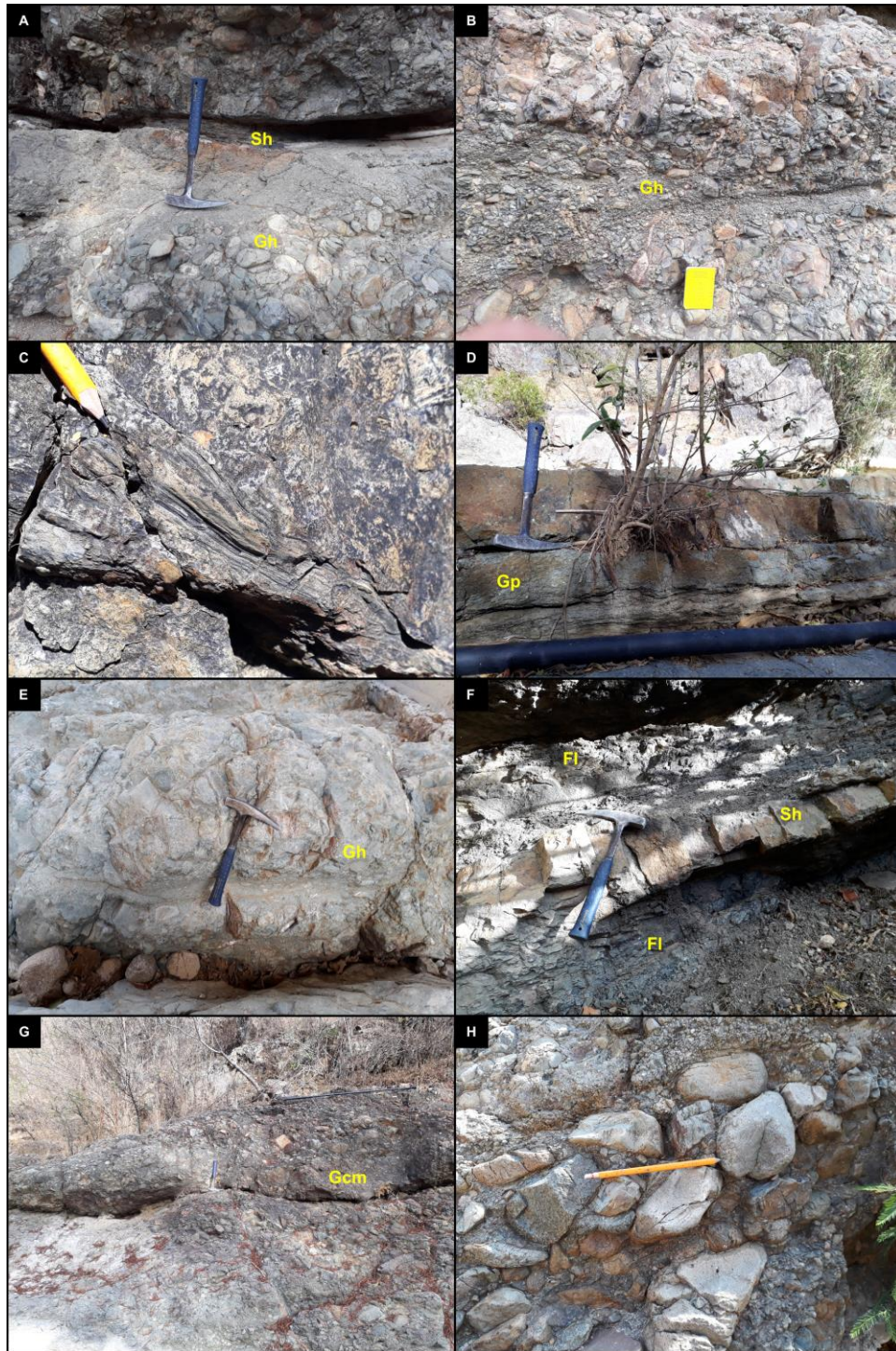


Figure 4-2. Outcrop characteristics and facies of Prieto conglomerate. Up in the figure represents up-section in the field. Only few beds at the base of the unit lack structures (G), whilst horizontal lamination is common through all the succession (A, B, and E) together with clast imbrication (H). Plant fossils are common in intervals with mudstones and sandstones (F). Also tree trunk fossils are common in all the succession (C). The planar cross stratification detected in D appears to form part of lateral accretion macroform.

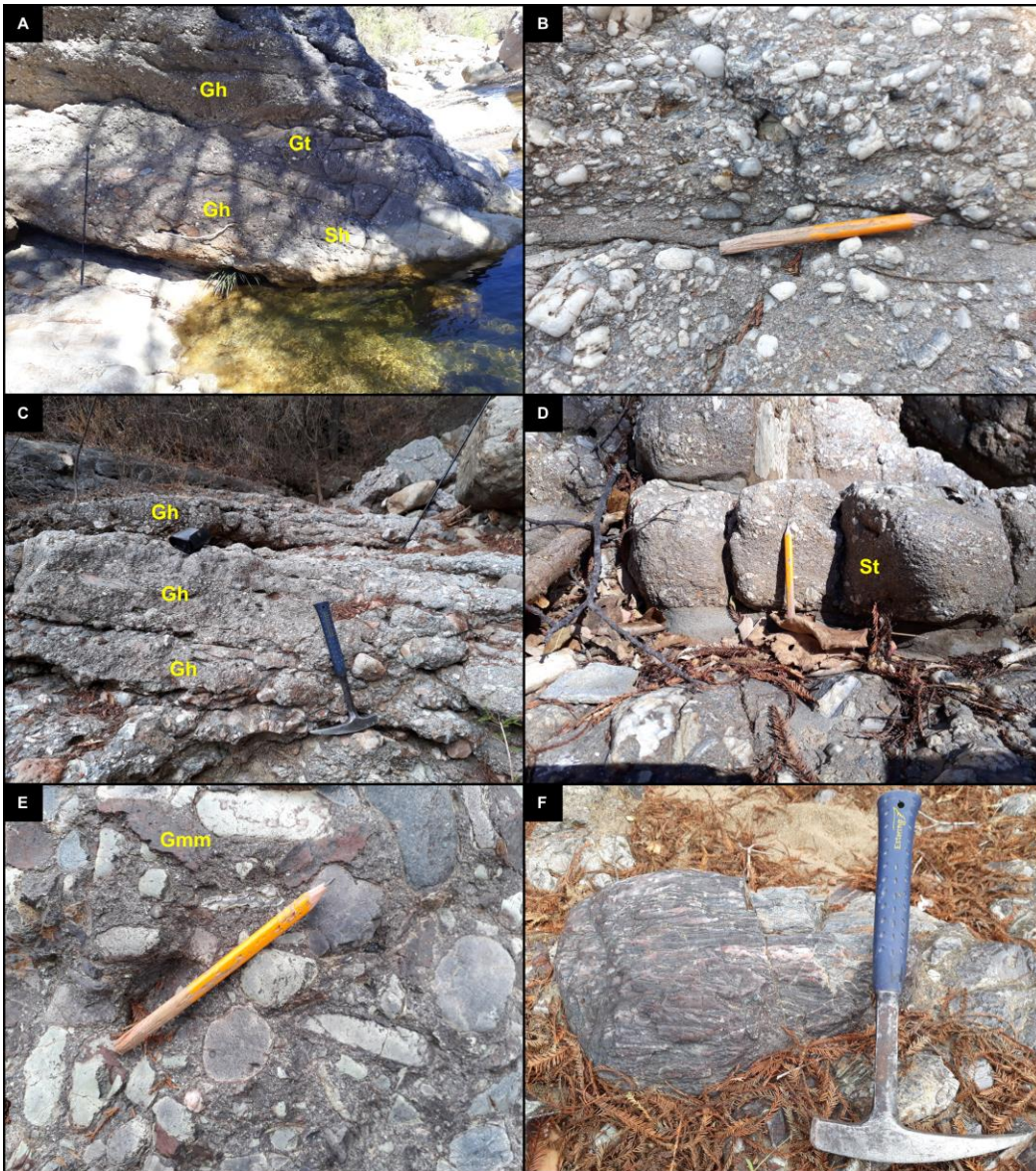


Figure 4-3. Outcrop characteristics and facies of the transition between Prieto conglomerate and Cualac conglomerate. Up in the figure represents up-section in the field. The purple matrix in (E) is common only in a ~10 m thick interval, which also have metamorphic clasts up to ~50 cm in diameter (F). Clast composition is varied and bed thickness decreases in the transition between Prieto and Cualac conglomerates (C). The base of the Cualac conglomerate is detected when the clast composition is predominantly quartzitic (A, B).

4.2 Petrography and provenance

The Prieto conglomerate sandstones (Appendix 5), unlike the conglomerates, have a high percentage of felsitic volcanic grains, and also a representative content of polycrystalline

quartz (Figure 4.5 D). Nevertheless, lathwork and microlithic volcanic lithic grains (corresponding to basalts and andesites) represent almost 50 percent of the sample composition (Table 4.3). Most clasts are rounded, some are intensely oxidized.

From the transition between Prieto conglomerate and Cualac conglomerate and up section, the sandstones lack andesite clasts and the felsitic grains become scarce. They are only present up to the first 15 m of Cualac conglomerate succession. Instead, metamorphic-quartzitic grain content increases and becomes dominant; grains such as slate, phyllite and schist are the most common (Figures 4.1, 4.5 C). They are mostly of pelitic sedimentary protolith, although a minor component is of meta-igneous character. Polycrystalline quartz is common since the transition and increases up-section reaching the highest contents in the middle upper part of Cualac conglomerate succession (Figure 4.5 B); some (10%) of these grains are deformed internally. Sedimentary lithic and monocrystalline quartz grains are representative only in the Zorrillo Formation samples (Figure 4.5 A). Most quartz grains are subrounded and show an axial elongation that together with mica generate a mesoscopically observable lamination. The presence of primary matrix is negligible. Instead, pseudomatrix (Dickinson, 1970) is filling spaces between grains together with kaolinite, hematite and calcite cement. Some finer samples (fine to very fine sand) were also described and have the same characteristics of the coarser samples, although higher calcite and hematite contents were detected. Also, some of these samples are cement-supported by calcite.

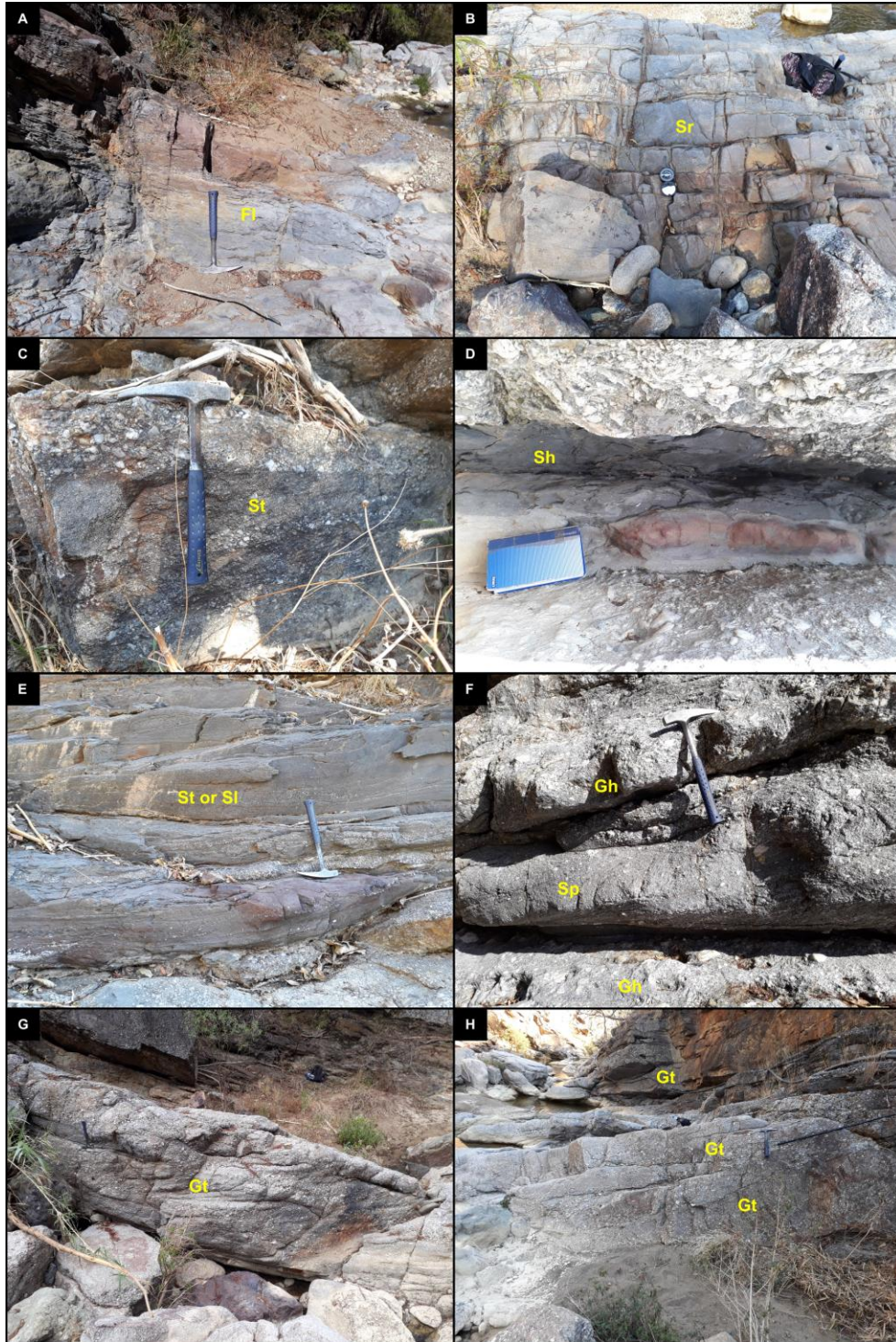


Figure 4-4. Outcrop characteristics and facies of Cualac conglomerate. Up in the figure represents up-section in the field. Curved cross stratification is the most common structure of this unit (G); together with planar and trough cross stratification that occur mostly on sandstones (E, F). The beds have lenticular shape (F, H). Hematitic nodules are common in the upper part of the succession (A, D), when the transition to the Zorrillo Formation starts.

The counted compositional parameters are presented in table 4.3. The samples plot in the litharenite field in the Folk (1974) classification triangle, and in the Quartzo-Lithic (Prieto conglomerate, transition) and Litho-Quartzose (Cualac conglomerate) fields in the Garzanti (2016) scheme (Figure 4.6 A, B). In the QtFL tectonic discrimination diagram (Dickinson, 1985) the Prieto conglomerate samples plot in the Non-Dissected Arc provenance, and the other samples plot in the Recycled Orogen field. In the QmFLt triangle (Dickinson, 1985) all the samples plot in the Recycled Lithic field (Figure 4.6). The lithic discrimination diagram (Figure 4.7) show an evolution from volcanic lithic rich samples of arc sources in Prieto conglomerate to metamorphic lithic and quartz rich rocks with sources either: in a collision suture, in a fold-thrust belt, or mixed sources for the Cualac conglomerate and Zorrillo Formation.

Table 4-3. Recalculated compositional parameters obtained for Prieto conglomerate, Cualac conglomerate, and Zorrillo Formation. All samples correspond to fine to medium size sandstones.

Sample	QtFL%			QmFLt%			QpLvLs%				
	Qt	F	L	Qm	F	Lt	Qp	Lv	Ls	Lv/L	Qp/Qt
Prieto conglomerate											
R1	14	0	86	0	0	100	14	86	0	1	1
R2	5	0	95	0	0	100	5	95	0	1	1
Transition											
R5	37	0	63	2	0	98	49	32	19	0.37	0.941
Cualac conglomerate											
R6	31	0	69	6	0	94	69	7	24	0.04	0.82
R7	60	0	40	2	0	98	81	3	16	0.04	0.962
R8	82	0	18	2	0	98	96	3	1	0.16	0.976
R10	54	0	46	2	0	98	81	0	19	0	0.957
R11	56	0	44	7	0	93	95	0	5	0	0.871
R14	79	0	21	5	0	95	94	0	6	0	0.935
R15	77	0	23	3	0	94	99	0	1	0	0.957
R16	79	0	21	5	0	95	100	0	0	0	0.943
Zorrillo Formation											
R19	83	0	17	29	0	71	82	0	18	0	0.656
R20	81	0	19	10	0	90	83	0	17	0	0.872

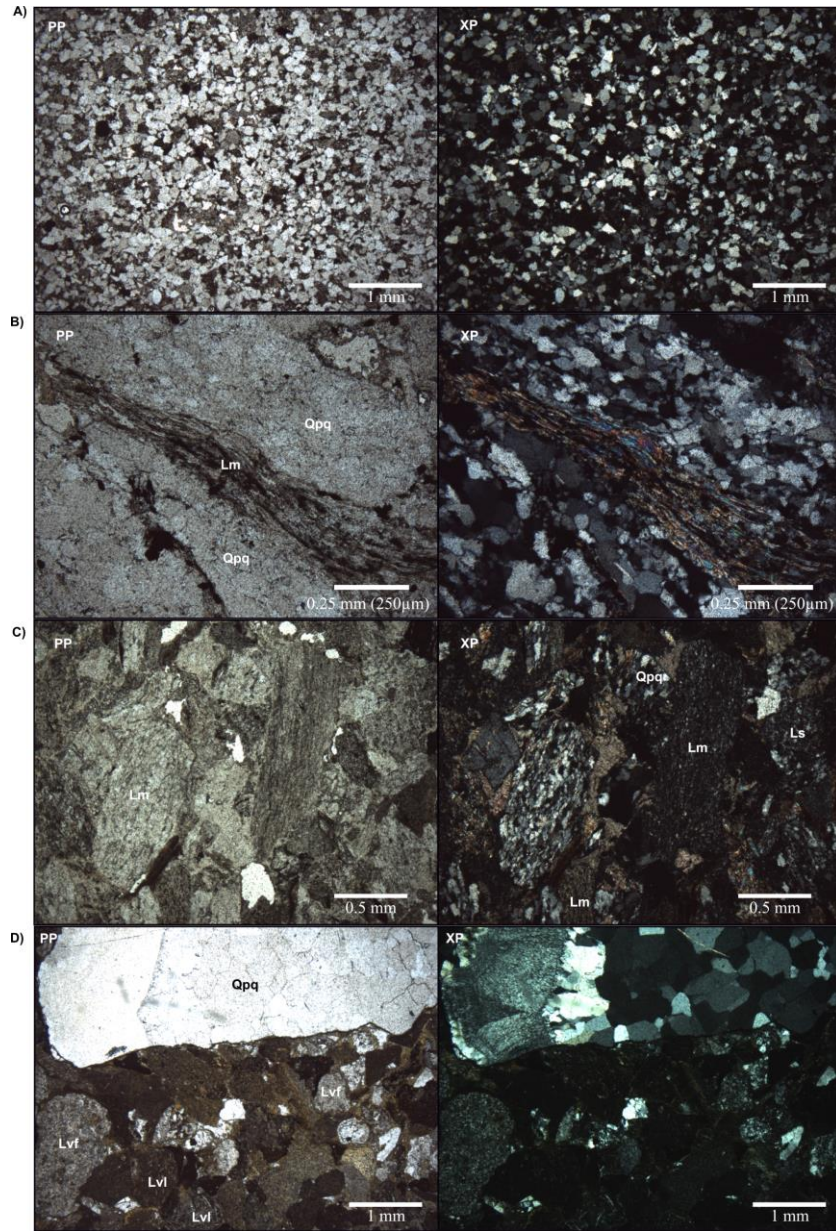


Figure 4-5. Photomicrographs representative of: A) Zorrillo Formation, B) Cualac conglomerate, C) Transition between Prieto and Cualac conglomerates, and D) Prieto conglomerate. The Qpq grain in D shows at its left side cryptocrystalline quartz resembling probably chalcedony, some of the darkest grains on the lower part of the photograph can correspond to Lvv. Notice the absence of fine grained metamorphic grains in the Cualac conglomerate (B) compared to the transition (C) where this type of grain is predominant.

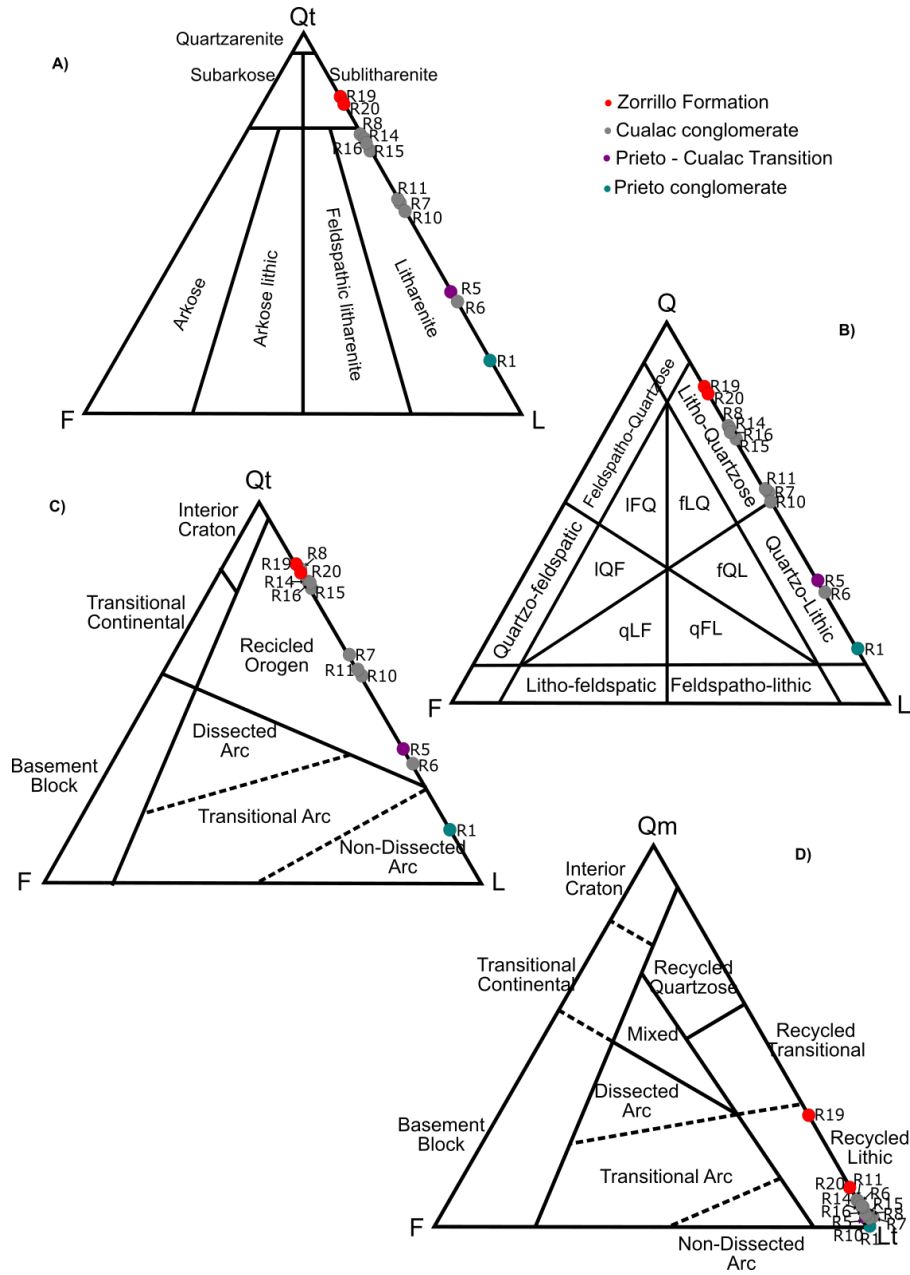


Figure 4-6. Classification and tectonic discrimination diagrams. Modified from: A) Folk, 1974; B) Garzanti, 2016; C, D) Dickinson, 1985. Notice the absence of potassium feldspar in all samples.

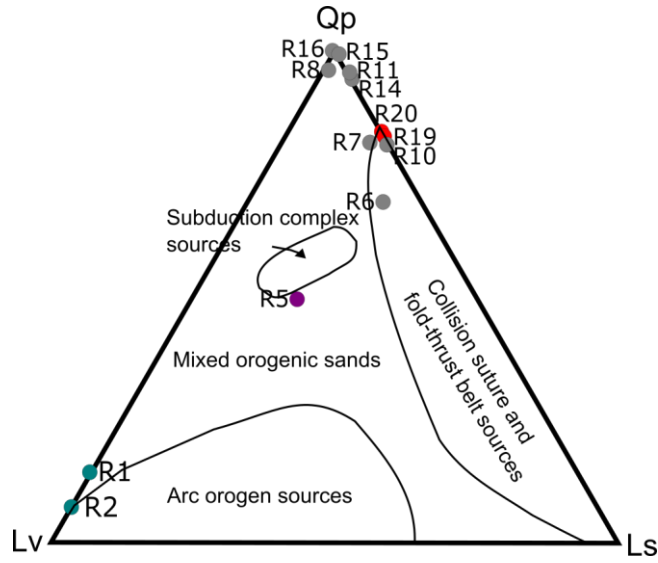


Figure 4-7. Ternary diagrams using lithic parameters. From Dickinson (1985). Notice the evolving trend from volcanic arc to orogenic sources.

5. Discussion

5.1 *Magnetic mineralogy*

The first direct tools we used were the petrographic and scanning electron microscopes; using these techniques we were able to identify minerals of the magnetite-ulvospinel and hematite-ilmenite series. Titanomagnetite is the most common magnetic mineral present in all the rocks analyzed; the biggest crystals develop intergrowth textures with ilmenite and hematite, result of high temperature oxidation during lava cooling (Watkins & Haggerty, 1967). These crystals are primary in origin. Some hematite needles and veins can be secondary in origin.

The EDS spectra show 30% of Ti related counts for both, the ferrimagnetic (titanomagnetite) and the antiferromagnetic (hematite) phases. If we assume that the amount of counts expresses closely the amount of Ti in the minerals, we have Ti contents higher than 20% (see Appendix 1). With these amounts of Ti the curie temperature for both hematite and titanomagnetite would be reduced to less than 500°; nevertheless, this curie temperature would still be higher enough for allowing the remanence to be stable and resist overprinting (Butler, 1998). Some other phases such as ilmenite and rutile, which are paramagnetic, show a larger number of counts of Ti.

IRM acquisition and DC demagnetization curves were obtained and interpreted with the methods of Kruiver *et al.* (2001). These results corroborate the mineralogy determined optically as sites DDP03, DDP05, DDP06, DDP07, DDP08, and DDP15 reach saturation below ~500 mT (Figure 3.6), and are dominated by phases with low and intermediate coercivities (20 – 140 mT) (Figure 3.7). This is in agreement with magnetite and/or titanomagnetite as the dominant phases, with perhaps a small contribution from a hard phase (hematite); some elongated magnetite particles may be present (although not observed) as they can reach coercivities as high as 150 mT. Sites DDP01, DDP09, DDP11, DDP12, DDP14, DDP18, DDP19, and DDP20, where hematite phases were observed at the microscope, show IRM acquisition curves that reach saturation with

higher fields up to ~2T or do not reach saturation after 3T (*e.g.* DDP01, DDP14, DDP18, DDP19, DDP20); similarly, they reach the H_{cr} point with higher fields than the magnetite dominated sites. The IRM acquisition curves were modeled using components in the range of coercivities from 20 to 1200 mT. Components with coercivities between 100 mT and 1000 mT that could represent hematite (Abrajevitch *et al.*, 2009) are important in sites DDP01, DDP14, DDP18, DDP19 and DDP20 reaching contribution percentages between 30% and 50% (Table 3.1, Figure 3.7); nevertheless, this contribution would require >95% wt of hematite in the complete magnetic fraction (Frank & Nowaczyk, 2008), this amount of hematite wasn't observed in any of the samples so the contribution will be less. The modeled IRM acquisition curves show the possible existence of goethite (>1000 mT), probably as result of weathering.

For magnetite dominated samples, the hysteresis parameters offer good information about the size of the magnetic carriers. The observed hysteresis loops vary from pot-bellied to wasp-waisted, shapes interpreted both as result of mixtures between phases of different coercivity (*e.g.* magnetite and hematite) or phases of different size (*e.g.* single domain (SD) magnetite and multidomain (MD) magnetite) (Roberts *et al.*, 1995; Tauxe *et al.*, 1996). All the samples where hematite is negligible (*e.g.* DDP03, DDP04, DDP06, DDP08, DDP15) have pot-bellied loops (Figure 3.8). This observation is probably due to a small SP (superparamagnetic) contribution from particles < ~10 nm (Tauxe *et al.*, 1996). The M_{rs}/M_s and H_{cr}/H_c ratios for these sites are consistent with PSD (pseudo-single domain) magnetitic grains of probable size >200 nm (Tauxe *et al.*, 1996; Dunlop, 2002) (Figure 3.9; Table 3.2). Site DDP06 has a large H_{cr}/H_c value, probably due to MD magnetite (Roberts *et al.*, 1995).

The sites where hematite was detected as an important magnetic phase (*e.g.* DDP11, DDP14, DDP17) show wasp-waisted loops (Figure 3.8). Although this phase is important, it must be hundreds of times more abundant than magnetite (fact that wasn't observed) to dominate the hysteresis properties (Roberts *et al.*, 1995), so the assigned PSD size for the magnetite of these sites is assumed as valid. The size of the hematite phase is difficult to assess using rock magnetic experiments due to the magnetite

predominance. Nevertheless, sites DDP01, DDP14, DDP19, and DDP20 do not reach saturation with the maximum applied induction; this can be ascribed to SD hematite (0.1 - 100 μm). Also, site DDP19 shows Hcr/Hc values close to 1, typical of SD hematite (Ozdemir & Dunlop, 2014). The previous observations about hematite size are not conclusive, but the size range at which hematite has an SD behavior is observable using microscopic techniques, and the whole range of sizes for stable hematitic remanence carriers are present in some of our sites (*e.g.* DDP01, DDP09, DDP11, DDP12, DDP14, DDP18, DDP19, and DDP20) (Figures 3.4 and 3.5).

The question that arises now is about the timing of the remanence acquired by the hematitic crystals. It is common that cooling lavas generate both magnetite and hematite during high-temperature oxidation (Watkins & Haggerty, 1973). Both minerals may lock similar remanence directions, but hematite may also be of secondary origin such as weathering. The similar directions of ChRM determined for magnetite and hematite dominated samples/sites (Table 3.3) supports the near synchronous and primary origin for both magnetic phases. This is also supported by the intergrowth textures and the distribution of hematite flakes across the matrix of the andesites. The second evidence favoring the primary nature of the hematite and its remanence are the positive conglomerate and tilt tests.

In summary, the sites analyzed are dominated by magnetite and titanomagnetites (low Ti) in the PSD-SP range, some of these sites may contain MD magnetite. Hematite is a magnetic phase important in some localities, with sizes in the SD range. Both hematite and magnetite carry a primary thermal remanence acquired during cooling and high-temperature oxidation of the lavas, that is, during its emplacement.

5.2 Paleomagnetic directions and paleopoles

As shown on Table 3.3, a total of 23 tilt corrected site means were used for the calculation of the mean paleomagnetic direction of the Diquiyú unit, and the corresponding paleopole. Sites DDP15 and DDP22 were excluded due to their high α_{95}

(34.9°, 25.1°). Site DDP16 was not used because its uncertain field relationships that preclude the assignment of a reliable age to this site. Site DDP13 was excluded due to its high inclination, this value can be result of a dubious field measurement of bedding attitude. Finally, sites DDP04, DDP14 and DDP19 were excluded from the calculation of both the paleomagnetic direction and the paleopole by applying a 45° cutoff; this cutoff is applied for the exclusion of sites whose dispersion is larger than expected for paleosecular variation (PSV) (Koymans *et al.*, 2016). For the calculation of the paleomagnetic direction all sites were transposed to the eastern quadrant, assumed to represent the closest direction to the northern hemisphere. The resulting paleomagnetic direction (n=23; Dec: 82.8°; Inc: -1.4°; α_{95} : 9.4; k: 11.25) represents the orientation of the geomagnetic field during emplacement of the Diquiyú unit (197-184 My, Sinemurian – Pliensbachian stages according to the 2018 IUGS International Chronostratigraphic Chart). The paleopole orientation was calculated using each site VGP and then averaging all the VGPs into a single result as proposed by Butler (1998), which is reported with its associated statistical parameters A95 and K; the resultant paleopole (N=23, Long: 175°E; Lat: 6.6°S; A95: 8.7°, K: 13.1) has a calculated A95 between 3.4° and 11.4°, so, according to Deenen *et al.* (2011) the dispersion has measured accurately the PSV (Figure 5.1). The resultant VGP distribution is dispersed along a minor circle whose center is located close to the sampling site (Figure 5.1), this distribution may not be result of PSV but of apparent tectonic rotation (MacDonald, 1980). The apparent tectonic rotation may be result of an incomplete tilt correction when the sampling site has been subjected to structural rotations with a non-horizontal axis or to numerous consecutive rotations (MacDonald, 1980). Although a double structural correction was applied, the most probable scenario is that these corrections were not enough to remove apparent tectonic rotations. The direct consequence of this is that the estimates of rotation would have a larger uncertainty and that the mean inclination would be biased towards higher inclinations (MacDonald, 1980). Nonetheless, the mean paleomagnetic direction and the paleopole are still useful for tectonic interpretations, but with certain caution.

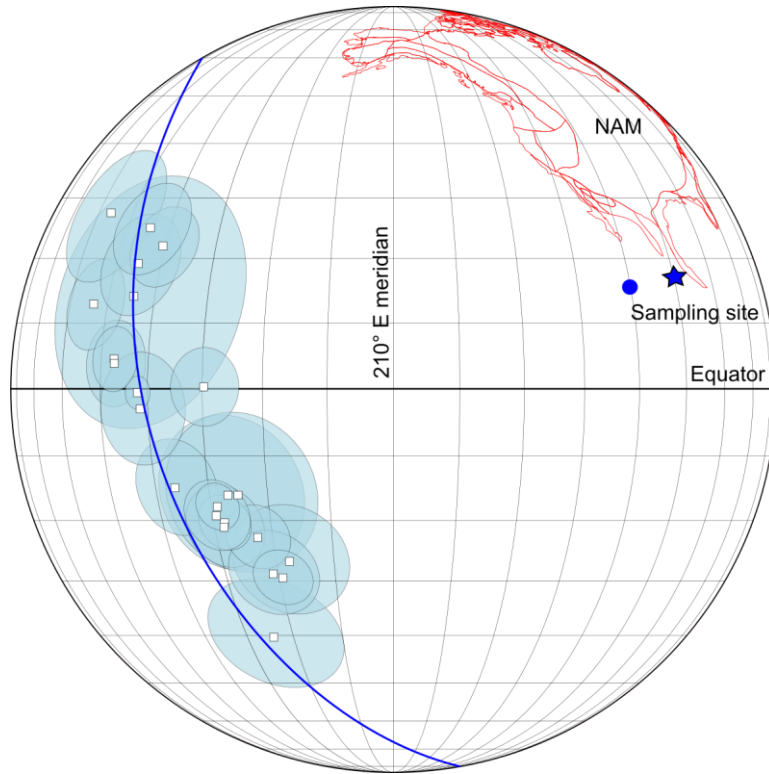


Figure 5-1. VGP distribution for the sites collected in the Diquiyú unit. Figure obtained with the software GMAP (Torsvik & Smethurst, 1999). The blue circular segment represents dispersion caused probably by apparent tectonic rotation (MacDonald, 1980).

In order to quantify the amount of translation and/or rotation of the crustal block containing the Diquiyú unit (Mixteca Terrane) with respect to North American Plate (NAM), the calculated direction and/or paleopole need to be compared with reference directions/poles of the same age and assumed to have been attached to the craton (Figure 5.2). We took into account published poles of 200-150 My, but the poles ranging from 197-184 My are the most relevant (Table 5.1). The oldest poles (200 Ma) come both from the northeast part of the NAM where igneous rocks from the Central Atlantic Magmatic Igneous Province (CAMP) crop out (Kent & Irving, 2010) and from the Colorado Plateau (CP) (Molina-Garza *et al.*, 2003b; Torsvik *et al.*, 2012; McCall & Kodama, 2014); poles from other plates were also used after rotating the poles to NAM coordinates (Kent & Irving, 2010). Although Kent & Irving (2010) included only poles from volcanic sequences and corrected sedimentary rocks, the data presented by them have been criticized by their low number of poles in the mean calculations (Torsvik *et al.*, 2012), so their apparent polar wander path (APWP) is different from older and recent compilations.

Also, the CAMP pole of Kent & Irving (2010) may not average PSV due to the rapid emplacement of these lavas. The Moenave Formation and Wingate Formation poles reported by Molina-Garza *et al.*, 2003b lack an inclination shallowing correction, so their certainty is questioned. Poles from the Moenave Formation (Torsvik *et al.*, 2012) and combined Moenave Formation + Wingate Formation (McCall & Kodama, 2014) are both corrected for inclination shallowing using E/C and anisotropy techniques respectively; although these two poles consider different amounts of CP rotation ($\sim 5^\circ$ by Torsvik *et al.*, 2010; $\sim 10^\circ$ by McCall & Kodama, 2014), the results they give concerning rotation and flattening are similar (Table 5.1). The last two poles will then receive greater focus than the other published for the same ages.

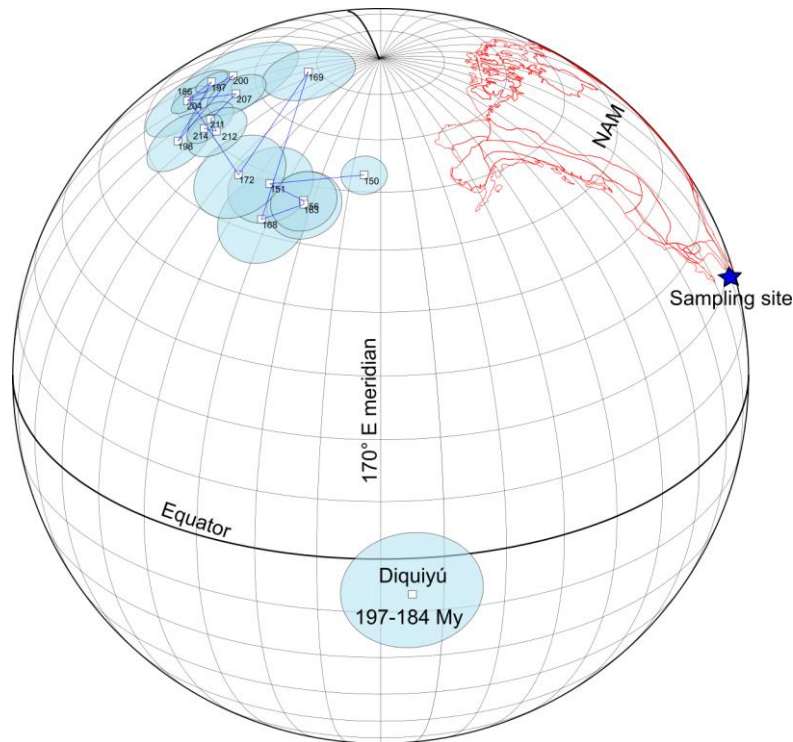


Figure 5-2. Comparison between Diquiyú unit pole and selected poles from the reference APWP of Torsvik *et al.*, 2012. Figure obtained with the software GMAP (Torsvik & Smethurst, 1999).

Table 5-1. Rotation and translation estimates between Diquiyú unit direction and reference directions for the North American Plate.

Pole	Age	N	Lat	Long	Exp. Dec	Exp. Inc	α_{95}	A95	R	ΔR	F	ΔF	Reference
------	-----	---	-----	------	----------	----------	---------------	-----	---	------------	---	------------	-----------

Compilation	160-150	6	69.7	167.2	339	27.8		8.4	103.8	10.1	29.2	8.4	Nova, 2016
Compilation	170-160	9	70.4	114.4	349.7	1.61		6.8	93.1	9.3	3.01	4.6	Nova, 2016
Corral Canyon Volcanics **	170	1	58	123.8	339.2	-13.7	7.8		103.6	9.8	-	3.6	Torsvik <i>et al.</i> , 2012
Corral Canyon Volcanics	170	1	61.8	116	344.6	-12.2	6.2		98.2	9	-	3.6	May <i>et al.</i> , 1986
Compilation ****	180-170	9	71.1	110.2	351.2	1.51		6.7	91.6	9.2	2.9	4.5	Nova, 2016
Canelo Hills Volcanics **, '''	179-173	1	58.7	135.1	335.5	-4.6	7		107.3	9.4	-3.2	4.1	Torsvik <i>et al.</i> , 2012
Canelo Hills Volcanics, '''	179-173	1	62.2	130.3	339.7	-3.4	6.7		103.1	9.2	-2	4.1	Kluth <i>et al.</i> , 1982
Compilation **, ' ,	180	8	79.9	100.4	356.8	15.6		5.5	86	8.7	17	5.3	Kent & Irving, 2010
Compilation	190-180	10	78	109.6	354.4	13.54		7.5	88.4	9.6	14.9	6.2	Nova, 2016
Compilation	195-185	8	71.2	82.1	0.01	-2.4		10.5	82.8	11.3	-1	5	Nova, 2016
Kayenta Formation **, ' ,	186	1	62	77.2	2.4	-20	3.3		80.4	8	-	3.5	Torsvik <i>et al.</i> , 2012
Kayenta Formation *	186	1	59	66.6	8.12	-23.7	3.3		74.7	7.8	-	3.5	Bazard & Butler, 1991
Compilation	200-190	10	61.7	69.2	6.19	-19.5		5.7	76.6	8.8	-	3.5	Nova, 2016
Compilation ****, ' ,	190	8	79.7	91.6	358.3	14.6		6.7	84.5	9.2	16	5.8	Kent & Irving, 2010
Moenave + Wingate Formations. ***, AN	200	1	62.5	69.9	5.7	-18.2	5.5		77.1	8.7	-	3.5	McCall & Kodama, 2014
Moenave Formation **, ,	200	1	62.5	71	5.19	-18.4	2.8		77.6	7.8	-17	3.5	Torsvik <i>et al.</i> , 2012

Wingate Formation *	200	1	57.4	56.6	13.7	-23.1	6.4		69.1	9	21.7	3.5	Molina-Garza <i>et al.</i> , 2003b
Moenave Formation *	200	1	63.7	59.7	9.8	-13.5	5		73	8.5	12.1	3.5	Molina-Garza <i>et al.</i> , 2003b
Compilation ****, †	200	7	67.8	81.8	0.1	-9.2		3.8	82.7	8.1	-7.8	3.6	Kent & Irving, 2010
CAMP	201	1	66.3	97.3	353.9	-10.6		5	88.9	8.5	-9.2	3.6	Kent & Irving, 2010

N= Number of paleomagnetic poles, Lat – Long= Coordinates of the reference pole, Exp. Dec – Inc= Expected directions for a site in Lat: 17.58, Long: 262.15, a95 = Error for reported paleomagnetic directions, A95= Error for reported paleomagnetic poles, R = Rotation estimate between expected and calculated pole or direction, ΔR = Uncertainty for rotation estimates, F = Flattening estimate between expected and calculated pole or direction, ΔF = Uncertainty for flattening estimates, ΔR and ΔF has the 20% reduced factor of Demarest (1983).

* Colorado Plateau <5° clockwise rotation restored

** Colorado Plateau 5.4° clockwise rotation restored

*** Colorado Plateau 10° clockwise rotation restored

**** When necessary Colorado Plateau 13° clockwise rotation restored

† E/I correction for inclination shallowing

‡ Anisotropy correction for inclination shallowing

''' Age revised by Lawton & McMillan, 1999

Because of the easterly shallow direction and its uncertainty, the hemisphere and polarity are ambiguous. As can be seen in figures 5.3 and 5.4, the comparison between the Diquiyú unit direction and directions derived from rocks of the same age range (197 – 185 My) gave similar discordant R values (75° to 83° in normal polarity, -95° to -105° in reverse polarity). Interpretation of latitudinal displacement is more problematic as three types of F values depend on the reference pole: The 190 Ma compiled pole of Kent & Irving (2010) shows a discordant result with positive F= 16°+/-5.8°, meaning a northward displacement of southern Mexico relative to NAM of 904 +/-323 km. The 200-190 My compilation of Nova (2016) and the CP Kayenta Formation of both Bazard & Butler

(1991) and Torsvik *et al.* (2012) show negative F values ($F = -18.1 \pm 3.5$; -22.3 ± 3.5 ; -18.6 ± 3.5 respectively), meaning a southward translation of (952 ± 195 km; 1213 ± 195 km and 985 ± 195 km respectively). From these, the Torsvik *et al.* (2012) pole is of higher inclination for it applies an E/C correction of 0.6. Finally, the 195-185 My compilation (the same age range of Diquiyú unit) of Nova (2016) shows a concordant F, meaning paleolatitudinal stability between NAM and southern Mexico. In the compilation of Nova (2016) North American and South American poles are combined with the mobile time window method. For this, the poles of South America were rotated into North America coordinates using the parameters of Pindell and Kennan (2009). Importantly, all Lower-Middle Jurassic units in the continental arc yield paleolatitudes between about 7°S and 7°N (*e.g.*, Godínez-Urban *et al.*, 2011b; Nova, 2016; Table 5.3).

The younger Middle Jurassic reference poles show similar rotation values and F values that range between ~ -2 and $\sim +12$ that are generally not statistically significant. The compilations made by Nova (2016) for comparing Jurassic rocks of central Mexico take into account stable poles from NAM and SAM; nevertheless, the author does not specify the poles he used.

Owing to hemisphere/polarity uncertainty, the sense of rotation cannot be assessed directly. In order to solve this problem we used the *in situ* RO pole published by Böhnel (1999) obtained from the same locality where Diquiyú unit was sampled, but for the Zorrillo Formation, assumed here to have an age of 168 Ma corresponding to the Bathonian stage (Sandoval & Westermann, 1986). The age and attitude of the beds was reassessed in this work after visiting the field locality; there we found core vestiges in Zorrillo Formation not in Rosario Formation as was published by Böhnel (1999). We applied to the *in situ* mean direction of Böhnel (1999) a tilt correction of Dip direction = 47° , Dip = 58° and obtained a mean direction of Dec = 230.4° Inc = 6° (D = 50.4° , I = -6°) with a corresponding paleomagnetic pole at Lat = -36 , Long: 190. Comparing with the reference poles ranging from 180 Ma to 160 Ma discordant R values between 59° and 74° in northern hemisphere (normal polarity) and between -108° to -120° in southern hemisphere are obtained (Table 5.2). As this pole is younger than the pole we calculated

for the Diquiyú unit, the amount of rotation registered by it should be less or equal than the rotation calculated from the Diquiyú pole. With this consideration, the declination of 82.8° reflects positive (clockwise) rotation and mean inclination of -1.4° reflects a normal polarity for rocks deposited in the southern hemisphere. This seems to be the most plausible scenario.

Table 5-2. Rotation and translation estimates between Zorrillo Formation (Modified from Böhnel, 1999) direction and reference directions for the North American plate. The same considerations as in Table 5.1.

Pole	Mean Age	N	Lat	Long	Exp Dec	Exp Inc	a95	A95	R	ΔR	F	ΔF	Reference
Compilation	160-150	6	69.7	167.2	339	27.8		8.4	71.4	8.2	33.8	7.9	Nova, 2016
Compilation	170-160	9	70.4	114.4	349.7	1.61		6.8	60.7	7.2	7.6	3.4	Nova, 2016
Corral Canyon Volcanics **	170	1	58	123.8	339.2	-13.7	7.8		71.2	7.8	-7.7	1.9	Torsvik <i>et al.</i> , 2012
Corral Canyon Volcanics	170	1	61.8	116	344.6	-12.2	6.2		65.8	6.9	-6.2	1.9	May <i>et al.</i> , 1986
Compilation ****	180-170	9	71.1	110.2	351.2	1.51		6.7	59.2	7.2	7.5	3.3	Nova, 2016
Canelo Hills Volcanics **, '''	190-170	1	58.7	135.1	335.5	-4.6	7		74.9	7.3	1.4	2.7	Torsvik <i>et al.</i> , 2012
Canelo Hills Volcanics, '''	190-170	1	62.2	130.3	339.7	-3.4	6.7		70.7	7.2	2.6	2.7	Kluth <i>et al.</i> , 1982
Compilation **, '´	180	8	79.9	100.4	356.8	15.6		5.5	53.6	6.5	21.6	4.3	Kent & Irving, 2010
Compilation	190-180	10	78	109.6	354.4	13.54		7.5	56	7.6	19.5	5.3	Nova, 2016
Compilation	195-185	8	71.2	82.1	0.01	-2.4		10.5	50.39	9.6	3.6	4	Nova, 2016

Kayenta Formation **,'	186	1	62	77.2	2.4	-20	3.3		48	5.4	-14	1.6	Torsvik <i>et al.</i> , 2012
Kayenta Formation *	186	1	59	66.6	8.12	-23.7	3.3		42.28	5.4	17.7	1.6	Bazard & Butler, 1991

5.2.1 Comparison with other results from the Mixteca terrane

The clockwise rotation obtained here for the Mixteca Terrane is comparable with rotations in the same sense obtained in the Otlaltepec Basin for Permian and Jurassic aged rocks (Totoltepec stock and Piedra Hueca Formation that was wrongly called Matzitzi Formation in the original reference of Fang *et al.*, 1989). Seven sites in the Early Permian Totoltepec stock yield a southwest directed mean direction of $D=204.3^\circ$ $I=-21.3^\circ$. At face value the mean suggests a clockwise rotation of about 60° . But this result is somewhat uncertain because there is no reference to the paleohorizontal in the pluton. The shallow negative inclination in the pluton suggests that a simple vertical axis rotation is not sufficient to bring the Totoltepec direction in agreement with the expected Permian direction, because the expected direction is to the southeast and of shallow positive inclination.

The characteristic magnetization isolated in the redbeds of the Piedra Hueca Formation (not Matzitzi Formation) north of the Totoltepec stock (Fang *et al.*, 1989) is interpreted there as acquired during folding previous to Cretaceous times. The age of this unit is Early Jurassic (Martini *et al.*, 2016). The magnetization reported is synfolding, and remagnetization should have occurred prior to deposition of the Middle Jurassic Otlaltepec Formation. The declination observed in the Piedra Hueca Formation is to the northeast with $D=17.9^\circ$ $I=-23.9^\circ$. The $\sim 30^\circ$ clockwise rotation of Otlaltepec Basin suggested by this declination value (Table 5.4) implies that at least 60° of clockwise rotation should have occurred during the lapse between Diquiyú unit emplacement and Piedra Hueca remagnetization, this if a regional rotation is considered. Nevertheless, the Zorrillo Formation pole, with an age somewhat closer to that of the Piedra Hueca

Formation remagnetization, reveals 70° of clockwise rotation; this would signify that both basins were subjected to different amounts of rotation.

Differential rotation for regions in southern Mexico is supported by Permian remagnetization directions obtained in the Oaxaca Terrane from Paleozoic strata and the contact aureole of the Etna Granite (McCabe *et al.*, 1988; Ballard *et al.*, 1989); these poles are concordant and reveal stability of the Oaxaca Terrane with respect to NAM since at least Permian times. The differential rotation between the Mixteca and Oaxaca terranes may have occurred before late Early Cretaceous, when all the southern Mexican blocks attained stability with North-American craton (Böhnel, 1999). The Caltepec Fault that marks the frontier between the Oaxaca and Mixteca blocks is postulated as reactivated in the Early Cretaceous (Elías-Herrera *et al.*, 2005), this implies that the relative movement between Mixteca and Oaxaca blocks would have been accommodated in part by this fault. The relative motion between the Jurassic basins inside the Mixteca Terrane may have been accommodated by structures like the Salado, Sabino and Matanza faults that served at these times as basin bordering faults, both along and across basin strike (Martini & Ortega-Gutierrez., 2016).

Table 5-3. Data from selected sites used for the construction of figures 5.3 and 5.4.

Unit	Age	D	I	ΔD	ΔI
Diquiyú unit	197 – 184 My ¹	82.8	-1.4	8.8	17.5
Zorrillo Formation	170 -168 My ²	50.4	-6	5	9.8
Nazas Formation	180 – 178 My ³	20.9	+9	5	10.3
La Boca Formation	167 – 163 My ⁴	358.1	-9.5	4.2	8.3
Piedra Hueca Formation	184 – 167 My ⁵	17.9	-23.9	5.5	8.8
La Silla Formation	190 – 194 My ⁶	325	+4.6	7.4	14.8

¹ Age according to Durán-Aguilar (2014), direction from here

² Age according to Sandoval & Westermann (1986), direction from Böhnel (1999) and modified here

³ Age according to Zavala-Monsivais (2012), direction from Nova (2016)

⁴ Age according to Rubio-Cisneros & Lawton (2011), direction from Nova (2016)

⁵ Age according to Martini *et al.* (2016), direction from Fang *et al.* (1989)

⁶ Age according to Godínez-Urban *et al.* (2011a), direction from Godínez-Urban *et al.* (2011b)

ΔD and ΔI were calculated in paleomagnetism.org with principles exposed by Butler (1998).

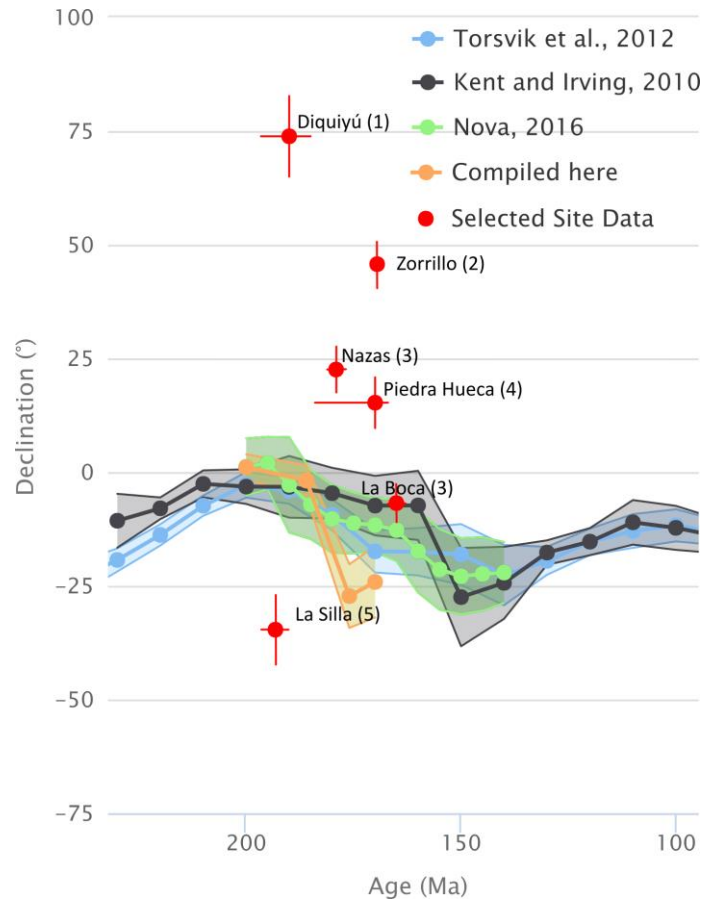


Figure 5-3. Declination comparison between selected Lower and Middle Jurassic poles and reference APWP's. Figure obtained with Paleomagnetism.org (Koymans et al., 2016). Poles from: 1) Studied here; 2) Modified from Böhnell, 1999; 3) Nova, 2016; 4) Fang et al., 1989; 5) Godínez-Urban et al., 2011b.

Using the best determined poles for the Lower-Middle Jurassic interval (Moenave, Kayenta, Corral Canyon, Canelo Hills) the direct interpretation is stability between Mixteca Terrane and NAM in terms of paleolatitude. Same conclusion can be reached between the Nazas Arc and NAM, as the calculated and compiled poles from this volcano-sedimentary province plot inside the bar errors of the latitudinal path of NAM (Figure 5.4). But differential clockwise rotation appears to have affected Lower-Middle Jurassic basins.

The southern displacement of the Oaxaca-Mixteca block in the Jurassic invoking a structure parallel to the Mojave-Sonora or the Trans-Mexican volcanic belt as proposed

by Anderson & Schmidt (1983), and again more recently by Martini & Ortega-Gutiérrez (2016), is not supported by the paleomagnetic data. There are no inclination anomalies and left lateral faults would inevitably require counter-clockwise rotation – opposite to what was observed. Also, the Böhnel (1999) type model of southern translation along Tamaulipas-Golden Lane-Chiapas or similar faults are discarded on the basis of the shallow inclinations (paleolatitudes) observed across the Mixteca Terrane in the Jurassic. The paleomagnetic data are in agreement with a western position of the Mixteca Terrane close to the Pacific Nazas trench, which is the most plausible scenario for Jurassic times (*e.g.*, Helbig *et al.*, 2012; Ocampo-Díaz *et al.*, 2019).

Northward absolute latitudinal displacement is predicted for the NAM craton in most published APWPs (*e.g.*, Kent & Irving, 2010; Torsvik *et al.*, 2012, Figure 5.4), and using these APWPs as reference a northward displacement relative to the craton is permissible for some poles in the Mixteca Terrane (Zorrillo Formation named after Rosario Formation pole of Böhnel, 1999; Piedra Hueca Formation Pole named after Matzitzzi Formation pole of Fang *et al.*, 1989), and also for some poles obtained along the Nazas Arc trace (Nazas Formation and La Boca Formation poles of Nova, 2016). Table 5.4 shows that the pole obtained by Nova (2016) in Charcas locality and dated as Toarcian by Zavala-Monsivais *et al.* (2012) describes a northward movement using Kent & Irving (2010) APWP as reference, and shows stability with the Canelo Hills pole of Torsvik *et al.* (2012) curve, that is the best pole of comparable age. The younger La Boca pole of Nova (2016), dated as Callovian by Rubio-Cisneros & Lawton (2011) shows northward displacements from ~950 to ~3500 km for all the collection of reference poles (Table 5.4). The Piedra Hueca pole of Fang *et al.* (1989) also shows similar displacements; nevertheless, the uncertainty in the age of the magnetization and also in the structural correction precludes any validation of the northward displacement. The La Silla Formation pole obtained by Godínez-Urban *et al.* (2011b) is located slightly northward with respect to the reference curves, so, a small southward displacement relative to the craton is interpreted. This movement is in accordance with several studies that explain opening of the Gulf of Mexico by rotation of the Maya Block (Pindell & Dewey, 1983; Molina-Garza *et al.*, 1992; Godínez-Urban *et al.*, 2011b).

The northward displacement of ~500 to ~1500 km of the Mixteca Terrane relative to North America, if real, may have occurred along faults with similar orientation to the Caltepec and Oaxaca faults or the Tamaulipas-Golden Lane-Chiapas transform occurring in the western border of Pangea. Models that propose margin parallel northward displacement have been proposed to explain Jurassic terrane displacement in the Northwestern Andes (Bayona *et al.*, 2006; Kennan & Pindell, 2009).

Table 5-4. Rotation and flattening parameters for selected sites related to Nazas arc. Age assignation explained in table 5.3.

Unit	Age	Dref	Iref	Ref	R	ΔR	F	ΔF
Nazas Formation	180 – 178 My	338	-1.36	Corral Canyon, 170 Ma (Torsvik <i>et al.</i> , 2012)	42.9	8.8	-10.36	5.4
		334.3	8	Canelo Hills, 179 – 173 My (Torsvik <i>et al.</i> , 2012)	46.6	8.4	-1	6
		356.2	25.9	180 My compilation (Kent & Irving, 2010)	24.7	7.6	16.9	6.7
La Boca Formation	167 - 163 My	325.8	35.7	Sumerville Formation Trujillo, 163 Ma (Torsvik <i>et al.</i> , 2012)	32.3	17.6	45.2	13.6
		338.8	-1.8	Corral Canyon, 170 Ma (Torsvik <i>et al.</i> , 2012)	19.3	15.5	7.7	4.6
		335	7.34	Canelo Hills, 179 – 173 My (Torsvik <i>et al.</i> , 2012)	23.1	15.3	16.8	5.2
		356.5	26.6	180 Ma compilation (Kent & Irving, 2010)	1.6	14.9	36.1	6.1
Piedra Hueca Formation	184 - 167 My	339.3	-12.5	Corral Canyon, 170 Ma (Torsvik <i>et al.</i> , 2012)	38.6	8.1	11.4	1.2
		335.5	-3.3	Canelo Hills, 179 – 173 My (Torsvik <i>et al.</i> , 2012)	42.4	7.6	20.6	2.3
		356.8	17	180 Ma compilation (Kent & Irving, 2010)	21.1	6.7	40.9	4
La Silla Formation	194 - 190 My	4.72	-22.15	Kayenta Formation 186 Ma (Torsvik <i>et al.</i> ,	-39.7	10	-26.75	5.9

				2012)				
		359.2	11.54	200 Ma compilation (Kent & Irving, 2010)	-34.2	10	6.9	6.4
		7.4	-20.1	Moenave Formation 200 Ma (Torsvik <i>et al.</i> , 2012)	-42.4	9.7	-24.7	5.9

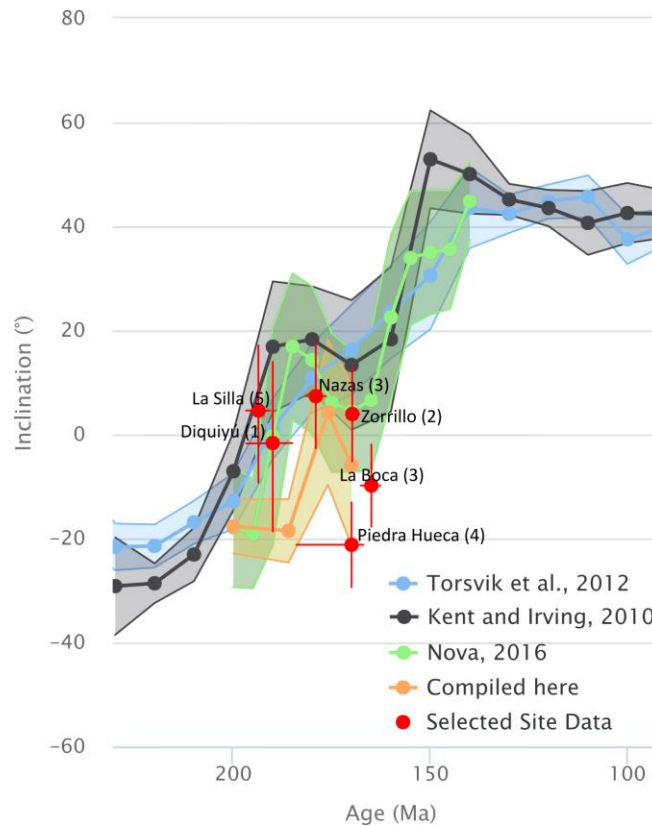


Figure 5-4. Paleolatitudinal comparison between selected Lower and Middle Jurassic poles and reference APWP's. Figure obtained with Paleomagnetism.org (Koymans et al., 2016) with paleolatitudes obtained using methods in Van Hinsbergen et al. (2015). Poles from 1) Studied here; 2) Modified from Böhnell, (1999); 3) Nova, (2016); 4) Fang et al. (1989); 5) Godínez-Urban et al. (2011b).

5.3 Facies and environment

According to Erben (1956), the Rosario Formation comprises two different rock types, conglomerate and mudstone, with significant spatial variations in their relative thickness. The conglomerates are abundant in the NE part of the Diquiyú Anticlinorium (Rosario

Nuevo succession) whereas they are scarce to the west and south of the structure. This observation was described in detail by Jiménez-Rentería (2004) in his bachelor thesis; he determined the need of separating the Rosario Formation into two units, namely, Rosario Formation in the base and Conglomerado Prieto Formation at the top, encompassing the muddy and conglomeratic facies respectively. He also proposed to group these two units in the Consuelo Group. Another way of showing the dual nature of the unit without obfuscating the traditional stratigraphic terms would be naming the body dominated by conglomeratic facies as a member (*i.e.* Prieto Conglomerate member) within the more regional Rosario Formation. Erben (1956) also proposed the existence of two lithostratigraphic groups in the area, namely, Consuelo Group and Tecocoyunca Group. The lower one (Consuelo Group) included the Rosario Formation at the base and the Cualac conglomerate at the top, and the upper one included the complete Tecocoyunca sequence from the Zorrillo Formation to the Yucufñuti Formation. As was first debated by Alcencaster (1965), Cualac conglomerate is better located at the base of the Tecocoyunca Group as it represents the initial stages of a shallowing upward succession. (Figure 5.5) Although a local transitional boundary between Prieto conglomerate member and Cualac conglomerate is recognized, a regional discordance between Rosario Formation and Cualac conglomerate is manifest (Zepeda-Martínez *et al.*, 2018) precluding any genetic grouping. In the sense of the discussion above, the Consuelo Group term is unnecessary. The relationship between these units could be as depicted in Figure 5.6.

		Erben, 1956	Alencaster, 1965	González-Torres, 1989	Jiménez-Rentería, 2004	Zepeda-Martínez et al., 2018	This study
Phanerozoic Mesozoic	Jurassic	Middle	Callovian	Otatera & Yucuñuti	Upper Tecocoyunca Gp.	Otatera & Yucuñuti	Otatera & Yucuñuti
			Bathonian	Simón Fm.	Simón Fm.	Simón Fm.	Simón Fm.
			Bajocian	Taberna Fm.	Taberna Fm.	Taberna Fm.	Taberna Fm.
		Lower	Aalenian	Zorrillo Fm.	Zorrillo Fm.	Zorrillo Fm.	Zorrillo Fm.
			Toarcian	Cualac Conglomerate	Cualac Conglomerate	Cualac Conglomerate	Cualac Fm.
			Pleinsbachian	Rosario Fm.	Rosario Fm.	Rosario Fm.	Rosario Fm.
	Triassic	Upper	Sinemurian			Quartzitic Cualac Fm.	
			Hettangian			Prieto Conglomerate Fm.	Diquiyú Fm.
			Raethian	Diquiyú Unit	Diquiyú Unit	Rosario Fm.	Diquiyú unit
		Lower	Norian				
			Carnian				

Figure 5-5. Different nomenclatures for the succession outcropping in Rosario Nuevo creek.

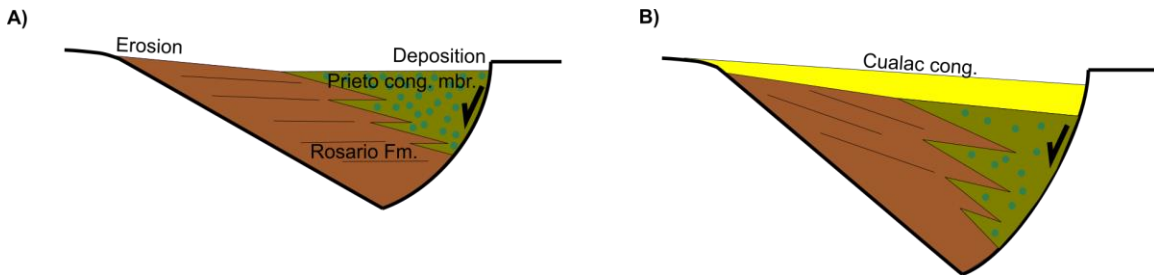


Figure 5-6. Stratigraphic relationships and basin interpretation for Rosario Formation, Prieto conglomerate member and Cualac conglomerate. A) Localized subsidence near a normal fault causes uninterrupted accumulation while the adjacent zones experience erosion due to lower subsidence rates; B) A regional depositional system covers the previous succession developing different stratigraphic contacts.

5.3.1 Lithofacies distribution

Prieto conglomerate member of the Rosario Formation

Prieto conglomerate member of the Rosario Formation is characterized by the predominance of Gh lithofacies with little Gcm, Gci, and Gmm as the subordinate gravel facies. Gh reveal the primary action of traction currents depositing the sediment, in the form of downstream gravel-bar migration (Miall, 2006) whereas the other gravel

lithofacies may be the result of localized debris flows (Miall, 2006). Nevertheless, only the Gmm facies is definite for defining debris flows as Gcm and Gci can be developed by low energy traction currents (Miall, 2006). A thin interval was observed containing Gt facies and making a possible lateral accretion (LA) or downstream accretion (DA) element, this observation is in good agreement with the predominance of traction currents as the primary agent on sediment mobilization. Thin intervals containing Sh and Fl lithofacies may represent the sporadic occurrence of flash floods (Miall, 2006).

Cualac conglomerate

This unit comprises a wider range of lithofacies than the underlying unit. Gh is common mainly in the lower part of the unit making continuous centimetric packs of beds with lenticular geometry. In the middle part of the unit Gt bedforms are the most common, resulting from the migration of transverse dunes or by the filling on minor channels (Miall, 2006), the latter occurring at the initiation of fining-upward cycles. Less common is the presence of Gp lithofacies generated by waning floods over gravel sheets. Two ways of gravel preservation are ubiquitous through all Cualac conglomerate succession: first, segregated packs of gravel and sand both with cross stratification (this structure is termed a humpback dune); the second is the presence of gravel sheets capping sandy bedforms, product of scour and fill caused by changing water depth and velocity during bar growth (Miall, 2006).

Sandy lithofacies are common from the middle to the upper part of the succession, where they are abundant. St is the most common lithofacies, representing the migration of 3D dunes, commonly followed by Sh and Sr creating fining upward cycles capped by Fl and coal in occasions, these cycles may represent the filling of channels in probable high flow regimes (Miall, 2006). Sl is a less common lithofacies and is related to the development of humpback dunes. To the top of the succession the presence of gravel facies is almost negligible giving way to Sr, Sh and Fl lithofacies commonly developing heterolithic strata, and also to thick beds of coal; some ferruginous nodules with varied shapes are

present, this is the initiation of the transitional-marine succession of the Zorrillo Formation.

5.3.2 Architectural elements

The architectural elements described here are based on those proposed by Miall (2006) (Table 5.3), their stratigraphic distribution is included in the Appendix 4. GB is the principal element developed in Prieto conglomerate member of the Rosario Formation, this is produced by horizontally stratified gravel sheets, although few accretion surfaces were recognized (DA or LA), the principal mode of sedimentation of this unit was aggradation, as series of GB are superposed, representing a high load of sediment in the transporting agent. Scarce SG elements represent local debris flows. The limited development of SB and OF can be interpreted in terms of low channel abandonment and low sinuosity of the river.

Table 5.5. Architectural element classification and interpretation according to Miall (2006).

Architectural element	Lithofacies	Description
GB	Gh, Gci, Gcm, Gp, Gt	Gravel bedforms deposited by traction currents
SG	Gmm, Gmg	Gravity driven deposits, debris flows
SB	Sp, St, Sh	Sandy bedforms deposited by traction currents
CH	Gh, Gp, Gt, Sp, Sh, St, Fl	Channel fill successions
LS	Sh, Sl	Laminated sands deposited in distal and/or overbank settings
OF	Sh, Sr, Fl	Fine sediments deposited in overbank settings

Cualac conglomerate comprises a larger amount of SB elements together with GB. No signs of accretion were recognized, so aggradation of bedforms is again the predominant process; this fact can be taken in account for excluding high sinuosity rivers as the dominant river type; nevertheless, the larger presence of fining upward cycles may be due to higher rates of channel avulsion, representing a probable highly sinuous river with low rates of subsidence. The major part of fining-upward cycles in the lower part of the succession start with Gh followed by Gt and grading into Sh a St, this cycle is typical in

the filling of minor channels and scours. In the upper part of the succession the fining upward cycles are sand dominated. Some LS elements composed by Sh and Fl are present, representing distal braid plains, again alluding for a low subsidence rate of the system (Miall, 2006).

5.3.3 Fluvial style

The shallow gravel river comprises Gh, Gp, and Gt lithofacies; some sand may be deposited at low stage and probably some SG elements can be interbedded, but in a low percentage. Although this river type encompasses all the facies observed in the Prieto conglomerate member succession, the outcrops of this unit adjacent to Rosario Nuevo creek are different, more sand and mud rich, so these successions need to be considered for better classifying the depositional environment. Also, the intertonguing relationship with Rosario Formation is important in this matter. Two configurations that can explain the facies development are: first, a braided delta in which the succession described here comprises the proximal facies closest to the high topographies and to the source rocks whereas the sandy-muddy facies represent distal parts of the system where more overbank facies develop (Figure 5.7 A); within this river system, the SW (SE, after back rotated) direction measured with paleocurrents would represent the flow direction of the whole river system, so the base level (sea, lake) would be somewhere in this direction. However, the development of a braided delta would suppose a progradational sequence whereas this succession is aggradational.

The second probable configuration is one with a transverse river and a longitudinal one; the transverse system would have flowed from the high topographies, depositing its sediment load near the topographic slope break, and would have joined to a longitudinal river. This latter would be more stable, probably more sinuous, flowing parallel to the mountain front. This longitudinal river would have deposited the Rosario Formation, whilst the transverse system corresponds only to the Prieto conglomerate member of the Rosario Formation (Figure 5.7 B). The second model would be preferred; nevertheless, paleocurrent indicators in the Rosario Formation are needed.

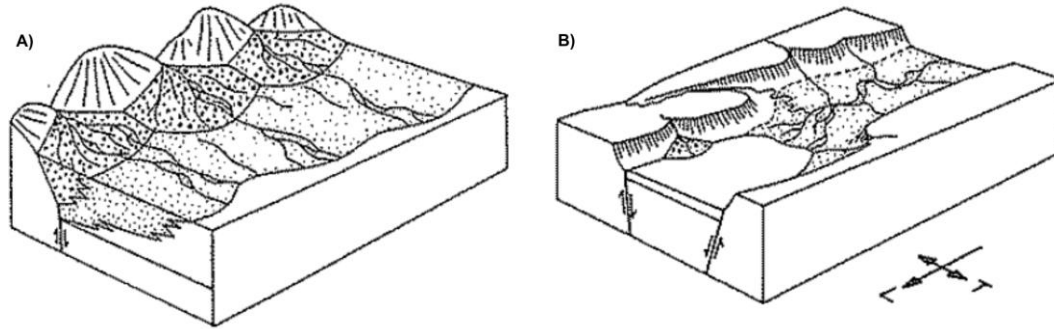


Figure 5-7. Two possible river system configurations for the Rosario Formation and for the Prieto conglomerate member of the Rosario Formation from Miall (2006).

The change from Prieto conglomerate member to Cualac conglomerate is observed here as transitional; in the lithofacies succession is expressed by an upward decrease in Gh elements with an increase in sand related lithofacies. One clear feature observable through the whole Cualac conglomerate succession is the ubiquitous development of fining upward cycles, with typical GB-SB-OF successions. Towards the top of the succession there are less to absent GB elements. These cycles can be both controlled by avulsion processes, thus alluding for higher sinuosity of this river, or by external climatic-tectonic factors. The architectural scheme observed in the Cualac conglomerate succession is comparable with two models: a deep gravel braided river or a wandering river. The second type cannot be regarded as definite due to the absence of DA or LA macroforms which represent the migration of alternate bars; this absence can be fictitious because of the outcrop conditions. The paleocurrent directions obtained in this succession (NW, SW with rotation correction) are of dubious character as the position of the bars inside the channels is uncertain.

Basins that subside rapidly deposit quickly their gravel content and develop a fast downstream reduction in grain size (Miall, 2006), as is observed in the Prieto conglomerate member of the Rosario Formation. In contrast, Cualac conglomerate shows a slow relative subsidence as its facies are present in a wider area (Oaxaca-Guerrero). To highlight this change in subsidence pattern we can observe the high content of less resistant clasts (andesitic) in Prieto conglomerate member, clasts that are better preserved

in high burial rates whereas Cualac conglomerate comprises a stable suite of minerals likely to be preserved in slow subsidence conditions. Finally, the higher rates of avulsion and overbank facies development in Cualac conglomerate support the interpretation of lower subsidence rates up-section.

Although neither straightforward nor excluding, many characteristics of both Prieto conglomerate member and Cualac conglomerate allude for a humid climate with constant rates of discharge during their deposition. The scarcity of gravity driven density and/or debris flows in both units is a good indicator of humid climate. The channel nature itself of Prieto conglomerate member that reflects aggradation as the primary process seem to relate to a channel that instead of eroding its banks is confined within its own channel, this is typical in environments with high vegetation cover that inhibits cutbank erosion. In the Cualac conglomerate the overwhelming presence of stable minerals indicate removal of unstable minerals both in the source area and during transport. The ubiquitous presence of coal in both units, as thin lenses, and in the overlying Zorrillo Formation as thick beds is one of the most direct humid condition indicators.

5.4 Petrography

The most evident observation in the Rosario Nuevo Creek succession is the textural and compositional change between the Prieto conglomerate member and the Cualac conglomerate, although with a transitional character revealed by a 30 m thick interval with mixed characteristics. The complete predominance of conglomerates in the Prieto conglomerate member succession was discussed as being related to a near source area; nevertheless, this nearby basin-source area relationship is contrary to the high roundness of the gravel and even the sand fraction of this unit; although the sand sized clasts are slightly more angular. One plausible explanation to this observation is an *in situ* rounding by weathering action, as it is common in volcanic rocks. Facial analysis and paleomagnetic results argued the possibility of an equatorial humid climate during this unit deposition; so, the high moisture conditions would have increased the chance of chemical disintegration of the source rock (Garzanti *et al.*, 2013). Cualac conglomerate

clasts are less rounded ranging from subangular to subrounded, and their sizes are smaller, this would imply the existence of different rock types in the source, more resistant to chemical abrasion, also, a probable longer travel distance would have occurred as the clasts are somewhat highly rounded for their mineralogy (quartz dominated) (Folk, 1978). The compositional change in the succession can be observed both in the gravel and sand fractions; the lower succession is volcanic lithic dominated and the upper is quartz and metamorphic lithic dominated (Figures 4.1, 4.6). The transitional interval has both compositional classes. An inference that can be deduced by the observation of gravel and sand composition in the Prieto conglomerate member is the complete prevalence of volcanic gravel clasts while the sandstones have a wider composition. This can be explained by the preference of aphanitic volcanic rocks to disintegrate in large blocks, contrary to the more crystalline rock types that tend to disintegrate in sand sizes (Garzanti *et al.*, 2019). Different sources for sandstones and conglomerates can also explain the difference in composition. It has been observed in modern streams located at equatorial latitudes that the lithic aphanitic detritus are washed away downstream both by mechanical disintegration processes and by dilution (Savage & Potter., 1991; Garzanti *et al.*, 2013). Although not a rule always applicable, as some rivers in the same latitudinal bands preserve lithics for thousands of kilometers (*e.g.* Nile River headwaters, Garzanti *et al.*, 2013), a long and durable transport of detritus for Cualac conglomerate can be proposed, at least longer than Prieto conglomerate member, as it is composed by both mechanical and chemical resistant minerals. This mineralogical stability increases upward in the succession, thus the sources were both being highly weathered and/or located more distant from the basin. Another possibility can be the reworking action of transitional to marine environments acting as homogenization tools. This action is discarded here for the Cualac conglomerate, as we did not observe any facial indication of marine activity. Nonetheless, for the Zorrillo Formation the effect of transitional environments is arguable, and in response, the sandstone composition is more stable composed by quartz and reworked sedimentary lithic grains.

The evolutionary compositional parameters once plotted in variety of discriminations triangles (Figure 4.6, 4.7) show a path from an undissected arc towards a recycled orogen. One important detected feature is the departure of my observations from common dismantling of both arcs and continental blocks (Dickinson & Suczek, 1979; Ingersoll, 2012; Garzanti, 2016; Marsaglia *et al.*, 2016) as I did not find feldspars in my samples that could represent provenance from the dissected parts of a continental arc or from a rifted continental block. The paths we found were directed towards quartz rich regions. We explain this behavior by the action of a humid climate with high moisture which washed away all non stable chemical minerals or by the absence of plutons in the source area. The presence of Permian plutonic detritus until Middle Jurassic times has been reported in the Otlaltepec Basin, located north of the area (Martini *et al.*, 2016), so the absence of exhumed plutons providing detritus during Lower Jurassic times is likely.

The best scenario obtained from the regional geology and combining both the facial and petrographic characteristics seem to correlate with the dissection of a metamorphic orogen (Oaxaca – Acatlán complexes), subjected to localized andesitic volcanism, divided in segments subjected to varying degrees of uplift, and with decreasing subsidence rates through time. These characteristics are common in extensional settings; nevertheless, these extensional settings can be developed both by rift systems and by arcs in which the subducting plate retreats (Gawthorpe & Leeder, 2000; Lawton & McMillan, 1999).

The faulting of the block was oriented SW-NE, perpendicular to the rotated paleocurrent direction, this faulting exposed block shoulders which first provided volcanic detritus derived from an andesitic cover (Diquiyú unit) to a basin close to the fault, generating the Prieto conglomerate member. Some andesitic eruptions, probably related with the same normal faults, were simultaneously deposited through this time. The back part of the uplifted block with less gradient and thus more stable and more exposed to weathering, was providing detritus of the Acatlán Complex. Sediment input was probably from a variety of tributaries to a medium scale (*e.g.* Orinoco River size) braided river, which probably traveled thousands of kilometers in a NW-SE direction (as revealed by its

presence in Olinalá and Ayuquila basins). Detrital zircon patterns reported by Zepeda-Martínez *et al.* (2018) support this interpretation as Prieto conglomerate member shows a predominance of Jurassic zircons related to the erosion of the Lower Jurassic volcanic rocks whilst Cualac conglomerate shows more Paleozoic and Precambrian peaks more likely related to the erosion of the metamorphic orogen of both Mixteca and Oaxaca terranes.

5.5 Arc and continental paleogeography

What was the tectonic entity responsible for the deposition of the succession outcropping along Rosario Nuevo Creek? The discussion of evidence presented until now indicate an extensional regime with uplifted blocks and close adjacent basins partially disconnected as the geometric configuration. These conditions have been determined in this and in other areas for rocks of the same age (Michalzik, 1991; Zepeda-Martínez *et al.*, 2018; Ocampo-Díaz *et al.*, 2019) and have been assigned to two different extensional mechanisms: extension in intra-arc and back-arc positions along the Jurassic Nazas Arc (Bartolini *et al.*, 2003; Barboza-Gudiño *et al.*, 2012; Ocampo-Díaz *et al.*, 2019), and extension provoked by the early phases of Yucatan Block rotation alluded to a NW-SE separation between North and South American plates, a rifting mechanism (Martini & Ortega-Gutierrez, 2016). In the first set of models the extensional stress that created the basins is generated by a slab retreat in the paleo-Pacific subduction, thus the basins would be parallel to the arc and would receive detritus directly from it, both as volcanics and as reworked detritus; these characteristics are widely distributed along continental Mexico, and extend northward to the United States and southward to Colombia (Bartolini *et al.*, 2003).

The Lower-Middle Jurassic plutons representing the arc roots are scarce in Mexico, cropping out mainly in the north (Sonora State) and in some wells in central Mexico (Bartolini *et al.*, 2003); conversely, in the state of Guerrero, Lower Jurassic plutons presence is common in the coastal Xolapa regions: this, and the recent proposal of Guerrero Terrane para-autochthony with respect to North America were some of the

reasons that led Martini & Ortega-Gutierrez (2016) to separate the Nazas volcanics from the magmatic arc in the Pacific. The common explanation for the scarcity of plutons by the authors that defend the arc model is that plutons are still covered by Jurassic and younger rocks (Bartolini *et al.*, 2003). Some recently found Early Jurassic plutons in the Cuicateco Terrane (Molina-Garza *et al.*, 2019, in press) would indicate that indeed these plutons exist. Also, presence of Middle Jurassic plutons in the northern Mixteca Terrane such as the San Miguel intrusives (Helbig *et al.*, 2012), Chilixtlahuaca lithodem (Campos-Madrigal *et al.*, 2013), and Yutandú intrusive (Díaz-Bahena, 2016) allow to infer the arc activity continued until this time.

The Nazas Arc in Mexico has been principally determined by its volcanic successions, cropping out from Sonora to Chiapas (Bartolini *et al.*, 2003; Barboza-Gudiño *et al.*, 2008; Godínez-Urban *et al.*, 2011a; Lawton & Molina-Garza, 2014). All these volcanic rocks have geochemical arc signatures (Bartolini *et al.*, 2003; Barboza-Gudiño *et al.*, 2008) even the Diquiyú unit (Díaz-Bahena, 2016) indicating at least an influence from the paleo-Pacific slab in the Nazas volcanism. Also, the nature of the volcanic succession (andesite dominated) would seem more related to an Andean type volcanic arc. Another fact that suggests high influence of the Pacific slab beneath Mixteca Terrane during Lower Jurassic times is the interpreted underthrusting of the Ayú Complex (Helbig *et al.*, 2012). The local nature of the lower part of the Tlaxiaco Basin succession can be explained as result of the high dissection of the blocks in which it was being emplaced, the presence of barriers along and across strike would have prevented the continuous flow of both volcanics and sediments trough all the basin, this pattern is common in the early stages of rifting (Gawthorpe & Leeder, 2000). The most plausible cause for the extension of the basin would be firstly related to an extensional arc, that developed intra-arc and back-arc successions along the western border of Pangea. This extensional regime would have received support from the early phases of rifting in the east. In this way the Diquiyú unit – Rosario Formation succession registered the processes occurring inside an intra-arc basin, with detritus derived directly from the arc. The Cualac conglomerate and the rest of Tecocoyunca Group are related with the arc waning and with the increasing rift activity, that enhanced the basin connectivity and the dominance

of regional sediment dispersal systems. The Jurassic basins along Mexico, the Southwestern USA, and also in Colombia reflect some of these characteristics.

5.6 Pangea

With the data discussed previously and in this section we can briefly discuss their relevance for western equatorial Pangea reconstructions. Recently, it has been argued that the A2 type reconstruction of Van der Voo and French (1974), similar to the classic Wegener's Pangea, but with additional 20° clockwise rotation of Gondwana is the best paleogeographic framework for Pangea in Early Jurassic times (Van der Voo, 1993; Domeier *et al.*, 2012). This reconstruction fills the Gulf of Mexico with Yucatan crust and leaves only continental areas in the western equatorial Pangea (Pindell & Dewey, 1982; Pindell 1985). The Pangea B and C types that place Gondwana in easternmost positions, although accepted to some extent in the past for early Permian times (Muttoni *et al.*, 1996), now seem to be unnecessary by correcting sediment data for inclination shallowing and by just selecting the best reference poles (Domeier *et al.*, 2012). In all the A-type Pangea reconstructions the central and southern Mexican blocks overlap with the northern South American plate, and almost all the authors dealing with this subject have solved the issue by placing the blocks NW of their present position (Pindell & Dewey, 1982; Pindell, 1985; Van der Voo, 1993; Pindell & Kennan, 2009; Martini & Ortega-Gutiérrez, 2016), without any substantial evidence for the faults responsible for the movement of the blocks (*e.g.*, Mojave-Sonora Megashear) proposing these faults are needed, but not because they indeed exist.

The paleomagnetic evidence found here and in other works (Molina-Garza & Geissman, 1999; Nova, 2016) argues against the NW placement of the Mexican blocks with respect to Pangea. Instead, they favor the placement of these Mexican blocks adjacent to the western NAM plate, or in slightly SW positions, being affected ubiquitously by a west facing continental volcanic arc (*i.e.*, Nazas Arc) that extended along all the western border of Pangea during Early and Middle Jurassic times (Bartolini *et al.*, 2003) (Figure 5.8). The posterior opening of the Gulf of Mexico and the drift of the NAM with respect

to the SAM would have caused the differential rotation between the blocks and probably some northward translation, accommodated by dextral faults similar to the Oaxaca fault.

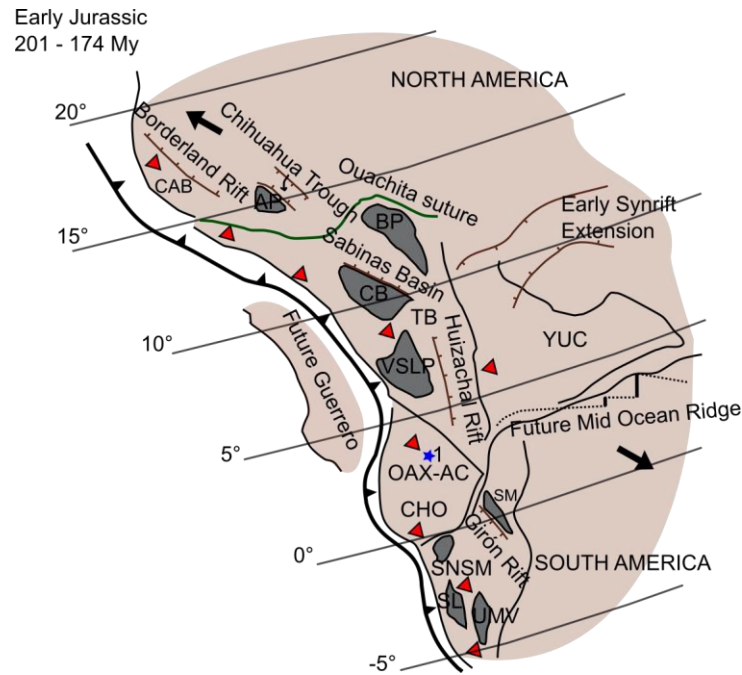


Figure 5-8. Paleogeographic reconstruction of continental masses in western equatorial Pangea during the Early Jurassic, this figure adjusts to a Pangea-A reconstruction and shows complete closure between all the continental blocks. Grey shaded polygons represent Paleozoic or older continental blocks; red triangles represent Nazas continental arc possible extension; black arrows indicate the separation direction between North and South American plates; blue star with 1 label indicates Diquiyú area studied here. CAB- Caborca Block; TB- Tampico Block; YUC- Yucatan Block; OAX-AC- Oaxaca-Acatlán block; CHO- Chortis Block; AP- Aldama Platform; BP- Burro Platform; CB- Coahuila Block; VSLP- Valles San Luis Platform; SM – Santander Massif; SNSM – Sierra Nevada de Santa Marta Massif; SL – San Lucas Range; UMV – Upper Magdalena Valley. Figure provided by Roberto Molina-Garza and based on Pindell (1985), paleolatitudes from Torsvik et al. (2012). Southern paleolatitudes for Colombian continental blocks (SNSM, SL, and UMV) are according to Bayona et al. (2006, 2010).

6. Conclusions

The paleomagnetic and stratigraphic analysis of the Jurassic volcanic and sedimentary successions that crop out in the Rosario Nuevo Creek I reach the following conclusion:

The volcanic rocks of the Diquiyú unit, which constitute the oldest rocks outcropping in the Diquiyú Anticlinorium possess a natural remanent magnetization characterized by two components in the majority of samples; the first component, removed with low AF (5 mT – 30 mT) and with low to intermediate laboratory blocking temperatures (90°C – 500°C) is north directed (N:13; Dec: 12.4°; Inc: 44.5°; α_{95} : 13°; k: 11.13) and represent a viscous secondary magnetization acquired in recent times. The high stability component, with coercivities between 15 mT and 180 mT and with laboratory blocking temperatures between 300°C and 690°C, is east directed and shallow (n: 23; Dec: 82.8°; Inc: -1.4°; α_{95} : 9.4°; k: 11.25). This component passes a conglomerate test, a DC fold test and a reversal test, and is interpreted as a primary TRM acquired during the emplacement and crystallization of the volcanic rocks of the unit.

I also conclude that the minerals that carry both magnetizations correspond mainly to PSD magnetite and SD hematite. These two minerals have been originated during the early phases of crystallization and during high temperature oxidation of the lavas, and so, their nature is primary.

The paleopole obtained for the Diquiyú unit (Lat: 6.6°S; Long: 175°E; A95: 8.7; K:13.1) possesses an A95 value that probably averaged PSV; it also classified as a good estimate with good quality statistical parameters, as a $A_{95} < 10$ and a $N > 10$. This paleopole, when compared with the best NAM cratonic reference poles for the lower Early Jurassic, and considering east directed magnetizations represent normal polarity postulates a clockwise rotation of about 90° for the study area and a stationary position relative to the North American craton in terms of latitude.

The amount of rotation registered by the Diquiyú unit rocks in the Tlaxiaco basin is different from the amount of clockwise rotation registered by other Jurassic rocks in adjacent basins, so, the rotation was not regional but segmented. The tectonic scenarios involving a southward displacement and counterclockwise rotation of southern Mexican blocks invoked by hypothetical NW trending left-lateral Jurassic shear zones is not supported by paleomagnetic data

In terms of sedimentology, the succession of conglomerates and subordinate sandstones, mainly composed by andesitic clasts, deposited over andesites of the Diquiyú unit and under Cualac conglomerate and outcropping along Rosario Nuevo's creek is best termed as Prieto conglomerate member of the Rosario Formation.

I sustain that the Cualac conglomerate should be extracted from the El Consuelo Group and placed at the base of the Tecocoyunca Group as previously suggested, representing the base of the fining upward succession that reveal the pass from continental to oceanic dominated environments in the basin. The term Consuelo Group is then unnecessary.

The facial characteristics observed in Prieto conglomerate member of the Rosario Formation reveal the prevalence of traction currents as the sedimentary agent, these currents deposited the sediment in aggradational patterns inside channels; also, the facial characteristics reveal the absence of important overbank environments. Also, the transition from Prieto conglomerate member to Cualac conglomerate is gradational, and there is a transitional zone of about 30 m that posses both facial and petrologic characteristics similar to both units

Finally, I conclude that the facial characteristics of Cualac conglomerate reveal the prevalence of traction currents also as the sedimentary agent, but with the development of more overbank environments. This suggests a more sinuous river than the one which deposited Prieto conglomerate member.

The regional presence of Cualac conglomerate together with the increase in overbank facies development represent a decrease in the degree of subsidence of the basin

The petrologic evolution from volcanic dominated in Prieto conglomerate member to quartz-metamorphic dominated in Cualac conglomerate reveal the progressive dismantling of a volcanic carapace covering a crustal metamorphic complex dominated by low to intermediate metamorphic rocks.

The facial patterns of both units dominated by aggradational processes, with scarce presence of debris flows, together with the absence of unstable minerals in the rock frameworks reveal the predominance of humid climates during the deposition of the sedimentary units.

The paleomagnetically rotated paleocurrents measured in imbricated clasts of the Prieto conglomerate member indicate a transport direction towards the SE, orthogonal to a volcanic chain straddling along the continent in a SW-NE direction.

The basins developed during the Early-Middle Jurassic times in southern Mexico were controlled by the Nazas Arc, the major part of basins were developed in a backarc position and affected by extensional processes, so their compartmentalization was controlled by basin parallel and perpendicular faults.

Both the paleomagnetic primary direction and the facial and petrologic characteristic obtained from the intertongued volcanic and sedimentary successions coincide with an equatorial paleoposition of the Mixteca Terrane during the Early-Middle Jurassic.

The position of the Mixteca Terrane relative to the NAM plate fits in a Pangea-A2 reconstruction, and that the overlap problem of southern Mexican blocks with the SAM plate can be reconciled by subdividing the overlapped zone in blocks and placing them adjacent to the craton or in a slightly SW position.

References

Abrajevitch, A., Van der Voo, R., Rea, D. K., 2009. Variations in relative abundances of goethite and hematite in Bengal Fan sediments: Climatic vs. diagenetic signals. *Marine Geology*, vol. 267, no. 3-4, p. 91-206.

Alencaster de Cserna, G., 1963. Pelecipodos del Jurasico medio del noroeste de Oaxaca y noreste de Guerrero. *Paleontología Mexicana*, Vol. 15, p. 1-52.

Anderson, T. H., & Schmidt, V. A., 1983. The evolution of Middle America and the Gulf of Mexico–Caribbean Sea region during Mesozoic time. *geological Society of America Bulletin*, vol. 94, no.8, p. 941-966.

Barboza-Gudiño, J.R., Orozco-Esquivel, M.T., Gómez-Anguiano, M., Zavala-Monsiváis, A., 2008, The early Mesozoic volcanic arc of western North America in northeastern Mexico. *Journal of South American Earth Sciences*, v. 25, p. 49–63

Barboza-Gudiño, J. R., Zavala-Monsiváis, A., Venegas-Rodríguez, G., Barajas-Nigoche, L. D., 2010. Late Triassic stratigraphy and facies from northeastern Mexico: Tectonic setting and provenance. *geosphere*, vol. 6, no. 5, p. 621-640.

Barboza-Gudiño, J. R., Molina-Garza, R. S., Lawton, T. F., 2012. Sierra de Catorce: Remnants of the ancient western equatorial margin of Pangea in central Mexico. The southern Cordillera and beyond, vol. 25, no. 1, p. 1 – 18.

Ballard, M. M., Van der Voo, R., Urrutia-Fucugauchi, J., 1989. Paleomagnetic results from Grenvillian-aged rocks from Oaxaca, Mexico: evidence for a displaced terrane. *Precambrian Research*, vol. 42, no. 3-4, p. 343-352.

Bartolini, C., H. Lang, and T. Spell, 2003, Geochronology, geochemistry, and tectonic setting of the Mesozoic Nazas arc in north-central Mexico, and its continuation to northern South America, in C. Bartolini, R. T. Buffler, and J. Blickwede, eds., *The*

Circum-Gulf of Mexico and the Caribbean: Hydrocarbon habitats, basin formation, and plate tectonics: AAPG Memoir no. 79, p. 427–461.

Bazard, D. R., & Butler, R. F., 1991. Paleomagnetism of the Chinle and Kayenta Formations, New Mexico and Arizona. *Journal of Geophysical Research: Solid Earth*, vol. 96, no. B6, 9847-9871.

Bayona, G., Rapalini, A., Costanzo-Alvarez, V., 2006. Paleomagnetism in Mesozoic rocks of the northern Andes and its implications in Mesozoic tectonics of northwestern South America. *Earth, planets and space*, vol. 58, no. 10, p. 1255-1272.

Bayona, G., Jiménez, G., Silva, C., Cardona, A., Montes, C., Roncancio, J., Cordani, U., 2010. Paleomagnetic data and K–Ar ages from Mesozoic units of the Santa Marta massif: a preliminary interpretation for block rotation and translations. *Journal of South American Earth Sciences*, vol. 29, no. 4, p. 817-831.

Birkinbine, J. L. W., 1911. Exploration of certain iron-ore and coal deposits in the State of Oaxaca: *Transactions of the American Institute of Mining Engineers*, vol. 41.

Böhnel, H., 1999. Paleomagnetic study of Jurassic and Cretaceous rocks from the Mixteca terrane (Mexico). *Journal of South American Earth Sciences*, vol. 12, no. 6, p. 545-556.

Burckhardt, C., 1927. Cefalópodos del Jurásico medio de Oaxaca y Guerrero: *Mexico Inst. Geol. Bol*, vol. 47, no. 108, p. 1930-31.

Butler, R. F., 1998. *Paleomagnetism: Magnetic domains to geologic terranes*. Electronic edition, vol. 23.

Campa, M.F., Coney, P.J., 1983. Tectono-stratigraphic terranes and mineral resources distribution in Mexico. *Can. J. Earth Sci*, vol. 26, p. 1040-1051.

Campa-Uranga, M. F., García-Díaz, J. L., Iriondo, A., 2004. El arco sedimentario del Jurásico Medio (Grupo Tecocoyunca y Las Lluvias) de Olinalá. GEOS Unión Geofísica Mexicana, vol. 24, no. 2, p. 174.

Campos-Madrigal, E., Centeno-García, E., Mendoza-Rosales, C.C., Silva-Romo, G., 2013. Sedimentología, reconstrucción paleoambiental y significado tectónico de las sucesiones clásticas del Jurásico Medio en el área de Texcalapa, Puebla-Huajuapán de León, Oaxaca: Revisión de las formaciones Ayuquila y Tecomazúchil. Revista Mexicana de Ciencias Geológicas vol. 30, no. 1, p. 34–50.

Cantú-Chapa, A., 1998. Las transgresiones Jurásicas en México. Revista Mexicana de Ciencias Geológicas, vol. 15, no. 1, p. 25-37.

Cediel, F., Shaw, R., Cáceres, C., 2003. Tectonic assembly of the Northern Andean block. in C. Bartolini, R. T. Buffler, and J. Blickwede, eds., The Circum-Gulf of Mexico and the Caribbean: Hydrocarbon habitats, basin formation, and plate tectonics: AAPG Memoir no. 79, p. 815– 848.

Chadima, M., & Hrouda, F., 2006. Remasoft 3.0 a user-friendly paleomagnetic data browser and analyzer. Travaux Géophysiques, vol. 27, p. 20-21.

Esquivel, R. C., 1981. Estratigrafía de la región de Olinalá-Tecocoyunca, noreste del Estado de Guerrero. Revista mexicana de ciencias geológicas, vol. 5, no. 1, p. 17-24.

Cortés-Obregón, S., Villegas, L. T., Bermudez, J. M., Larios, J. P., Aritia, A. G., Castelan, S. C., Peralta, M. P., 1957. La cuenca carbonifera de la Mixteca: Banco de Mexico. Dpto. Invest. Industriales, pt. I.

De Anda García, M.A., 2008. Estudio petrológico del Grupo Consuelo (*sensu* Jiménez Rentería, J., 2004) en la localidad de Rosario Nuevo, Municipio de Tezoatlán, Oax.

Bachelor Thesis, Instituto Politécnico Nacional, Escuela Superior de Ingeniería y Arquitectura, Unidad Ticomán, 234 p.

Deenen, M. H., Langereis, C. G., van Hinsbergen, D. J., Biggin, A. J., 2011. Geomagnetic secular variation and the statistics of palaeomagnetic directions. *Geophysical Journal International*, vol. 186, no. 2, p. 509-520.

Díaz Bahena, A., 2016. Geoquímica de la unidad Diquiyú y geocronología del intrusivo Yutandú en San Juan Diquiyú, Oaxaca, México. Bachelor Thesis, Universidad Autónoma de Guerrero, Taxco, Mexico., 66 p.

Dickinson, W. R., 1970. Interpreting detrital modes of graywacke and arkose. *Journal of Sedimentary Research*, vol. 40, no. 2, p. 695-707

Dickinson, W. R., Helmold, K. P., Stein, J. A. 1979. Mesozoic lithic sandstones in central Oregon. *Journal of Sedimentary Research*, vol. 49 no. 2, p. 501-516.

Dickinson, W. R., & Suczek, C. A., 1979. Plate tectonics and sandstone compositions. *Aapg Bulletin*, vol. 63, no. 12, p. 2164-2182.

Dickinson, W. R., 1985. Interpreting provenance relations from detrital modes of sandstones. In *Provenance of arenites*. Springer, Dordrecht, p. 333-361.

Dickinson, W. R., & Lawton, T. F., 2001. Carboniferous to Cretaceous assembly and fragmentation of Mexico. *Geological Society of America Bulletin*, vol. 113, no. 9, p. 1142-1160.

Domeier, M., Van der Voo, R., Torsvik, T. H., 2012. Paleomagnetism and Pangea: the road to reconciliation. *Tectonophysics*, vol. 514, p. 14-43.

Dunlop, D. J., 2002. Theory and application of the Day plot (Mrs/Ms versus Hcr/Hc) 1. Theoretical curves and tests using titanomagnetite data. *Journal of Geophysical Research: Solid Earth*, vol. 107, no. B3, p. EPM-4.

Durán-Aguilar, R. F., 2014. Sedimentología y geocronología de los lechos rojos del Jurásico, Región Norte de la Cuenca de Tlaxiaco, Tezoatlán, Oaxaca; correlaciones y procedencia. Master's thesis, Instituto de Geología, UNAM, 87 p.

Elías-Herrera, M., Ortega-Gutiérrez, F., Sánchez-Zavala, J. L., Macías-Romo, C., Ortega-Rivera, A., Iriondo, A., 2005. La falla de Caltepec: raíces expuestas de una frontera tectónica de larga vida entre dos terrenos continentales del sur de México. *Boletín de la Sociedad Geológica Mexicana*, vol. 57, no. 1, p. 83-109.

Enkin, R. J., 2003. The direction–correction tilt test: an all-purpose tilt/fold test for paleomagnetic studies. *Earth and Planetary Science Letters*, vol. 212, no. 1-2, p. 151-166.

Erben, H.K., 1956. El Jurásico medio y el calloviano de México: XX Congreso Geológico Internacional, Monografía, México. D.F., México, p. 140.

Fang, W., Van der Voo, R., Molina-Garza, R., Morán-Zenteno, D., Urrutia-Fucugauchi, J., 1989. Paleomagnetism of the Acatlán terrane, southern Mexico: evidence for terrane rotation. *Earth and Planetary Science Letters*, vol. 94, no.1-2, p. 131-142.

Fisher, R. A., 1953. Dispersion on a sphere. *Proceedings of the Royal Society of London. Series A. Mathematical and Physical Sciences*, vol. 217, no. 1130, p. 295-305.

Fitz-Díaz, E., Lawton, T. F., Juárez-Arriaga, E., Chávez-Cabello, G., 2018. The Cretaceous-Paleogene Mexican orogen: Structure, basin development, magmatism and tectonics. *Earth-Science Reviews*, vol. 183, p. 56-84.

Folk, R. L., 1974. *Petrology of sedimentary rocks*: Austin. Texas, Hemphill, 182 p.

Frank, U., & Nowaczyk, N. R., 2008. Mineral magnetic properties of artificial samples systematically mixed from haematite and magnetite. *Geophysical Journal International*, vol. 175, no. 2, p. 449-461

Garzanti, E., Padoan, M., Andò, S., Resentini, A., Vezzoli, G., Lustrino, M., 2013. Weathering and relative durability of detrital minerals in equatorial climate: sand petrology and geochemistry in the East African Rift. *The Journal of Geology*, vol. 121, no. 6, p. 547-580.

Garzanti, E., 2016. From static to dynamic provenance analysis—Sedimentary petrology upgraded. *Sedimentary Geology*, vol. 336, p. 3-13.

Garzanti, E., Limonta, M., Vezzoli, G., An, W., Wang, J., and Hu, X., 2018, Petrology and multimineral fingerprinting of modern sand generated from a dissected magmatic arc (Lhasa River, Tibet), in Ingersoll, R.V., Lawton, T.F., and Graham, S.A., eds., *Tectonics, Sedimentary Basins, and Provenance: A Celebration of William R. Dickinson's Career: Geological Society of America Special Paper 540*.

Gawthorpe, R. L., & Leeder, M. R., 2000. Tectono-sedimentary evolution of active extensional basins. *Basin Research*, vol. 12, no. 3-4, p. 195-218.

Godínez-Urban, A., Lawton, T. F., Molina Garza, R. S., Iriando, A., Weber, B., López-Martínez, M., 2011a. Jurassic volcanic and sedimentary rocks of the La Silla and Todos Santos Formations, Chiapas: Record of Nazas arc magmatism and rift-basin formation prior to opening of the Gulf of Mexico. *Geosphere*, vol. 7, no. 1, p. 121-144

Godínez-Urban, A., Molina Garza, R. S., Geissman, J. W., Wawrzyniec, T., 2011b. Paleomagnetism of the Todos Santos and La Silla Formations, Chiapas: implications for the opening of the Gulf of Mexico. *Geosphere*, vol. 7, no. 1, p. 145-158.

Goldhammer, R.K., 1999. Mesozoic sequence stratigraphy and sedimentary evolution of northeast Mexico, in Bartolini, C., Wilson, J.L., and Lawton, T.F., eds., *Mesozoic Sedimentary and Tectonic History of North- Central Mexico*: Geological Society of America Special Paper 340, p. 1–58.

Goldhammer, R. K., & Johnson, C. A., 2001. Middle Jurassic-Upper Cretaceous paleogeographic evolution and sequence-stratigraphic framework of the northwest Gulf of Mexico rim. *Memoirs-AAPG*, p. 45-82.

González-Torres, E., 1989. *Geología y paleomagnetismo del área de Tezoatlán, Oaxaca*. Bachelor Thesis, UNAM, Facultad de Ingeniería, 188 p.

Helbig, M., Keppie, J. D., Murphy, J. B., Solari, L. A., 2012. U–Pb geochronological constraints on the Triassic–Jurassic Ayú Complex, southern Mexico: derivation from the western margin of Pangea-A. *Gondwana Research*, vol. 22, no. 3-4, p. 910-927.

Ingersoll, R. V., 2012. Composition of modern sand and Cretaceous sandstone derived from the Sierra Nevada, California, USA, with implications for Cenozoic and Mesozoic uplift and dissection. *Sedimentary Geology*, vol. 280, p. 195-207.

Ingersoll, R. V., & Eastmond, D. J., 2007. Composition of modern sand from the Sierra Nevada, California, USA: implications for actualistic petrofacies of continental-margin magmatic arcs. *Journal of Sedimentary Research*, vol. 77, no. 9, p. 784-796.

Ingersoll, R. V., Bullard, T. F., Ford, R. L., Grimm, J. P., Pickle, J. D., Sares, S. W., 1984. The effect of grain size on detrital modes: a test of the Gazzi-Dickinson point-counting method. *Journal of Sedimentary Research*, vol. 54, no. 1, p. 103-116.

Jiménez Rentería, J., 2004. *Estudio palinoestratigráfico de los grupos Consuelo y Tecocoyunca (Triásico- Jurásico) en la barranca Rosario Nuevo, región de Tezoatlán al*

noroeste del estado de Oaxaca, México. Bachelor Thesis, Universidad Nacional Autónoma de México, Facultad de Ingeniería, 284 p.

Kennan, L., & Pindell, J. L., 2009. Dextral shear, terrane accretion and basin formation in the Northern Andes: best explained by interaction with a Pacific-derived Caribbean Plate?. *Geological Society, London, Special Publications*, vol. 328, no. 1, p. 487-531.

Kent, D. V., & Irving, E., 2010. Influence of inclination error in sedimentary rocks on the Triassic and Jurassic apparent pole wander path for North America and implications for Cordilleran tectonics. *Journal of Geophysical Research: Solid Earth*, vol. 115, no. B10.

Keppie, J. D., Nance, R. D., Fernández-Suárez, J., Storey, C. D., Jeffries, T. E., Murphy, J. B., 2006. Detrital zircon data from the Eastern Mixteca Terrane, Southern Mexico: Evidence for an Ordovician—Mississippian continental rise and a Permo-triassic clastic wedge adjacent to Oaxaquia. *International Geology Review*, vol. 48, no. 2, p. 97-111.

Kirschvink, J. L., 1980. The least-squares line and plane and the analysis of palaeomagnetic data. *Geophysical Journal International*, vol. 62, no. 3, p. 699-718.

Koymans, M. R., Langereis, C. G., Pastor-Galán, D., van Hinsbergen, D. J., 2016. Paleomagnetism.org: An online multi-platform open source environment for paleomagnetic data analysis. *Computers and Geosciences*, vol. 93, p.127

Kluth, C. F., Butler, R. F., Harding, L. E., Shafiqullah, M., Damon, P. E., 1982. Paleomagnetism of Late Jurassic rocks in the northern Canelo Hills, southeastern Arizona. *Journal of Geophysical Research: Solid Earth*, vol. 87, no. B8, p. 7079-7086.

Labails, C., Olivet, J. L., Aslanian, D., Roest, W. R., 2010. An alternative early opening scenario for the Central Atlantic Ocean. *Earth and Planetary Science Letters*, vol. 297, no. 3-4, p. 355-368.

Kruiver, P. P., Dekkers, M. J., Heslop, D., 2001. Quantification of magnetic coercivity components by the analysis of acquisition curves of isothermal remanent magnetisation. *Earth and Planetary Science Letters*, vol. 189, no. 3-4, p. 269-276.

Lawton, T. F., & McMillan, N. J., 1999. Arc abandonment as a cause for passive continental rifting: Comparison of the Jurassic Mexican Borderland rift and the Cenozoic Rio Grande rift. *Geology*, vol. 27, no. 9, p. 779-782.

Lawton, T. F., Bradford, I. A., Vega, F. J., Gehrels, G. E., Amato, J. M., 2009. Provenance of Upper Cretaceous–Paleogene sandstones in the foreland basin system of the Sierra Madre Oriental, northeastern Mexico, and its bearing on fluvial dispersal systems of the Mexican Laramide Province. *geological Society of America Bulletin*, vol. 121, no. 5-6, p. 820-836.

Lawton, T.F., & Molina-Garza, R.S., 2014. U-Pb geochronology of the type Nazas Formation and superjacent strata, northeastern Durango, Mexico: Implications of a Jurassic age for continental- arc magmatism in north-central Mexico: *Geological Society of America Bulletin*, vol. 126, no. 9-10, p. 1181-1199.

Lottes, A. L., & Rowley, D. B., 1990. Early and late Permian reconstructions of pangaia. *Palaeozoic palaeogeography and biogeography: Geological Society of London, Memoir*, vol. 2, p. 383-395.

MacDonald, W. D., 1980. Net tectonic rotation, apparent tectonic rotation, and the structural tilt correction in paleomagnetic studies. *Journal of Geophysical Research: Solid Earth*, vol. 85, no. B7, p. 3659-3669.

MacKenzie, W. S., Donaldson, C. H., Guilford, C., 1982. *Atlas of igneous rocks and their textures* (Vol. 12). Harlow: Longman.

Marsaglia, K. M., Barone, M., Critelli, S., Busby, C., Fackler-Adams, B., 2016. Petrography of volcanoclastic rocks in intra-arc volcano-bounded to fault-bounded basins of the Rosario segment of the Lower Cretaceous Alisitos oceanic arc, Baja California, Mexico. *Sedimentary geology*, vol. 336, p. 138-146.

Martini, M., Ramírez-Calderón, M., Solari, L., Villanueva-Amadoz, U., Zepeda-Martínez, M., Ortega-Gutiérrez, F., Elías-Herrera, M., 2016. Provenance analysis of Jurassic sandstones from the Otlaltepec Basin, southern Mexico: Implications for the reconstruction of Pangea breakup. *Geosphere*, vol. 12, no. 6, p. 1842-1864.

Martini, M., & Ortega-Gutiérrez, F., 2016. Tectono-stratigraphic evolution of eastern Mexico during the break-up of Pangea: A review. *Earth-science reviews*, vol. 183, p. 38-55.

May, S. R., Butler, R. F., Shafiqullah, M., Damon, P. E., 1986. Paleomagnetism of Jurassic volcanic rocks in the Patagonia Mountains, southeastern Arizona: Implications for the North American 170 Ma reference pole. *Journal of Geophysical Research: Solid Earth*, vol. 91, no. B11, p. 11545-11555.

McCabe, C., Van der Voo, R., Urrutia-Fucugauchi, J., 1988. Late Paleozoic or early Mesozoic magnetizations in remagnetized Paleozoic rocks, State of Oaxaca, Mexico. *Earth and planetary science letters*, vol. 91, no. 1-2, p. 205-213.

McCall, A. M., & Kodama, K. P., 2014. Anisotropy-based inclination correction for the Moenave Formation and Wingate Sandstone: implications for Colorado Plateau rotation. *Frontiers in Earth Science*, vol. 2, 15.

McFadden, P. L., & McElhinny, M. W., 1990. Classification of the reversal test in palaeomagnetism. *Geophysical Journal International*, vol. 103, no. 3, p. 725-729.

McHone, J. G., 2000. Non-plume magmatism and rifting during the opening of the central Atlantic Ocean. *Tectonophysics*, 316(3-4), 287-296.

McPhie, J., 1993. *Volcanic textures: a guide to the interpretation of textures in volcanic rocks*.

Michalzik, D., 1991. Facies sequence of Triassic-Jurassic red beds in the Sierra Madre Oriental (NE Mexico) and its relation to the early opening of the Gulf of Mexico: *Sedimentary Geology*, vol. 71, p. 243-259

Miall, A. D., 2006. *The geology of fluvial deposits: sedimentary facies, basin analysis, and petroleum geology*. Heidelberg, Germany, Springer, 582 p.

Molina-Garza, R. S., Van Der Voo, R., & Urrutia-Fucugauchi, J., 1992. Paleomagnetism of the Chiapas Massif, southern Mexico: Evidence for rotation of the Maya Block and implications for the opening of the Gulf of Mexico. *Geological Society of America Bulletin*, vol. 104, no. 9, p. 1156-1168.

Molina Garza, R. S., & Geissman, J. W., 1999. Paleomagnetic data from the caborca terrane, Mexico: implications for cordilleran tectonics and the mojave-sonora megashear hypothesis. *Tectonics*, vol. 18, p. 293-325.

Molina-Garza, R. S., Böhnel, H. N., Hernández, T., 2003a. Paleomagnetism of the Cretaceous Morelos and Mezcala formations, southern Mexico. *Tectonophysics*, vol. 361, no. 3-4, p. 301-317.

Molina-Garza, R. S., Geissman, J. W., Lucas, S. G., 2003b. Paleomagnetism and magnetostratigraphy of the lower Glen Canyon and upper Chinle Groups, Jurassic-Triassic of northern Arizona and northeast Utah. *Journal of Geophysical Research: Solid Earth*, vol. 108, no. B4.

Molina-Garza, R. S., Geissman, J. W., & Lawton, T. F., 2014. Jurassic Paleolatitudes, Paleogeography, and Climate Transitions In the Mexican Subcontinent. In AGU Fall Meeting Abstracts.

Molina-Garza, R.S., Lawton, T.F., Barboza, J.R., Sierra-Rojas, MI, Figueroa-Guadarrama, J.A., Pindell J., 2019, in press. Geochronology and correlation of the Todos Santos Formation, western Veracruz and eastern Oaxaca states, Mexico: Implications for regional stratigraphic relations and the rift history of the Gulf of Mexico: Geological Society of America Special Paper.

Morán-Zenteno, D. J., Urrutia-Fucugauchi, J., Böhnell, H., González-Torres, E., 1988. Paleomagnetismo de rocas jurásicas del norte de Oaxaca y sus implicaciones tectónicas. *Geofísica Internacional*, vol. 27, no. 4.

Morán-Zenteno, D.J., Caballero-Miranda, C. I., Silva-Romo, G., Ortega- Guerrero, B., González-Torres, E., 1993. Jurassic-Cretaceous paleogeographic evolution of the northern Mixteca terrane southern México: *Geofísica Internacional*, vol. 32, p. 453–473.

Muttoni, G., Kent, D. V., Channell, J. E., 1996. Evolution of Pangea: paleomagnetic constraints from the Southern Alps, Italy. *Earth and Planetary Science Letters*, vol. 140, no.1-4, p. 97-112.

Nova, E.G., 2016. Paleomagnetismo de rocas jurásicas en el bloque Oaxaquia: Implicaciones paleogeográficas para Pangea ecuatorial. Master's Thesis. UNAM, Centro de Geociencias, 53 p.

Ocampo-Díaz, Y. Z. E., Torres-Sánchez, S. A., Augustsson, C., Barboza-Gudiño, J. R., García-Díaz, J. L., Talavera-Mendoza, O., Aceves de Alba, J., Castro-Larragoitia, J., Martínez-Paco, M., Saucedo, R., Aguillón-Robles, A., 2019. Provenance and tectonic setting of the Jurassic Huayacocotla Formation and Alamitos Sandstone, Central Mexico. *Geochemistry*.

Ochoa-Camarillo, H. R., Buitrón, B. E., Silva-Pineda, A., 1998. Contribución al conocimiento de la bioestratigrafía, paleoecología y tectónica del Jurásico (anticlinorio de Huayacocotla) en la región de Molango, Hidalgo, Mexico. *Revista Mexicana de Ciencias Geológicas*, vol. 15, no. 1, p. 57-63.

Ochoterena, F.M., 1981. Evolución de las unidades morfoestructurales de la región de Diquiyú, Oaxaca. UNAM, Instituto de Geografía, *Boletín* 10, p. 285-317.

Ortega Guerrero, B., & Urrutia-Fucugauchi, J., 1993. Jurassic palaeomagnetic results constraining southerly motions of the Mixteca terrane, southern Mexico. *Geofísica Internacional*, vol. 32, no. 3.

Ortega-Guerrero, B., 1989. Paleomagnetismo y Geología de las unidades clásticas Mesozoicas del área Totoltepec-Ixcaquixtla, estados de Puebla y Oaxaca. Master's Thesis, Instituto de Geofísica, Universidad Nacional Autónoma de México.

Ortega-Gutiérrez, F., 1978. Estratigrafía del Complejo Acatlán en la Mixteca baja, estados de Puebla y Oaxaca. *Revista mexicana de ciencias geológicas*, vol. 2, no. 2, p. 112-131.

Ortega-Gutiérrez, F., Sedlock, R. L., Speed, R. C., 1994. Phanerozoic tectonic evolution of Mexico. Phanerozoic evolution of North American continent-ocean transitions: Geological Society of America, Decade of North American Geology Summary Volume to accompany the DNAG Continent-Ocean Transects Series, p. 265-306.

Ortega-Gutiérrez, F., Elías-Herrera, M., Morán-Zenteno, D. J., Solari, L., Weber, B., Luna-González, L., 2018. The pre-Mesozoic metamorphic basement of Mexico, 1.5 billion years of crustal evolution. *Earth-science reviews*, vol. 183, p. 2-37.

Özdemir, Ö., & Dunlop, D. J., 2014. Hysteresis and coercivity of hematite. *Journal of Geophysical Research: Solid Earth*, vol. 119, no. 4, p. 2582-2594.

Pindell, J. L., 1985. Alleghenian reconstruction and subsequent evolution of the Gulf of Mexico, Bahamas, and proto-Caribbean. *Tectonics*, vol. 4, no. 1, p. 1-39

Pindell, J., & Dewey, J. F., 1982. Permo-Triassic reconstruction of western Pangea and the evolution of the Gulf of Mexico/Caribbean region. *Tectonics*, vol. 1, no. 2, p. 179-211.

Pindell, J. L., & Kennan, L., 2009. Tectonic evolution of the Gulf of Mexico, Caribbean and northern South America in the mantle reference frame: an update. *geological Society, London, Special Publications*, vol. 328, no. 1, p. 1-55.

Roberts, A. P., Cui, Y., Verosub, K. L., 1995. Wasp-waisted hysteresis loops: Mineral magnetic characteristics and discrimination of components in mixed magnetic systems. *Journal of Geophysical Research: Solid Earth*, vol. 100, no. B9, p. 17909-17924.

Rubio-Cisneros, I. I., & Lawton, T. F., 2011. Detrital zircon U-Pb ages of sandstones in continental red beds at Valle de Huizachal, Tamaulipas, NE Mexico: Record of Early-Middle Jurassic arc volcanism and transition to crustal extension. *Geosphere*, vol. 7, no. 1, p. 159-170.

Rueda-Gaxiola, J., 2009. Sedimentary provenance of the Grupo Consuelo in the Tlaxiaco Anticlinorium, at Rosario Nuevo, Oaxaca, Mexico. In 2009 Portland GSA Annual Meeting.

Sanchez-Zavala, J. L., Ortega-Gutierrez, F., Keppie, J. D., Jenner, G. A., Belousova, E., Maciás-Romo, C. 2004. Ordovician and Mesoproterozoic zircons from the Tecamate Formation and Esperanza granitoids, Acatlán Complex, southern Mexico: local

provenance in the Acatlán and Oaxacan complexes. *International Geology Review*, vol. 46, no. 11, p. 1005-1021.

Sandoval, J., & Westermann, G. E. (1986). The Bajocian (Jurassic) ammonite fauna of Oaxaca, Mexico. *Journal of Paleontology*, 60(6), 1220-1271.

Savage, K. M., & Potter, P. E., 1991. Petrology of modern sands of the rios Guaviare and Inirida, southern Colombia: tropical climate and sand composition. *The Journal of Geology*, vol. 99, no. 2, p. 289-298.

Sedlock, R. L., Ortega-Gutiérrez, F., Speed, R. C., 1993. Tectonostratigraphic terranes and tectonic evolution of Mexico. *Geological Society of America*, vol. 278.

Silva-Pineda, A., 1970. Plantas fósiles del Jurásico medio de la región de Tezoatlán. Oaxaca: Sociedad Geológica Mexicana, Libroto guía de la excursión México-Oaxaca, p. 129-153.

Silva-Pineda, A., 1984. Revisión taxonómica y tipificación de las plantas jurásicas colectadas y estudiadas por Wieland (1914) en la región de El Consuelo, Oaxaca. *Paleontología Mexicana*, vol. 49, p. 1-112.

Silva-Romo, G., Mendoza-Rosales, C. C., Campos-Madrigal, E., Centeno-García, E., Peralta-Salazar, R., 2015. Early Mesozoic Southern Mexico–Amazonian connection based on U–Pb ages from detrital zircons: the La Mora Paleo-River in the Mixteca Terrane and its paleogeographic and tectonic implications. *Gondwana Research*, vol. 28, no. 2, p. 689-701.

Streckeisen, A., 1980. Classification and nomenclature of volcanic rocks, lamprophyres, carbonatites and melilitic rocks IUGS Subcommittee on the systematics of igneous rocks. *Geologische Rundschau*, vol. 69, no. 1, p. 194-207.

Tauxe, L., Mullender, T. A. T., Pick, T., 1996. Potbellies, wasp-waists, and superparamagnetism in magnetic hysteresis. *Journal of Geophysical Research: Solid Earth*, vol. 101, no. B1, p. 571-583.

Tauxe, L., 2005. *Lectures in Paleomagnetism*.

Teixeira, W., Tassinari, C. C. G., Cordani, U. G., & Kawashita, K., 1989. A review of the geochronology of the Amazonian Craton: tectonic implications. *Precambrian Research*, vol. 42, no. 3-4, p. 213-227.

Torsvik, T. H., & Smethurst, M. A., 1999. Plate tectonic modelling: virtual reality with GMAP. *Computers & Geosciences*, vol. 25, no. 4, p. 395-402.

Torsvik, T. H., Van der Voo, R., Preeden, U., Mac Niocaill, C., Steinberger, B., Doubrovine, P. V., Van Hinsbergen, D., Domeier, M., Gaina, C., Tohver, E., Meert, J. G., McCausland, P., Cocks, R., 2012. Phanerozoic polar wander, palaeogeography and dynamics. *Earth-Science Reviews*, vol. 114, no. 3-4, p. 325-368.

Van der Plas, L., & Tobi, A. C., 1965. A chart for judging the reliability of point counting results. *American Journal of Science*, vol. 263, no. 1, p. 87-90.

Van der Voo, R., & French, R. B., 1974. Apparent polar wandering for the Atlantic-bordering continents: Late Carboniferous to Eocene. *Earth-Science Reviews*, vol. 10, no. 2, p. 99-119.

Van Der Voo, R., 1993. *Paleomagnetism of the Atlantic, Tethys and Iapetus oceans*. Cambridge University Press.

Van Hinsbergen, D. J., de Groot, L. V., van Schaik, S. J., Spakman, W., Bijl, P. K., Sluijs, A., Langereis, C., Brinkhuis, H., 2015. A paleolatitude calculator for paleoclimate studies. *PloS one*, vol. 10, no. 6.

Vite del Ángel, A. O., 2014. Estudio petrológico de la secuencia basal del Grupo Tecocoyunca (*sensu* Jiménez-Rentería, J., 2004) en la cañada de Rosario Nuevo, Oax. De Tezoatlán, Oax. Bachelor Thesis. Escuela Superior de Ingeniería y Arquitectura, Unidad Ticomán, IPN.

Watkins, N. D., & Haggerty, S. E., 1967. Primary oxidation variation and petrogenesis in a single lava. *Contributions to Mineralogy and Petrology*, vol. 15, no. 3, p. 251-271.

Wieland, G. R., 1914. La flora liásica de la Mixteca Alta: *Inst. Geol. México, Bol*, vol. 165, p. 31.

Zavala-Monsiváis, A., Barboza-Gudiño, J. R., Velasco-Tapia, F., García-Arreola, M. E., 2012. Sucesión volcánica Jurásica en el área de Charcas, San Luis Potosí: Contribución al entendimiento del Arco Nazas en el noreste de México. *Boletín de la Sociedad Geológica Mexicana*, vol. 64, no. 3, p. 277-293.

Zepeda-Martínez, 2017. Petrología de las areniscas continentales de la localidad de Rosario Nuevo, Oaxaca. Master's Thesis, UNAM, Instituto de Geología.

Zepeda-Martínez, M., Martini, M., Solari, L., 2018. A major provenance change in sandstones from the Tezoatlán basin, southern Mexico, controlled by Jurassic, sinistral normal motion along the Salado River fault: Implications for the reconstruction of Pangea. *Journal of South American Earth Sciences*, vol. 86, p. 447-460.

Zijderveld, J. D. A., 1967. AC demagnetization of rocks: Analysis of results, *Methods in Paleomagnetism* DW Collinson, KM Creer, SK Runcorn, p. 254–286.

Zuluaga, C. A., Pinilla, A., Mann, P., 2015. Jurassic silicic volcanism and associated Continental-arc Basin in northwestern Colombia (southern boundary of the Caribbean

plate). Memoir 108: Petroleum Geology and Potential of the Colombian Caribbean Margin, p. 137-159.

Appendix 1

Microscopy and scanning electronic microscope (SEM) results

Sample DDP01

Petrography

In hand specimen, DDP01 is a green aphanitic rock with vesicles filled with a probably zeolite and with incipient flow structure. At microscopic scale (Figure A1-1) displays a sacaroid texture composed of a cryptocrystalline aggregate of quartz and feldspar; some altered subhedral plagioclase crystals are disseminated in the matrix. Inside the matrix there are vesicles filled with a crustiform aggregate of calcite at the center and zeolite and/or chalcedony at the borders. Bordering these vesicles and disseminated in the matrix there are opaque minerals of different sizes and some of them resemble plagioclase pseudomorphs. The vesicles have the appearance of a banded structure, and inside some of them there are folded crystals. The rock is interpreted as an extrusive volcanic rock primarily composed of a vitreous matrix with some plagioclase crystals, later altered and slightly deformed.

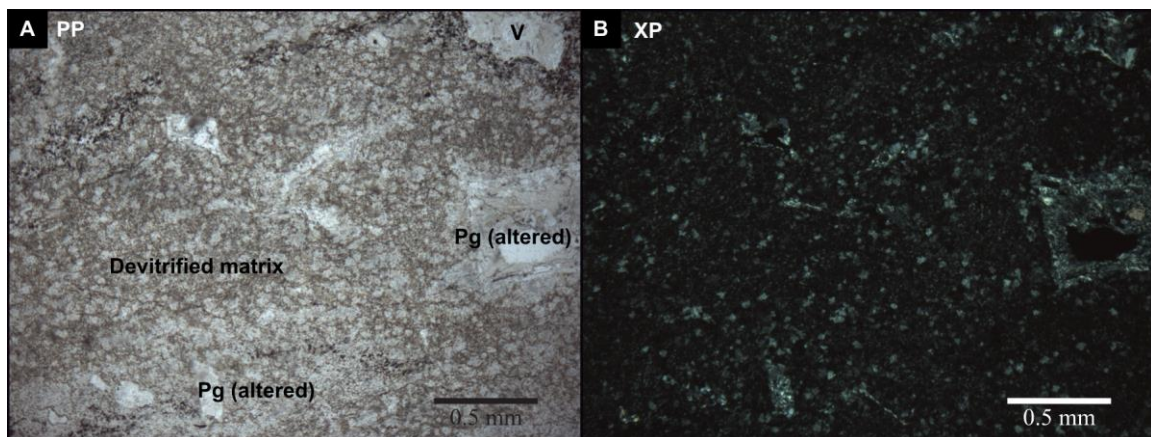


Figure A1-1. Plane (A) and polarized (B) light micrographs of sample DDP01. Pg – Plagioclase; V – Void. The sample is almost completely composed of a devitrified matrix

with some plagioclase crystals within it. The bigger plagioclase crystal to the right is bordered by chlorite, product of alteration.

Reflected petrography

The most abundant ferromagnetic mineral observed in this sample is magnetite (Figure A1-2); the largest size observed for this mineral is 0.2 mm (Figure A1-2 A), being 0.04 mm the average diameter; these crystals are subhedral to euhedral, and their origin is interpreted as primary based on its euhedral shape and the lack of alteration. Bordering plagioclase crystals there are ilmenite and hematite crystals, with ilmenite developing lamellae and acicular habit typical of this mineral; hematite may originate from the oxidation of magnetite, and is interpreted as secondary due to its disposition bordering other crystals. Around vesicles there are small magnetite crystals of ~0.008 mm diameter, ubiquitous through the whole sample and secondary in origin (Figure A1-2 C). Finally, there are ilmenite–hematite veins cutting through magnetite (Figure A1-2 D). According to Watkins & Haggerty (1967) this sample has an oxidation state IV.

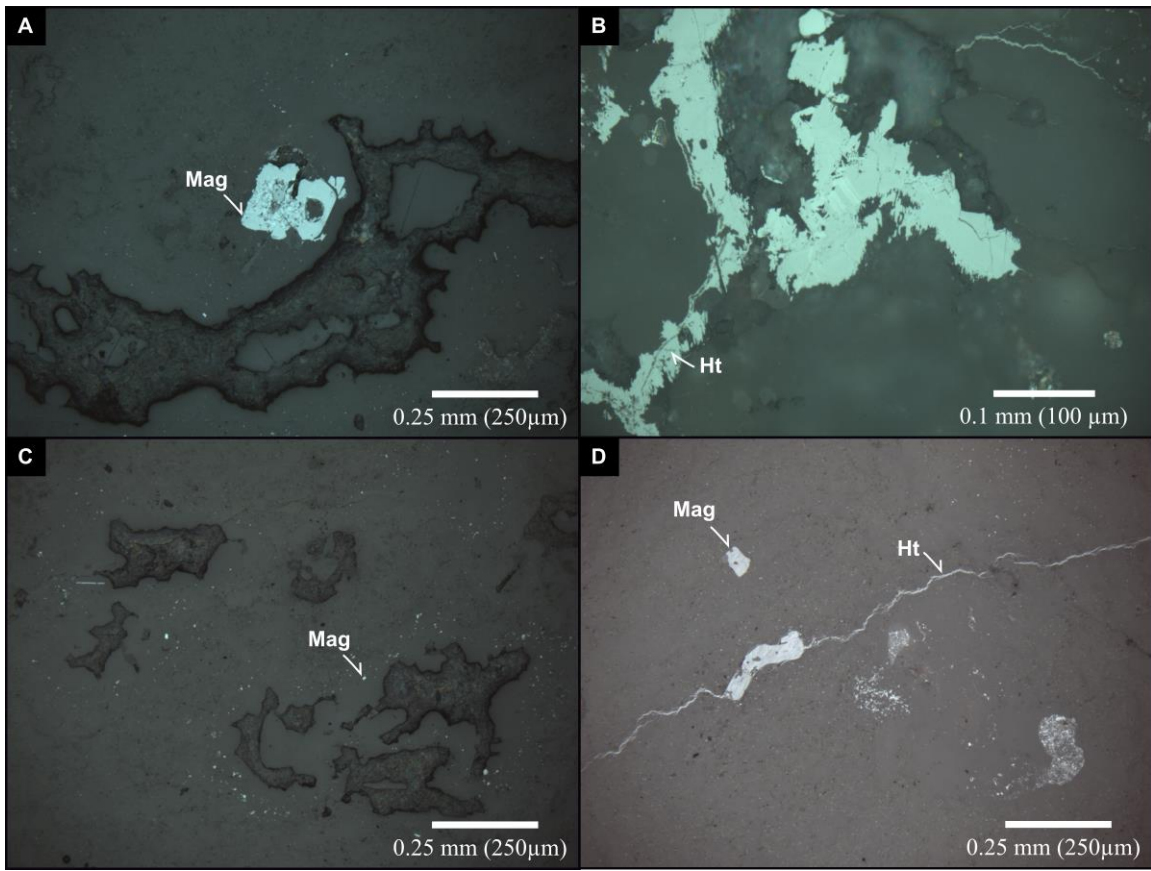


Figure A1-2. Reflected light micrographs of sample DDP01. Mag – Magnetite; Ht – Hematite. Most magnetite have a cubic phase. In (B) lamellae developed between ilmenite and hematite is observed for the central crystal. In (C) the hematite veins cross the rock sample.

SEM

Figure A1-3 A shows a magnetite-ilmenite crystal with euhedral shape; the element spectrum shows that the Ti content is relatively higher than the Fe; therefore, this crystal could correspond to a titanomagnetite (TM60). The darker and lighter crystal intergrowth with the titanomagnetite corresponds to non-magnetic minerals, due to their high content in Ca and Zr; they probably correspond to apatite and zircon inclusions, respectively. Thus titanomagnetite is the only primary magnetic mineral in this sample. Figure A1-3 B shows the fill of a vesicle with a dendritic habit mineral, in the spectrum the high Ti content and low Fe are manifest, so, this mineral is not a good magnetic carrier, and may

correspond to rutile. Sheet-like minerals (Figure A1-3 C) are found inside larger crystals and are secondary in origin; in the spectrum they show high Fe content; due to this fact and to its habit this mineral corresponds to hematite. Figure A1-3 D corresponds to a hematite vein.

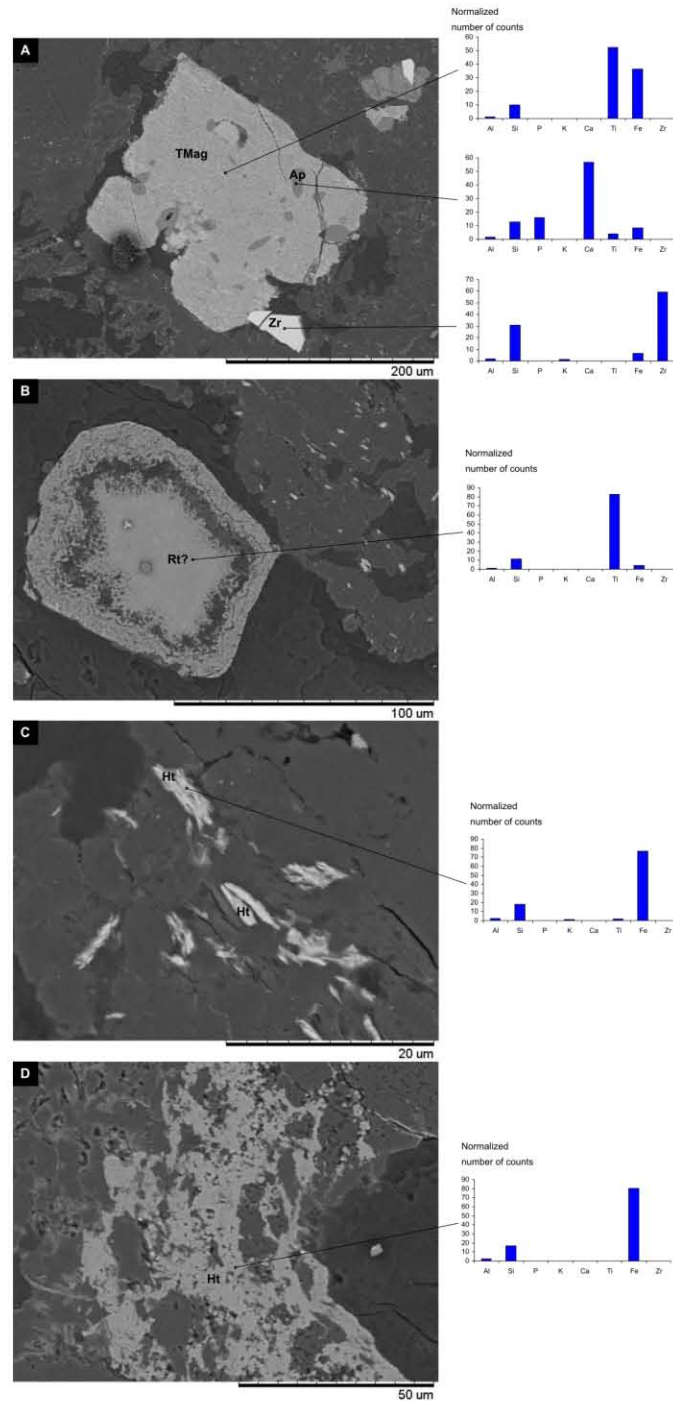


Figure A1-3. SEM micrographs and EDS results of sample DDP01. TMag – Titanomagnetite; Ap – Apatite; Zr – Zircon; Rt – Rutile; Ht- Hematite. Circle diameter

marks the diameter of the spot in the EDS analysis. The histograms show the result of 700 to 1200 counts detected by the EDS, each bar represent the number of counts (normalized to the higher value) assigned to the energy level of the corresponding atom, symbols represent elements (*e.g.*, K – Potassium).

Sample DDP02

Petrography

Megascopically the sample DDP02 shows a porphyritic texture, with white elongated crystals in a black matrix. At microscopic scale (Figure A1-4) euhedral to subhedral plagioclase crystals compose both the framework and the matrix; some altered ferromagnesian minerals are also present. Plagioclase crystals are partially to fully altered forming chlorite and sericite. Some voids are filled with calcite and clay minerals. The rock is interpreted as an andesite with an intratelluric phase composing the framework and an eruptive phase making the matrix, both phases with the same composition varying only in the crystal size. The rock was later altered.

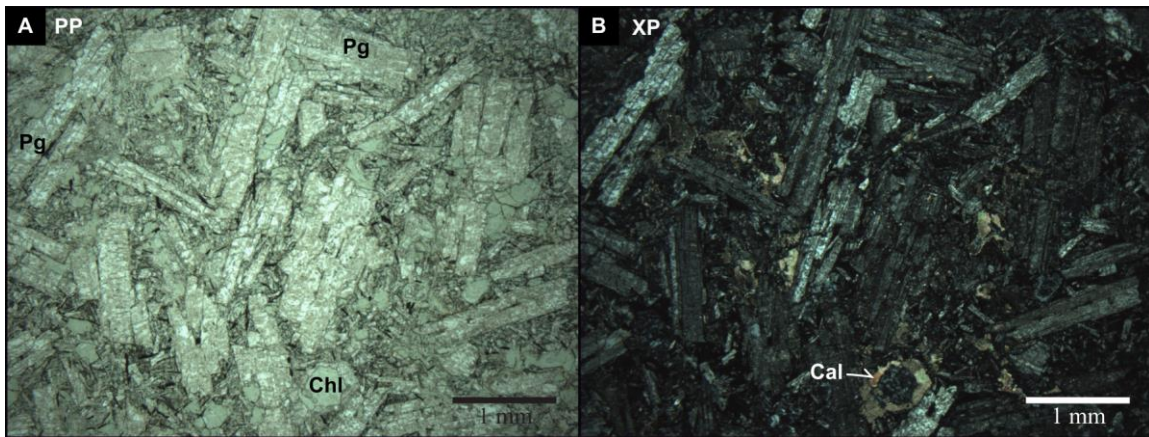


Figure A1-4. Plane and polarized light micrographs of sample DDP02. Pg – Plagioclase; Chl – Chlorite; Cal - Calcite.

Sample DDP03

Petrography

Megascopically the sample a bluish gray aphanitic rock is the only observable attribute for DDP03. In the microscope the rock has a porphyritic texture (Figure A1-5), with plagioclase phenocrysts and microphenocrysts embedded in a plagioclase+cryptocrystalline quartz-feldspar matrix. There are biotite and amphibole pseudomorphs totally replaced by opaque minerals. At all scales, and with paragenetic relation, several alteration minerals such as chlorite, sericite, microcrystalline quartz and calcite can be recognized. The rock is interpreted as an andesite with intratelluric and eruptive crystallization phases, whose ferromagnesian minerals were replaced by opaque minerals during decompression and devitrified, and subsequently altered by weathering and/or hydrothermalism.

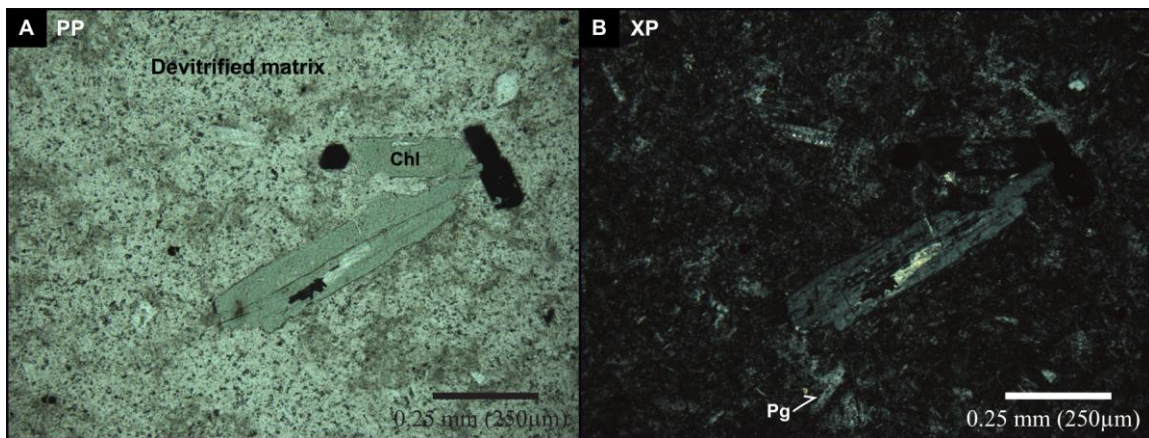


Figure A3-5. Plane (A) and polarized (B) light micrographs of sample DDP03. Chl – Chlorite; Pg – Plagioclase. The large crystal now replaced by chlorite could have been originally a plagioclase crystal.

Reflected petrography

There are two types of ferromagnetic (*sensu lato*) minerals in this sample (Figure A1-6). The first one is subhedral to euhedral magnetite, with observable mean diameter of 0.02 mm, although it is assumed that the bulk of these crystals are too small for microscope observation; the largest crystal of this type has a diameter of 0.1 mm (Figure A1-6 A);

these phase is interpreted as primary. The second type of ferromagnetic mineral observed corresponds to magnetite replacing older amphiboles (Figure A1-6 B); grains are disposed as tiny crystals inside other crystals and are of inclusions of primary origin. According to Watkins & Haggerty (1967) this sample has an oxidation state I.

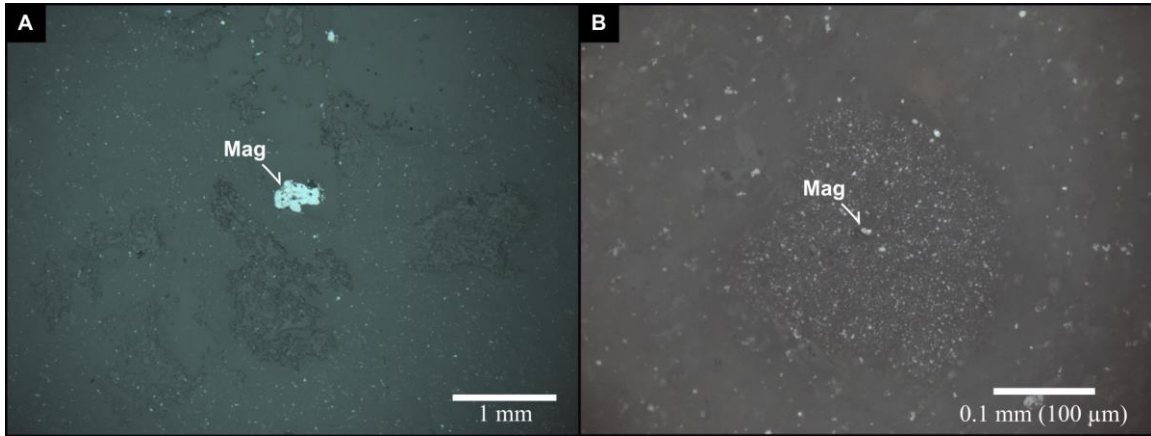


Figure A1-6. Reflected light micrographs of sample DDP03. Mag – Magnetite. In (B) the Magnetite crystals are within a bigger crystal, probably a ferromagnesian mineral.

SEM

In this sample two modes of magnetic minerals were analyzed: euhedral to subhedral crystals dispersed in the matrix (Figure A1-7 B), and subhedral crystals replacing ferromagnesian silicate crystals (Figure A1-7 A). Figure A1-7 A shows that the minerals inside ferromagnesian silicate minerals correspond to titanomagnetites (low Ti). Dispersed in the matrix there are anhedral crystals of grey and white color, whose element spectra show high Zr and Ti counts (Figure A1-7 B), these minerals correspond to zircon and rutile, respectively.

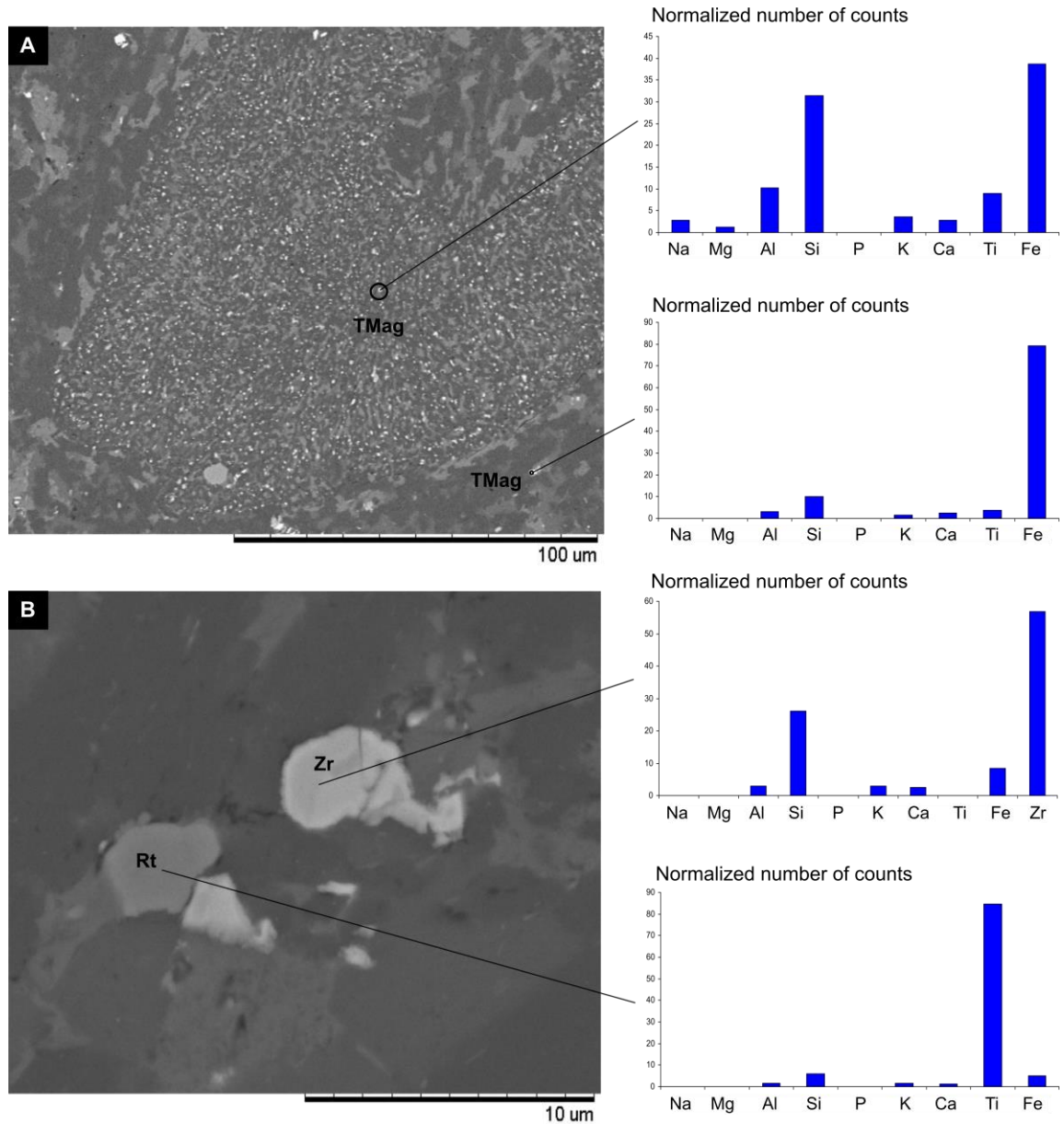


Figure A1-7. SEM micrographs and EDS results of sample DDP03. TMag–Titanomagnetite; Zr – Zircon; Rt – Rutile. Circle diameter marks the diameter of the EDS analysis spot; so, in the case of big circle diameters the element spectrum is contaminated by the background.

Sample DDP04

Petrography

Under the microscope DDP04 presents a porphyritic texture with 15% of plagioclase phenocrysts inside a plagioclase matrix (Figure A1-8). A pilotaxitic texture is observed inside this matrix. A banded structure is slightly developed by the alternance of bands moderately devitrified. Ubiquitous presence of completely opaque replaced biotite and/or amphibole crystals is recognized. There is development of chloritic and calcitic alterations. Mafic and quartzitic veins are present. The rock is interpreted as an andesite with low percentage of mafic crystals and with an intratelluric phase developed.

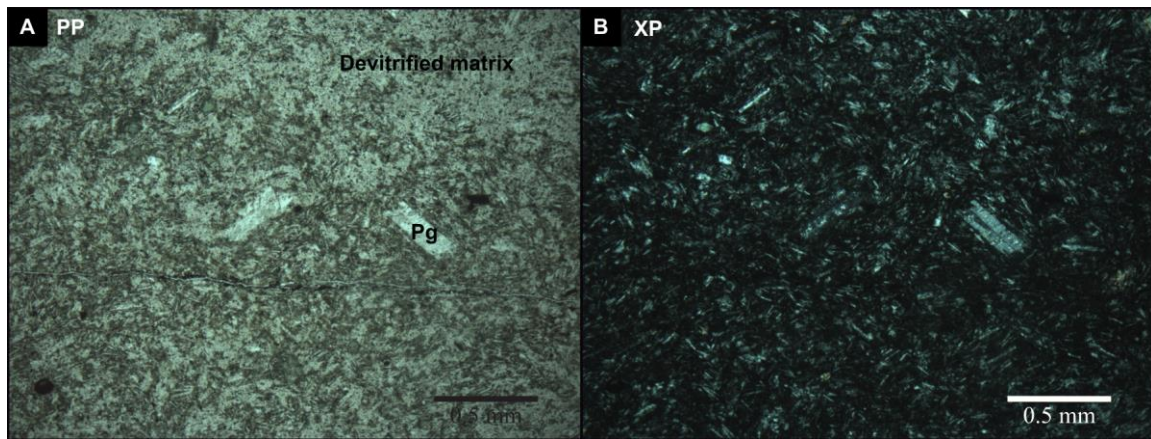


Figure A1-8. Plane (A) and polarized (B) light micrographs of sample DDP04. Pg – Plagioclase. A coarse lamination is detected between plagioclase rich bands and devitrified matrix.

Sample EXTRA

Petrography

At the top of the previous described rocks we sampled a rock with a brechoid aspect in outcrop. Under the microscope the rock (Figure A1-9) also presents the same brechoid texture, composed by microporphyritic andesites and rhyolites filled by a siliceous matrix in the voids. This rock is interpreted as the frontal part of a lava flow, which incorporated into its body the external crystallized rocks.

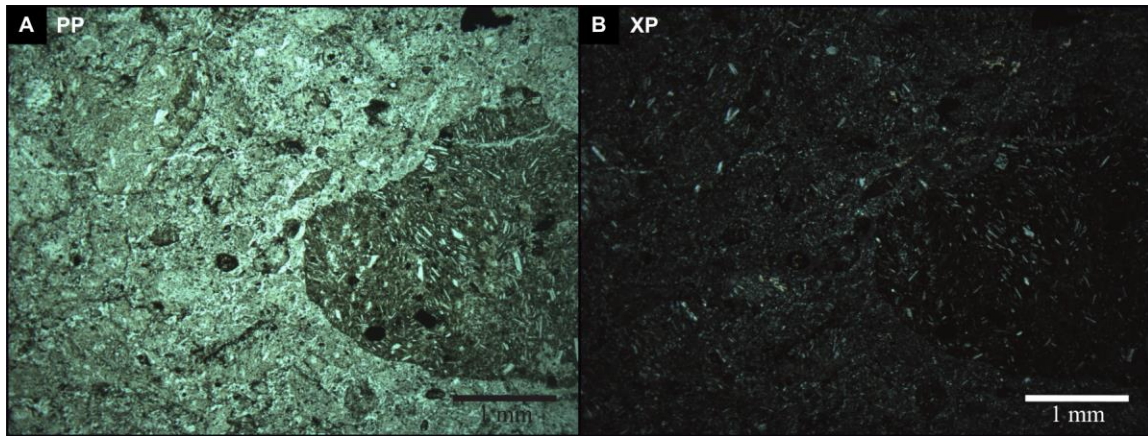


Figure A1-9. Plane (A) and polarized (B) light micrographs of sample EXTRA. Pg – Plagioclase. The dark crystal to the right of the photograph is subroundes, and corresponds to a dacite fragment, some other fragments of smaller size can also be seen.

Sample DDP06

Reflected petrography

As in the locality DDP03 this sample has two different occurrences of ferromagnetic (s.l.) (Figure A1-10) minerals: the first and most common are disseminated magnetite crystals trough all the sample. These crystals are subhedral to euhedral, the largest size is 0.2 mm (Figure A1-10 A, B) tough the mean size is less than 0.01mm, and the petrographic microscope scale cannot detail these crystals; the largest crystals develop alteration to maghemite in their borders (Figure A1-10 B). This magnetite occurrence is interpreted as primary. The second occurrence of ferromagnetic minerals is the replacement of mafic crystals (amphibole, biotite) by magnetite (Figure A1-10 C, D); this magnetite follows previous anisotropies of the crystals as cleavage and fractures, and also grows in the internal parts of the crystals. This magnetite occurrence is interpreted as primary growing during decompression of the lava at the time of eruption. According to Watkins & Haggerty (1967) this sample has an oxidation state I.

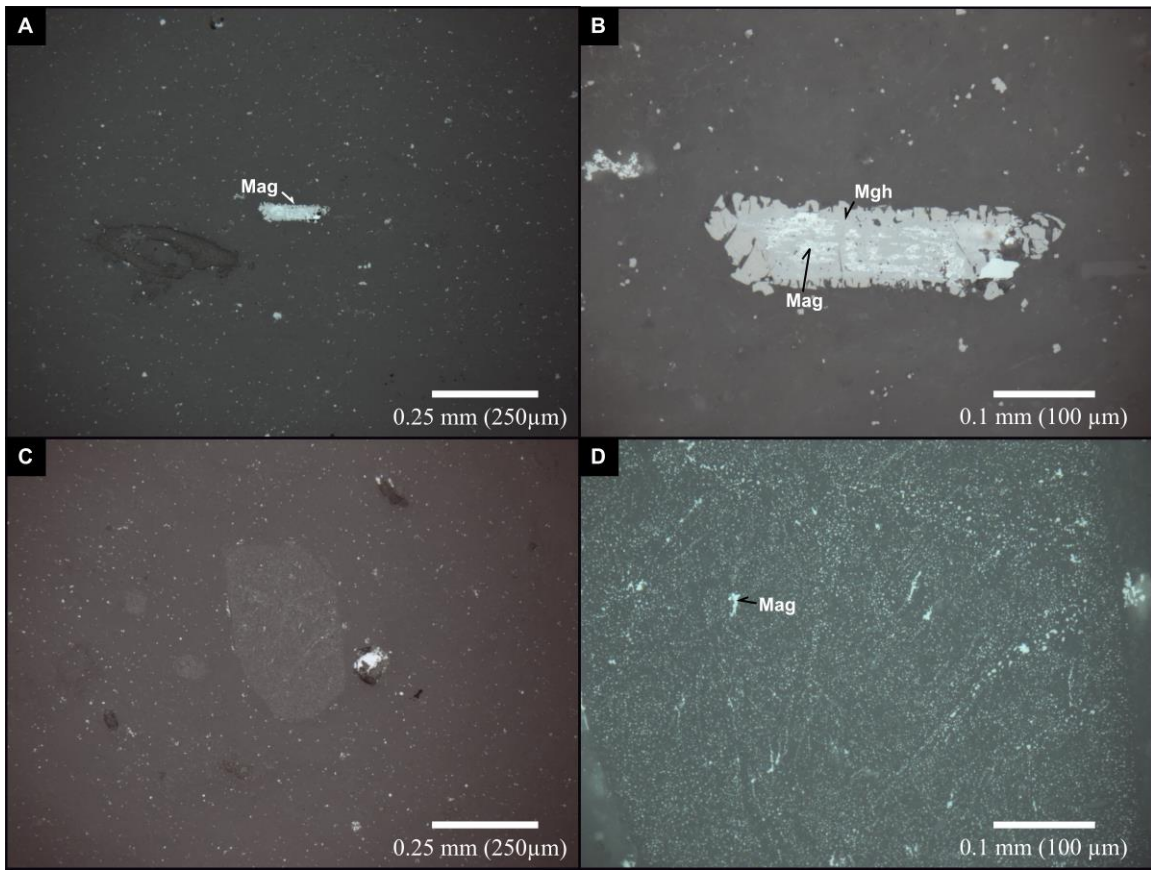


Figure A1-10. Reflected light micrographs of sample DDP06. Mag – Magnetite; Mgh – Maghemite. The maghemite coating detected in (B) is secondary, but some skeletal magnetite is preserved. In (D) the magnetite inclusions in the bigger ferromagnesian (?) crystal are oriented along previous fractures and/or cleavage planes.

SEM

The two different dispositions of magnetic in the sample (dispersed in the matrix and replacing amphibole) (Figure A1-11) were analyzed giving similar results; the Fe proportion is higher than titanium, so, the magnetic minerals correspond in all cases to low Ti titanomagnetites. Both types of magnetite occurrence are interpreted as primary.

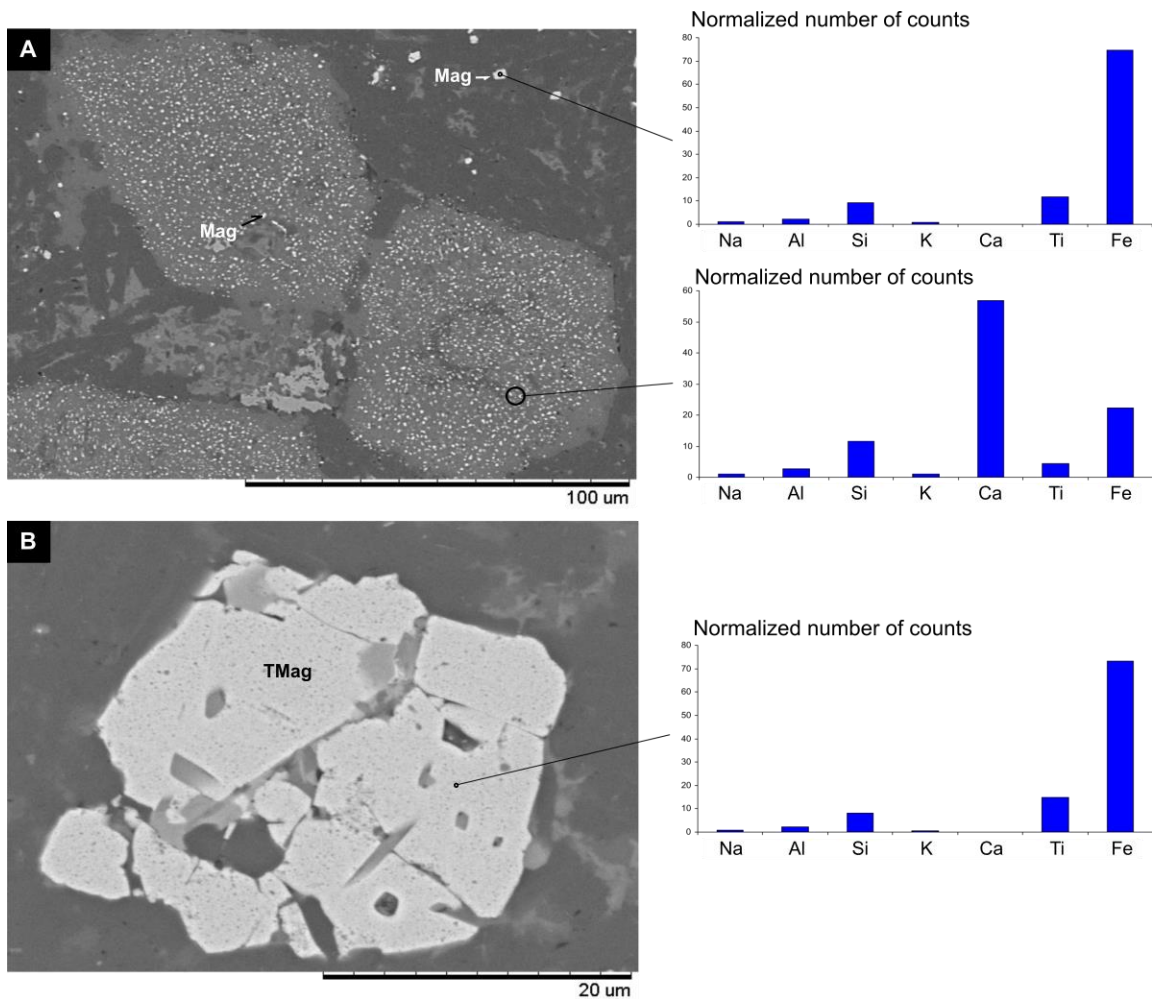


Figure A1-11. SEM micrographs and EDS results of sample DDP06. TMag – Titanomagnetite; Mg- Magnetite. Magnetite and titanomagnetite is present both as individual crystals and inside bigger ferromagnesian (?) crystals.

Sample DDP08

Petrography

In hand sample DDP08 has a banded appearance with grayish to pinkish bands and with white crystals inside the bands. Under the microscope the banded structure is seen as darker and lighter patches (Figure A1-12); these patches are composed of a mosaic of quartz and plagioclase with saccharoid texture, probably as a result of devitrification. The darker and lighter patches differ in crystal size; inside these patches there are euhedral to

subhedral oriented plagioclase phenocrysts. There is presence of quartz veins. The rock is interpreted as altered vitreous lava, for which a banded or patched texture resulted from its previous flow structure.

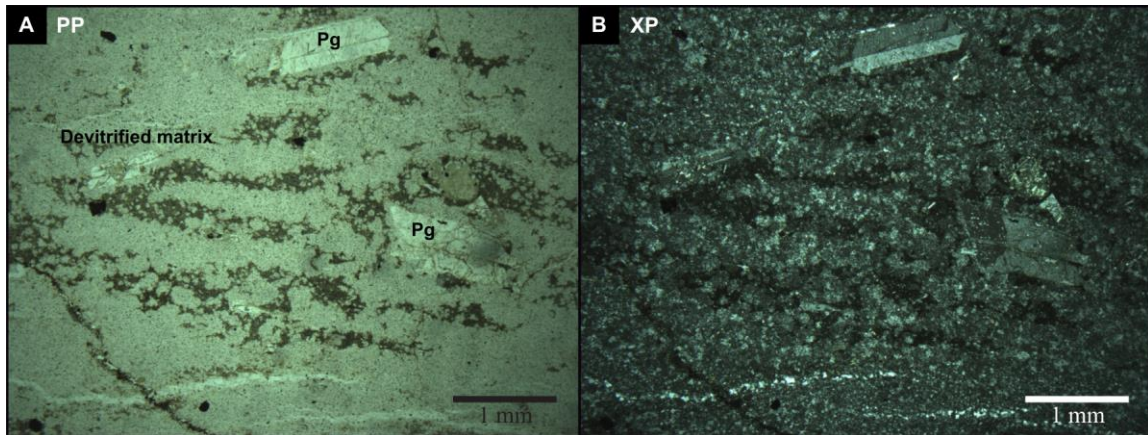


Figure A1-12. Plane (A) and polarized (B) light micrographs of sample DDP08. Pg – Plagioclase. The devitrified matrix has oriented patches of hematite.

Reflected petrography

Sample DDP08 has ferromagnetic (s.l.) minerals occurring in two manners (Figure A1-13). The first, and most common throughout the whole sample, is the occurrence of subhedral to euhedral magnetite mostly too small for microscope observation (seen as small points; A, B). Some crystals reach diameters as high as 0.6 mm (B); in these crystals an intergrowth between ilmenite and hematite is developed (Figure A1-13). The second type of occurrence of ferromagnetic minerals is along the borders of other crystals, presumably plagioclase (A) where an ilmenite-hematite coating is bordering crystals and along some fractures. According to Watkins & Haggerty (1967) this sample has an oxidation state IV.

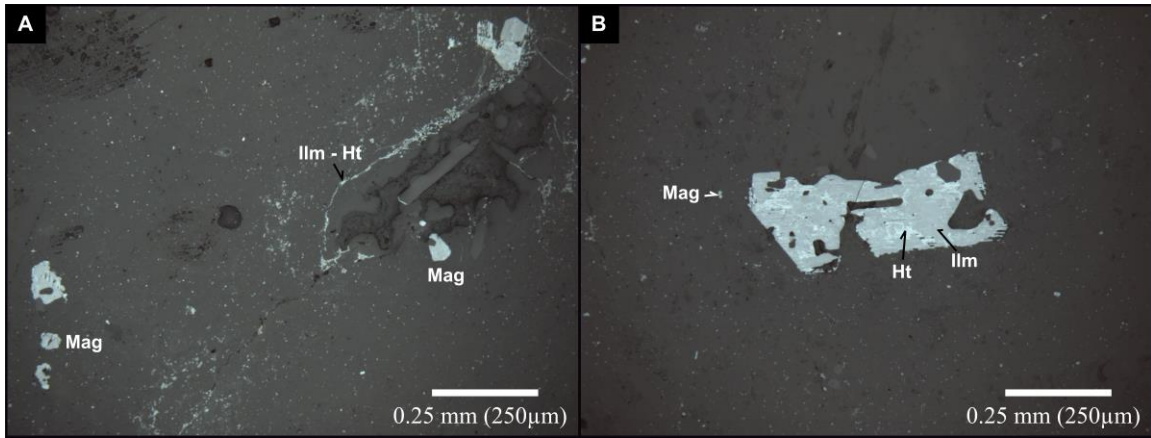


Figure A1-13. Reflected light micrographs of sample DDP08. Mag – Magnetite; Ilm – Ilmenite; Ht - Hematite. Fine hematite and ilmenite border bigger grains and is dispersed along fractures, the bigger magnetite crystals have cubic geometry.

SEM

Sample DDP08 has the occurrence of subhedral crystals of a large range of sizes; the largest crystals exhibit lamellae of ilmenite and hematite and some rutile patches, with an increase in Ti content as the lamellae acquires a darker tone that corresponds to ilmenite and rutile (Figure A1-14 A). The smaller crystal sizes do not present this texture, being only low Ti titanomagnetites. Some ilmenite-rutile veins appear as injected in the sample (Figure A1-14 B).

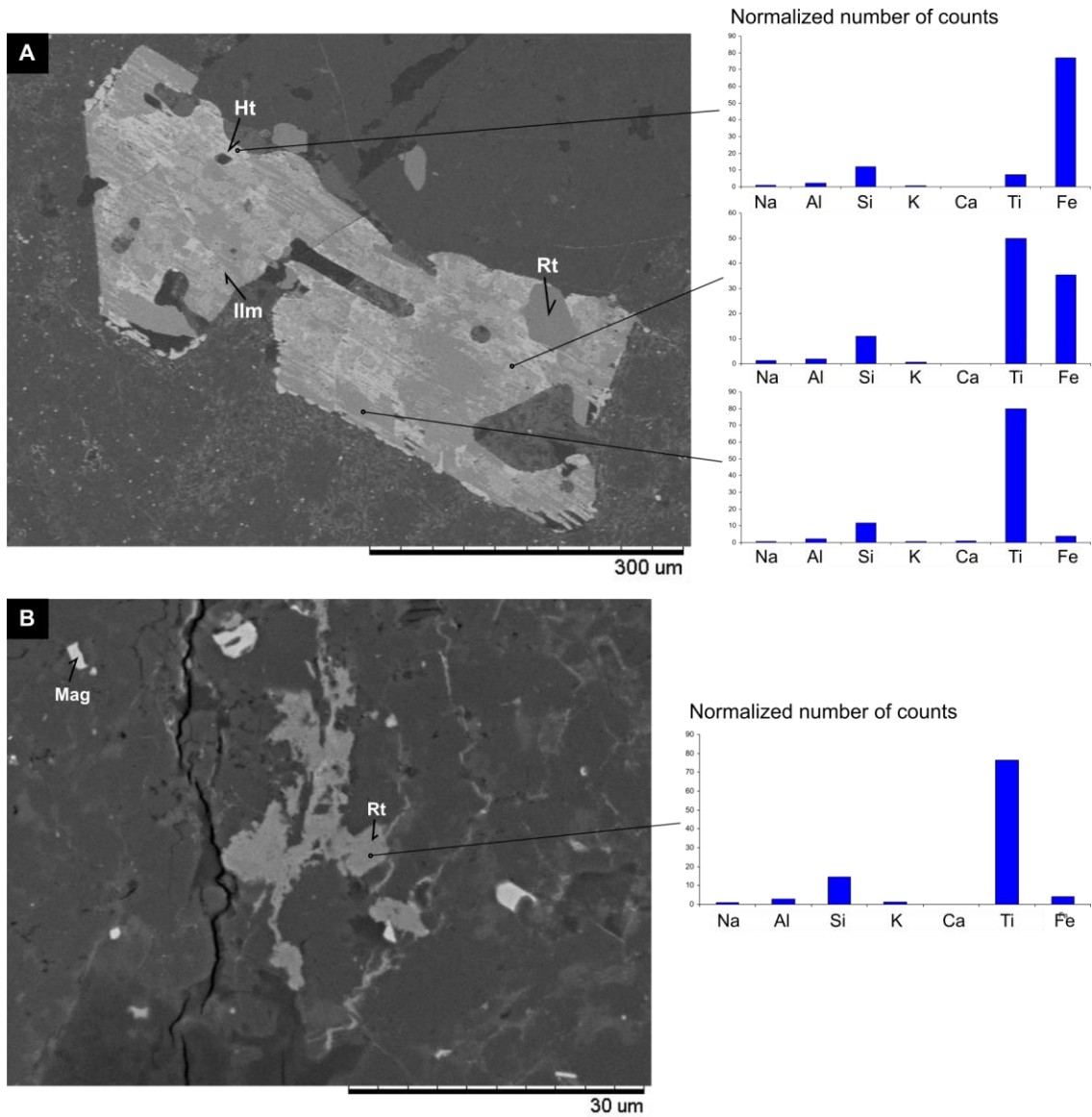


Figure A1-14. SEM micrographs and EDS results of sample DDP08. Mag- Magnetite; Ilm – Ilmenite; Ht – Hematie; Rt – Rutile. The Rutile paramagnetic crystals have the biggest counts of Ti.

Sample DDP09

Petrography

Under the microscope sample DDP09 has a porphyritic texture (Figure A1-15), with euhedral to subhedral twinned plagioclase phenocrysts in a plagioclase matrix with pilotaxitic texture. There are oval shaped voids filled with chalcedony. The plagioclase phenocrysts are sometimes replaced by opaque minerals and/or by microcrystalline quartz. The rock is interpreted as an andesite with voids filled by minerals of hydrothermal origin.

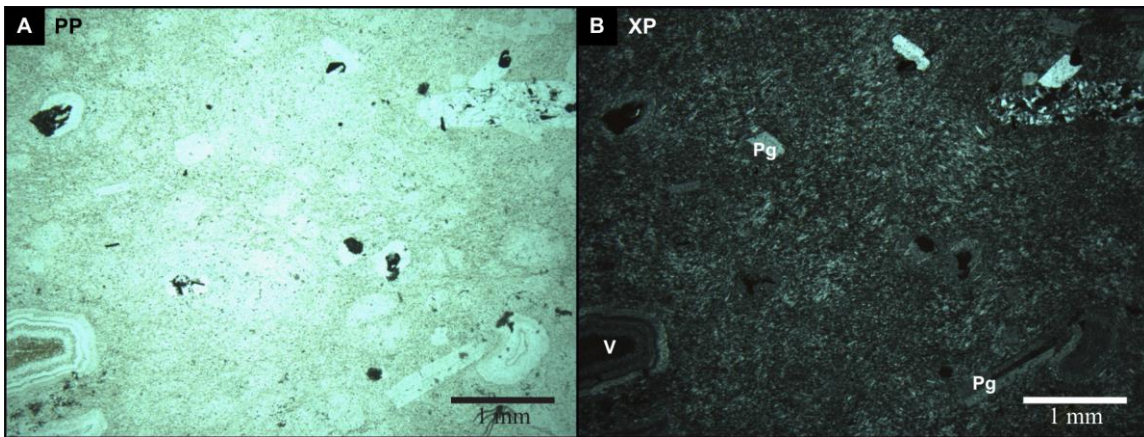


Figure A1-15. Plane (A) and polarized (B) light micrographs of sample DDP09. Pg – Plagioclase; V - Vesicle. The pilotaxitic texture, with oriented plagioclase crystals is easily seen in (B), also the concentric filling of the vesicles. In the upper corner a crystal is fully replaced by silica.

Reflected petrography

This sample has two principal phases of ferromagnetic minerals (Figure A1-16). The first are magnetite crystals present throughout the whole sample, with subhedral to euhedral habits, and with a cryptocrystalline size (Figure A1-16 B, C). Another occurrence of magnetite is as inclusions inside primary ilmenite-hematite crystals (Figure A1-16 A, D), some of these crystals show martitization along cracks (Figure A1-16 A) and some of them have developed a hematite coating (Figure A1-16 D). This hematite occurrence is the second most common ferromagnetic phase, and is present growing together with ilmenite in the largest grains, along some grain borders (Figure A1-16 C, D), and filling cracks within crystals (Figure A1-16 B) and voids between them. Both magnetite and

hematite are primary; nevertheless, the hematite veins are secondary. According to Watkins & Haggerty (1967) this sample has an oxidation state IV.

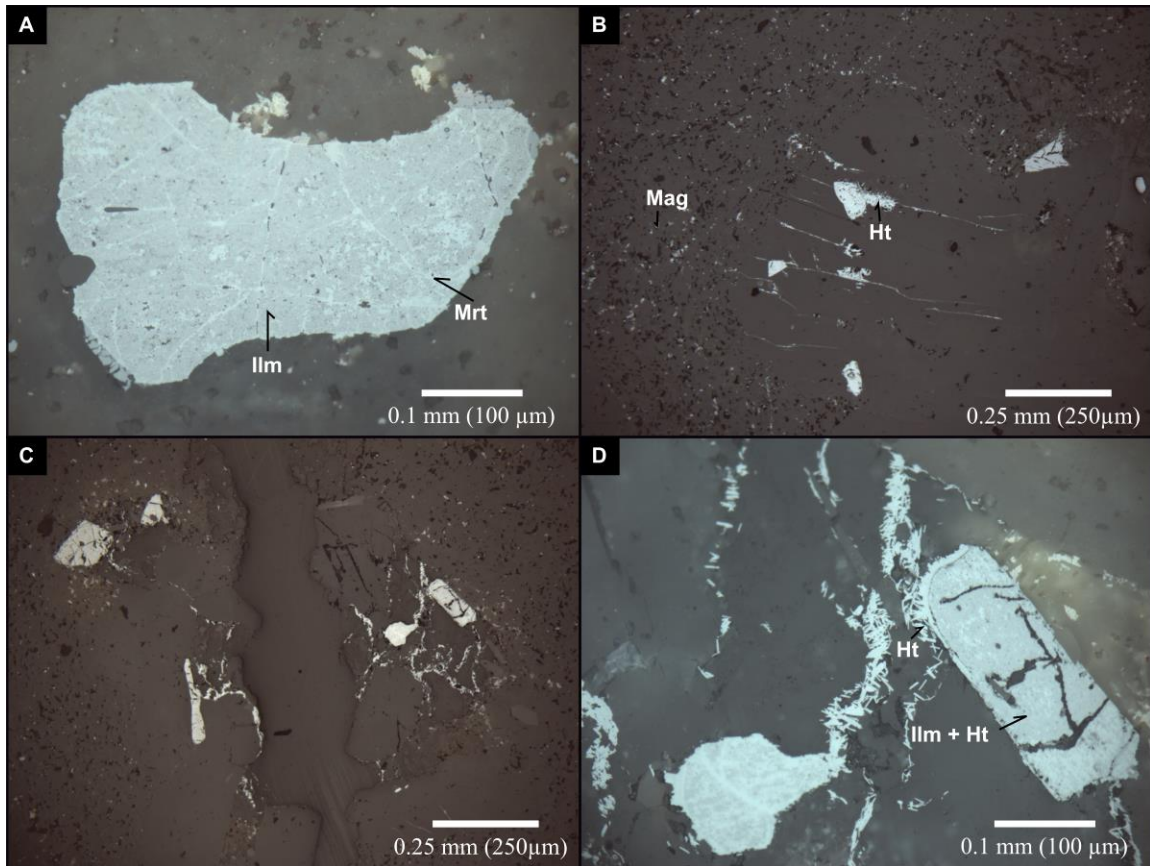


Figure A1-16. Reflected light micrographs of sample DDP09. Mag – Magnetite; Ilm – Ilmenite; Ht – Hematite; Mrt - Martite. Hematite needles are distributed along fractures and fillig voids, also replacing bigger crystals.

SEM

Sample DDP09 has a common intergrowth texture between hematite and ilmenite; some magnetite inclusions are present inside ilmenite (Figure A1-17). Secondary hematite with a low Ti content is present along crystal borders, filling voids, and as veins. There's observed an anomalous high content in Al, this probably may be due to the high hematite content.

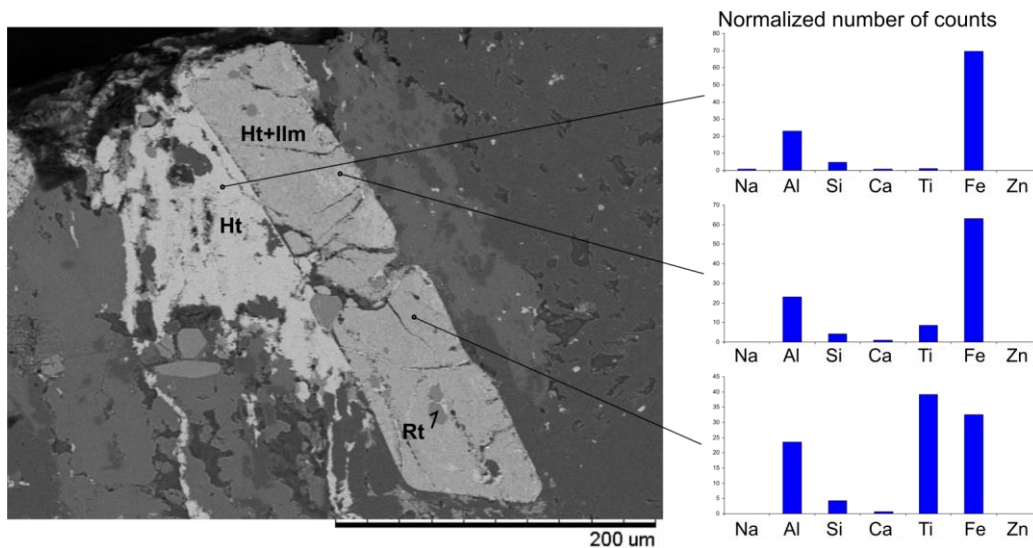


Figure A1-17. SEM micrographs and EDS results of sample DDP09. Ilm – Ilmenite; Ht – Hematic; Rt – Rutile. Notice that the number of counts of Ti increase as the color gets darker.

Sample DDP11

Petrography

Megascopically sample DDP11 has an aphanitic appearance, with reddish brown color crossed by a series of white veins. Under the microscope (Figure A1-18) the rock has a porphyritic texture, with euhedral to subhedral plagioclase phenocrysts in a plagioclase matrix with pilotaxitic texture; some of the plagioclase phenocrysts are replaced by cryptocrystalline quartz. The rock is cut by series of vesicles filled with quartz at the borders and chlorite at the center; opaque minerals border the outer parts of these vesicles. The rock is interpreted as an andesite with amygdaloidal texture filled by posterior hydrothermal and/or supergene activity.

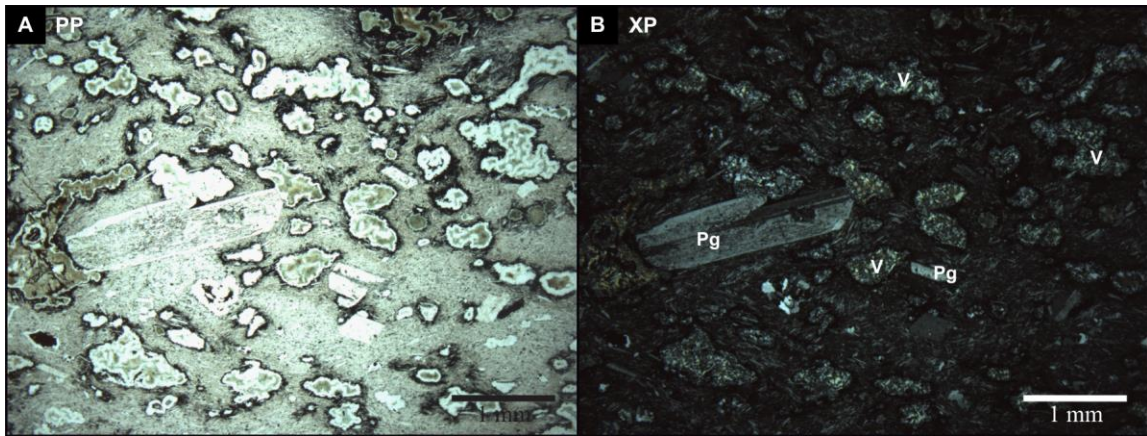


Figure A1-18. Plane (A) and polarized (B) light micrographs of sample DDP11. Pg – Plagioclase; V - Vesicle. The sample is crossed by a multitude of vesicles, filled with chlorite and silica and bordered by hematite.

Reflected petrography

This sample has at least three different magnetic phases within its opaque minerals. The primary phases are ilmenite and magnetite, present as euhedral to subhedral crystals; only the finer sizes may still remain unaltered, due to a replacement by hematite in the coarser crystal sizes (Figure A1-19 A, B). The coarser crystal has a diameter of 0.3 mm and is constituted by ilmenite (dark grey) and hematite (light grey) (Figure A1-19 B). These three phases (magnetite, ilmenite, and hematite) are equally abundant in the sample and originated as primary (magnetite, ilmenite) and as replacement product of magnetite and bordering vesicles (hematite). Hematite crystals are euhedral and have acicular habit and are secondary in origin. According to Watkins & Haggerty (1967) this sample has an oxidation state IV.

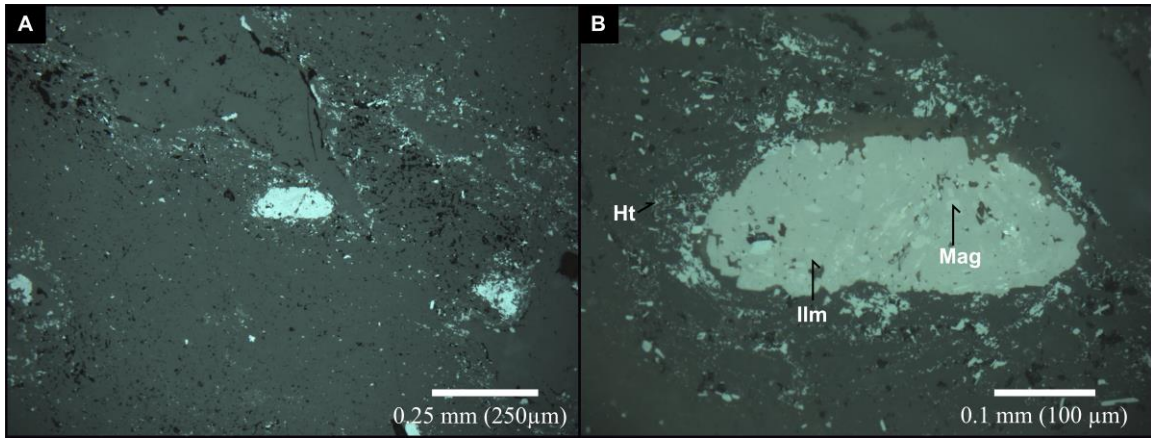


Figure A1-19. Reflected light micrographs of sample DDP11. Mag – Magnetite; Ilm – Ilmenite; Ht – Hematite. Hematite needles are dispersed through the matrix (A), and replace the larger crystals (B).

SEM

The elemental spectrum show that all the lighter crystals have a high Fe composition with a low Ti content, whilst the darker crystals have a high Ti and a low Fe content (Figure A1-20). Most of the minerals correspond to titanomagnetite, although many of these crystals are replaced by hematite; some magnetite crystals are preserved in the finest crystal sizes. The darker crystals rich in Ti correspond to rutile.

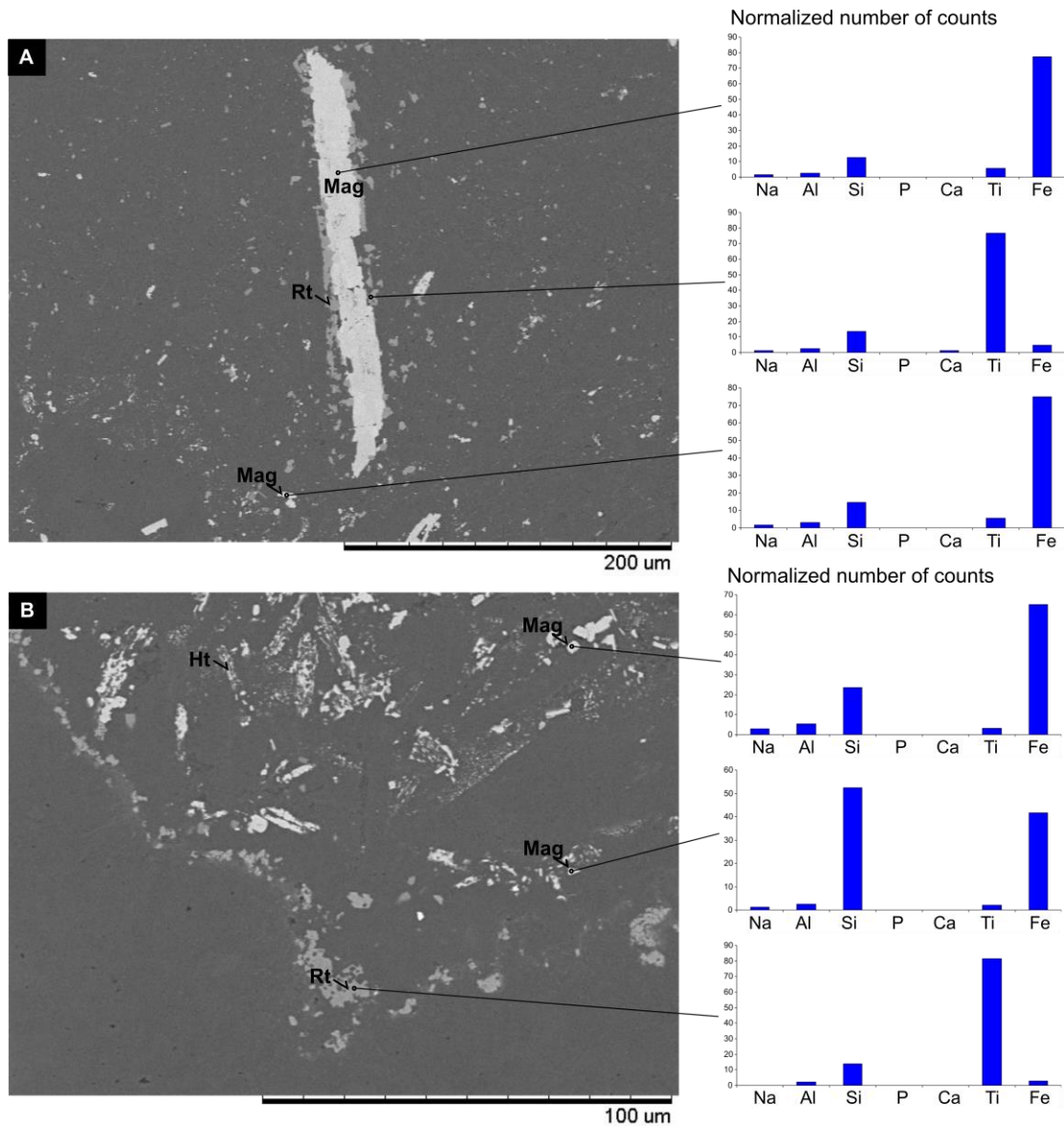


Figure A1-20. SEM micrographs and EDS results of sample DDP11. Mag – Magnetite; Ht – Hematite; Rt – Rutile.

Sample DDP12

Petrography

The rock sample at DDP12 has an aphanitic texture (Figure A1-21) with subhedral plagioclase crystals in a dark matrix, probably vitreous, in which opaque minerals can be seen. The dark matrix is full of vesicles filled with chlorite, calcite and/or

microcrystalline quartz. In some places there are white patches of rock composed of a plagioclase matrix with plagioclase phenocrysts, the borders of this patches are irregular. A mafic lava with some explosive action in its emplacement can be the origin of this rock.

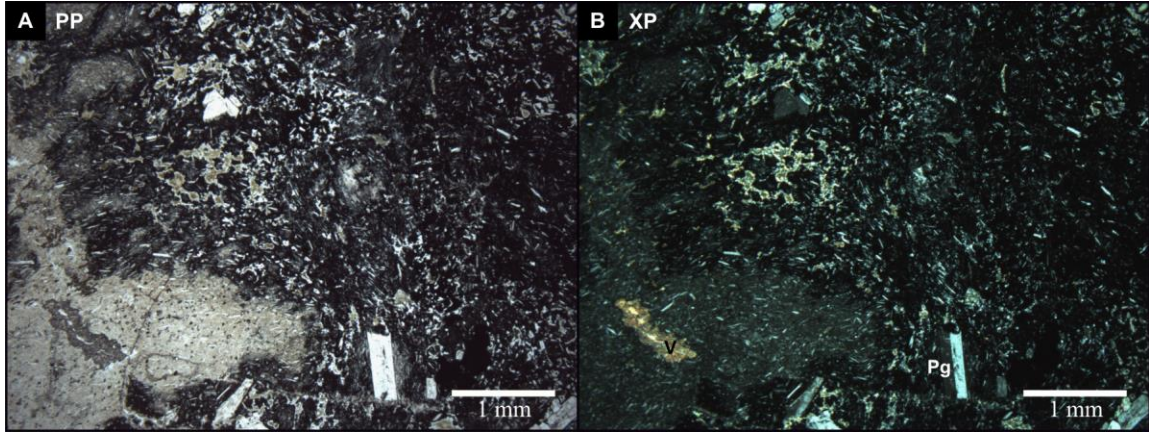


Figure A1-21. Plane and polarized light micrographs of sample DDP12. Pg – Plagioclase; V – Vesicle. To the left down corner the matrix is white, different from the rest of the photograph.

Sample DDP13

Petrography

Megascopically sample DDP13 is aphanitic with a bluish grey color. In the microscope (Figure A1-22) a subhedral plagioclase framework is recognized, with unimodal crystal size. The plagioclase is locally altered to sericite and calcite; some crystals are completely replaced by chlorite; originally they could have been amphiboles and/or biotite. The voids within crystals are filled with calcite, chlorite and opaque minerals. Some circular vesicles filled with chalcedony are recognized. There is kaolinitic cement in between crystals, as well as quartz veins. The rock is interpreted as an andesite.

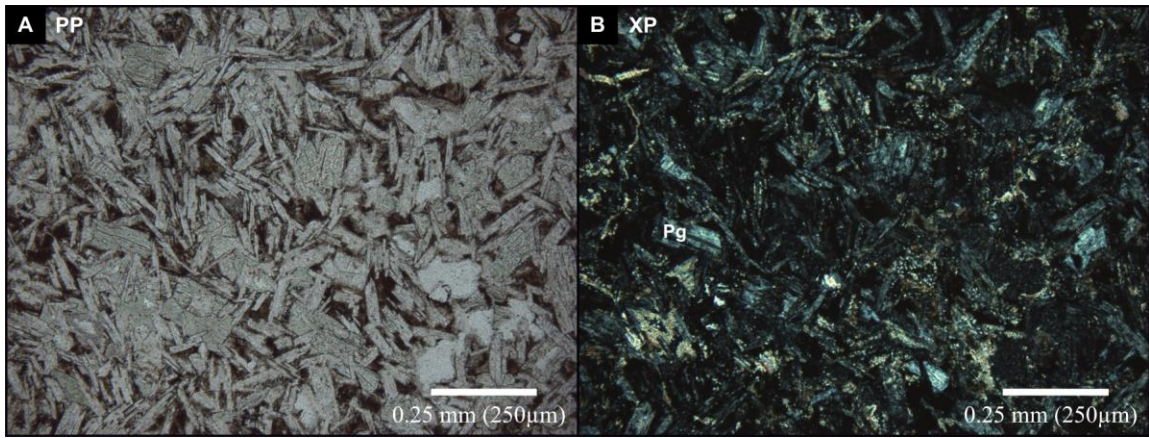


Figure A1-22. Plane and polarized light micrographs of sample DDP13. Pg – Plagioclase. Most plagioclase crystals are replaced by alteration products with high birefringence.

SEM

This sample has a principal magnetic phase corresponding to magnetite, without any Ti content. Some other crystals are identified as primary ilmenite and apatite (Figure A1-23).

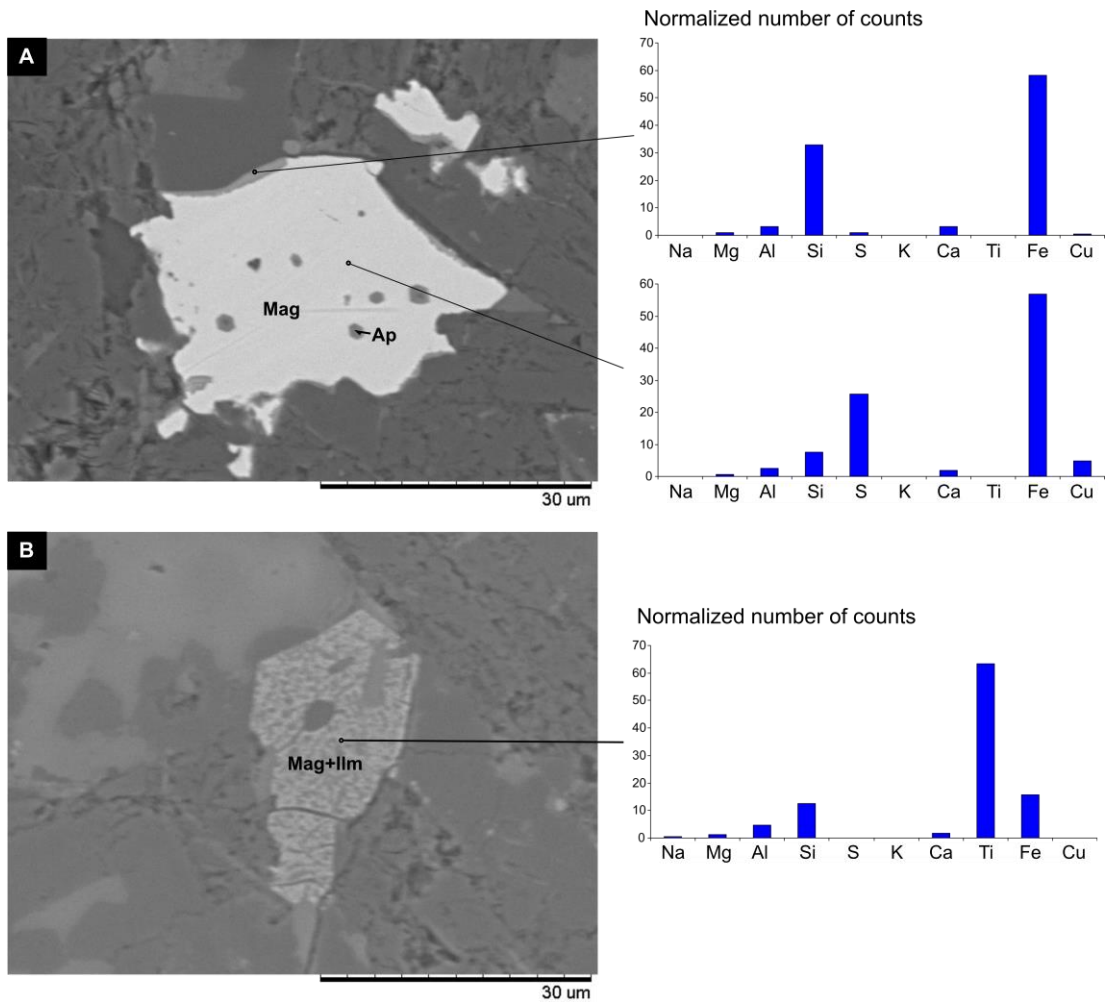


Figure A1-23. SEM micrographs and EDS results of sample DDP13. Mag – Magnetite; Ilm - Ilmenite; Ap – Apatite. The texture of the ilmenite crystal may resemble a primary origin.

Sample DDP14

Reflected petrography

The most abundant magnetic mineral in sample DDP14 is titanomagnetite, which occurs distributed throughout the entire sample as anhedral crystals of various sizes (Figure A1-24 A, B). Hematite and magnetite occur together as patches filling voids between plagioclases (Figure A1-24 C, D); these occurrences can be primary in origin. Finally

some hematite veins can be observed in various zones in the sample (Figure A1-24 A, B). According to Watkins & Haggerty (1967) this sample has an oxidation state IV.

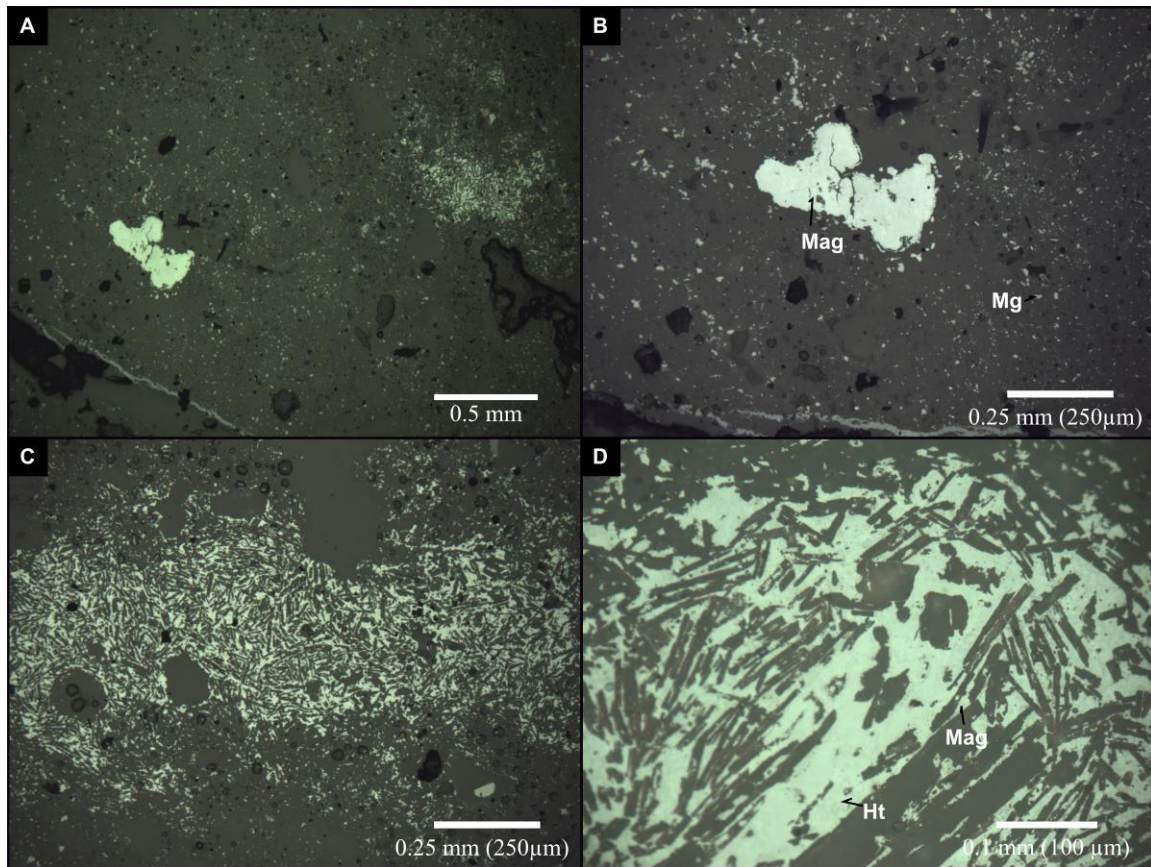


Figure A1-24. Reflected light micrographs of sample DDP14. Mag – Magnetite; Ht – Hematite. C and D show patches of hematite that dominate the sample.

SEM

Sample DDP14 has anhedral magnetite crystals and hematite-magnetite intergrowth in localized patches between plagioclase crystals; according to the measured counts magnetic phases have low contents of Ti (Figure A1-25). In the largest magnetite grains a coating of probably hematite is recognizable, arguing a possibly secondary origin for this cover (Figure A1-25 A). Some rutile crystals are present in the sample (Figure A1-25 A). Hematite veins are crossing the sample (Figure A1-25 C).

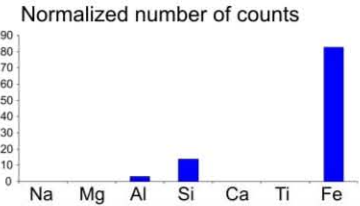
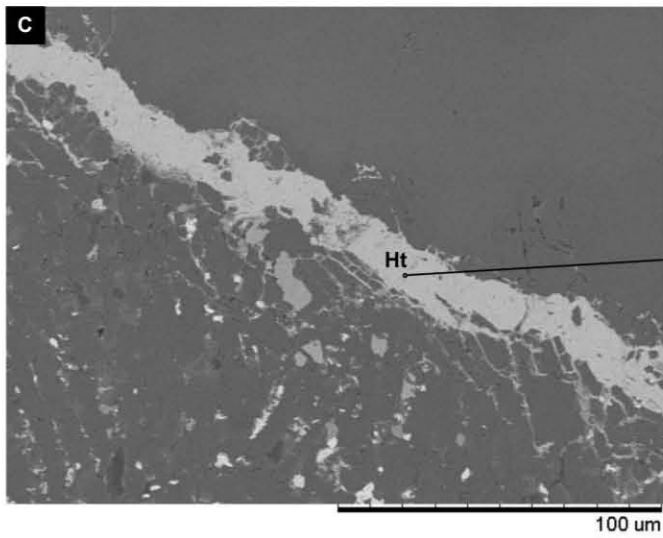
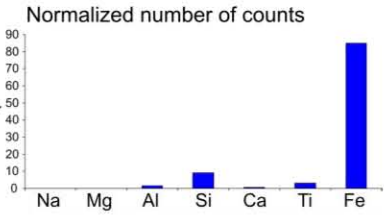
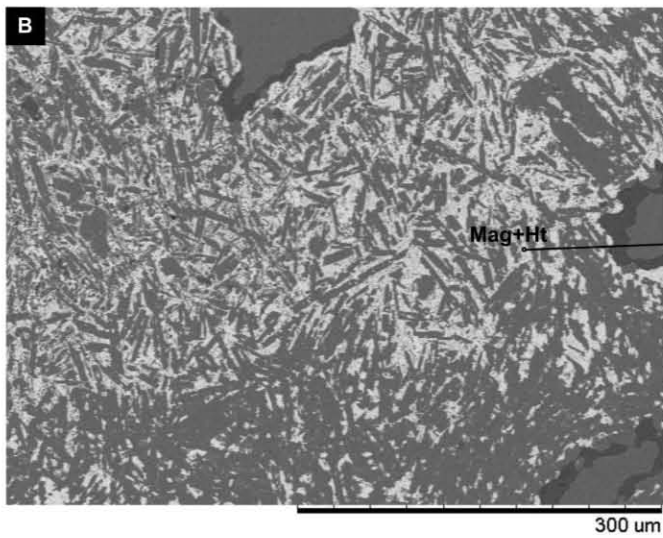
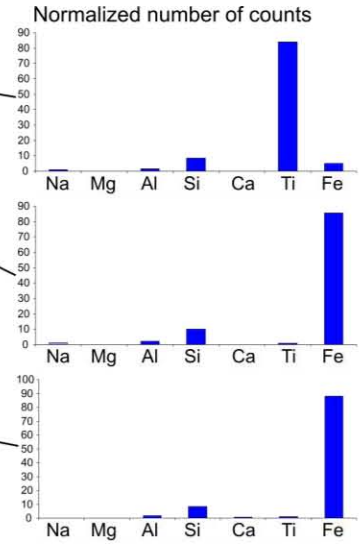
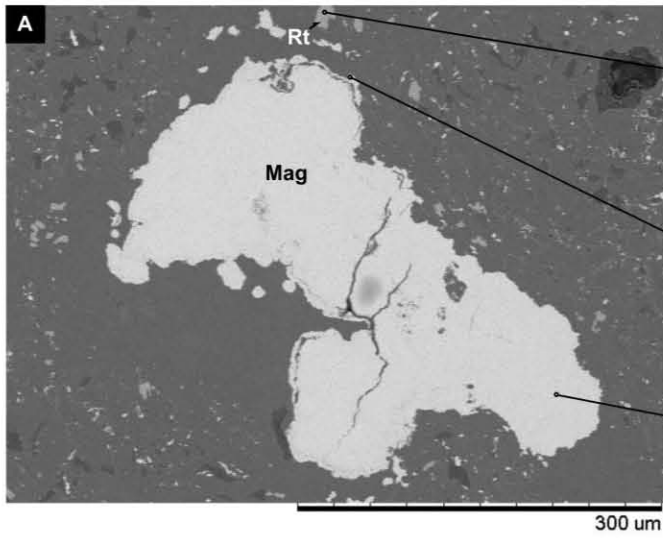


Figure A1-25. SEM micrographs and EDS results of sample DDP14. Mag – Magnetite; Ht - Hematite; Rt - Rutile. The crystal in A probably reflect various adjoined magnetite crystals, as its shape is irregular and uncommon for magnetite. The hematite veins in C cross the sample.

Sample DDP15

Petrography

In hand sample the rock sampled at DDP15 has a breccoid texture; different color fragments inside a light brown matrix can be recognized. Under the microscope the breccoid texture is better observed as a mosaic of subangular andesite-dacite fragments with varying quantities of mafic and felsic minerals, some of them with pilotaxitic texture and some other with banded structure, they are cemented by microcrystalline quartz. There are some plagioclase xenocrysts (Figure A1-26).

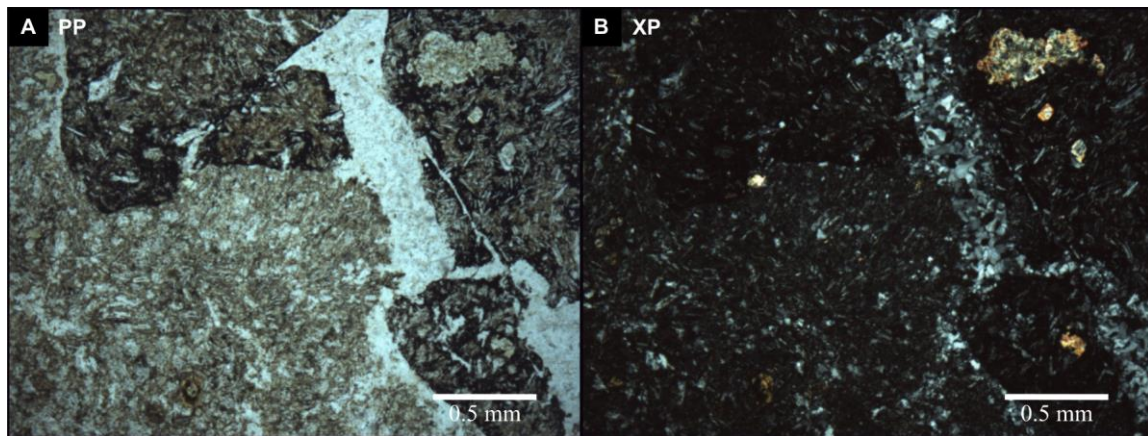


Figure A1-26. Plane (A) and polarized (B) light micrographs of sample DDP15. Several fragments of andesite of different color can be detailed in A.

Reflected petrography

This sample has only one magnetic phase, magnetite. This mineral is present in a wide range of sizes from submicroscopic to 0.12 mm that is the largest diameter (Figure A1-27

A, B). The crystals are subhedral to euhedral and some show exsolution lamellae of ilmenite, which is distributed along the matrix and inside the grains, and inside some vesicles (Figure A1-27 A). The largest grains have developed martitization at their borders (Figure A1-27 B). Some magnetite veins are cutting the specimen (Figure A1-27 A). According to Watkins & Haggerty (1967) this sample has an oxidation state II.

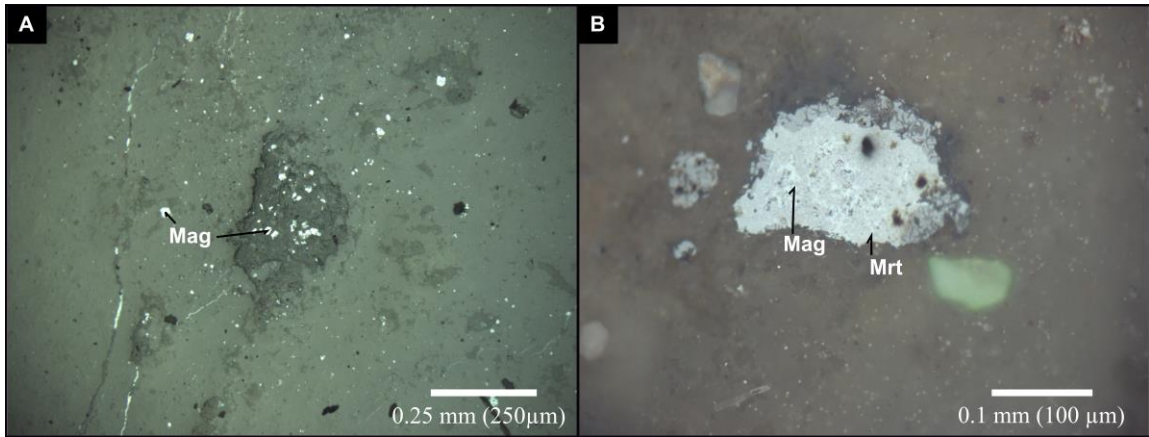


Figure A1-27. Reflected light micrographs of sample DDP15. Mag – Magnetite; Mrt – Martite. Some magnetite crystals in A are filling vesicles.

SEM

In this sample only magnetite is present. It is seen that the clean, tiny, anhedral to subhedral crystals correspond to pure magnetite, with negligible Ti quantities; nonetheless, some grains develop alteration that increases the Ti content giving as result titanomagnetites (Figure A1-28); these crystals are primary in origin.

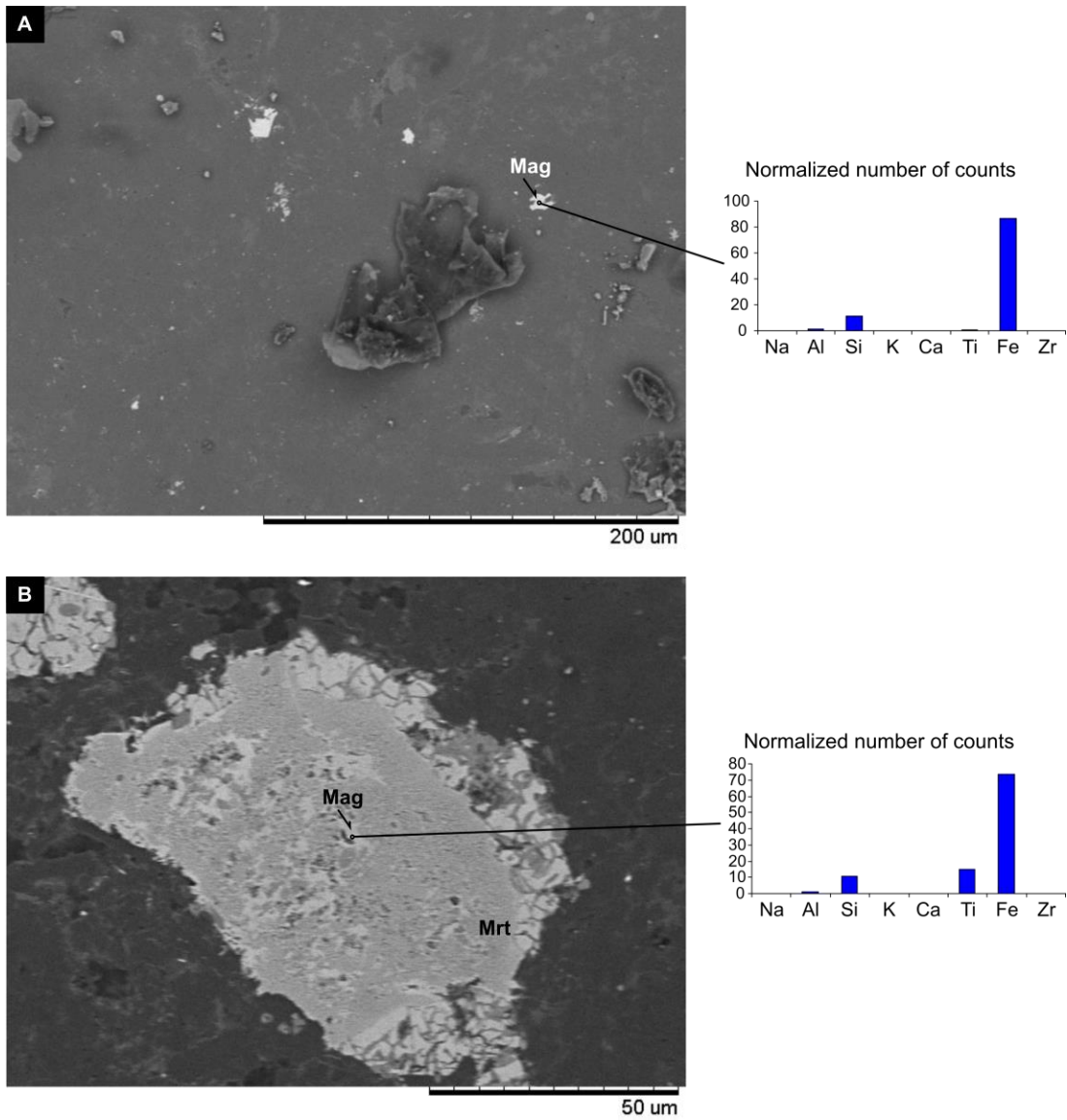


Figure A1-28. SEM micrographs and EDS results of sample DDP15. Mg – Magnetite; Ht – Hematite.

Sample DDP16

Petrography

Megascopically sample DDP16 displays a porphyritic texture, with white elongated crystals in a brownish green matrix. Under the microscope (Figure A1-29) we observed that the white crystals correspond to subhedral plagioclase as phenocrysts in

cryptocrystalline matrix, which is probably comprised of alteration products (mica, quartz, feldspar, clay minerals); other components of the rock correspond to subrounded andesitic xenoliths with variable mafic and felsic content. The whole sample is altered forming sericite, chlorite and calcite. The rock is interpreted as a volcanic hypabasal igneous rock with andesitic composition.

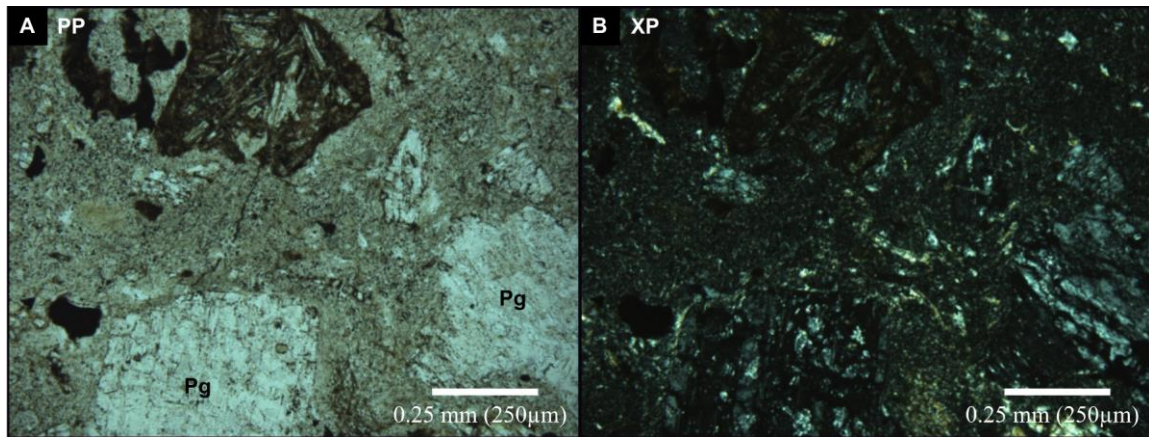


Figure A1-29. Plane (A) and polarized (B) light micrographs of sample DDP16. Pg – Plagioclase.

Reflected petrography

This sample has two magnetic phases, hematite and ilmenite (Figure A1-30). The hematite is present in the whole area in the form of subhedral to euhedral crystals (A, B); the largest crystal has a diameter of 0.25 mm (B). Some veins of hematite are cutting the sample. According to Watkins & Haggerty (1967) this sample has an oxidation state V.

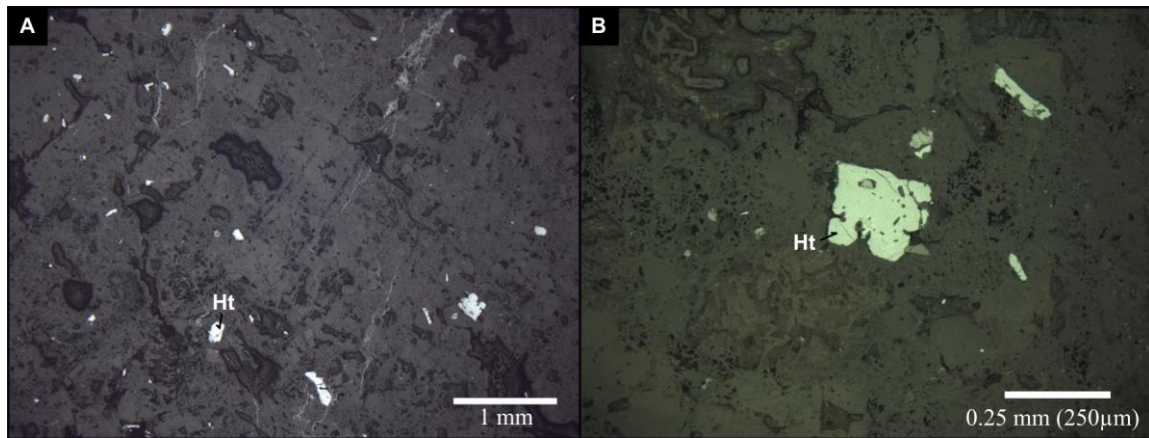


Figure A1-30. Reflected light micrographs of sample DDP16. Ht - Hematite. The shape of the hematite crystal in B may resemble a full replacement of an original magnetite crystal.

SEM

Two magnetic phases are distinguished in this sample. The subhedral to euhedral crystals are a mixture of ilmenite and hematite, the latter in the borders of the crystals and as bands. According to the relative major element composition the hematite bordering the larger grains is low in Ti content while the tiny hematite dispersed in the matrix lacks Ti almost completely (Figure A1-31 A). Secondary hematitic veins lacking Ti are cutting the sample (Figure A1-31 B).

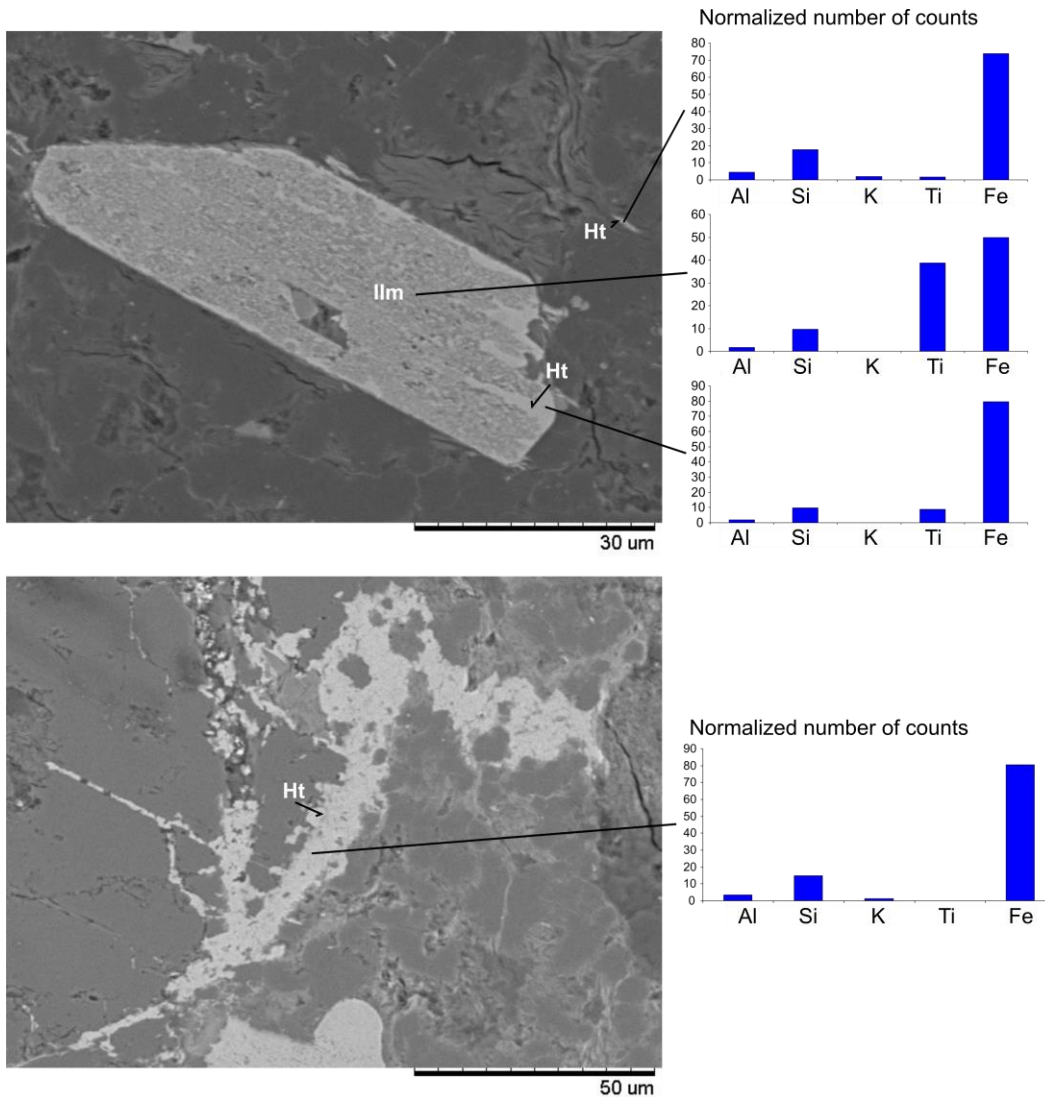


Figure A1-31. SEM micrographs and EDS results of sample DDP16. Ilm – Ilmenite; Ht – Hematite.

Sample DDP17

Petrography

Sample DDP17 is an aphanitic rock composed of subhedral to euhedral plagioclase crystals presenting pilotaxitic texture. Some randomly orientated plagioclase phenocrysts are present (Figure A1-32). There are opaque minerals as singular subhedral crystals and bordering plagioclase crystals; they occur also as patches isolated in the sample. The

plagioclase crystals are ubiquitously altered to sericite. The voids are filled with calcite. Some calcite veins are present. The rock is interpreted as an andesite.

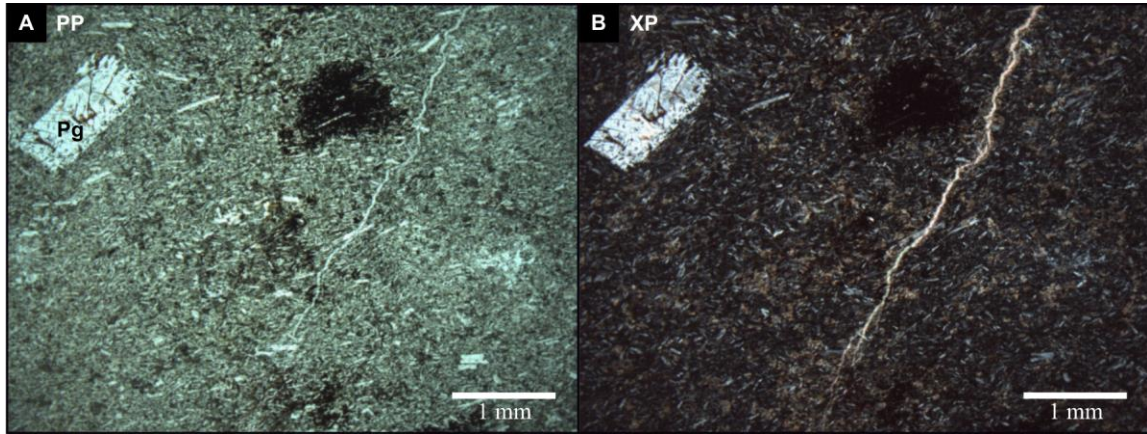


Figure A1-32. Plane and polarized light micrographs of sample DDP17. Pg – Plagioclase. Pilotaxitic texture is easily observed, together with large plagioclase phenocrysts.

Sample DDP18

Petrography

Sample DDP18 is an aphanitic rock composed by subhedral plagioclase with pilotaxitic texture, where some plagioclase phenocrysts are present (Figure A1-33). Alteration to chlorite is observed in the entire sample. The voids are filled with calcite and in less degree by microcrystalline quartz. Patches with opaque minerals are present in localized areas.

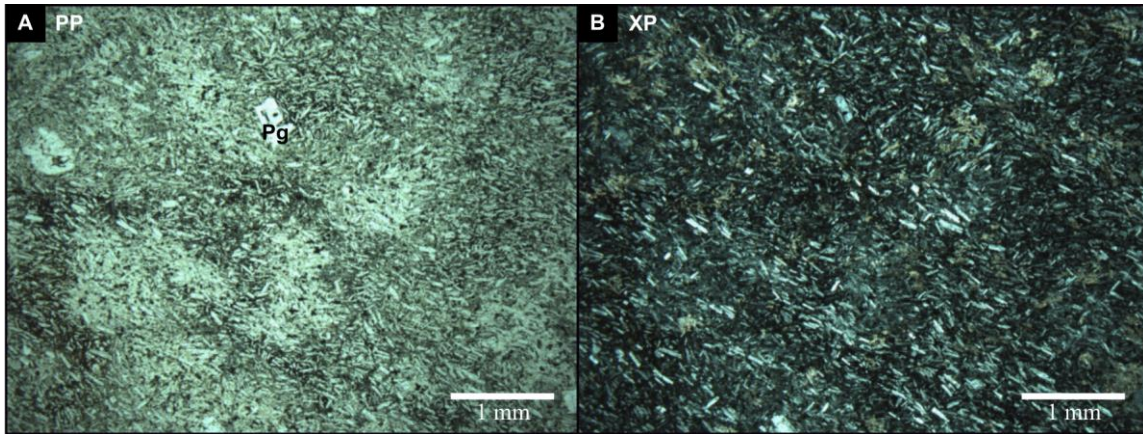


Figure A1-33. Plane (A) and polarized (B) light micrographs of sample DDP18. Pg – Plagioclase. Pilotaxitic texture is easily observed.

Reflected petrography

This sample has three magnetic phases: magnetite, ilmenite and hematite. The three are present in the whole sample, being the magnetite more abundant in the smaller crystal sizes (Figure A1-34 A); the larger crystals (0.22 mm diameter the biggest) tend to be of a rutile-hematite intergrowth (Figure A1-34 B). The magnetite and ilmenite crystals are of primary origin being the hematite an oxidation product. According to Watkins & Haggerty (1967) this sample has an oxidation state IV.

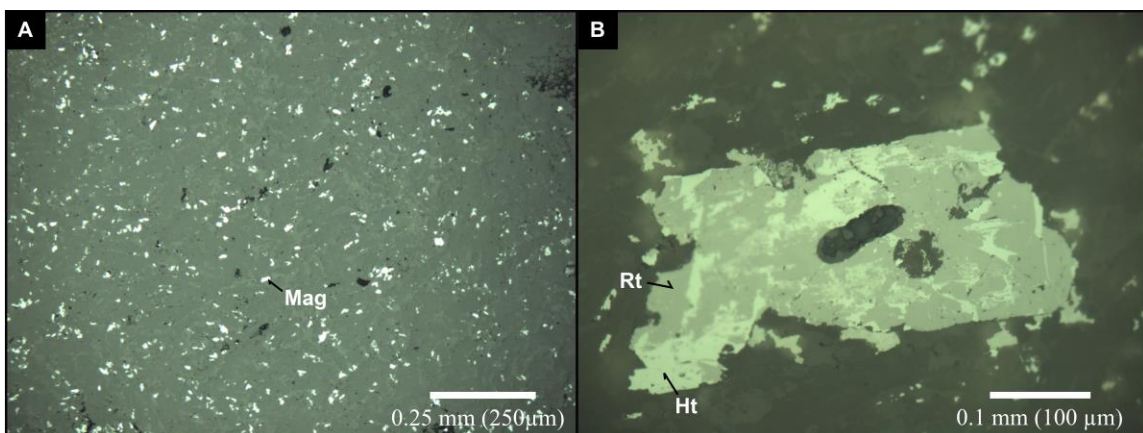


Figure A1-34. Reflected light micrographs of sample DDP18. Mag – Magnetite; Ht – Hematite; Rt - Rutile. The larger crystals are fully replaced by hematite and even rutile.

SEM

The intergrowth between rutile and hematite (TH10-TH20) in lamellae is typical in relatively large crystals (Figure A1-34 B). Some crystals of primary ilmenite have low contents of Fe (Figure A1-34 B); the finest crystals, on the other hand preserve Fe rich composition and are of magnetite.

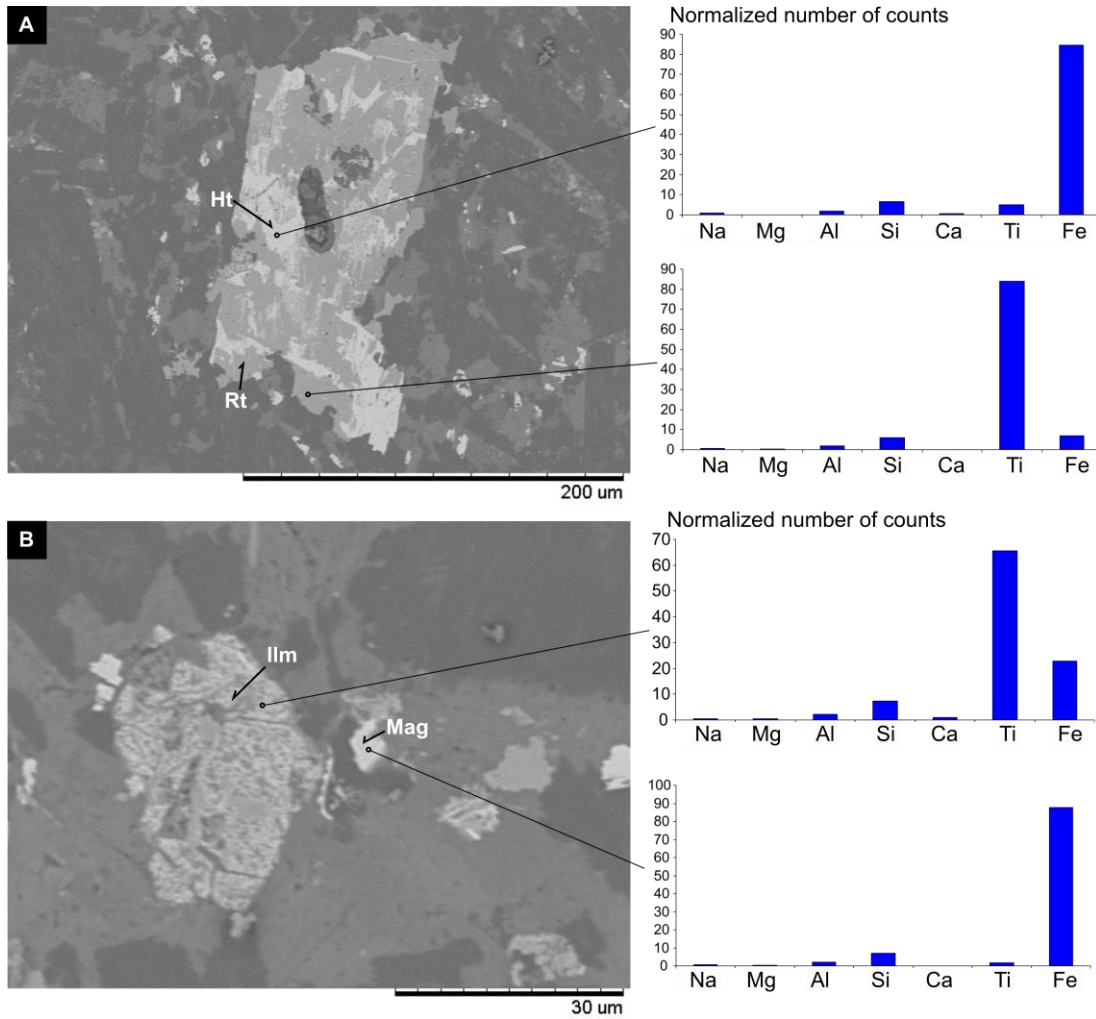


Figure A3-35. SEM micrographs and EDS results of sample DDP16. Mag – magnetite; Ilm – Ilmenite; Ht – Hematite.

Sample DDP20

Petrography

In hand sample the DDP20 has an aphanitic texture, white color, and some reddish brown crystals can be seen. Under the microscope (Figure A1-36) the sample has a porphyritic texture, with a matrix composed of plagioclase and quartz, in equal proportions. The phenocrysts correspond to euhedral plagioclase and opaque replaced ferromagnesian silicate minerals.

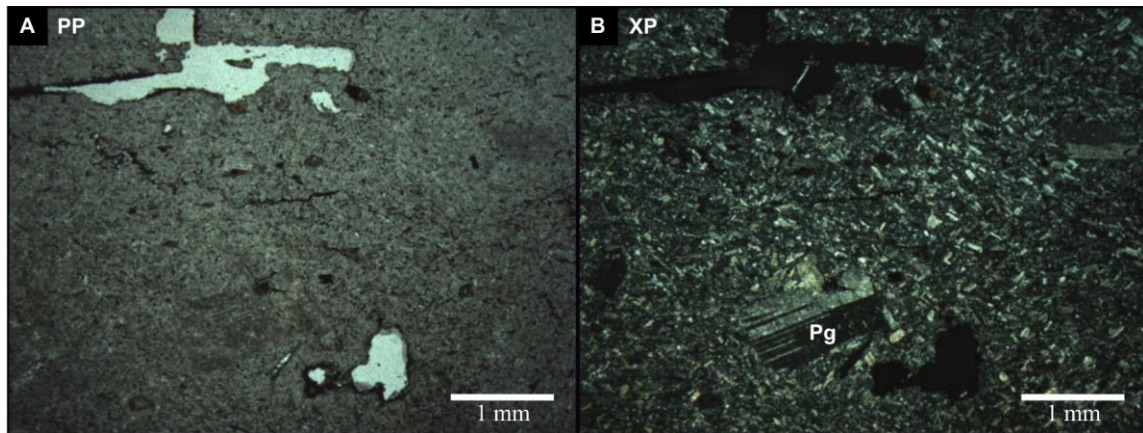


Figure A1-36. Plane (A) and polarized (B) light micrographs of sample DDP20. Pg – Plagioclase. The matrix contains equal quantity of plagioclase and quartz.

Reflected petrography

This sample has three magnetic phases. The first, and primary in origin, is magnetite; it is present as subhedral to euhedral crystals disseminated throughout the sample (Figure A1-37 A). Some of these crystals develop lamellae rutile inclusions (Figure A1-37 B). A particular type of occurrence of magnetite and hematite are inside and bordering ferromagnesian crystals (Figure A1-37 C, D). In this mode of occurrence the subhedral elongated crystals both of magnetite (whitish grey) and hematite (bluish grey) are disposed primarily bordering and sometimes in the inside of the crystals. According to Watkins & Haggerty (1967) this sample has an oxidation state IV.

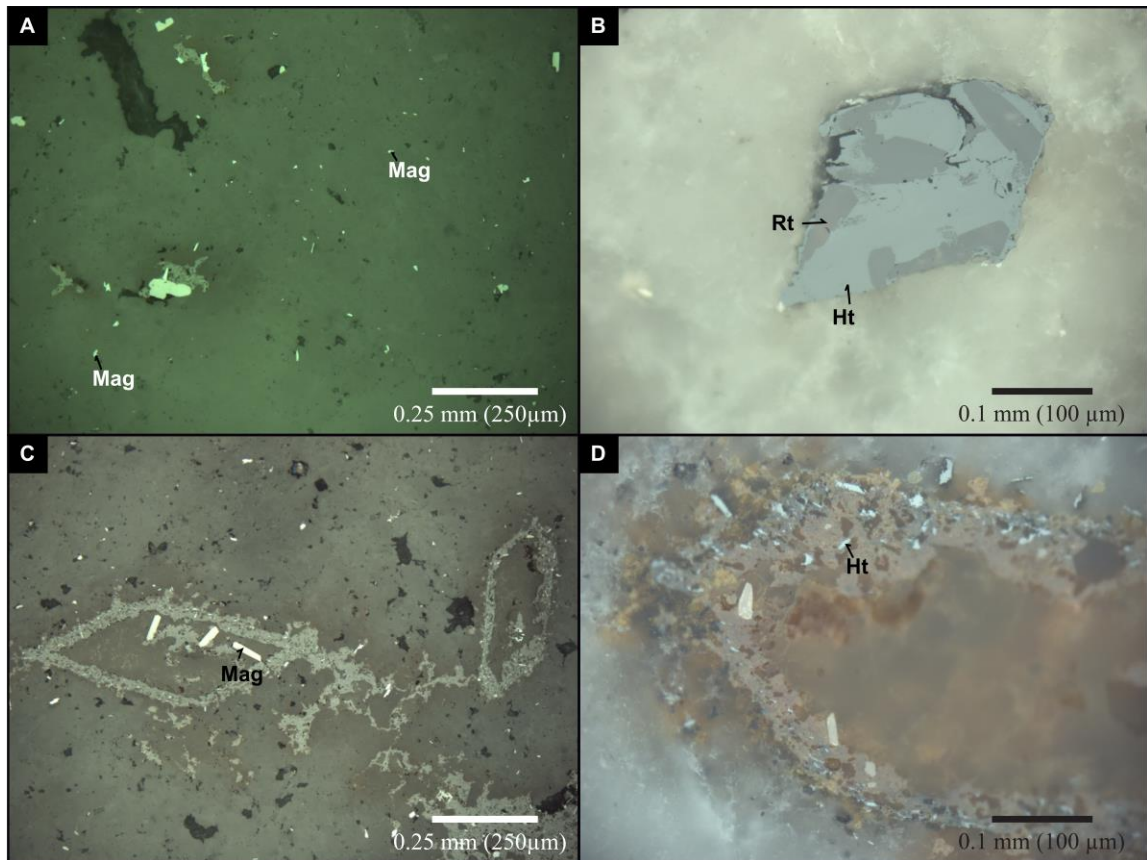


Figure A1-37. Reflected light micrographs of sample DDP20. Mag – Magnetite; Ht – Hematite; Rt - Rutile. The magnetite crystals are elongated, different from the other samples of other localities.

SEM

This sample has magnetite, hematite and rutile. The large euhedral crystal is made of titanohematite with some rutile inclusions (Figure A1-38). The finer crystals could correspond to hematite and magnetite. Some replaced ferromagnesian crystals develop a magnetite coating with dispersed titanohematite and titanomagnetite along the borders and inside the crystals.

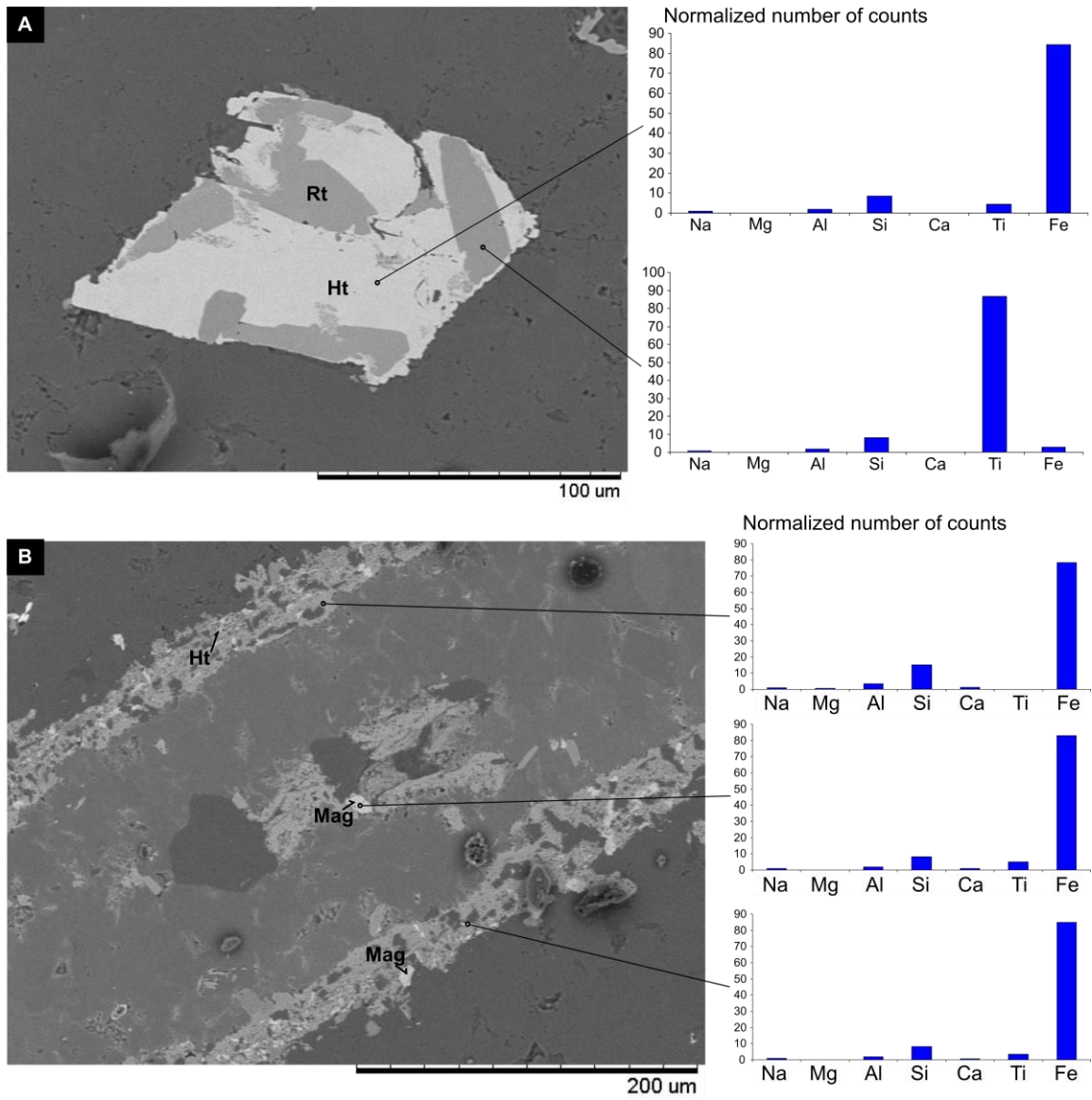


Figure A1-35. SEM micrographs and EDS results of sample DDP20. Mag – Magnetite; Ht – Hematite; Rt – Rutile.

Appendix 2

Isothermal remanent magnetism (IRM) modeling

Site DDP01 was modeled with three components, from these the low coercivity component (63.1 mT) contribute with 47.7%, suggesting magnetite presence (Figure A3-1 C). Components with High (>100 mT) and very high (>300 mT) coercivities are present in proportions of 10.8% and 41.5% respectively. This suggests that hematite is an important ferromagnetic phase in the sample (Figure A2-1 C); the interpreted S-ratio (0.433) also helps this inference. This S-ratio is calculated by the classical formula $-IRM_{0.3T}/IRM_{1T}$, if no magnetic interaction occurs and the hysteresis loop is closed from 300 mT on, then the S-ratio correspond to $2*(IRM_{+0.3T}/IRM_{1T}) - 1$ (Kruiver *et al.*, 2001).

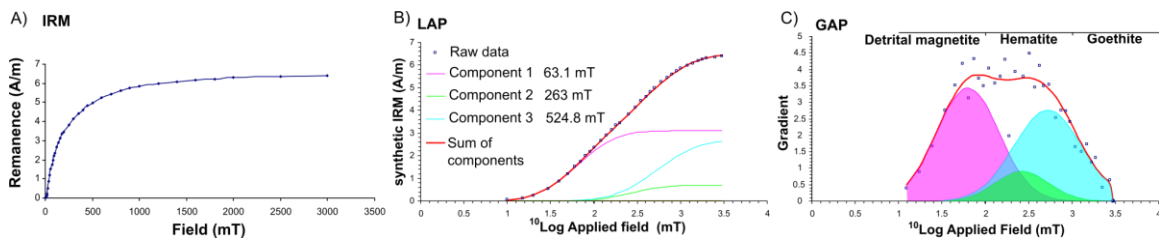


Figure A2-1. Isothermal remanent magnetization (IRM) acquisition curve and modeled results using linear acquisition plot (LAP) and gradient acquisition plot (GAP) after Kruiver *et al.* (2001) for site DDP01. Blue squares represent raw data, purple, green, and blue lines and polygons represent the different interpreted components. $B_{1/2}$ values are indicated in the LAP diagram for each component. Interpreted magnetic minerals in GAP after Abrajevich *et al.* (2009).

DDP02

Site DDP02 was modeled with a single low coercivity component (51.3 mT) (Figure A2-2), this suggest that magnetite is the only magnetic carrier in site DDP02.

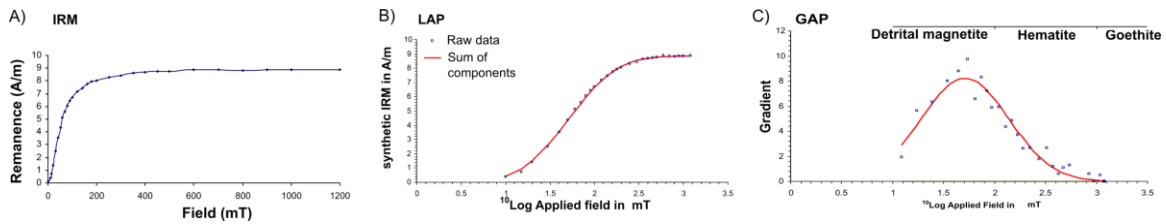


Figure A2-2. Isothermal remanent magnetization (IRM) acquisition curve and modelled results using linear acquisition plot (LAP) and gradient acquisition plot (GAP) after Kruiver *et al.* (2001) for site DDP02. Blue squares represent raw data. Interpreted magnetic minerals in GAP after Abrajevich *et al.* (2009).

DDP03

Site DDP03 was modeled with two components, from these the low coercivity component (50.1 mT) contribute with 67.7%, suggesting important magnetite presence (Figure A2-3). The second component has high coercivity (131.8 mT) and contributes in 32.3% to the total. This last component would suggest hematite presence; nevertheless, the obtained high S-ratio (0.945) alludes to a single magnetitic composition.

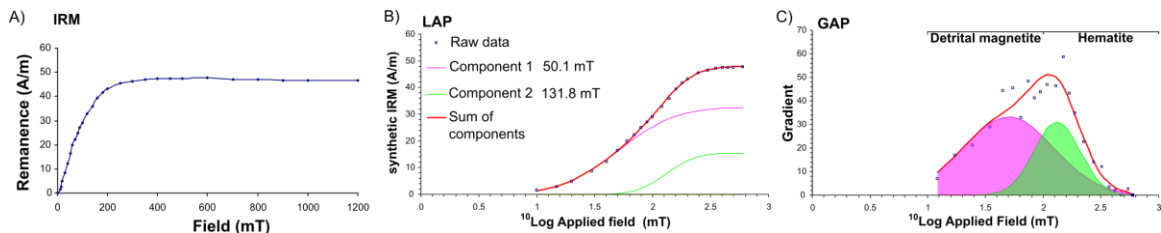


Figure A2-3. Isothermal remanent magnetization (IRM) acquisition curve and modelled results using linear acquisition plot (LAP) and gradient acquisition plot (GAP) after Kruiver *et al.* (2001) for site DDP03.

DDP05

Site DDP05 was modeled with two components, from these the low coercivity component (70.8 mT) contribute with 33.1%, suggesting magnetite presence (Figure A2-

4). The second component has high coercivity (112.2 mT) and contributes with 66.9% to the total. This last component would suggest hematite presence; nevertheless, the obtained high S-ratio (0.960) alludes to a single magnetitic composition.

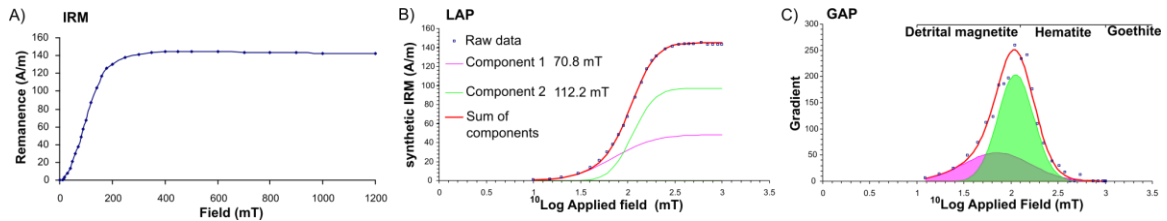


Figure A2-4. Isothermal remanent magnetization (IRM) acquisition curve and modelled results using linear acquisition plot (LAP) and gradient acquisition plot (GAP) after Kruiver *et al.* (2001) for site DDP05.

DDP06

Site DDP06 was modeled with two components, from these the low coercivity component (31.6 mT) contribute with 21.3% suggesting magnetite presence (Figure A2-5). The second component has high coercivity (134.9 mT) and contributes with 78.7% to the total. The high coercivity component suggests hematite presence; nevertheless, the obtained high S-ratio (0.921) alludes to a single magnetitic composition.

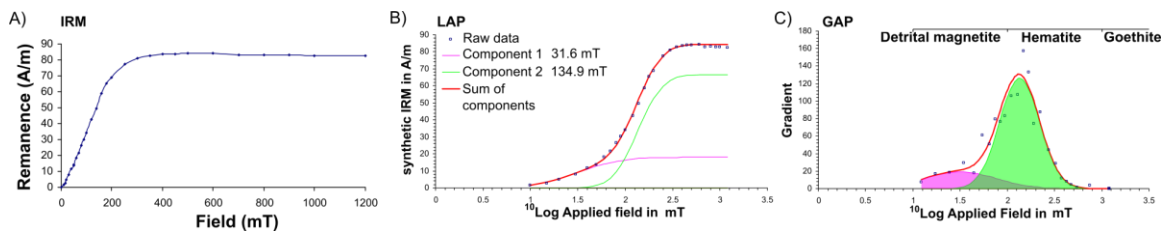


Figure A2-5. Isothermal remanent magnetization (IRM) acquisition curve and modelled results using linear acquisition plot (LAP) and gradient acquisition plot (GAP) after Kruiver *et al.* (2001) for site DDP06.

DDP07

Site DDP07 was modeled with two components, from these the low coercivity component (57.5 mT) contributes with 38.6% to the IRM suggesting magnetite presence (Figure A2-6). The second component has high coercivity (104.7 mT) and contributes with 61.4% to the total. The high coercivity component suggests hematite presence; nevertheless, the obtained high S-ratio (0.98) alludes to a single magnetitic composition.

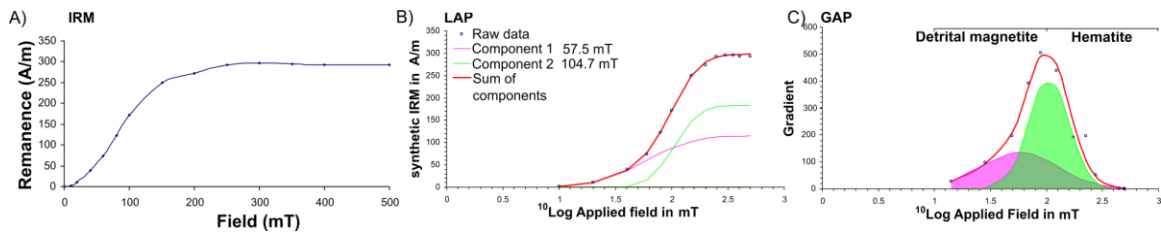


Figure A3-6. Isothermal remanent magnetization (IRM) acquisition curve and modelled results using linear acquisition plot (LAP) and gradient acquisition plot (GAP) after Kruiver *et al.* (2001) for site DDP07.

DDP08

Site DDP08 was modeled with two components both with low coercivity (31.6 mT, 79.4 mT) these components contribute with 35.2% and 64.8% respectively and suggest a magnetitic composition (Figure A2-7); this magnetitic composition is supported by the calculated S-ratio (0.990).

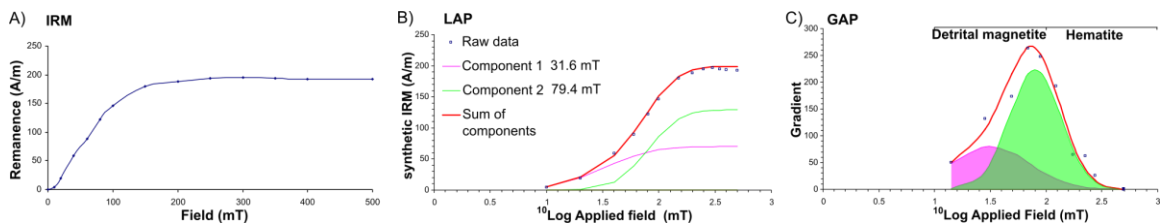


Figure A2-7. Isothermal remanent magnetization (IRM) acquisition curve and modelled results using linear acquisition plot (LAP) and gradient acquisition plot (GAP) after Kruiver *et al.* (2001) for site DDP08.

DDP09

Site DDP09 was modeled with three components; two have low coercivity (20 mT, 55 mT) and contribute in 18.6% and 70.6% respectively, this suggests that magnetite presence is important (Figure A2-8). The third component has high coercivity (199.5 mT) and contributes with 10.8% to the total, this suggests slight hematite presence.

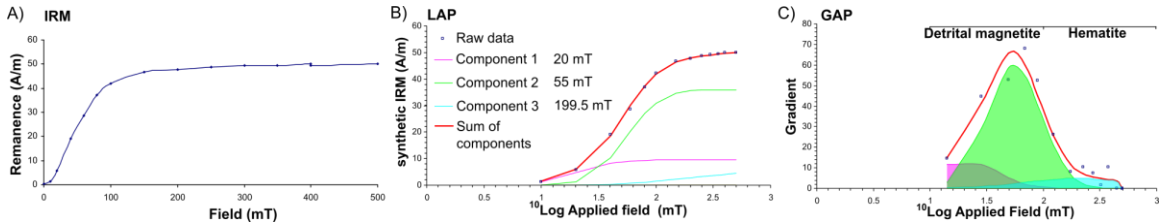


Figure A2-8. Isothermal remanent magnetization (IRM) acquisition curve and modelled results using linear acquisition plot (LAP) and gradient acquisition plot (GAP) after Kruiver *et al.* (2001) for site DDP09.

DDP11

Site DDP11 was modeled with four components; two have low coercivity (23.4 mT, 66.1 mT) and contribute with 12.3% and 50.4% respectively, this suggests magnetite presence (Figure A2-9). The third and fourth components have very high coercivity (323.6 mT, 1349 mT) and contribute with 35.3% and 2% to the total; this suggests important hematite presence, supported by an S-ratio of 0.604.

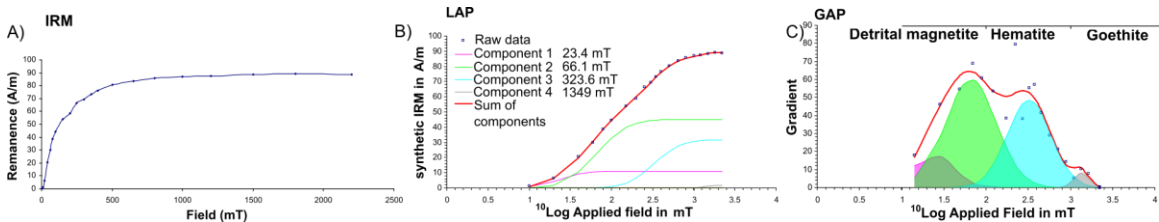


Figure A2-9. Isothermal remanent magnetization (IRM) acquisition curve and modelled results using linear acquisition plot (LAP) and gradient acquisition plot (GAP) after Kruiver *et al.* (2001) for site DDP11.

DDP12

Site DDP12 was modeled with four components; two have low coercivity (31.6 mT, 89.1 mT) and contribute with 14.2% and 28.9% respectively, this suggests magnetite presence (Figure A2-10). The third and fourth components have very high coercivity (371.5 mT, 1000 mT) and contribute with 42.7% and 14.2% to the total; this suggests important hematite presence, supported by an S-ratio of 0.221. The sample may contain some goethite.

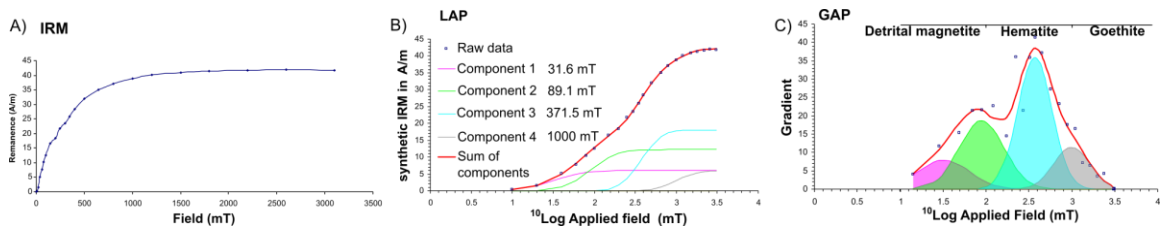


Figure A2-10. Isothermal remanent magnetization (IRM) acquisition curve and modelled results using linear acquisition plot (LAP) and gradient acquisition plot (GAP) after Kruiver *et al.* (2001) for site DDP12.

DDP13

Site DDP13 was modeled with three components; two have low coercivity (25.1 mT, 66.1 mT) and contribute in 9.3% and 84.9% respectively, this suggests that magnetite is the dominant magnetic mineral (Figure A2-11). The third component has very high coercivity (398.1 mT) and contributes with 5.8% to the total, this suggests slight to negligible hematite presence.

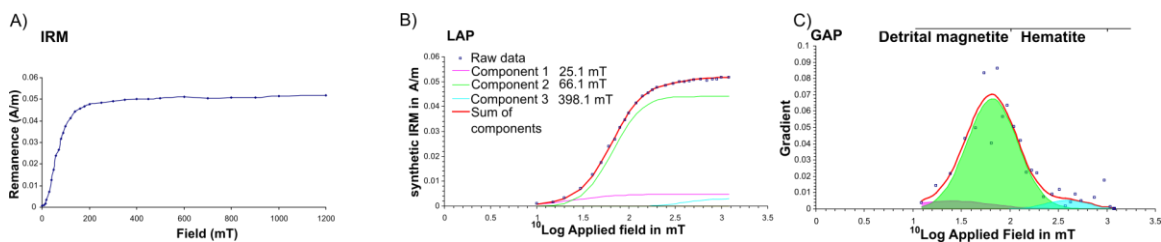


Figure A2-11. Isothermal remanent magnetization (IRM) acquisition curve and modelled results using linear acquisition plot (LAP) and gradient acquisition plot (GAP) after Kruiver *et al.* (2001) for site DDP13.

DDP14

Site DDP14 was modeled with three components; the first with low coercivity (72.4 mT) contribute in 61%, this suggests that magnetite is the most important magnetic mineral (Figure A2-12). The second and third components have very high coercivity (354.8 mT, 1258.9) and contribute with 28.2% and 10.8% to the total; this suggests important hematite presence, supported by the S-ratios of 0.403.

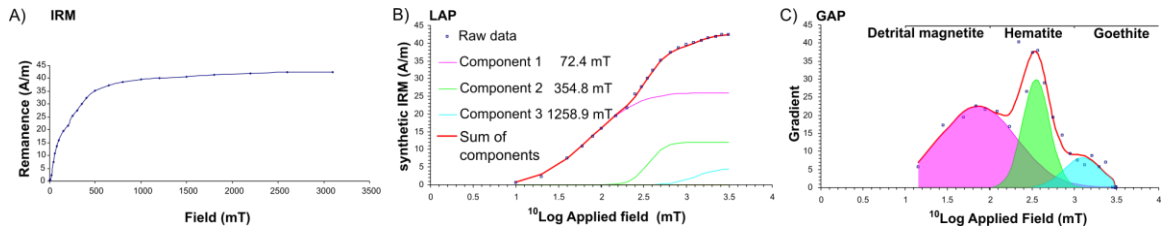


Figure A2-12. Isothermal remanent magnetization (IRM) acquisition curve and modelled results using linear acquisition plot (LAP) and gradient acquisition plot (GAP) after Kruiver *et al.* (2001) for site DDP14.

DDP15

Site DDP15 was modeled with two components, from these the low coercivity component (97.7 mT) contribute with 43.9%, suggesting important magnetite presence (Figure A2-13). The second component has high coercivity (125.9 mT) and contributes in 56.1% to the total. This last component would suggest hematite presence supported at some degree by the obtained S-ratio (0.899).

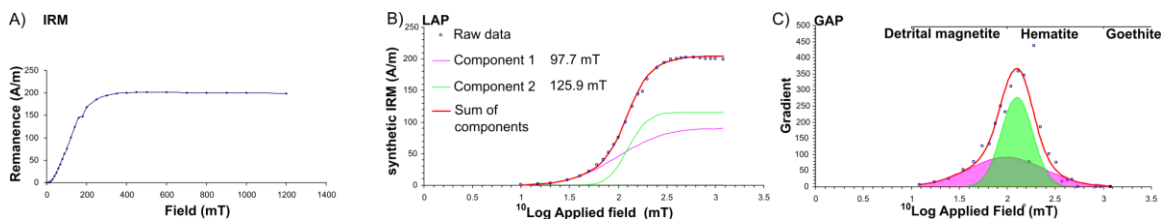


Figure A2-13. Isothermal remanent magnetization (IRM) acquisition curve and modelled results using linear acquisition plot (LAP) and gradient acquisition plot (GAP) after Kruiver *et al.* (2001) for site DDP15.

DDP16

Site DDP16 was modeled with three components; from these the two with low coercivity (46.8 mT, 79.4) contribute in 8% and 6.6%, this suggest that magnetite presence is negligible (Figure A2-14). The third component has very high coercivity (631 mT) and contributes with 85.4% to the total; this suggests important hematite presence.

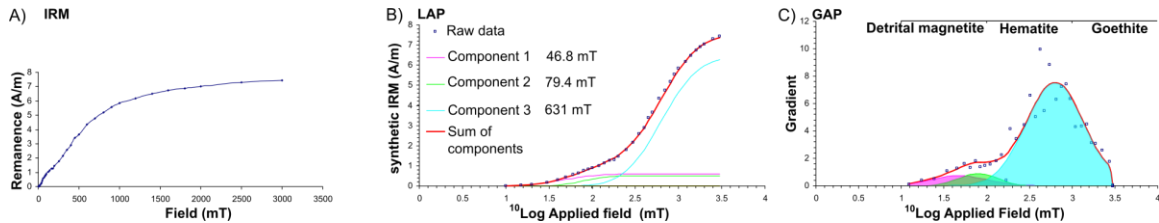


Figure A2-14. Isothermal remanent magnetization (IRM) acquisition curve and modelled results using linear acquisition plot (LAP) and gradient acquisition plot (GAP) after Kruiver *et al.* (2001) for site DDP16.

DDP18

Site DDP18 was modeled with four components; two have low coercivity (46.8 mT, 93.3 mT) and contribute with 16.5% and 34.6% respectively, this suggests magnetite presence (Figure A2-15). The third and fourth components have very high coercivity (380.2 mT, 1412 mT) and contribute with 34.6% and 14.2% to the total; this suggests important hematite presence, supported by an S-ratio of 0.39. The sample can contain some goethite.

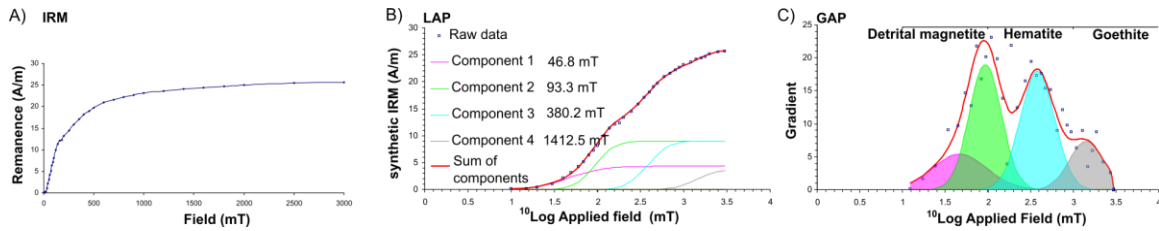


Figure A2-15. Isothermal remanent magnetization (IRM) acquisition curve and modelled results using linear acquisition plot (LAP) and gradient acquisition plot (GAP) after Kruiver *et al.* (2001) for site DDP18.

DDP19

Site DDP19 was modeled with three components; from these the low coercivity component (55 mT) contributes in 84.7%, this suggests that magnetite presence is important (Figure A2-16). The second and third components have very high coercivity (380.2 mT, 1122 mT) and contribute with 5.8% and 9.5% to the total; this suggests slight hematite presence, supported by the S-ratio 0.826.

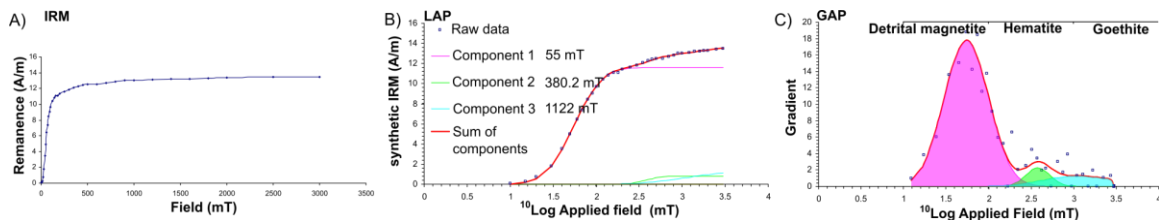


Figure A2-16. Isothermal remanent magnetization (IRM) acquisition curve and modelled results using linear acquisition plot (LAP) and gradient acquisition plot (GAP) after Kruiver *et al.* (2001) for site DDP19.

DDP20

Site DDP20 was modeled with four components; from these the low coercivity component (31.6 mT) contributes with 25.5%, this suggests magnetite presence (Figure A2-17). The second component has high coercivity (125.9 mT) and contributes with 37.5% to the total. The third and fourth components have very high (416 mT, 1778 mT)

coercivities, which suggest important hematite presence that supported by an S-ratio of 0.522. The sample can contain some goethite.

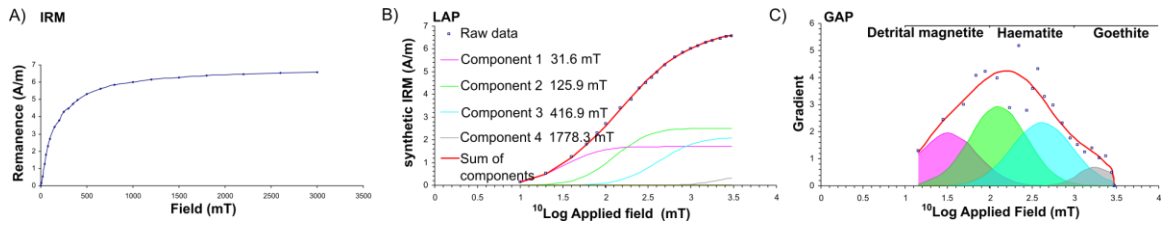


Figure A2-17. Isothermal remanent magnetization (IRM) acquisition curve and modelled results using linear acquisition plot (LAP) and gradient acquisition plot (GAP) after Kruiver *et al.* (2001) for site DDP20.

Appendix 3

Demagnetization results

DDP01

After applying alternating field demagnetization (AFD from 5mT - 40 mT) followed by thermal demagnetization (THD) (100°C - 625°C), samples of DDP01 locality present two-component demagnetization diagrams (Figure A3-1 A,B). The "soft" or A component is clearly traceable from AF's of 5mT up to 40mT, and is still present until laboratory temperatures of 400°C when it is totally removed; at this point the remanence intensity has dropped to a 40% of its initial value (Figure A3-1 C). Component A of DDP01 points towards the N-NW with moderate positive inclinations (Figure A3-1 D; *in situ* site mean Dec: 343.7°; Inc: 31°; α_{95} : 7.3°; k: 111.02 n=5; this direction was calculated using PCA without including the origin giving MAD results from 2.4 to 10). The "hard" or B component is traceable from temperatures of 400°C up to 550°C (Figure A3-1 A-B), in this temperature range the B component is directed towards the origin of the Zijderveld diagram, and at the highest temperatures (550°C-625°C) the intensity of magnetization is less than 10% of its initial values; for these reasons the B component is interpreted as the characteristic remanent magnetization (ChRM). The B component aims towards the N-NW with steep negative inclinations (Figure A3-1 D; *in situ* site mean Dec: 315; Inc: -60.6; α_{95} : 19.9°; k: 12.3, n= 6; this direction was calculated using PCA without including the origin giving MAD results from 3.3 to 9.4).

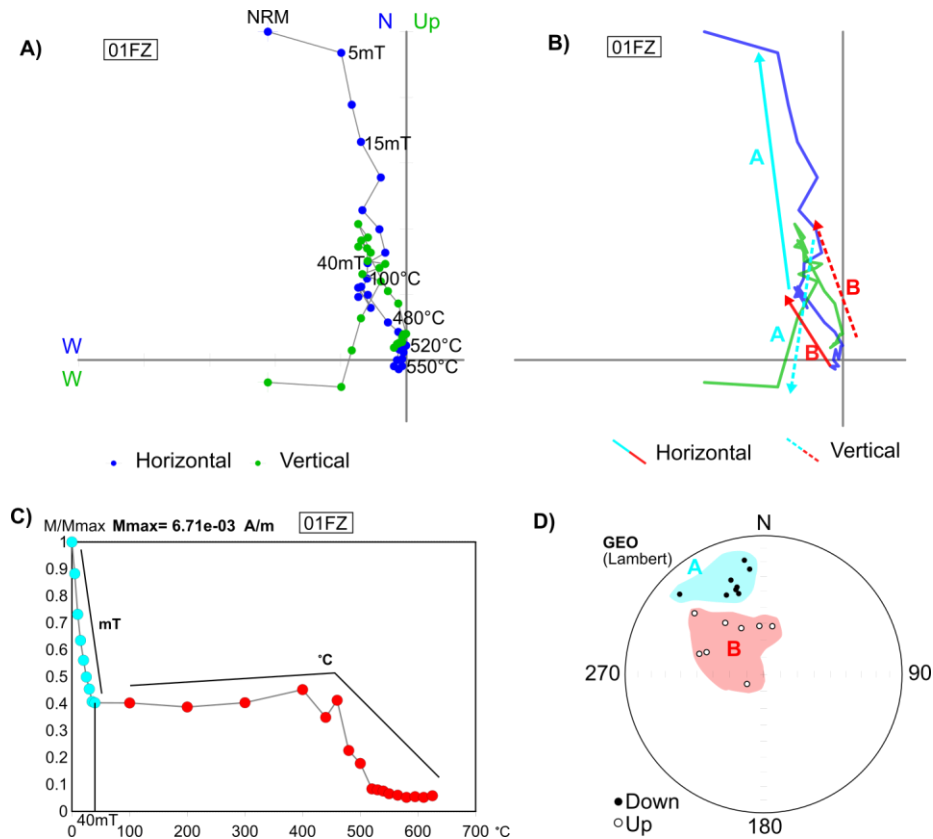


Figure A3-1. Orthogonal demagnetization diagrams, J_{max} normalized remanence intensity evolution, and component plots of site DDP01. A) Raw data; B) interpreted components; C) Intensity values resulting from combined AFD - THD; D) Equal-area stereographic plot of combined specimens.

DDP02

After applying AFD (5mT - 20 mT) followed by THD (100°C - 590°C), some samples of DDP02 locality present a two-component demagnetization diagram (Figure A3-2 A, B). The "soft" or A component is traceable from AF's of 5mT up to laboratory temperatures of 450°C; at this point the remanence intensity has dropped to a 50% of its initial value (Figure A3-2 C). Component A of DDP02 points towards the ESE with steep negative inclinations (Figure A3-2 D; *in situ* site mean Dec: 109.7°; Inc: -57.7°; α_{95} : 16.8°; k: 13.84, n=7; values calculated with PCA without including the origin giving MAD results between 2 and 6). The "hard" or B component is traceable from temperatures of 490°C up

to 590°C (Figure A3-2 A-B). The path ascribed to this component is not directed to the origin, and at the highest temperatures the intensity of magnetization is almost 15% of the initial value. The major part of DDP02 specimens do not show a B component (Figure A3-2 D) showing only paths interpreted as A components reaching the origin at temperatures of 300°C. The B component aims towards the NE-ESE with positive and negative inclinations (Figure A3-2 D; *in situsite* mean Dec: 78.3°; Inc: 20.6°; α_{95} : 54.4°; k: 6.21, n=3, values calculated with PCA without including the origin giving MAD results between 4 and 11).

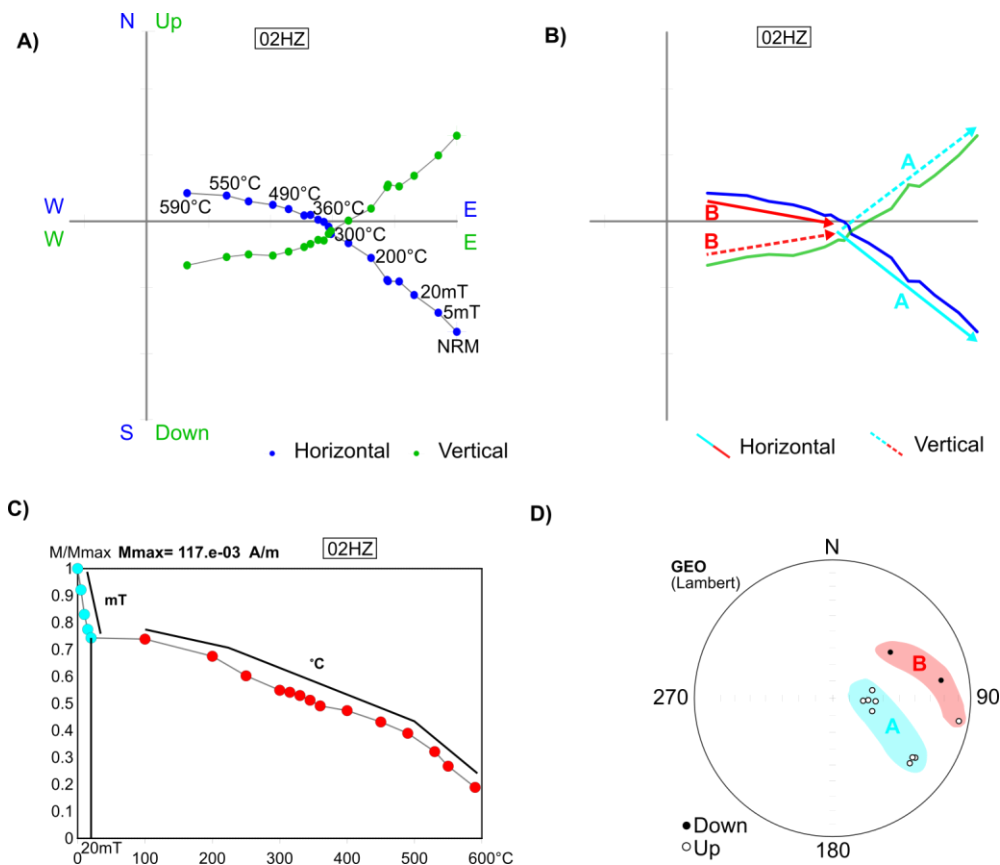


Figure A3-2. Orthogonal demagnetization diagrams, J_{max} normalized remanence intensity evolution, and component plots of site DDP02. A) Raw data; B) interpreted components; C) Intensity values resulting from combined AFD - THD; D) Equal-area stereographic plot of combined specimens.

DDP03

After applying AFDs (3mT - 90 mT), THDs (90°C - 570°C), and combined AFD – THD (5 mT – 90 mT; 100°C – 300°C), some samples of DDP03 locality present a two-component demagnetization diagram (Figure A3-3 A, B). The "soft" or A component is traceable in Zijderveld diagrams from 5 mT to 90 mT and from laboratory temperatures of 90°C up to 350°C. At this point the remanence intensity has dropped to less than 20% of the initial value (Figure A3-3 C). Component A of DDP03 points towards N with moderate positive inclinations (Figure A3-3 D; *in situ* site mean Dec: 3°; Inc: 42°; α_{95} : 10°; k: 56.69, n= 5 ;these mean was weighted from values calculated by PCA with MAD values between 2.5 to 6.7). The "hard" or B component is traceable from alternating fields of 3 mT up to 60 mT and from temperatures 375°C up to 570°C (Figure A3-3 A-B). In this temperature range the B component directs towards the origin of the Zijderveld diagram, and after the 520°C the intensity of magnetization decreases from a stable point at 0.15 to 0. The B component aims towards the NE with positive inclinations (Figure A3-3 D; site mean Dec: 38°; Inc: 55.7°; α_{95} : 7.2°, k: 115.11, n= 5; these mean was weighted from values calculated by PCA with MAD values between 2.6 to 11.9). The B component is interpreted as a characteristic component partially overlapped with the A component of lower blocking temperatures and/or coercivities.

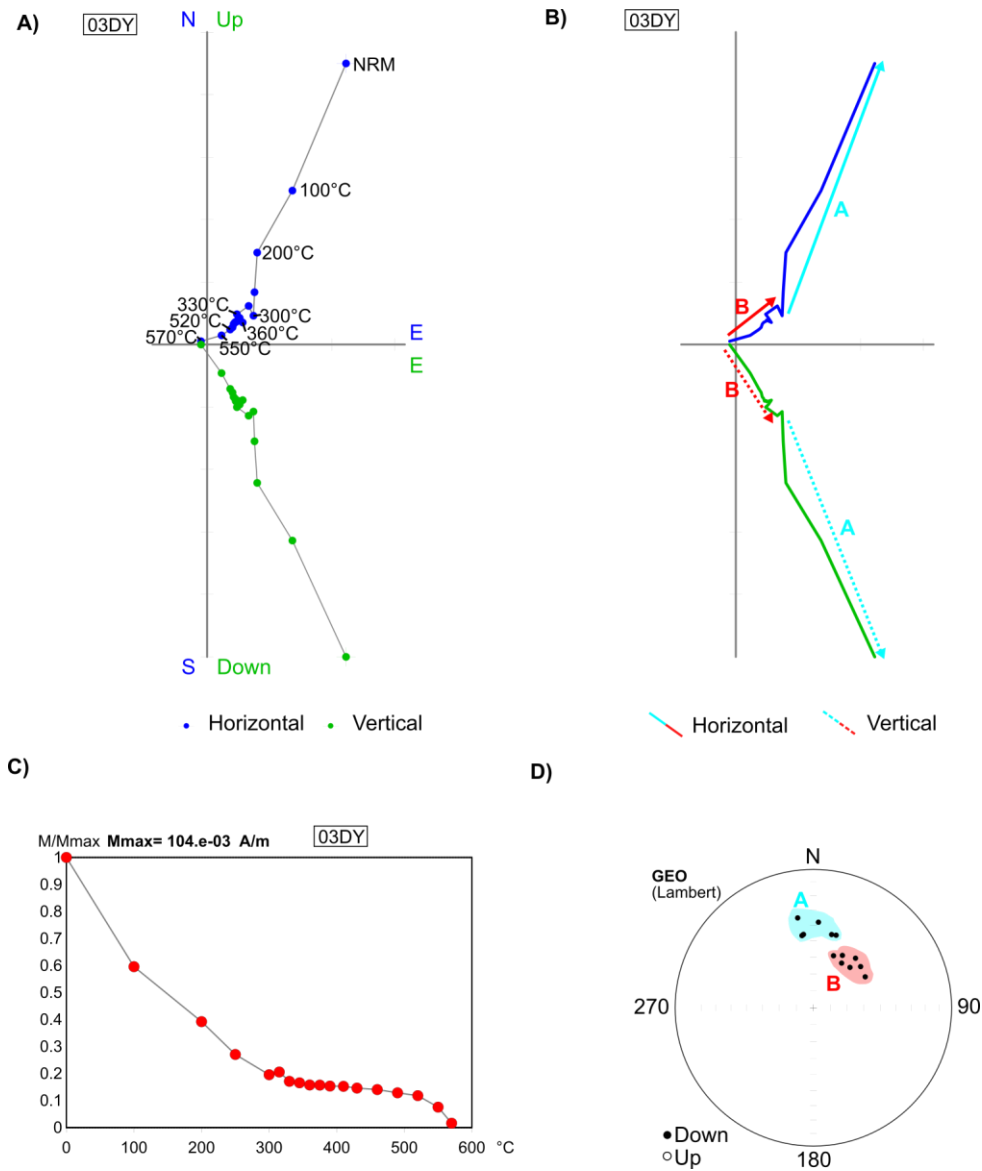


Figure A3-3. Orthogonal demagnetization diagrams, J_{max} normalized remanence intensity evolution, and component plots of site DDP03. A) Raw data; B) interpreted components; C) Intensity values resulting from THD; D) Equal-area stereographic plot of combined specimens.

DDP04

After applying AFDs (5mT - 90 mT), THDs (100°C - 490°C), and combined AFD – THD (5 mT – 90 mT; 100°C – 350°C), all the samples of locality DDP04 show

univectorial behavior (Figure A3-4 A, B). The interpreted characteristic component, B, is traceable in all the ranges of applied AF's and laboratory temperatures (Figure A3-4 A-B). The intensity of magnetization decreases to less than 20% of the initial value at AF's of 90 mT and temperatures in the range of 200°C to 350°C. The B component aims towards the N with moderate positive inclinations (Figure A3-4 D; *in situ* site mean Dec: 6.4°; Inc: 41.8°; α_{95} : 11.5°; k: 24.34, n=8 ; this direction was weighted from calculated values using PCA without including the origin giving MAD results from 1.9 to 6.3). The B component is interpreted as the ChRM.

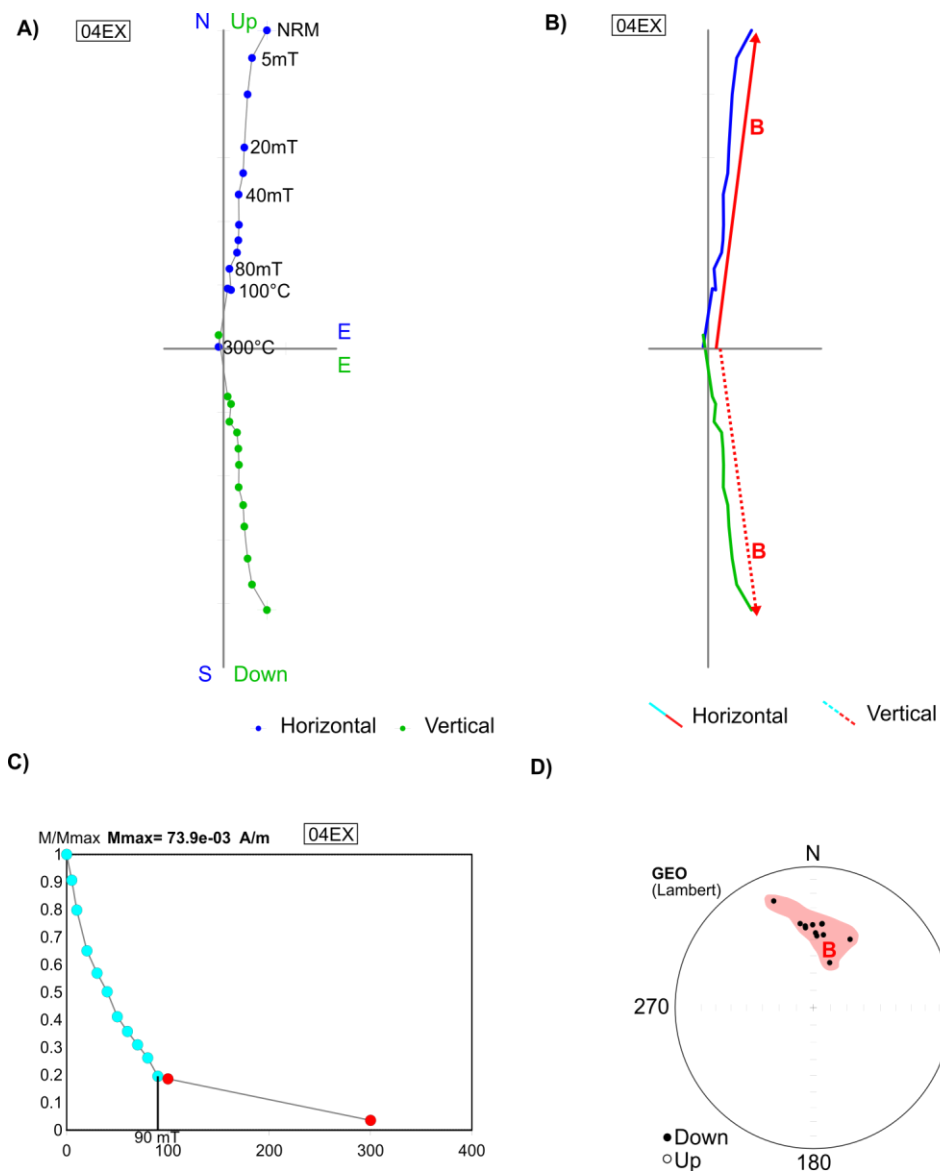


Figure A3-4. Orthogonal demagnetization diagrams, J_{max} normalized remanence intensity evolution, and component plots of site DDP04. A) Raw data; B) interpreted components; C) Intensity values resulting from combined AFD - THD; D) Equal-area stereographic plot of combined specimens.

DDP05

After applying AFD (3mT - 90 mT) and THD (100°C - 580°C), samples of locality DDP05 present a two-component demagnetization diagram (Figure A3-5 A, B). The "soft" or A component is traceable from AF's between 3mT and 45mT and from laboratory temperatures of 100°C up to 180°C. The remanence intensity decreases to an 80% of its initial value at 180°C and to a 60% at 45 mT (Figure A3-5 C). Component A of DDP05 is north directed with shallow positive and negative inclinations (Figure A3-5 D; *in situ* site mean Dec: 1.6°; Inc: 5.5°; α_{95} : 11°; k: 38.02, n=6, calculated by PCA with MAD between 2 and 8.9). The "hard" or B component is traceable from temperatures of 230°C up to 580°C (Figure A3-5 A-B); in this temperature range the B component directs towards the origin of the Zijderveld diagram. The intensity of magnetization decreases in two ways, from temperatures between 270°C and 360° the decrease rate is steep reaching values lower than the 20% of the initial value, above 360° the amount of change in intensity is less until negligible values at 560°C-570°C. The B component aims towards the SE-NW with steep negative inclinations (Figure A3-5 D; *in situ* site mean Dec: 331°; Inc: -65.9°; α_{95} : 7°; k: 118.8, n= 5; this direction was calculated using PCA without including the origin giving MAD results from 1.4 to 3).

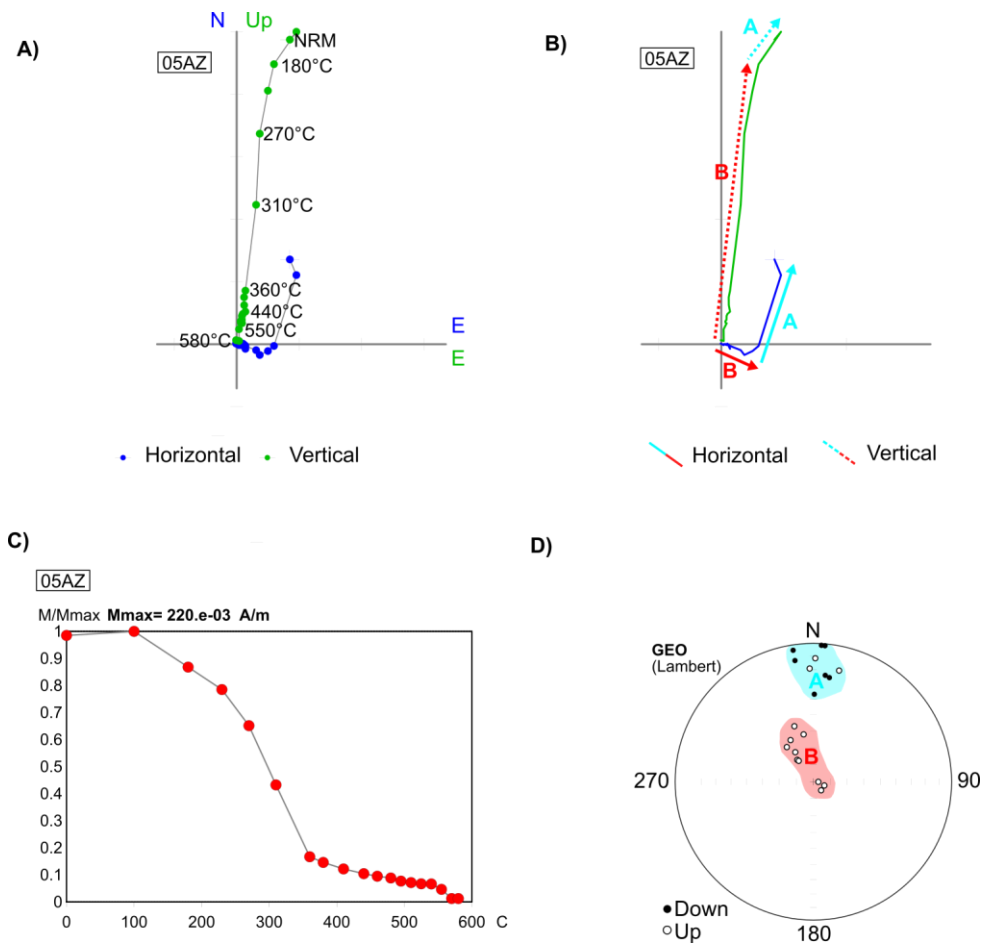


Figure A3-5. Orthogonal demagnetization diagrams, M_{max} normalized remanence intensity evolution, and component plots of site DDP05. A) Raw data; B) interpreted components; C) Intensity values resulting from THD; D) Equal-area stereographic plot of combined specimens.

DDP06

After applying THD from 100°C to 660°C, some samples of the DDP06 site show a two-component demagnetization diagram, although the majority of samples show univectorial behavior (Figure A3-6 A,B). The "soft" or A component is traceable from temperatures of 100°C up to 400°C; at this temperature the remanence intensity decreases to less than 40% of the initial value (Figure A3-6 C). Component A of DDP06 points towards N, NE and E with positive inclinations, due to the low presence of this component, a site mean

was not calculated. The "hard" or B component is traceable from temperatures of 100°C, in univectorial samples, to temperatures of 570 °C (Figure A3-6 A-B). In this temperature range the B component directs towards the origin of the Zijderveld diagram, and the intensity drops uniformly; only after the 555°C step the intensity of magnetization decreases from a stable point at 0.20 to 0 NO ENTIENDO (Figure A3-6 C). The B component aims towards the N-NE with positive inclinations (Figure A3-6 D; *in situ* site mean Dec: 15.6°; Inc: 54.1°; α_{95} : 10.8°; k: 31.9, n=7; this direction was calculated using PCA without including the origin giving MAD results from 6.7 to 11.8). The B component is interpreted as a characteristic component partially overlapped with the A component of lower blocking temperatures and/or coercivities.

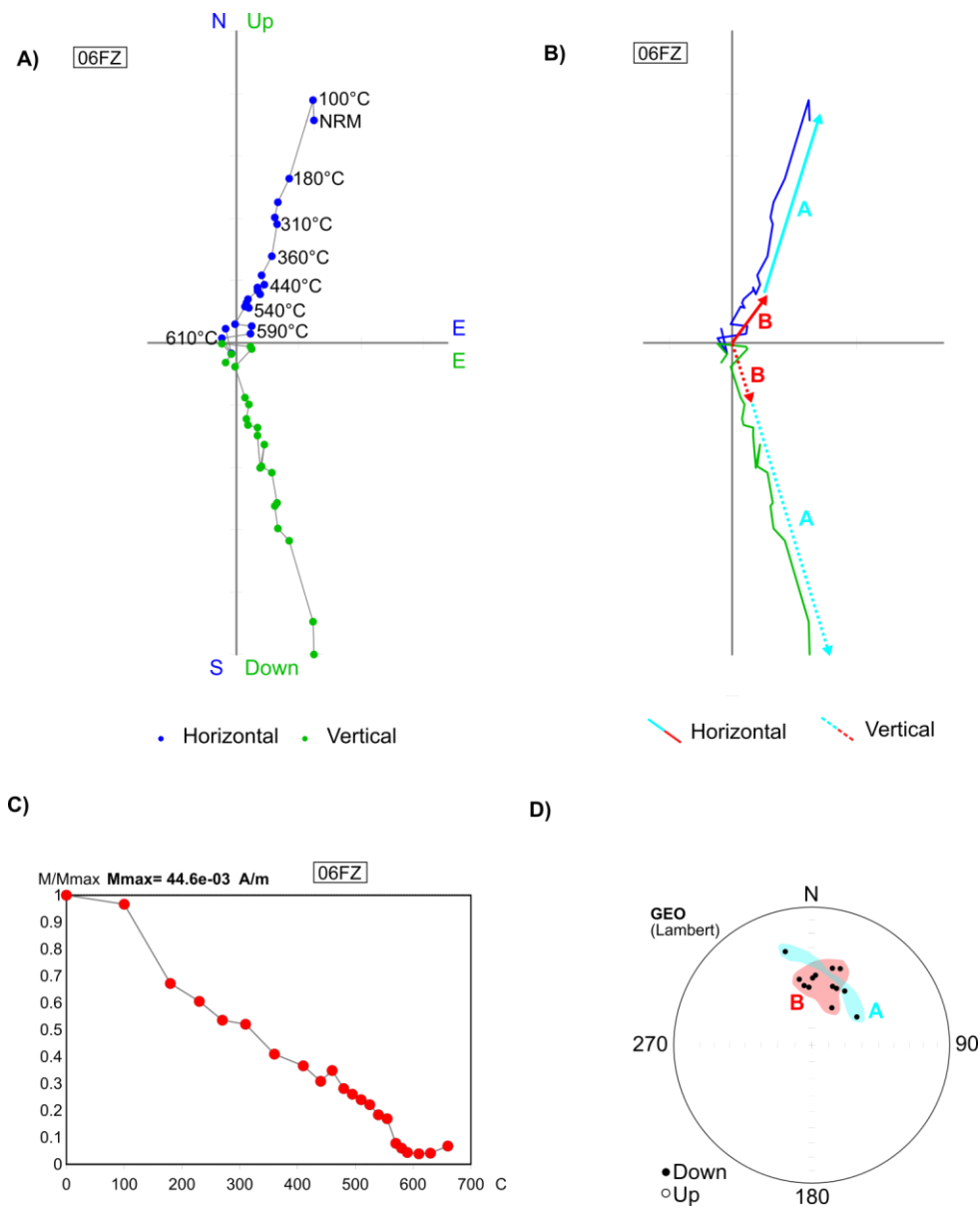


Figure A3-6. Orthogonal demagnetization diagrams, J_{max} normalized remanence intensity evolution, and component plots of site DDP06. A) Raw data; B) interpreted components; C) Intensity values resulting from THD; D) Equal-area stereographic plot of combined specimens.

DDP07

After applying THD from 90°C to 610°C, all the specimens of DDP07 locality show a two-component demagnetization diagram (Figure A3-7 A, B). The "soft" or A component is traceable from temperatures of 90°C up to 500°C, at this temperature the remanence intensity decreases to less than 20% of the initial value (Figure A3-7 C). Component A of DDP07 points towards the N-NNW with moderately steep positive inclinations (Figure A3-7; *in situ* site mean Dec: 353.2°; Inc: 51.1°; α_{95} : 5.6°; k: 97.32, n=8; this direction was calculated using PCA without including the origin giving MAD results from 2 to 8.2). The "hard" or B component is traceable from temperatures of 440°C to 610 °C (Figure A3-7 A-B); in this temperature range the B component is tracks towards the origin of the Zijderveld diagram, and the intensity of magnetization begins to decrease after 500°C (Figure A3-7 C). The B component aims towards the W with steep negative inclinations (Figure A3-7 D; *in situ* site mean Dec: 286.7°; Inc: -64.8°; α_{95} : 2.5°; k: 511.29, n=8; this direction was calculated using PCA without including the origin giving MAD results from 2.1 to 5.7). The B component is interpreted as a ChRM clearly separated from the A component of lower blocking temperatures and/or coercivities, which may represent a viscous remagnetization.

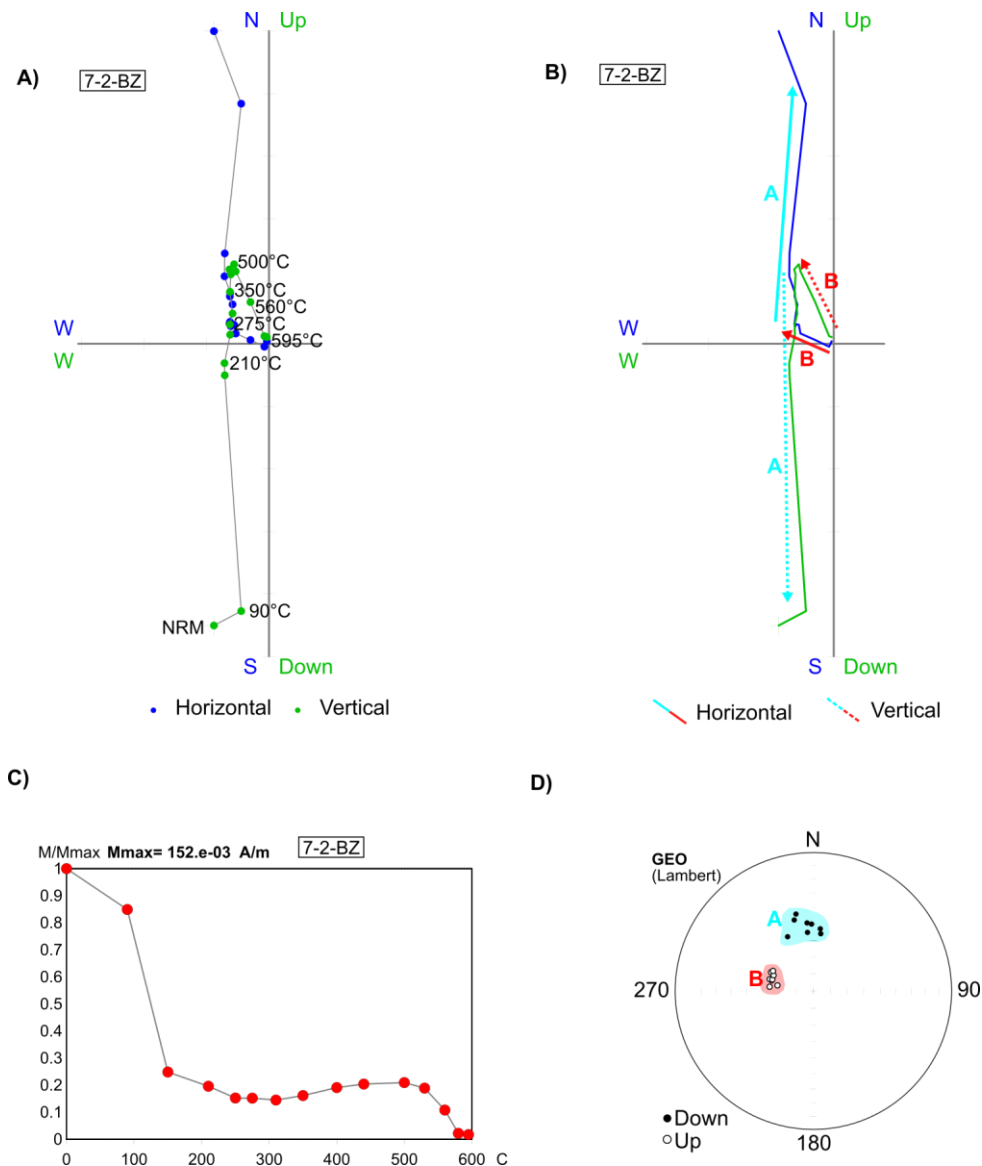


Figure A3-7. Orthogonal demagnetization diagrams, J_{max} normalized remanence intensity evolution, and component plots of site DDP07. A) Raw data; B) interpreted components; C) Intensity values resulting from THD; D) Equal-area stereographic plot of combined specimens.

DDP08

After applying THD from 90°C to 620°C, the specimens of DDP08 locality show a multicomponent demagnetization diagram (Figure A3-8 A,B); nevertheless, the majority

of samples show only two components. The "soft" A and A1 components are traceable from temperatures of 90°C up to 440°C; at this temperature the remanence intensity decreases to less than 20% of the initial value (Figure A3-8 C). A and A1 are similar in direction and will be treated as component A of DDP08, which points towards the N-NW with positive inclinations (Figure A3-8 D, *in situ* site mean Dec: 343.5°; Inc: 37.6°; α_{95} : 7.7°; k: 99.84, n=5; this direction was calculated using PCA without including the origin giving MAD results from 3.6 to 5.6). The "hard" or B component is traceable from temperatures of 440°C to 620 °C (Figure A3-8 A-B); in this temperature range the B component tracks towards the origin of the Zijdeveld diagram, and the intensity of magnetization begins to decrease after 530°C (Figure A3-8 C). The B component aims towards the W with steep negative inclinations (Figure A3-8 D; *in situ* site mean Dec: 271°; Inc: -69.5°; α_{95} : 4.9°; k: 248, n=5; this direction was calculated using PCA without including the origin giving MAD results from 2.1 to 12.1). The B component is interpreted as a ChRM clearly separated from the A component of lower blocking temperatures and/or coercivities, which may represent a viscous remagnetization.

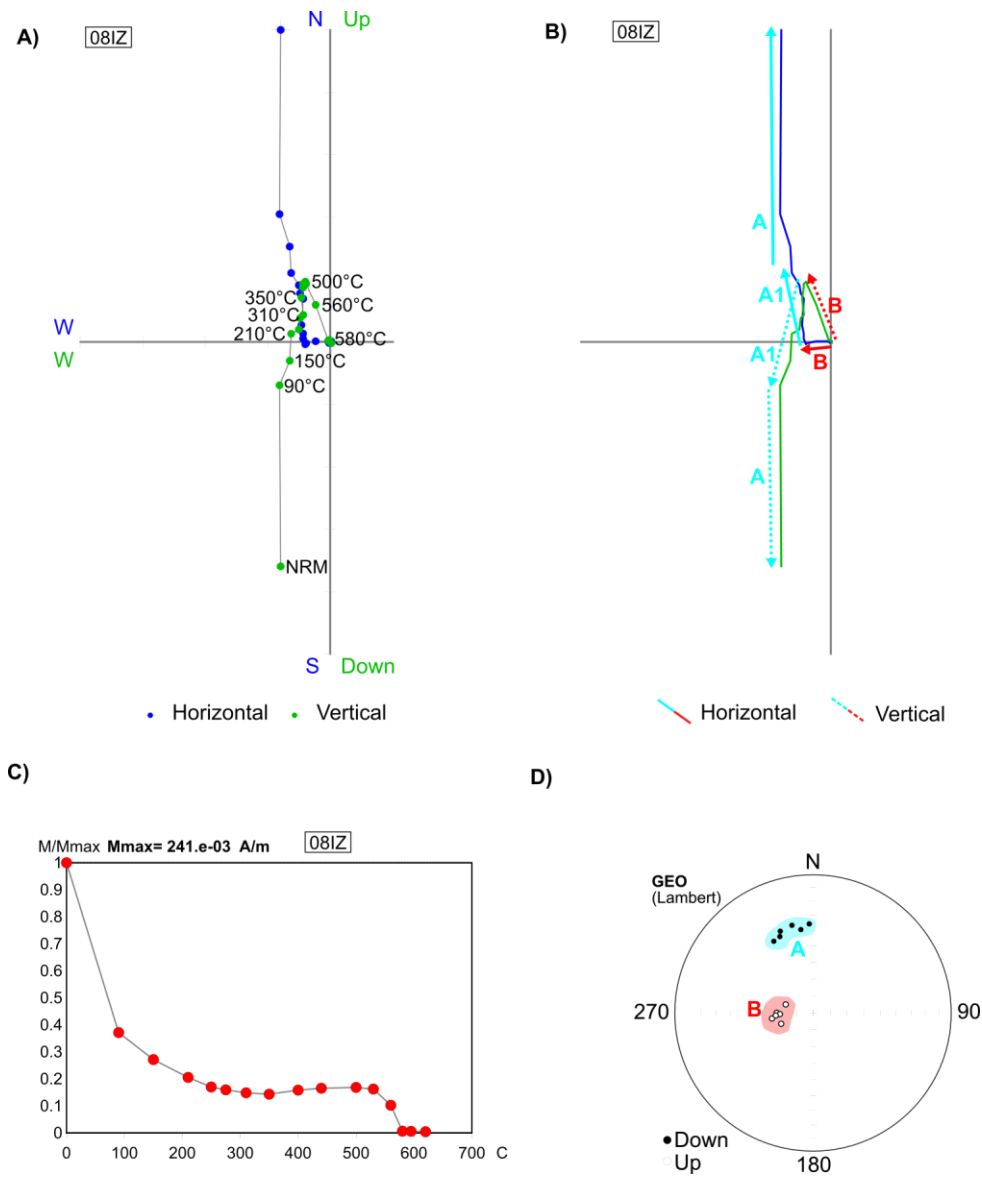


Figure A3-8. Orthogonal demagnetization diagrams, J_{max} normalized remanence intensity evolution, and component plots of site DDP08. A) Raw data; B) interpreted components; C) Intensity values resulting from THD; D) Equal-area stereographic plot of combined specimens.

DDP09

After applying AFD from 2.5 mT to 160 mT and THD from 90°C to 620°C, the specimens of DDP09 locality show a multicomponent demagnetization diagram (Figure

A3-9 A, B). The "soft" A component is traceable from alternating fields of 2.5 mT to 10 mT and from temperatures of 90°C up to 500°C; at these fields and temperatures the remanence intensity decreases to less than the 20% of the initial value (Figure A3-9 C) with a steep slope. The A component points towards the E, SE and S with positive inclinations (Figure A3-9 D; *in situ* site mean Dec: 153.7°; Inc: 67.9°; α_{95} : 12.6; k: 20.37, n=8; this direction was calculated using PCA without including the origin giving MAD results from 0.6 to 6.1). The intermediate A1 component is traceable from AF's of 15 mT to 35 mT and from temperatures of 350 °C up to 500°C, the remanence intensity experiences a subtle increase during these intervals (Figure A3-9 C). A1 component point towards the W-NW with positive inclinations (Figure A3-9 D; *in situ* site mean Dec: 284.2°; Inc: 68.1°; α_{95} : 15.6°; k: 24.88, n=5; direction calculated by PCA without including the origin, MAD: 3.9 – 8.6). The "hard" or B component is traceable from alternating fields of 40 mT to 160 mT and from temperatures of 500°C to 660 °C (Figure A3-9 A-B), in these ranges the B component directs towards the origin of the Zijderveld diagram, and the intensity of magnetization to decrease smoothly in AFD and rapidly after 530°C in THD (Figure A3-9 C). The B component aims towards the SW with negative inclinations (Figure A3-9 D; *in situ* site mean Dec: 221°; Inc: -52.1°; α_{95} : 5.2; k: 112.95, n=8; this direction was calculated using PCA without including the origin giving MAD results from 2.1 to 12). The B component is interpreted as a ChRM clearly separated from the A and A1 components that could represent Cretacic remagnetization.

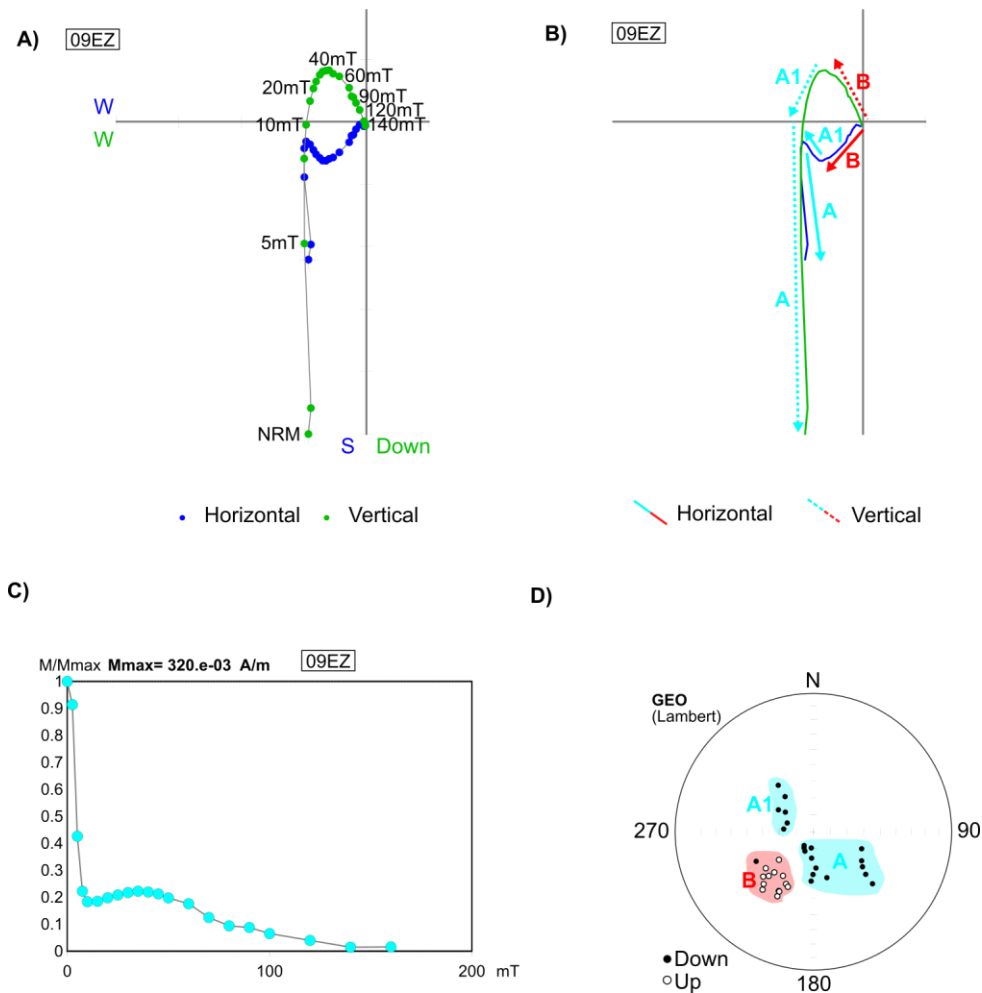


Figure A3-9. Orthogonal demagnetization diagrams, J_{max} normalized remanence intensity evolution, and component plots of site DDP09. A) Raw data; B) interpreted components; C) Intensity values resulting from AFD; D) Equal-area stereographic plot of combined specimens.

DDP11

After applying THD from 90°C to 700°C, the specimens of DDP11 locality show a two-component demagnetization diagram (Figure A3-11 A, B). The "soft" or A component is traceable from temperatures of 90°C up to 530°C, in this temperature interval the remanence intensity stays unchanged or decreases a little, to then increase slightly (Figure A3-11 C). The A component is dispersed; however, the majority of A directions

point towards the NE quadrant with positive inclinations (Figure A3-11 D; *in situ* site mean Dec: 29.7°; Inc: 57.2°; α_{95} : 10.3°; k: 22.75, n=10; this direction was calculated using PCA without including the origin giving MAD results from 3.1 to 12.1). The "hard" or B component is traceable from temperatures of 360°C to 700 °C (Figure A3-11 A-B), in these ranges the B component directs towards the origin of the Zijderveld diagram, and the intensity of magnetization decreases steeply mainly in the 530°C – 580°C temperature interval (Figure A3-11 C). The B component aims towards the W-SW with steep negative inclinations (Figure A3-11 D; *in situ* site mean Dec: 273.1°; Inc: -62.8°; α_{95} : 6.5°; k: 63.28; n=9; this direction was calculated using PCA without including the origin giving MAD results from 2.6 to 10.4). The B component is interpreted as a ChRM clearly separated from the A component.

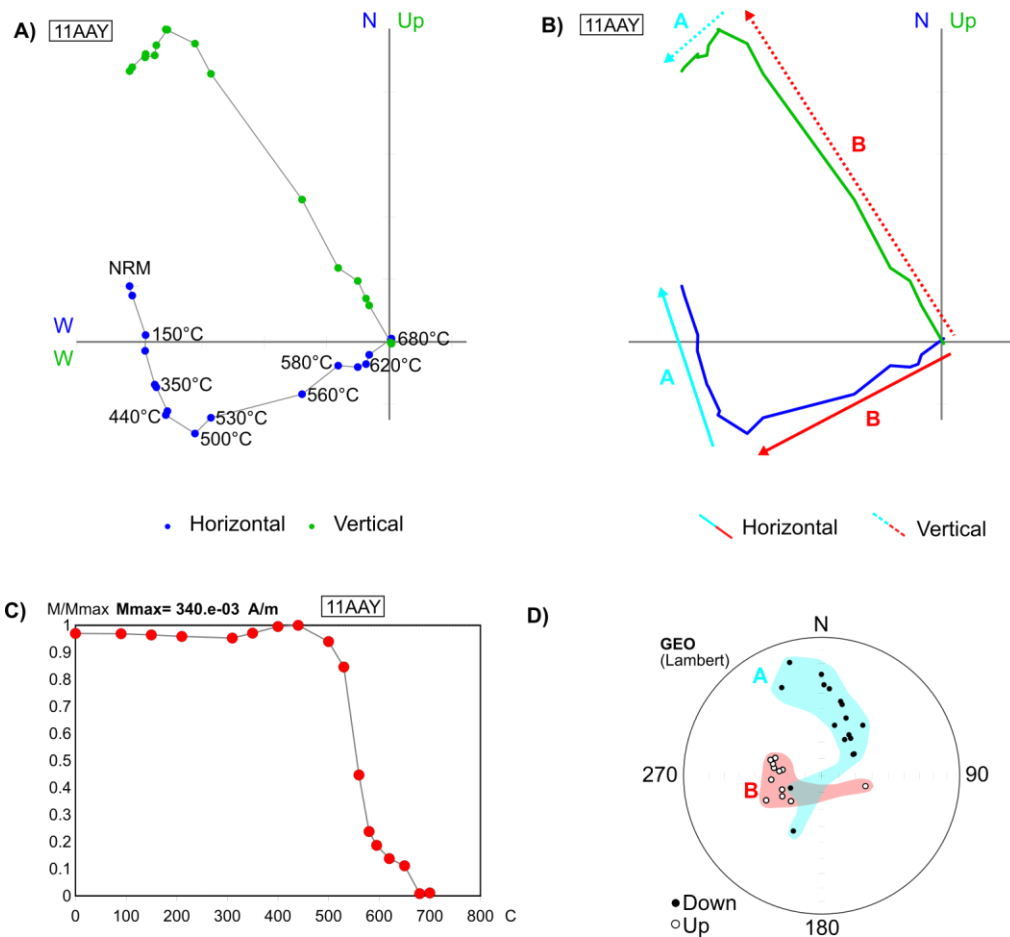


Figure A3-11. Orthogonal demagnetization diagrams, J_{max} normalized remanence intensity evolution, and component plots of site DDP011. A) Raw data; B) interpreted components; C) Intensity values resulting from THD; D) Equal-area stereographic plot of combined specimens.

DDP12

After applying THD from 90°C to 700°C, the specimens of DDP12 locality show a two-component demagnetization diagram (Figure A3-12 A, B). The "soft" or A component is traceable from temperatures of 90°C up to 530°C; in this temperature interval the remanence intensity decreases smoothly the 80% of the initial value (Figure A3-12 C). The A component points towards the NNE with moderate positive inclinations (Figure A3-12 D; *in situ* site mean Dec: 26.5°; Inc: 29.5°; α_{95} : 6.1°; k: 156.4, n=5; this direction was calculated using PCA without including the origin giving MAD results from 9.7 to 16.4). The "hard" or B component is traceable from temperatures of 400°C to 700 °C (Figure A3-12 A-B); in these ranges the B component directs towards the origin of the Zijderveld diagram, and the intensity of magnetization decreases steeply mainly in the 530°C – 580°C temperature interval (Figure A3-12 C). The B component aims towards the NW with negative inclinations (Figure A3-12 D; *in situ* site mean Dec: 320.4; Inc: -47.4; α_{95} : 11.8; k: 33.4; n=6; this direction was calculated using PCA without including the origin giving MAD results from 0.8 to 8.2). The B component is interpreted as a ChRM clearly separated from the A component.

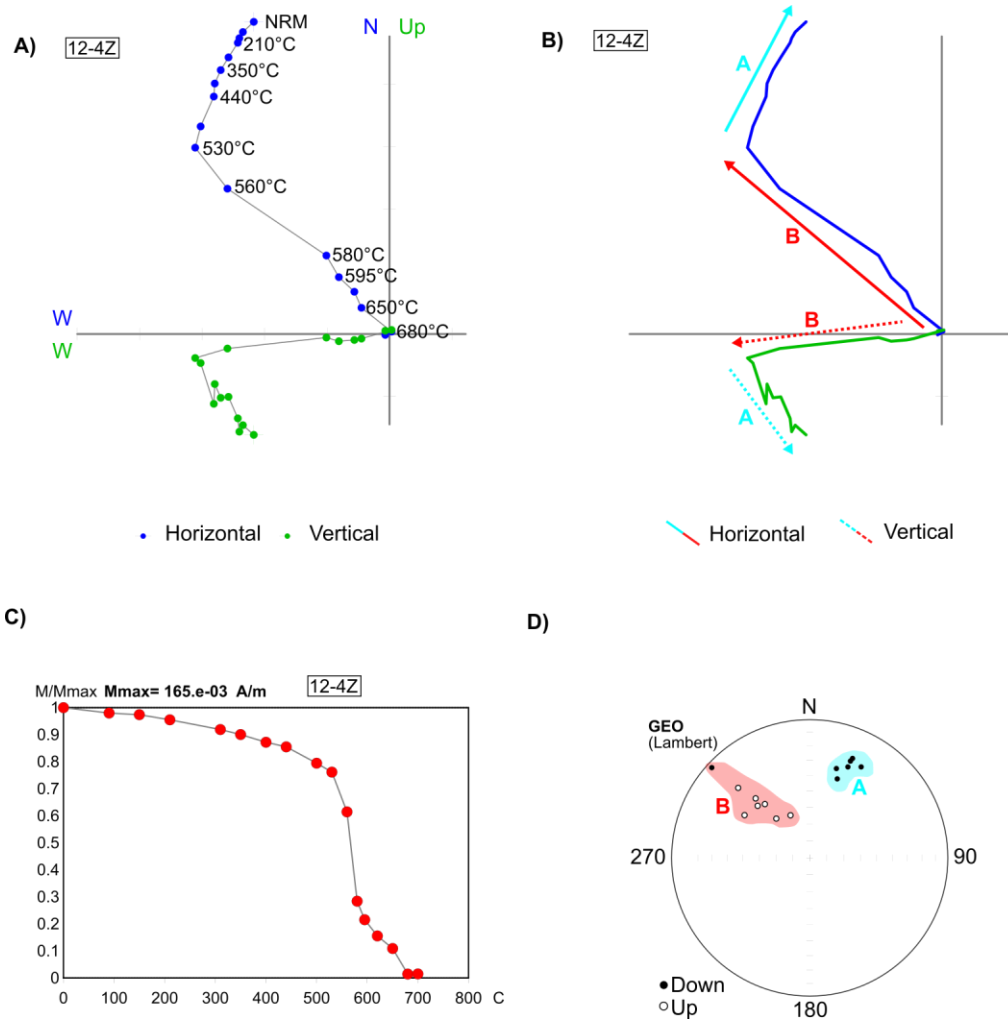


Figure A3-12. Orthogonal demagnetization diagrams, J_{max} normalized remanence intensity evolution, and component plots of site DDP012. A) Raw data; B) interpreted components; C) Intensity values resulting from THD; D) Equal-area stereographic plot of combined specimens.

DDP13

After applying AFD from 2.5 mT to 160 mT, the specimens of DDP13 locality show a two-component demagnetization diagram (Figure A3-13 A, B). The "soft" or A component is traceable from alternating fields of 2.5 mT up to 60 mT; in this interval the remanence intensity decreases steeply to 30% of the initial value (Figure A3-13 C). The

A component points towards the N-NW with positive inclinations (Figure A3-13 D; *in situ* site mean Dec: 352.1°; Inc: 42.5°; α_{95} : 8.4°; k: 38.66, n=9; this direction was calculated using PCA without including the origin giving MAD results from 1.3 to 8.1). The "hard" or B component is traceable from fields of 15 mT to 160 mT (Figure A3-13 A-B); in these ranges the demagnetization path appears to be directed to the origin without actually reaching it. The intensity of magnetization decreases smoothly to values lower than 10% of the initial (Figure A3-13 C). The B component is dispersed, and aims towards the NW - SW with positive inclinations (Figure A3-13 D; *in situ* site mean Dec: 282.1°; Inc: 56.3°; α_{95} : 20.2°; k: 11.95; n=6; this direction was calculated using PCA without including the origin giving MAD results from 5 to 14.9).

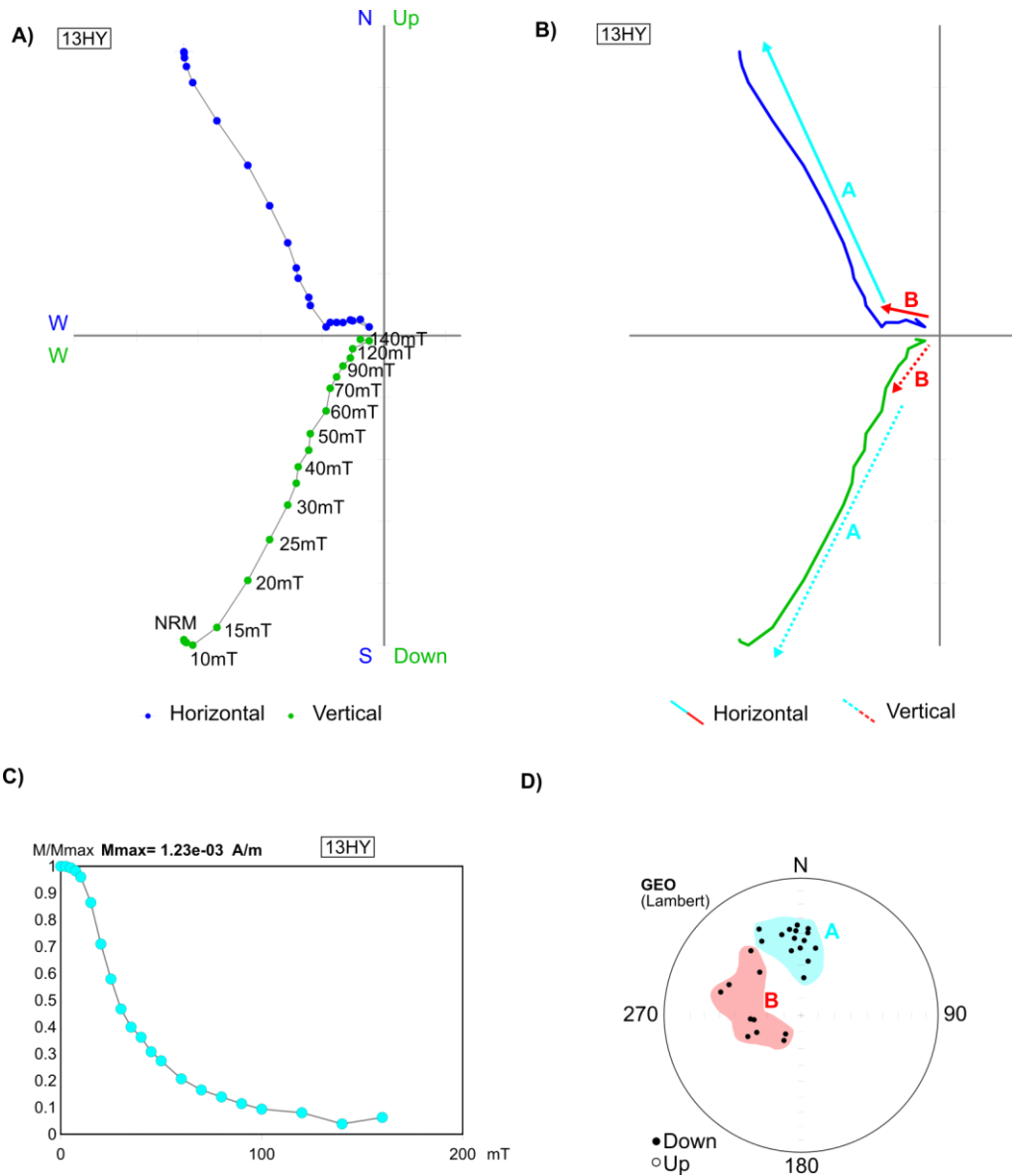


Figure A3-13. Orthogonal demagnetization diagrams, J_{max} normalized remanence intensity evolution, and component plots of site DDP013. A) Raw data; B) interpreted components; C) Intensity values resulting from AFD; D) Equal-area stereographic plot of combined specimens.

DDP14

After applying THD from 90°C to 650°C, the specimens of DDP14 locality show a univectorial behavior in the demagnetization diagram (Figure A3-14 A, B). The

component interpreted, called “B” is traceable through the whole range of applied temperatures (Figure A3-14 A-B); in this range the demagnetization path is directed to the origin. The intensity of magnetization decreases continuously (Figure A3-13 C). The B component is well grouped, and aims towards the SW with shallow positive inclinations (Figure A3-14 D; *in situ* site mean Dec: 221.9°; Inc: 6°; α_{95} : 4.4°; k: 156.63; n=8; this direction was calculated using PCA without including the origin giving MAD results from 0.9 to 3.5).

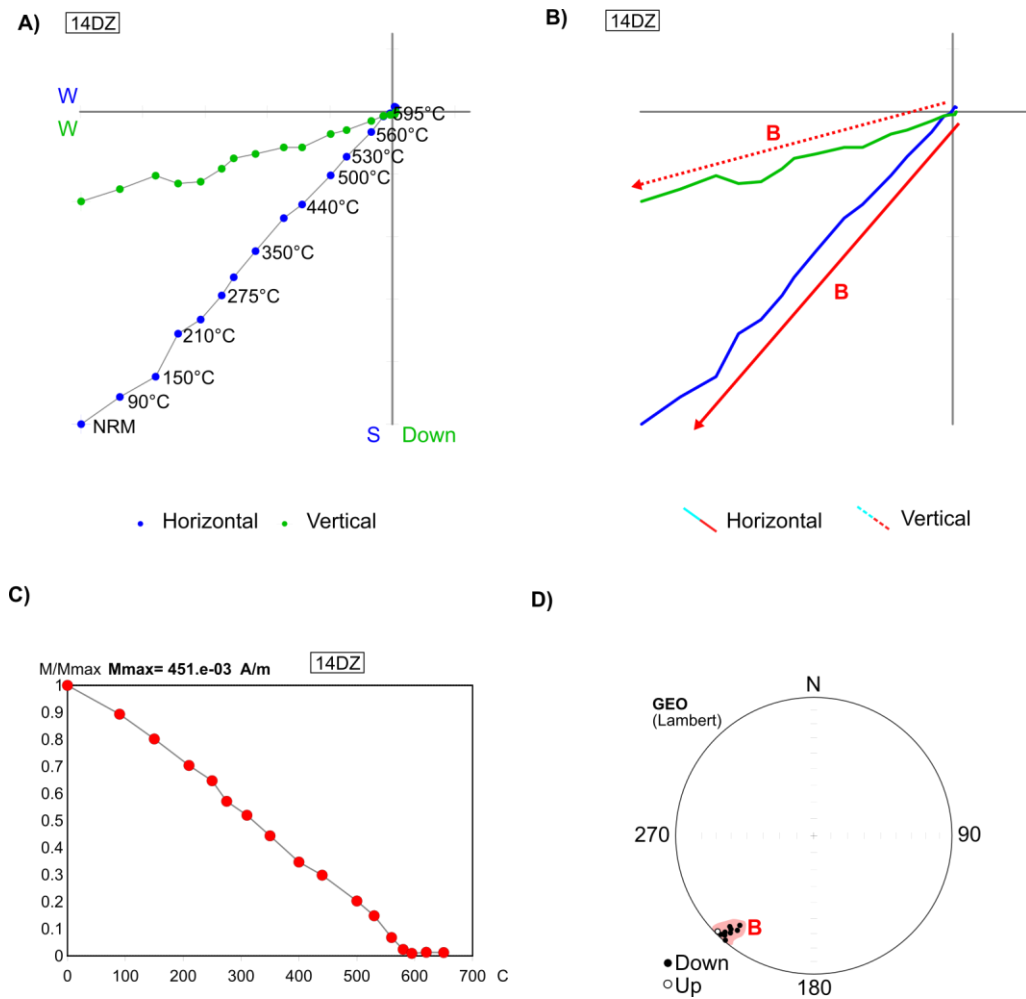


Figure A3-14. Orthogonal demagnetization diagrams, J_{max} normalized remanence intensity evolution, and component plots of site DDP14. A) Raw data; B) interpreted components; C) Intensity values resulting from THD; D) Equal-area stereographic plot of combined specimens.

DDP15

After applying AFD from 5mT to 90mT, the specimens of site DDP15 show a bivectorial demagnetization behavior (Figure A3-15 A, B). The interpreted “soft” or A component is traceable from alternating field ranges between 5mT and 90 mT, although the most common range is between 5 mT and 50 mT. In these intervals the intensity of magnetization reduces to less than 40% of the initial value in uniformly (Figure A3-15 C). Component A points towards the north with moderate positive inclinations (Figure A3-15 D; *in situ* site mean Dec: 358.7°; Inc: 24.4°; α_{95} : 4.8°; k: 195.71; n=6). Hard or “B” component is traceable in an alternating field range between 60 mT and 90 mT (Figure A3-15 A-B); in this range the demagnetization path deviates from the origin, and the intensity of magnetization decreases continuously with a less steep gradient (Figure A3-15 C). The B component is highly dispersed and aims towards the NW with moderate positive inclinations (Figure A3-15 D; *in situ* site mean Dec: 334.8°; Inc: 39.3°; α_{95} : 34.9°; k: 5.75; n=5, this direction was calculated using PCA without including the origin giving MAD results from 2.3 to 17.5).

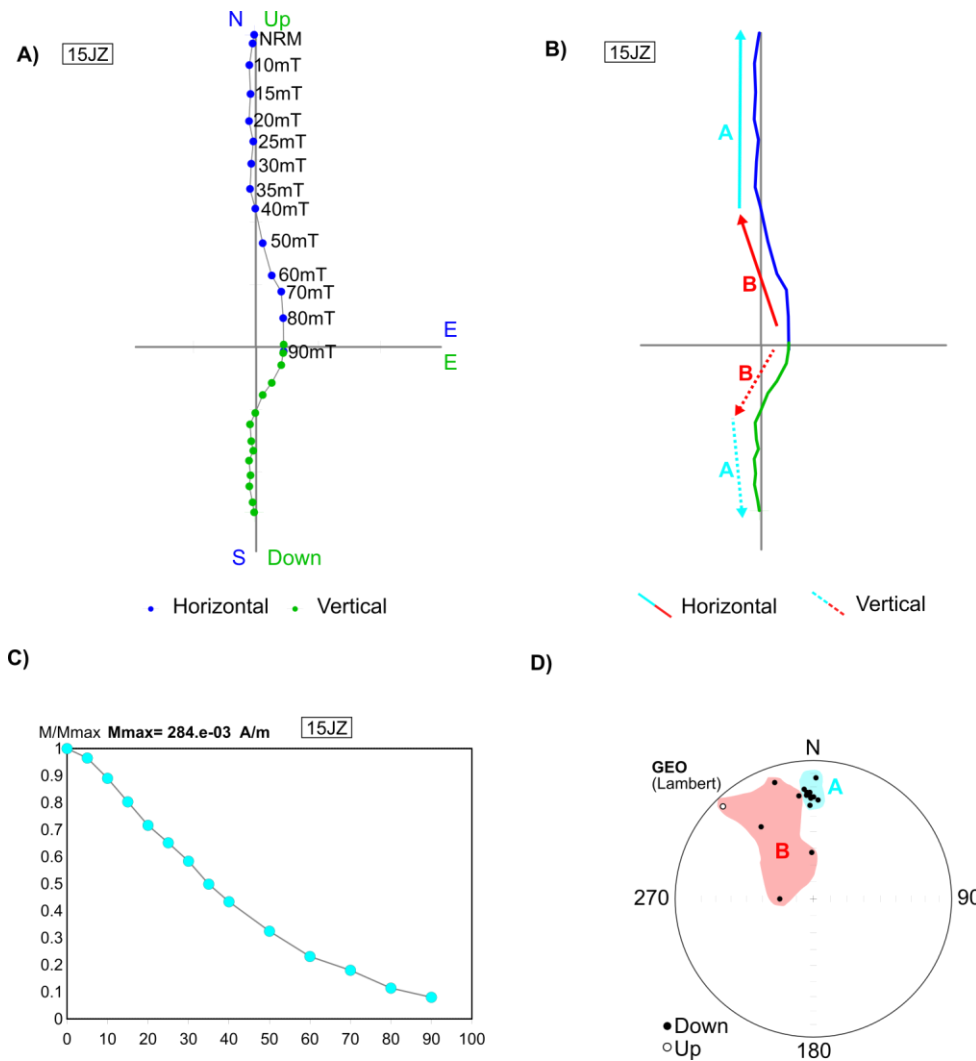


Figure A3-15. Orthogonal demagnetization diagrams, J_{max} normalized remanence intensity evolution, and component plots of site DDP15. A) Raw data; B) interpreted components; C) Intensity values resulting from AFD; D) Equal-area stereographic plot of combined specimens.

DDP16

After applying THD from 90°C to 590°C, the specimens of site DDP16 show a bivectorial demagnetization path (Figure A3-16 A, B). The interpreted “soft” or A component is traceable from laboratory temperature ranges between 90°C and 380 °C; in this interval the intensity of magnetization reduces to less than 40% of the initial value

with a moderately steep slope (Figure A3-16 C). Component A points towards the NE with positive inclinations (Figure A3-16 D; *in situ* site mean Dec: 35.2°; Inc: 19°; α_{95} : 5.8°; k: 109.08; n=7). The hard or “B” component is traceable between temperatures of 380 °C and 590 °C (Figure A3-16 A-B); in this range the demagnetization path is directed towards the origin and the intensity of magnetization decreases continuously with a less steep gradient; the most important drop in intensity of magnetization occurs between 420°C and 440°C (Figure A3-16 C). The B component aims towards the N-NE with positive inclinations (Figure A3-16 D; site mean Dec: 15°; Inc: 41.4°; α_{95} : 6.1°; k: 98.03; n=7, this direction was calculated using PCA without including the origin giving MAD results from 3.5 to 10.7).

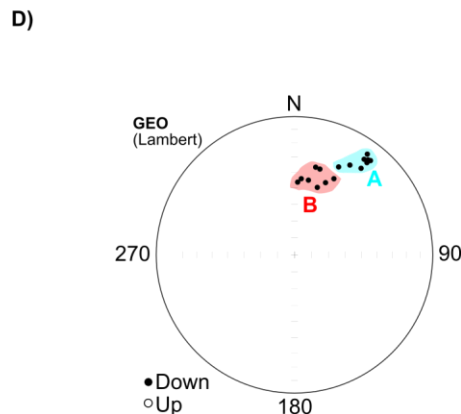
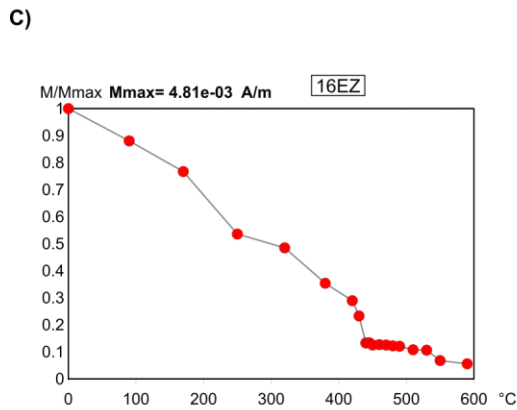
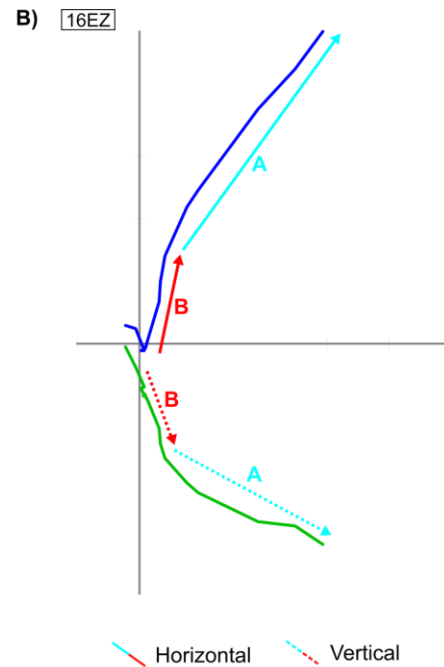
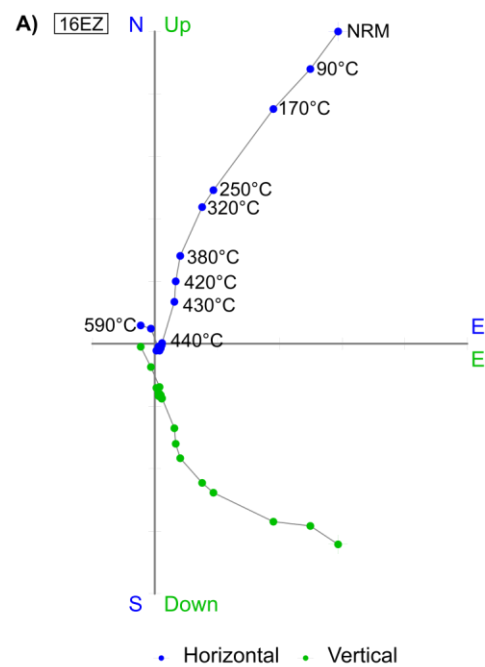


Figure A3-16. Orthogonal demagnetization diagrams, J_{max} normalized remanence intensity evolution, and component plots of site DDP16. A) Raw data; B) interpreted components; C) Intensity values resulting from THD; D) Equal-area stereographic plot of combined specimens.

DDP17

After applying THD from 100°C to 660°C and AFD from 2.5 mT to 160 mT, the specimens of site DDP17 show a bi-vectorial demagnetization path (Figure A3-17 A, B). The interpreted “soft” or A component is traceable from laboratory temperature ranges between 100°C and 410 °C and from alternating fields from 2.5 mT up to 30 mT; in these intervals the intensity of magnetization increases slightly (Figure A3-17 C). Component A points towards the N-NNE with positive inclinations (Figure A3-17 D; *in situ* site mean Dec: 9.9°; Inc: 49.5°; α_{95} : 8.4°; k: 52.82, n=7, calculated with PCA without including the origin, MAD: 1.3 – 13.2). Hard or “B” component is traceable between temperatures of 480 °C and 580 °C and in alternating field ranges between 15 mT and 160 mT (Figure A3-17 A-B); in these ranges the demagnetization path is directed towards the origin of the diagram and the intensity of magnetization decreases continuously with a steep slope; the most important drop in intensity occurs between 510°C and 555°C (Figure A3-17 C). The B component aims towards the SW with shallow negative inclinations (Figure A3-17 D; *in situ* site mean Dec: 236.5°; Inc: -15.3°; α_{95} : 4.7°; k: 122.5; n=9; this direction was calculated using PCA without including the origin giving MAD results from 0.7 to 10).

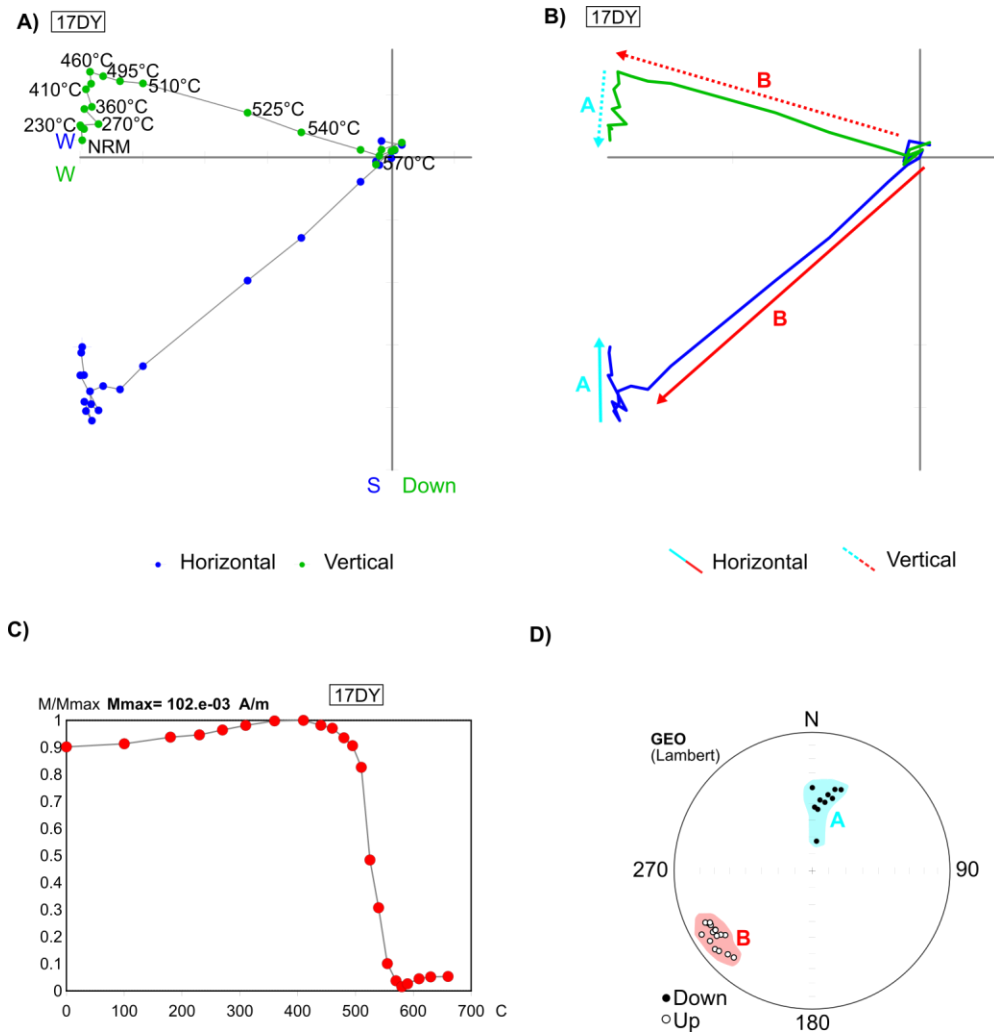


Figure A3-17. Orthogonal demagnetization diagrams, J_{max} normalized remanence intensity evolution, and component plots of site DDP17. A) Raw data; B) interpreted components; C) Intensity values resulting from THD; D) Equal-area stereographic plot of combined specimens.

DDP18

After applying THD from 100°C to 660°C and AFD from 2.5 mT to 160 mT, the specimens of site DDP18 show a bi-vectorial demagnetization path (Figure A3-18 A, B). The interpreted “soft” or A component is traceable from laboratory temperature ranges between 100°C and 480 °C and from alternating fields from 2.5 mT up to 25 mT; in these

intervals the intensity of magnetization increases slightly (Figure A3-18 C). Component A points towards the N-NNE with positive inclinations (Figure A3-18 D; *in situ* site mean Dec: 5.5°; Inc: 43.3°; α_{95} : 8.7°; k: 77.64, n=5; calculated with PCA without including the origin, MAD: 2.6 – 9.6). Hard or “B” component is traceable between temperatures of 510 °C and 570 °C and in alternating field ranges between 35 mT and 160 mT (Figure A3-18 A-B); in these ranges the demagnetization path is directed towards the origin of the diagram and the intensity of magnetization decreases continuously with a steep slope; the most important drop in intensity occurs between 540°C and 570°C (Figure A3-18 C). The B component aims towards the WSW with negative inclinations (Figure A3-18 D; *in situ* site mean Dec: 255.3°; Inc: -26.9°; α_{95} : 4.5°; k: 178.28;n=7, this direction was calculated using PCA without including the origin giving MAD results from 1.7 to 7.2).

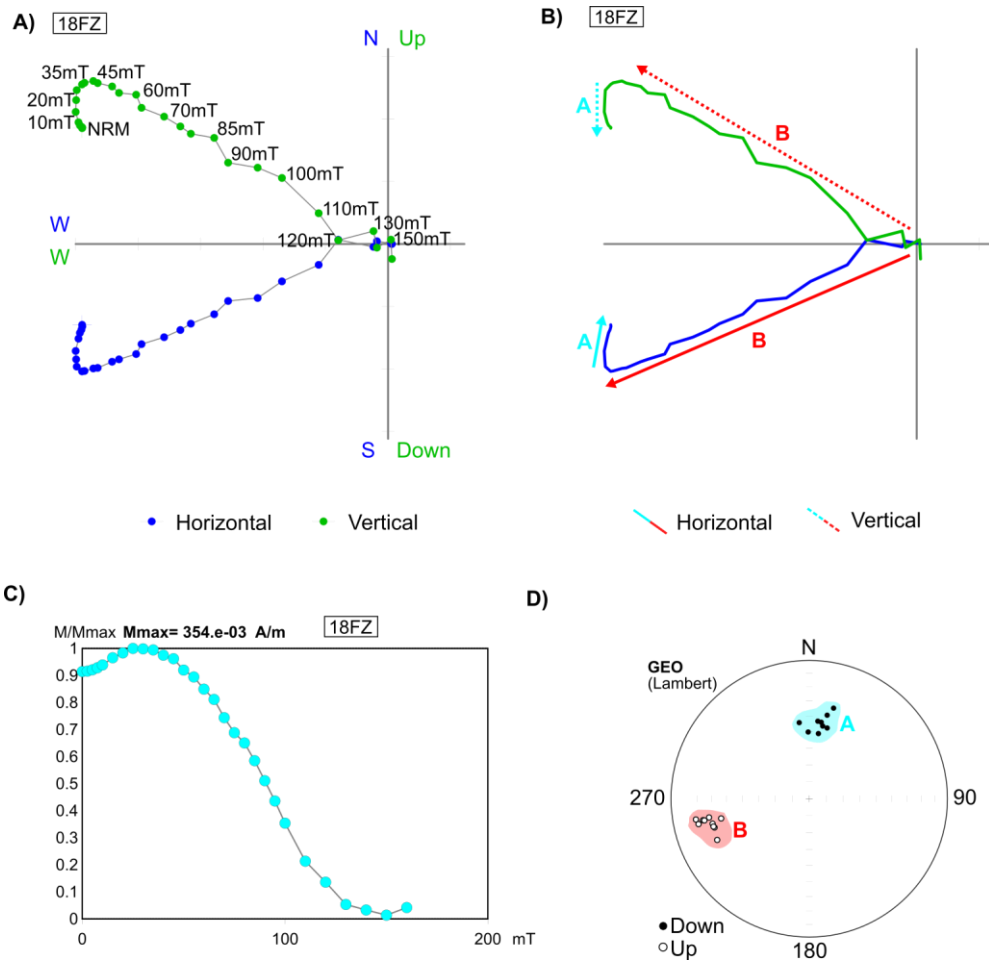


Figure A3-18. Orthogonal demagnetization diagrams, J_{max} normalized remanence intensity evolution, and component plots of site DDP18. A) Raw data; B) interpreted components; C) Intensity values resulting from AFD; D) Equal-area stereographic plot of combined specimens.

DDP19

After applying THD from 100°C to 660°C and AFD from 2.5 mT to 160 mT, the specimens of site DDP19 show a bi-vectorial demagnetization path (Figure A3-19 A, B). The interpreted “soft” or A component is traceable from laboratory temperature ranges between 100°C and 525°C and from alternating fields from 2.5 mT up to 20 mT; in these intervals the intensity of magnetization increases slightly (Figure A3-19 C). Component A points towards the NE-E with positive inclinations (Figure A3-19 D; *in situ* site mean Dec: 69.8°; Inc: 41.7°; α_{95} : 16.4°; k: 17.54, n=6; it was calculated with PCA without including the origin, MAD: 4.5 – 19.7). Hard or “B” component is traceable between temperatures of 525 °C and 660 °C and in alternating field ranges between 20 mT and 160 mT (Figure A3-19 A-B), in these ranges the demagnetization path is directed towards the origin of the diagram and the intensity of magnetization decreases continuously with a steep slope; the most important drop in intensity occurs between 555°C and 580°C (Figure A3-19 C). The B component aims towards the SW with negative inclinations (Figure A3-19 D; *in situ* site mean Dec: 232.9°; Inc: -38.4°; α_{95} : 7.9°; k: 50.16;n=8, this direction was calculated using PCA without including the origin giving MAD results from 2.1 to 5.8).

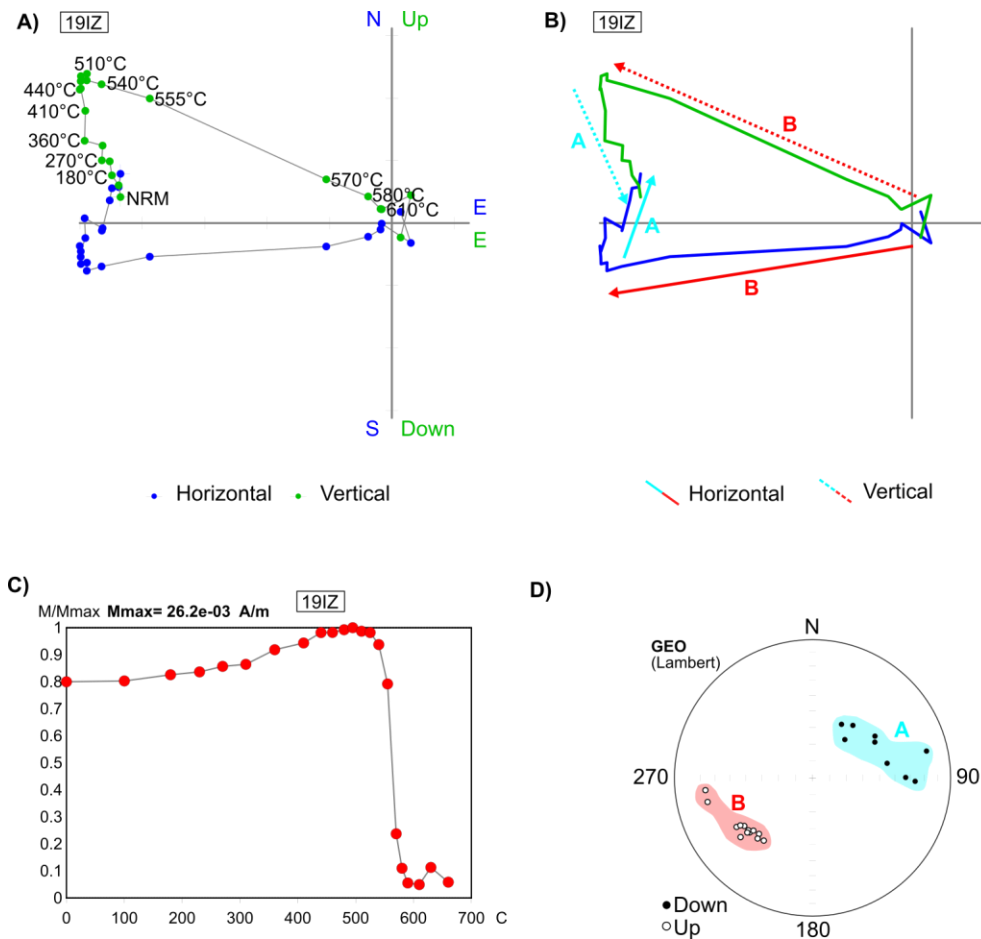


Figure A3-19. Orthogonal demagnetization diagrams, J_{max} normalized remanence intensity evolution, and component plots of site DDP19. A) Raw data; B) interpreted components; C) Intensity values resulting from THD; D) Equal-area stereographic plot of combined specimens.

DDP20

After applying THD from 90°C to 700°C, the specimens of DDP09 locality show a multicomponent demagnetization diagram (Figure A3-20 A, B). The "soft" A component is traceable from temperatures of 90°C up to 440°C; at these temperatures the remanence intensity decreases to 80% of the initial value (Figure A3-20 C). The A component is highly dispersed pointing towards the W, N and NE with positive inclinations (Figure A3-20 D; *in situ* site mean Dec: 79.5°; Inc: 68.2°; α_{95} : 12°; k: 26.46, n=7; this direction

was calculated using PCA without including the origin giving MAD results from 5.4 to 13.2). The intermediate A1 component is traceable from temperatures of 440 °C up to 560°C, and the remanence intensity decreases to half of the initial values (Figure A3-20 C). A1 component points towards the E-SE with shallow positive and negative inclinations (Figure A3-20 D; *in situ* site mean Dec: 103.1°; Inc: -5.3°; α_{95} : 23°; k: 9.42, n=6, direction calculated by PCA without including the origin, MAD: 7.6 – 15.5). The "hard" or B component is traceable from temperatures of 580 °C to 700 °C (Figure A3-20 A-B); in this range the B component directs towards the origin of the Zijderveld diagram and the intensity of magnetization decreases rapidly to zero values (Figure A3-20 C). The B component aims towards the SSE with negative inclinations (Figure A3-20 D; *in situ* site mean Dec: 142.7°; Inc: -52.9°; α_{95} : 8.1°; k: 47.48, n=8; this direction was calculated using PCA without including the origin giving MAD results from 2.6 to 11.2).

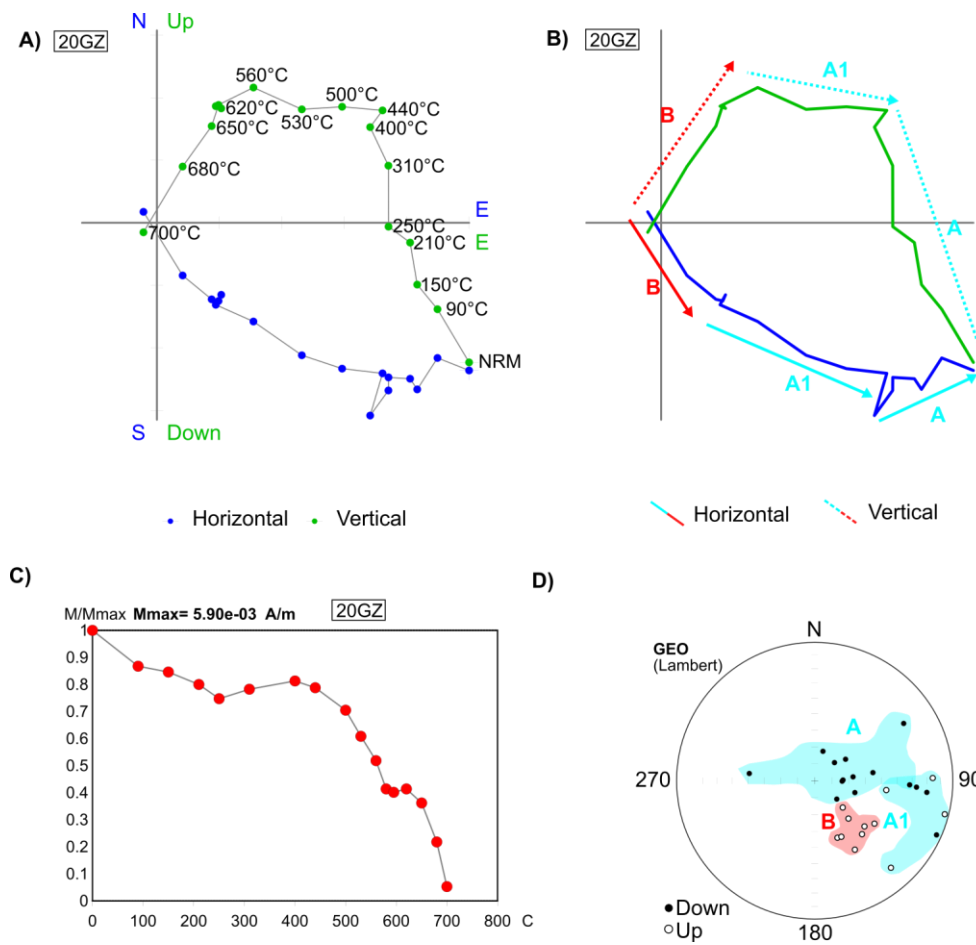


Figure A3-20. Orthogonal demagnetization diagrams, J_{\max} normalized remanence intensity evolution, and component plots of site DDP20. A) Raw data; B) interpreted components; C) Intensity values resulting from THD; D) Equal-area stereographic plot of combined specimens.

DDP22

After applying THD from 100°C to 605°C and AFD from 5 mT to 80 mT, the specimens of site DDP22 show a bi-vectorial demagnetization path (Figure A3-22 A, B). The interpreted “soft” or A component is traceable from laboratory temperature ranges between 100°C and 400°C and from alternating fields from 5 mT up to 20 mT; in these intervals the intensity of magnetization increases slightly (Figure A3-22 C). Component A points towards the N-NW with positive inclinations (Figure A3-22 D; *in situ* site mean Dec: 348°; Inc: 40.1°; α_{95} : 22.5°; k: 17.6; n=4, calculated with PCA without including the origin, MAD: 2.4 – 15.9). Hard or “B” component is traceable only in alternating field ranges between 15 mT and 80 mT (Figure A3-22 A-B); in this range the demagnetization path is directed towards the origin of the diagram and the intensity of magnetization decreases continuously with a steep slope (Figure A3-22 C). The B component aims towards the WSW - SSW with negative inclinations (Figure A3-22 D; *in situ* site mean Dec: 226.2°; Inc: -18.5°; α_{95} : 25.1°; k: 10.26; n=5; this direction was calculated using PCA including the origin giving MAD results from 1.9 to 3.4).

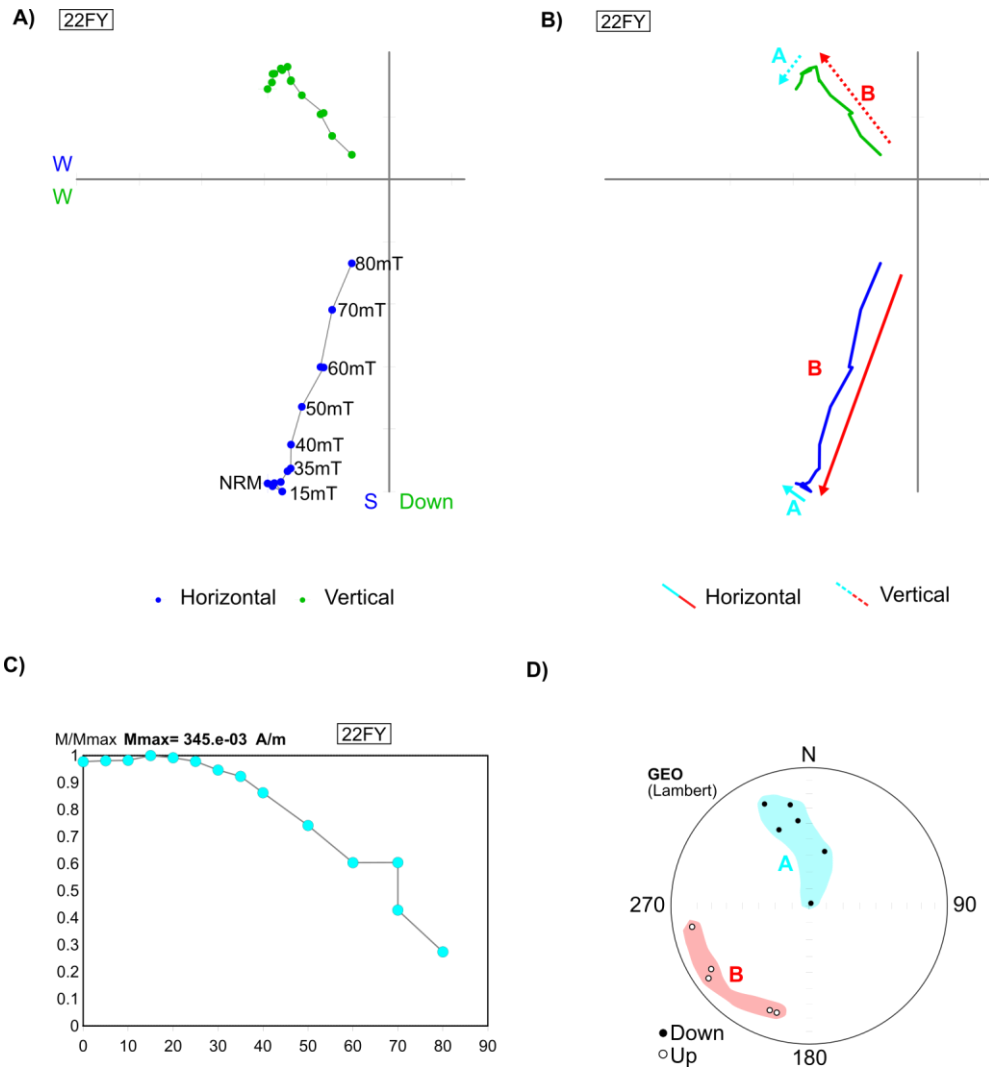


Figure A3-22. Orthogonal demagnetization diagrams, J_{max} normalized remanence intensity evolution, and component plots of site DDP22. A) Raw data; B) interpreted components; C) Intensity values resulting from AFD; D) Equal-area stereographic plot of combined speci

Appendix 4

Stratigraphic section along Rosario Nuevo Creek

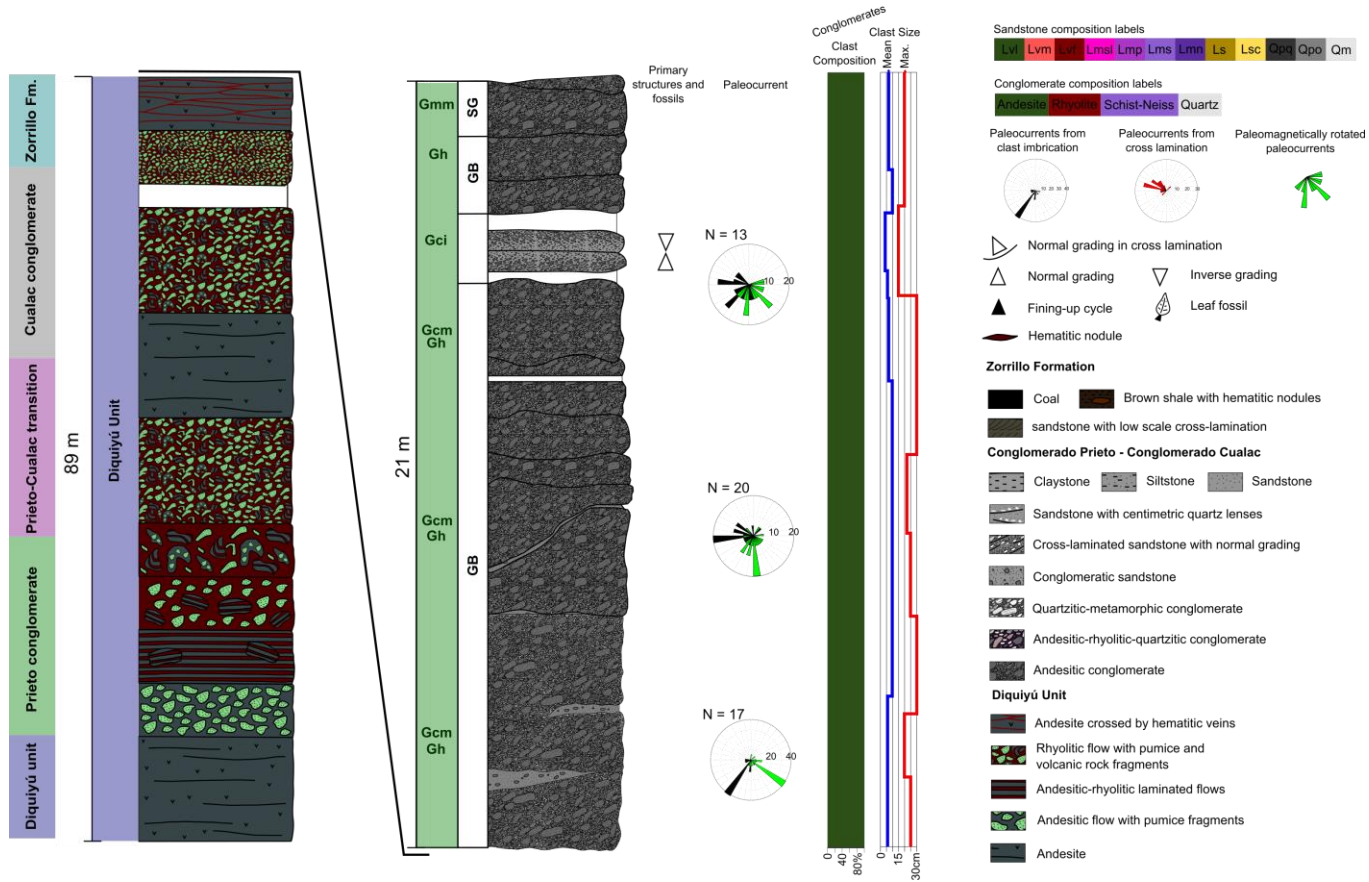


Figure A4-1. Column along Rosario Nuevo's creek, part I.

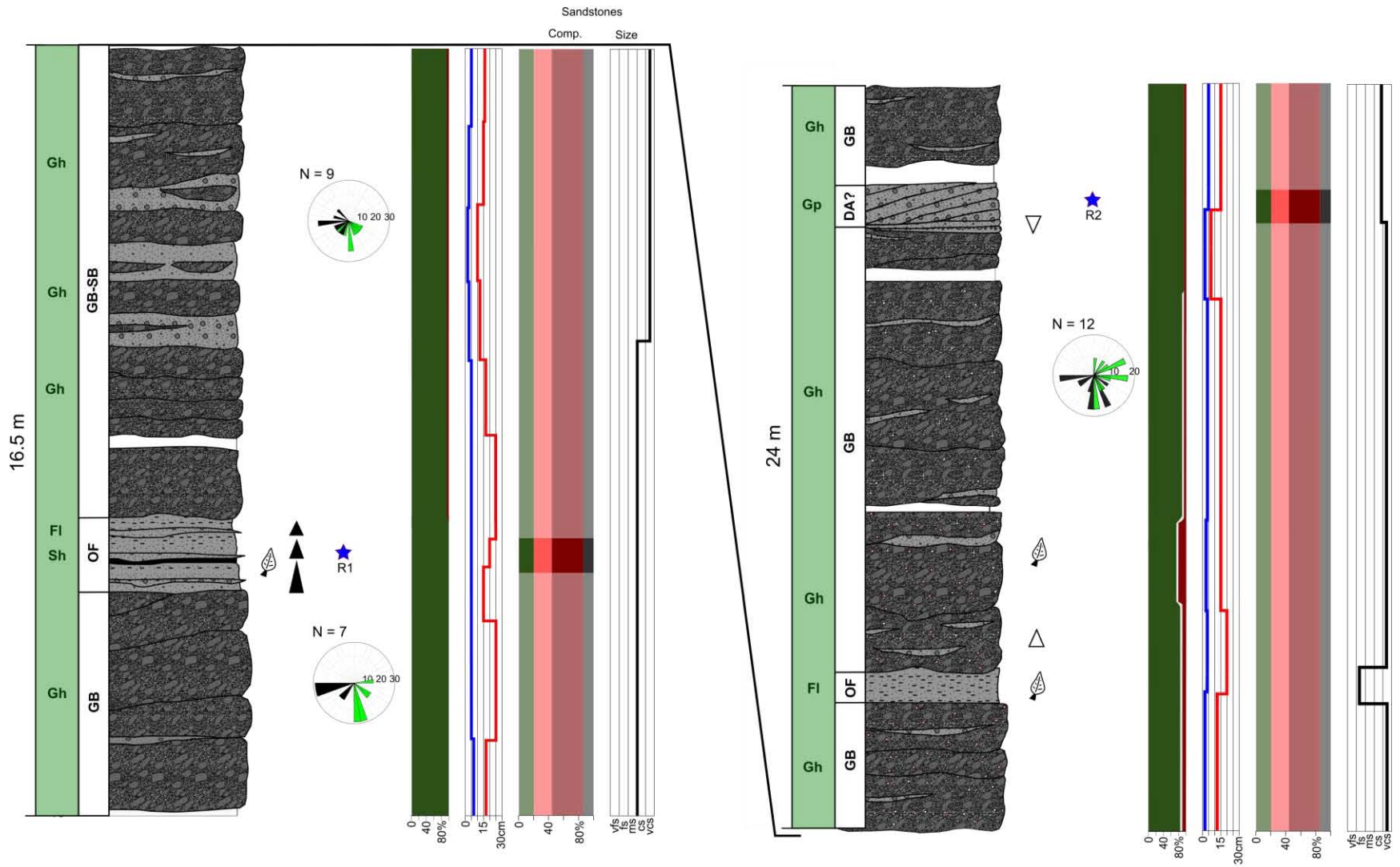


Figure A4-2. Column along Rosario Nuevo's creek, part II.

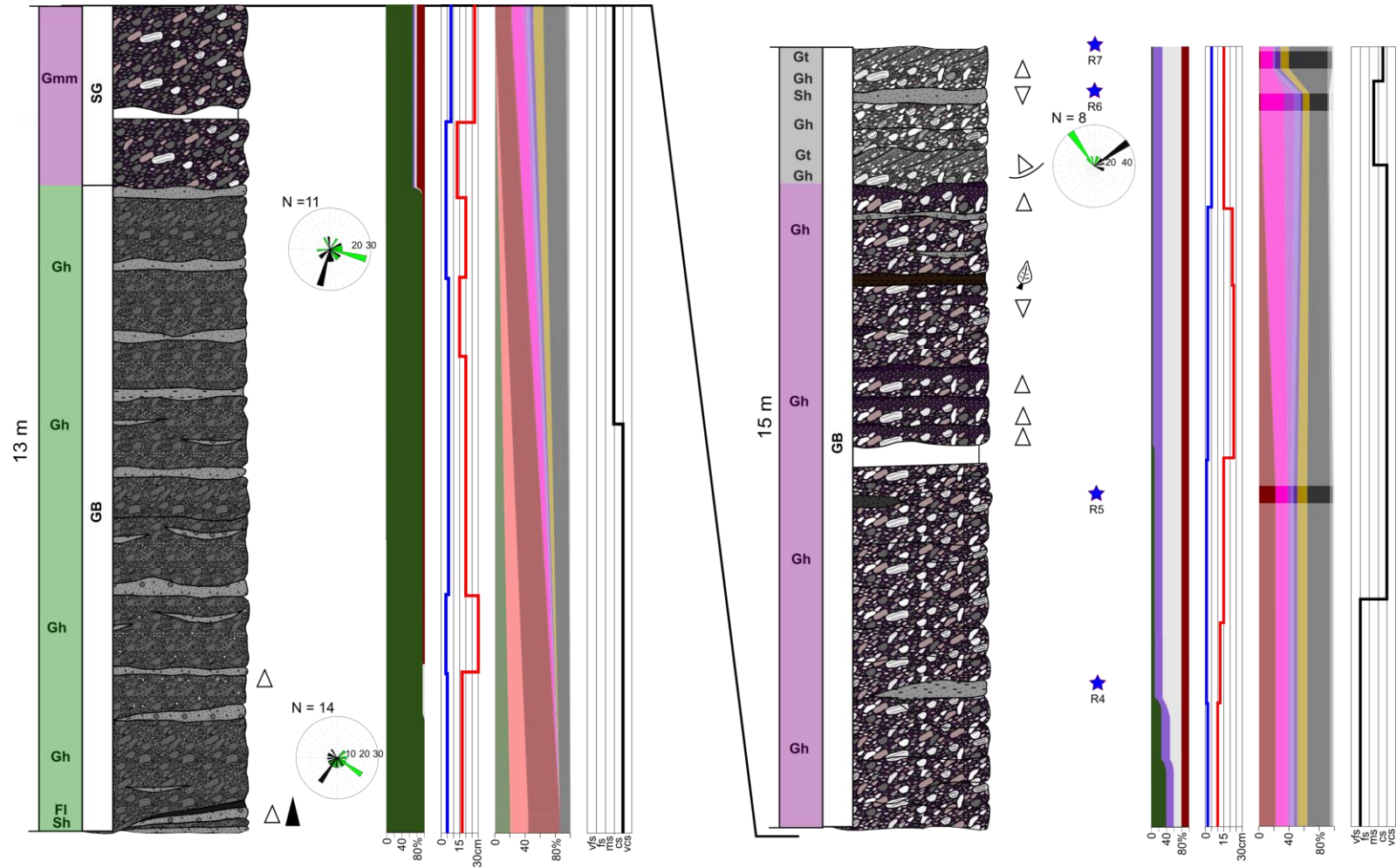


Figure A4-3. Column along Rosario Nuevo's creek, part II

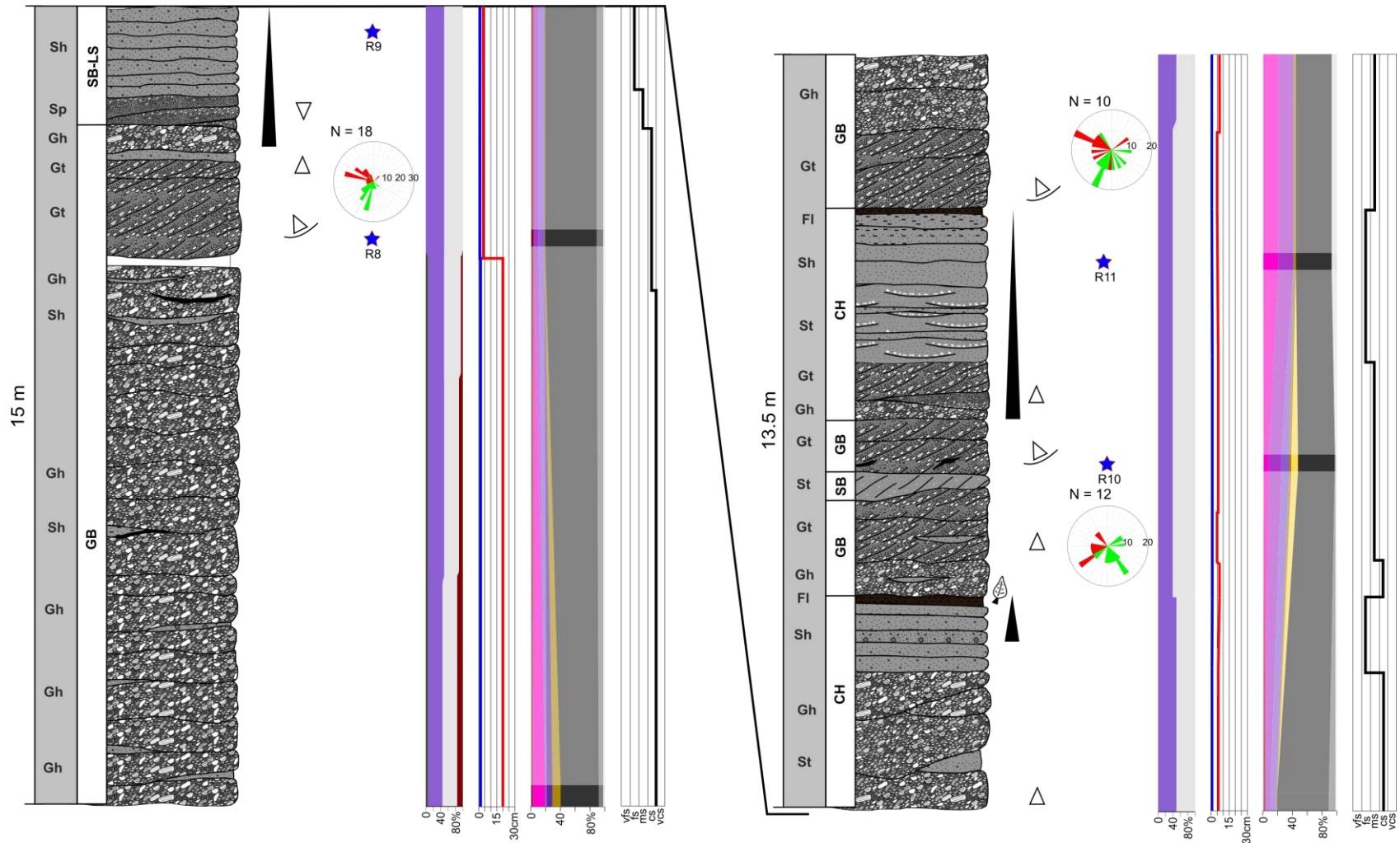


Figure A4-4. Column along Rosario Nuevo's creek, part IV.

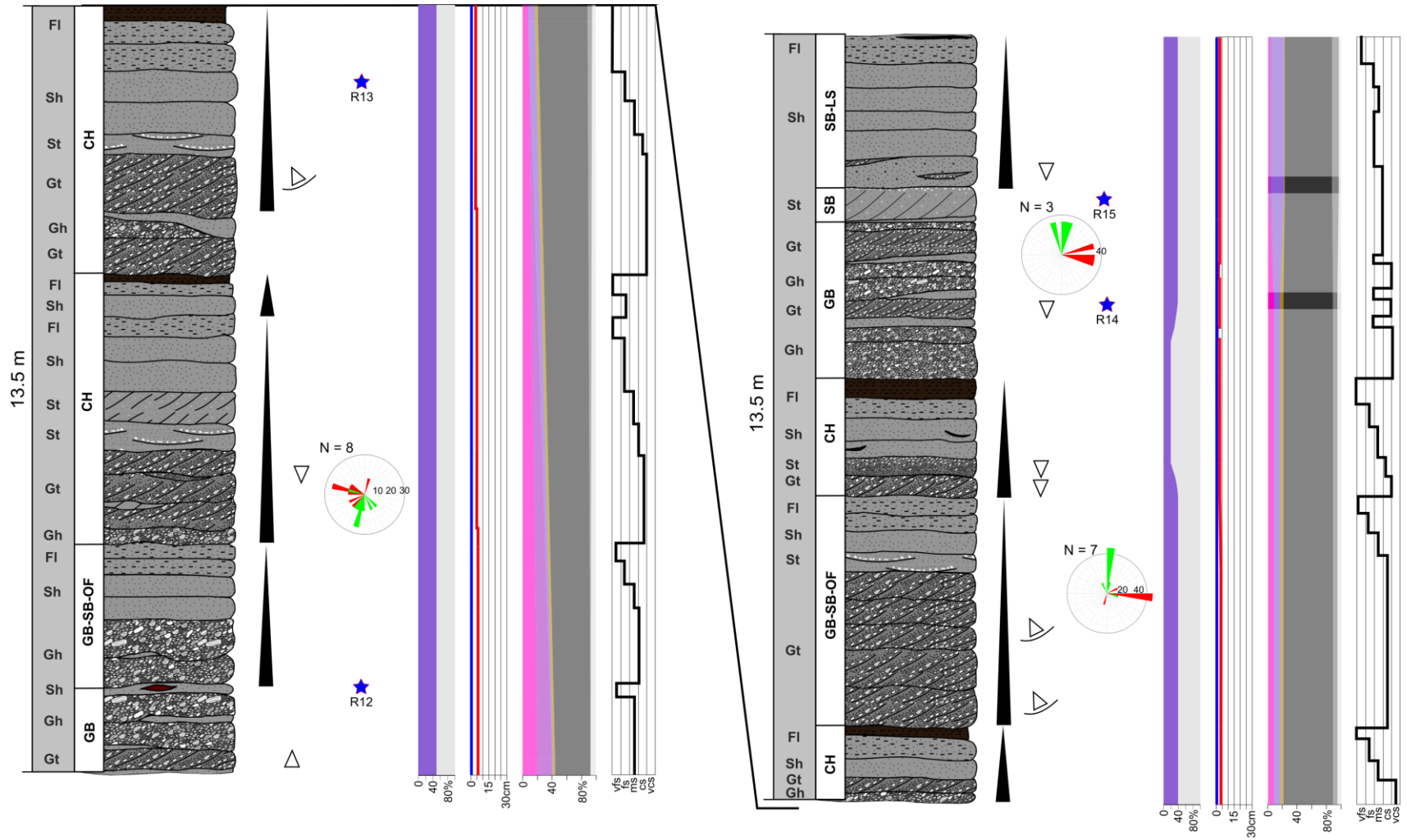


Figure A4-5. Column along Rosario Nuevo's creek, part V.

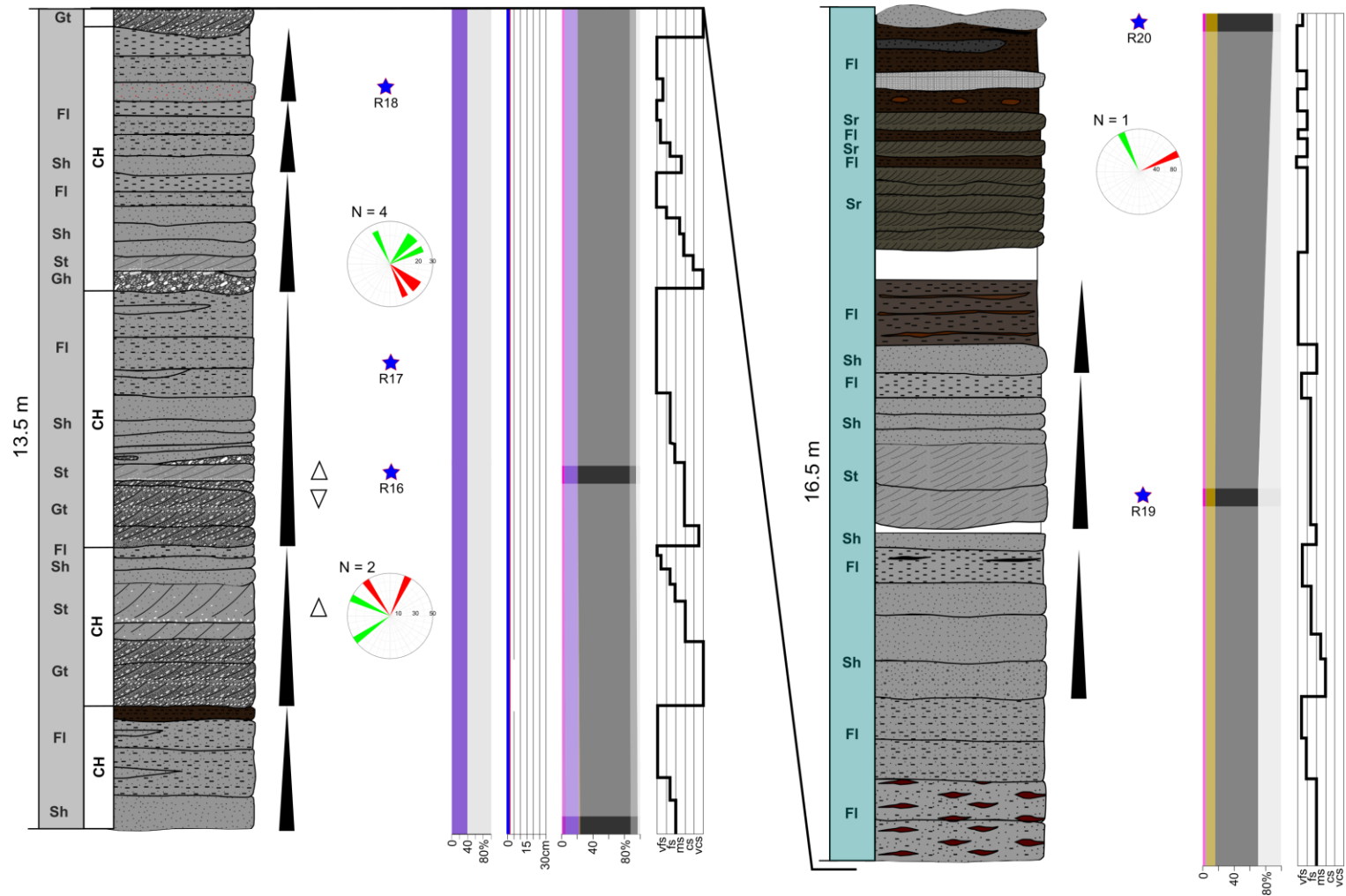


Figure A4-6. Column along Rosario Nuevo's creek, part VI.

Appendix 5

Sedimentary petrography

R1

This sample was taken from the first (oldest) sandy-muddy package found in the Prieto Conglomerate Formation. In hand sample, R1 is green-brown colored conglomeratic sandstone; the biggest grains are andesitic in composition. The framework consists of medium to coarse (0.25 mm – 1 mm) sand grains. Microscopically, the sample has a predominance of volcanic grains with subordinate polycrystalline quartz (Figure A5-1). The volcanic grains present two principal affinities, namely, felsitic (Lvf) and basaltic-andesitic (Lvl). The first type of grains (Lvf) is recognized by its texture which exhibits a cryptocrystalline quartz-feldspar mosaic (Figure A5-2), the product of recrystallization of older mineral phases; some Lvf grains were crossed by quartzitic veins prior to their erosion and deposition (Figure A5-3). The Lvl type is easily recognizable by the internal disposition of elongate plagioclase crystals within the grains; some of these grains are darker than others, and in general, in this sample, these grains present a rare opacity, due probably to weathering effects. The third type of grain recognized is quartz, principally polycrystalline (Qpq) although some monocrystalline quartz (Qm) grains were recognized; the largest Qpq grain has a cryptocrystalline silica texture in one of its edges (Figure A5-1) resembling a probable alteration prior to the grain erosion, due probably to the effect of circulating hydrothermal fluids. Some pseudomatrix (*sensu* Dickinson, 1970) is developed between grains, along with alteration products (white mica, oxides, kaolinite).

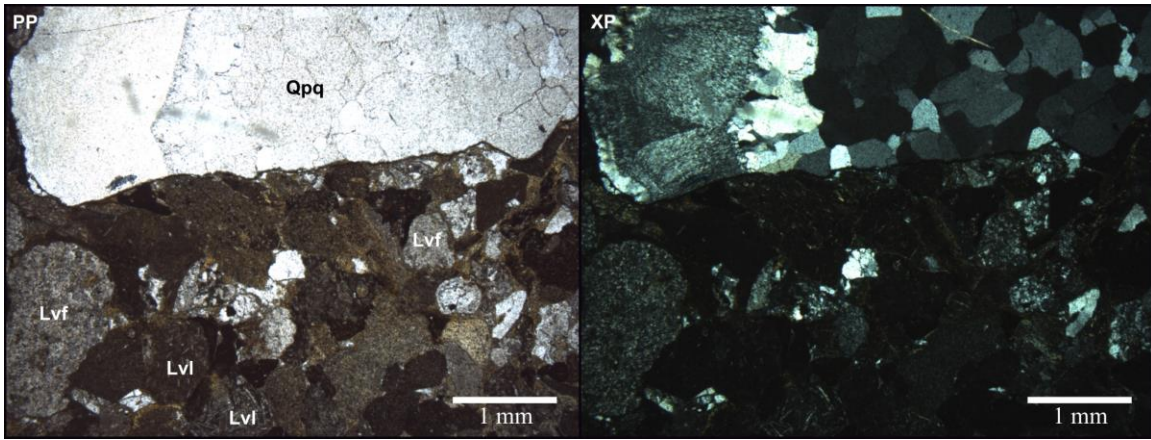


Figure A5-1. Plane and polarized light micrograph of sample R1. Qp – Polycrystalline quartz, Lvf – Felsitic lithic volcanic fragment, Lvl – Lathwork lithic volcanic fragment

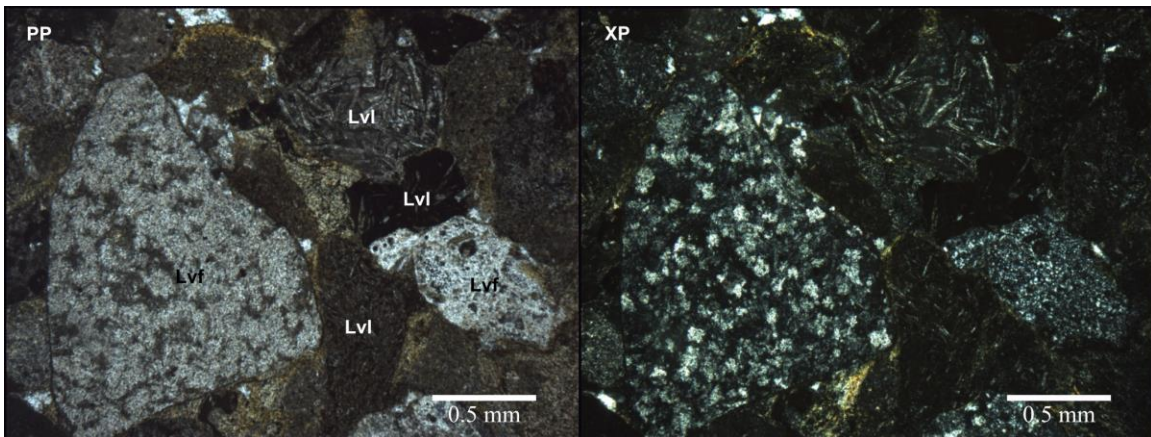


Figure A5-2. Plane and polarized light micrograph of sample R1

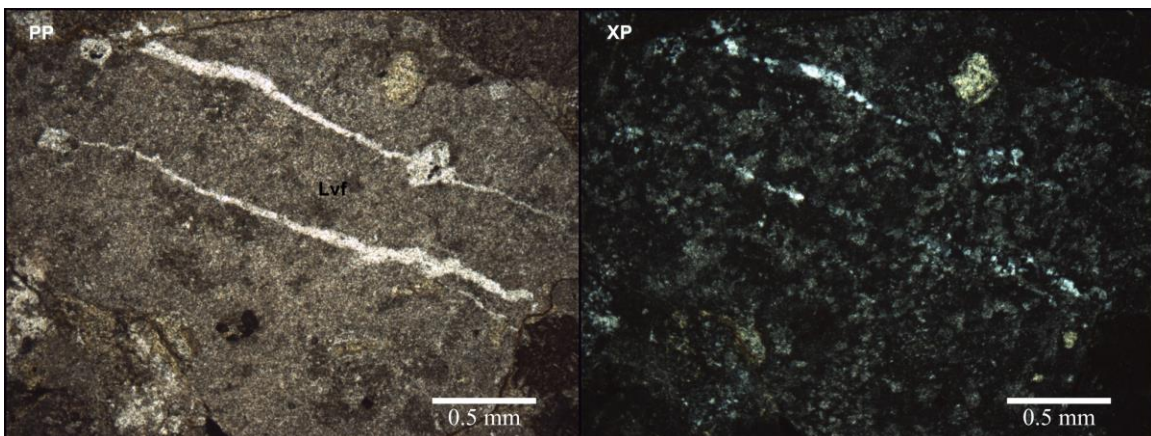


Figure A5-3. Plane and polarized light micrograph of sample R1

R2

Clast supported, poor to moderately sorted sandstone with the majority of grains in the granule to pebble size category. The larger grains are subrounded to subangular and elongated; the smaller grains are subangular to subrounded and subspherical. The predominant compositional class is Lvm, composed of a matrix of tiny plagioclase with porphyritic plagioclase inclusions; some of these grains have a pilotaxitic texture. The second predominant class is Lvf with cryptocrystalline aggregates of silica and feldspar. Less common are Lvv and Lvl grains. Some xenocrystals with corroded edges, undulatory extinction and some glomeroporphyritic aggregates of Qpq and probably feldspar. Some grains have a developed reaction rim. The matrix of most grains is composed of feldspar, silica, opaque minerals and devitrified products.

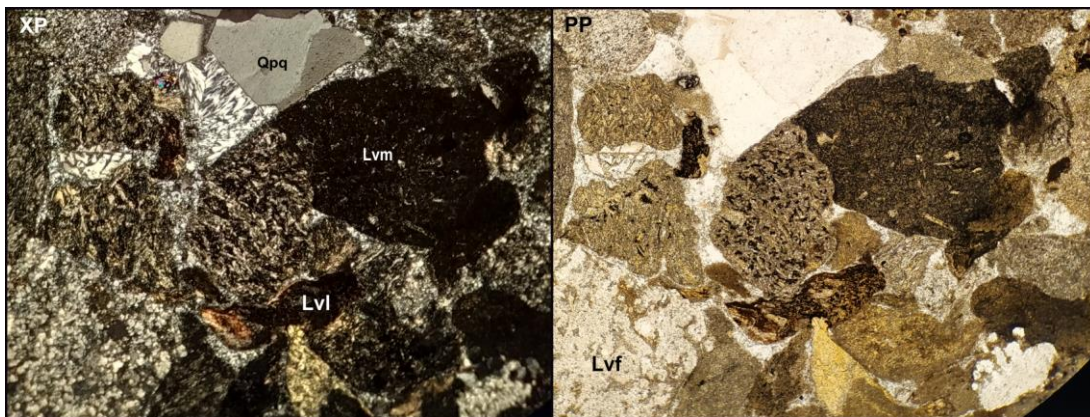


Figure A5-4. Plane and polarized light micrograph of sample R2. Micrographs taken in 4x.

R4

Sample R4 corresponds to sandy siltstone, matrix-supported. In hand specimen, the sample is light grey with tiny red dots and thin red veins crossing. Microscopically can be seen that the silt and clay fractions are composed primarily by mica, monocrystalline

quartz and by cryptocrystalline aggregates difficult to describe individually (Figure A5-4). All these components are interpreted as a pseudomatrix product of mechanical disintegration of bigger grains. The larger fractions, in general fine sand, but in few cases reaching middle sand grain sizes, are constituted by polycrystalline quartz, metamorphic fragments (Phyllite, schist) and the smallest ones by monocrystalline quartz.

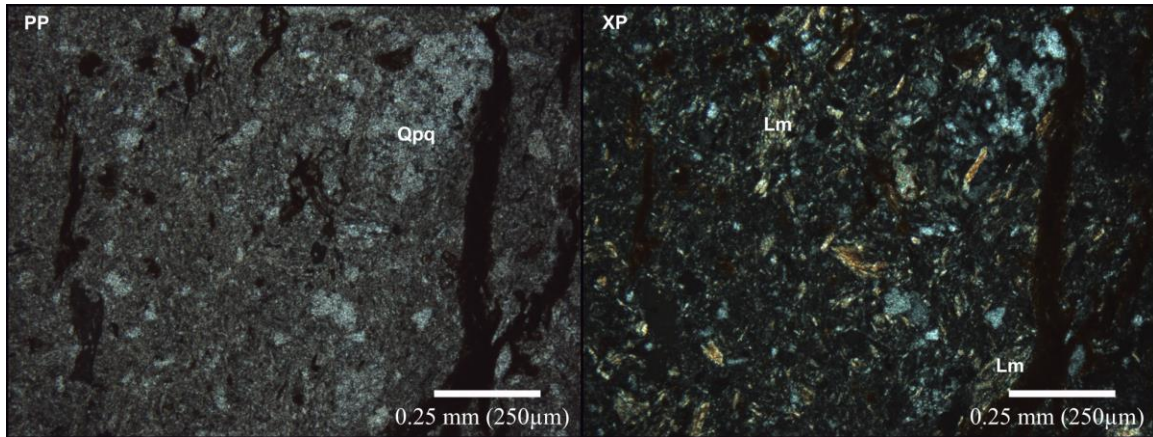


Figure A5-5. Plane and polarized light micrograph of sample R4. Lm – Metamorphic lithic clast

R5

Sample R5 was taken from a sandstone lens packed between conglomerate beds in an interval of the Prieto Conglomerate Formation close to the contact with Cualac Formation. The sample corresponds to a coarse to very coarse (0.5 mm – 1 mm) sandstone; the majority of grains are subrounded and elongate along one axis, and in general, its contacts are tangential. The majority of the grains correspond to metamorphic clasts of different grade and protolith, polycrystalline quartz, felsitic igneous clasts, sedimentary clasts, and monocrystalline quartz (Figures A5-5-7). The metamorphic clasts range in grade from slaty to phyllitic (Figures A5-5, A5-6), and its protoliths are interpreted as volcanic felsic (Figure A5-5) and sedimentary pelitic (Figures A5-5, A5-6); some grains constituted by oriented polycrystalline quartz are interpreted as metamorphic (Figure A5-7). The felsitic igneous clasts (Lvf) have a recrystallized texture and absent

foliation. The sedimentary lithic grains (Ls) are recognized by their texture in which a matrix and a framework coexist within the same grain (Figure A5-6), and most of these grains correspond to siltstones and fine sandstones some of them having infilling calcite. Monocrystalline quartz constitutes the smallest grain size (fine to very fine sand), and can proceed from the disaggregation of larger Lm and Qpq grains. The space between grains is filled by mica, opaque minerals and calcite.

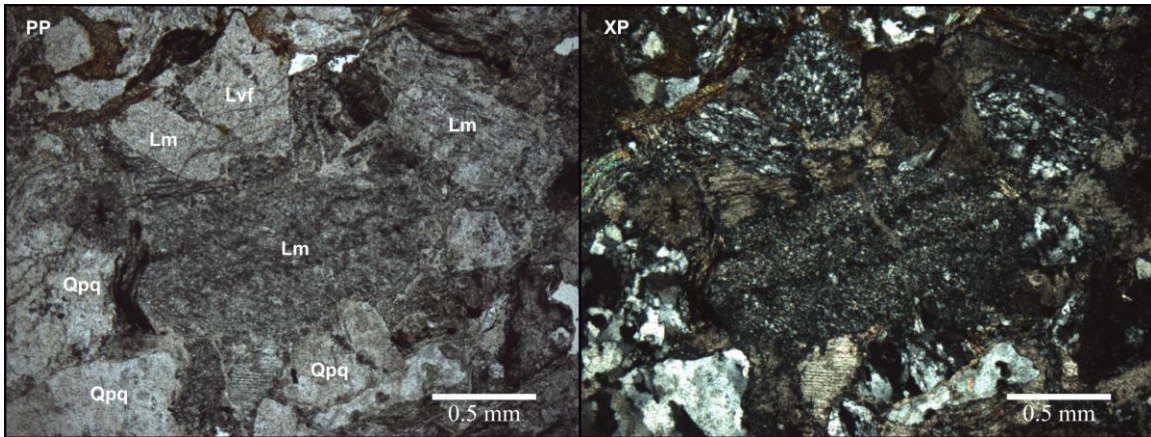


Figure A5-6. Plane and polarized light micrograph of sample R5. Lm in the center interpreted as felsitic slate, Lm in the right and left corners interpreted as pelitic schists.

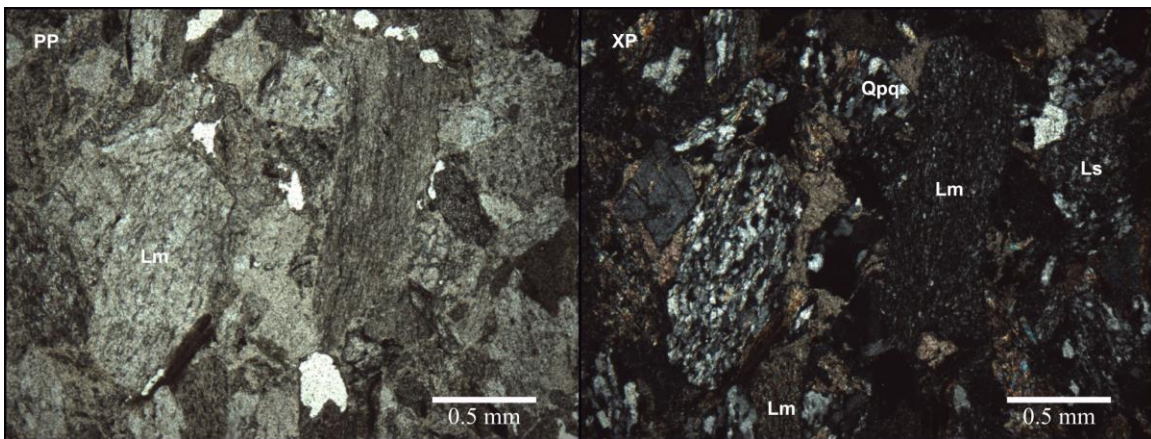


Figure A5-7. Plane and polarized light micrograph of sample R5. Lm to the left corresponds to pelitic phyllite; Lm grain to the right corresponds to a pelitic slate.

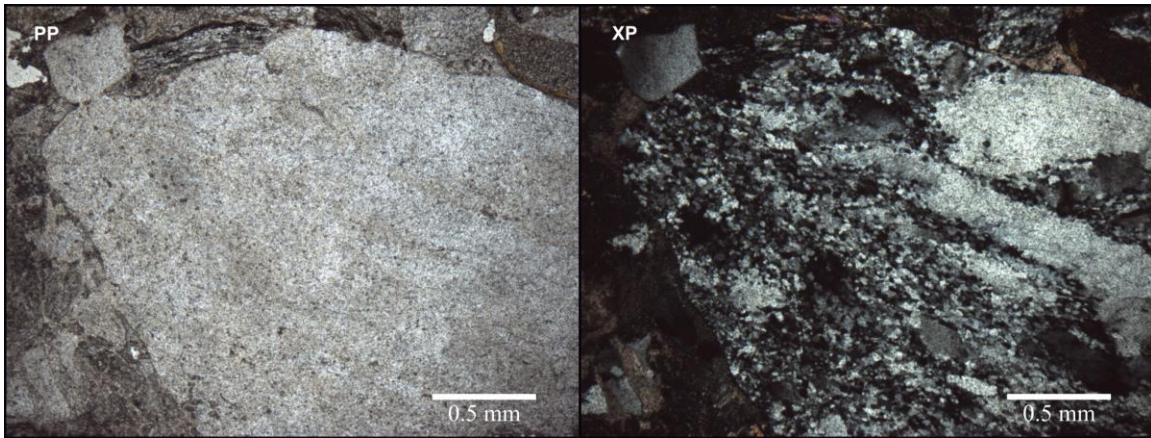


Figure A5-8. Plane and polarized light micrograph of sample R5.

R6

Sample R6 ranges from fine to coarse-grained sand, being medium sand size the mean. The framework is clast supported. The composition of the sample is in a major part dominated by metamorphic clasts (Lm), whose characteristics (planar foliation, the abundance of tiny (0.01 mm) micas) allow classifying them as pelitic slates and/or phyllites (Figure A5-8). The second most abundant grain is polycrystalline quartz (Qpq) dispersed throughout the sample, some of these grains are elongated and internally deformed. These characteristics classify these grains as Lm; the Lm grains are oriented parallel to a planar foliation in the sample. Sedimentary lithic grains (Ls) are the third in abundance, principally siltstones and fine sandstones. Some hematitic grains with detrital appearance (abraded borders) appear across the sample together with calcite bordered by a hematitic coating. The spaces between grains are filled by pseudomatrix composed of mica, submicroscopic quartz and probably clay minerals along with opaque minerals and calcite.

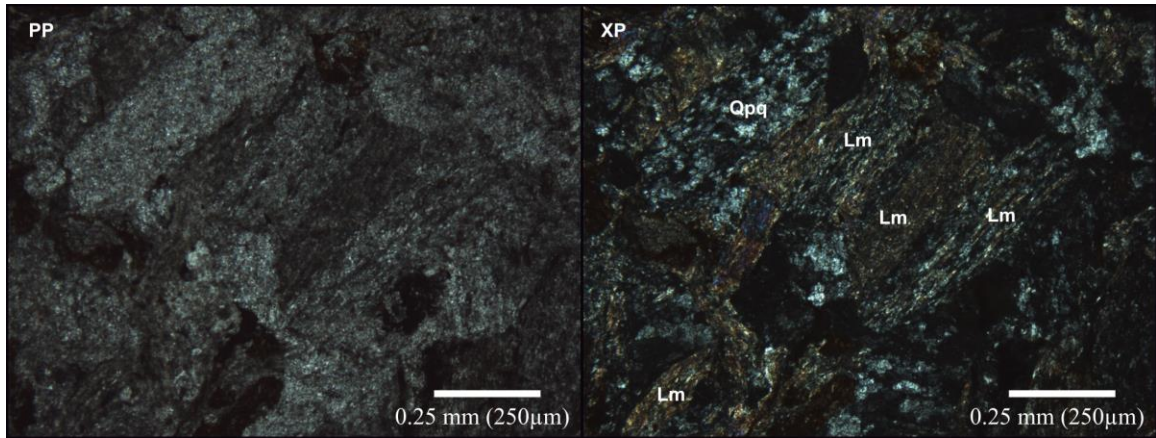


Figure A5-9. Plane and polarized light micrograph of sample R6.

R7

Sample R7 was taken from the sandy part of a conglomeratic - sandy channel of the base of Cualac Formation. Its size fractions encompass from medium sand to very coarse sand, being the coarse sand size the mean. This sample has some well-rounded grains, although the majority of grains are subrounded. Most grains correspond to Qpq. Lm grains of diverse types are the second in abundance, being pelitic slates and schists the most representative; some metafelsitic grains are found, presenting the same characteristics of a felsitic grain (Lvf), but with weak foliation development (Figure A5-9). Some Qpq grains with internal uniaxial deformation are considered Lm. Some Ls grains of siltstone and claystone are present, some of the latter containing large (1mm) euhedral calcite inclusions (Figure A5-10). Qm and Lvf are also present in the sample but in low proportion. The space between grains is filled by vermicular kaolinite and calcite.

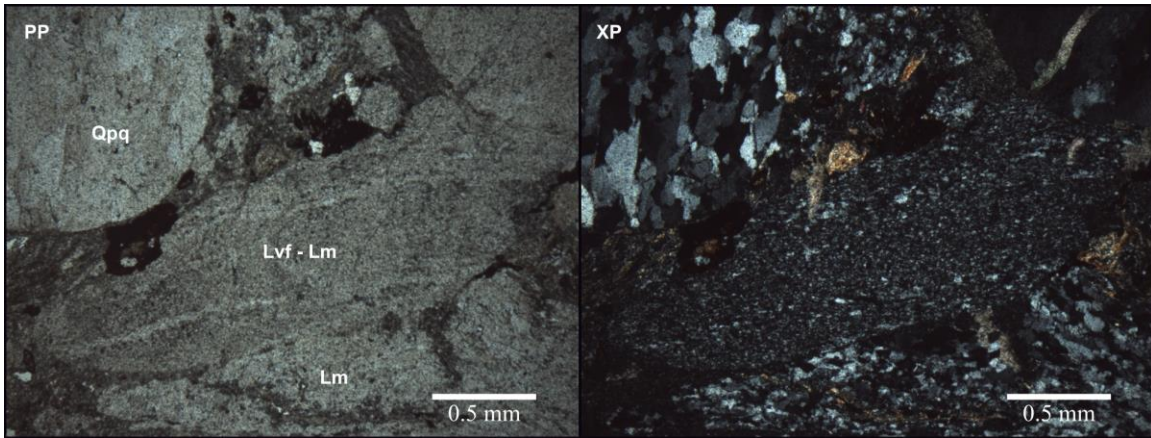


Figure A5-10. Plane and polarized light micrograph of sample R7.

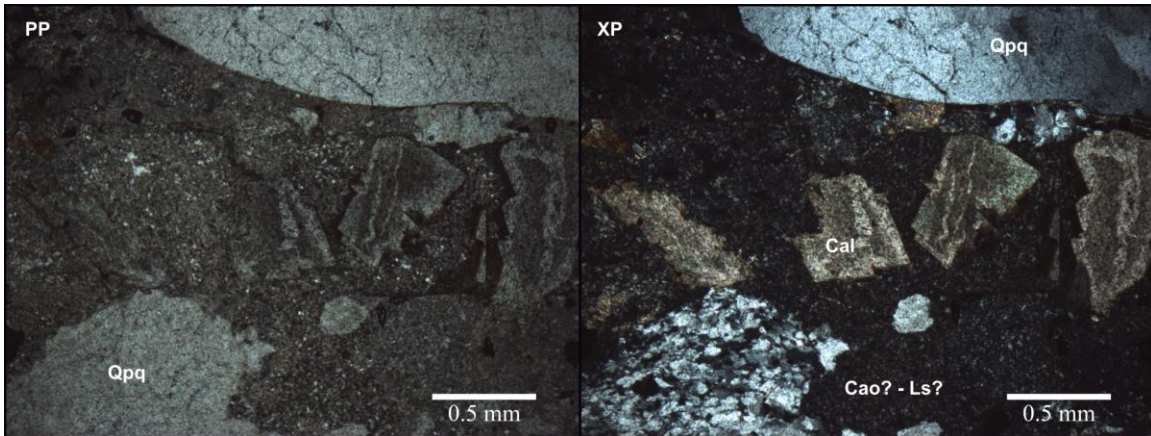


Figure A5-11. Plane and polarized light micrograph of sample R7.

R8

Sample R8 has a grain size range between coarse and very coarse sand, with elongate subrounded grains. Compositionally, this sample has two important types of grains, namely, Qpq and Lm. The first is the most abundant, ubiquitous through the sample. The Lm grains correspond principally to pelitic schists; nevertheless, some phyllitic and gneissic grains are found (Figure A5-11). In some schistose grains an internal crystal size decrease occurs as these grains are subjected to compression by surrounding grains (Figure A5-12); this is the onset of pseudomatrix generation (Dickinson, 1970). Some Ls

and Lv_f are observed but with low proportion. Vermicular kaolinite fills the voids between grains.

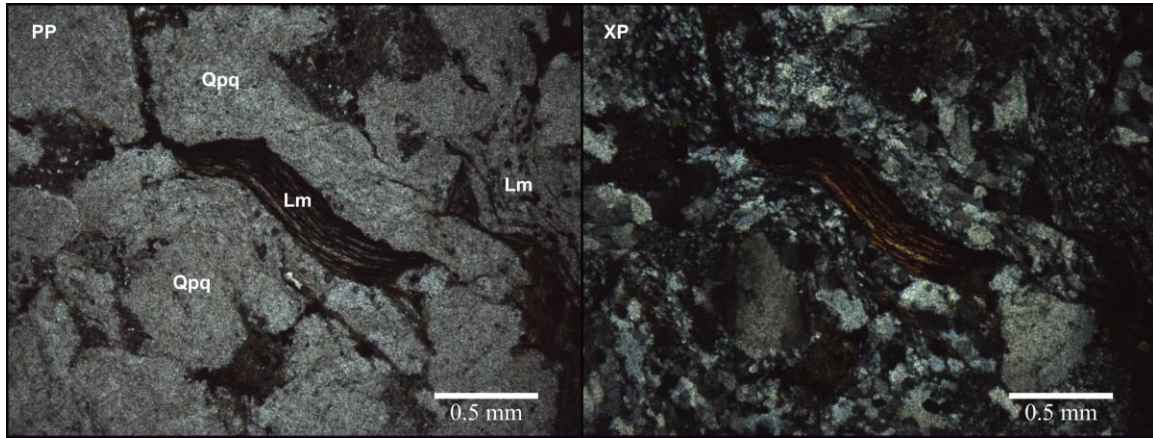


Figure A5-12. Plane and polarized light micrograph of sample R8. Lm in center corresponds to a phyllite.

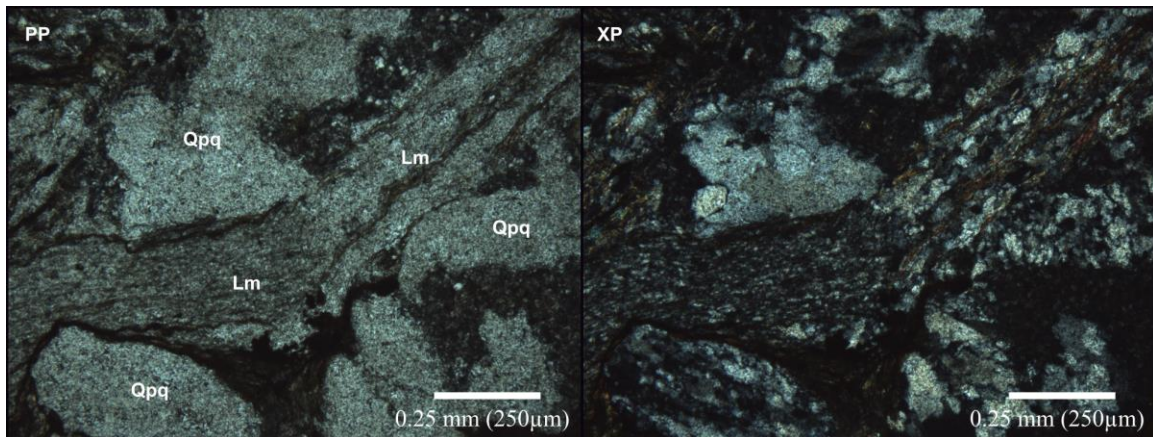


Figure A5-13. Plane and polarized light micrograph of sample R8. Lm in center appears to decrease in crystal size as it's compacted between two grains.

R9

Sample R9 pertains to a 2 m tabular sandstone package of Cualac Formation. The mean grain size of R9 is fine sand and the grains are mostly subrounded. The grains are

supported by the cement, so the contacts are floating. In decreasing abundance R9 is composed by Qpq, Lm, and Ls (Figure A5-13). Lm grains correspond to schists, and Ls to fine sandstones. Calcite and hematite cement are the most abundant components in the sample.

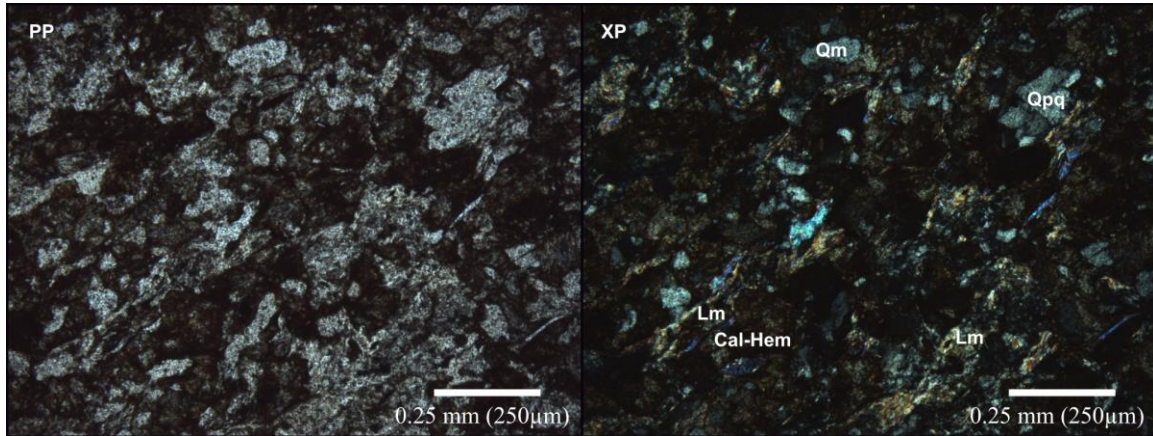


Figure A5-14. Plane and polarized light micrograph of sample R9.

R10

Sample 10 is a clast-supported, medium sand sized sandstone with sub-rounded grains. The form of the grains is distinctive of their composition, being the quartzitic grains sub-spherical and the metamorphic elongate (Figure A5-14). Compositionally, Qpq and Lm dominate the sample; the latter fraction corresponds to phyllites and slates (Figures A5-14, 15). The abundance of loose mica may represent the dismemberment of schistose and/or gneissic grains. Ls and Lsc (carbonatitic sedimentary grains) are also found, the latter consisting of hematite bordered-covered calcite grains with detrital characteristics. The space between grains is filled by pseudomatrix.

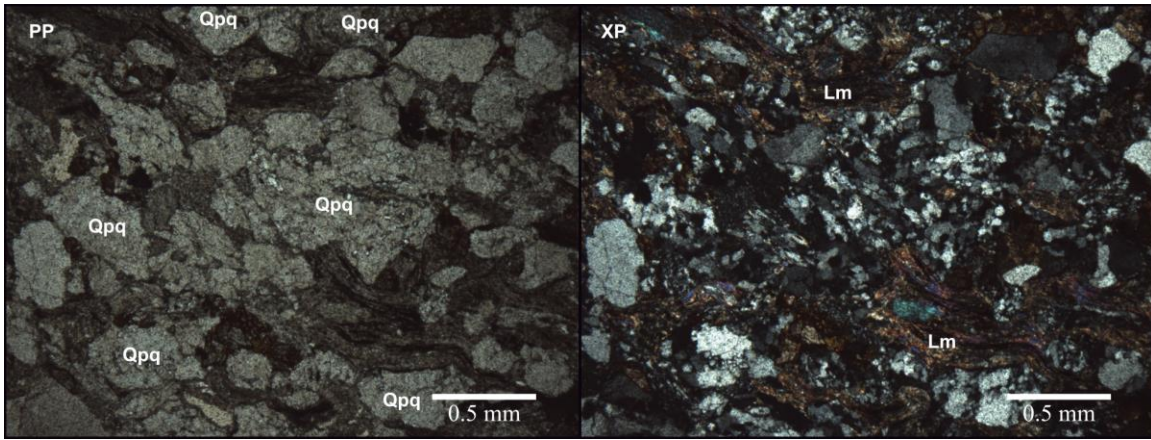


Figure A5-15. Plane and polarized light micrograph of sample R10.

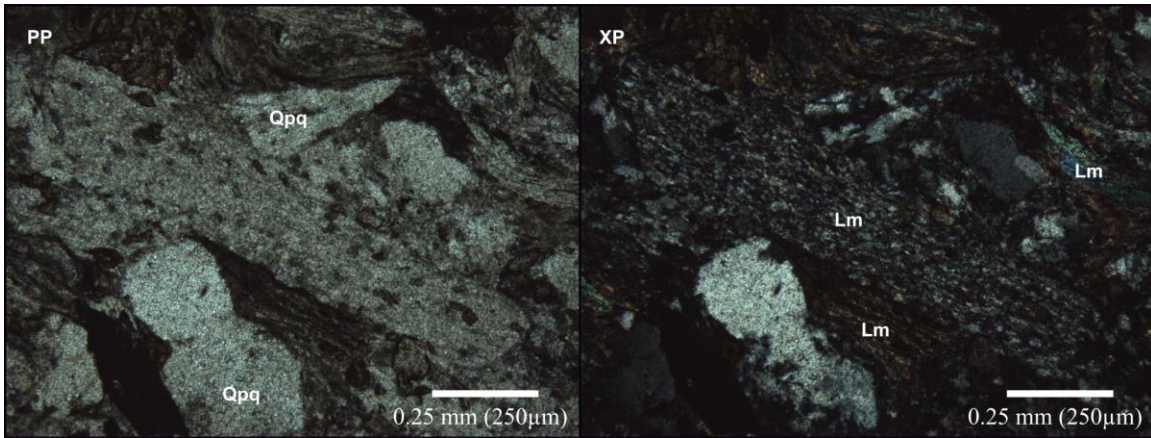


Figure A5-16. Plane and polarized light micrograph of sample R10.

R11

R11 corresponds to a grain-supported fine to very fine-grained sandstone, with subrounded elongated grains (Figure A5-16). The contacts between grains are longitudinal, reflecting a high degree of compaction. The principal detritic components of the sample are Qpq, Lm, and Ls. The Lm grains correspond principally to slaty and schistose pelitic clasts. Some modification in texture and mineralogy in these grains may have occurred due to compaction, augmented by the high percentage of pseudomatrix in the sample. The Ls grains are of silty and clayey nature. Loose muscovite sheets are

ubiquitous throughout the sample, marking a distinctive plane parallel lamination (Figures A5-16 – A5-17).

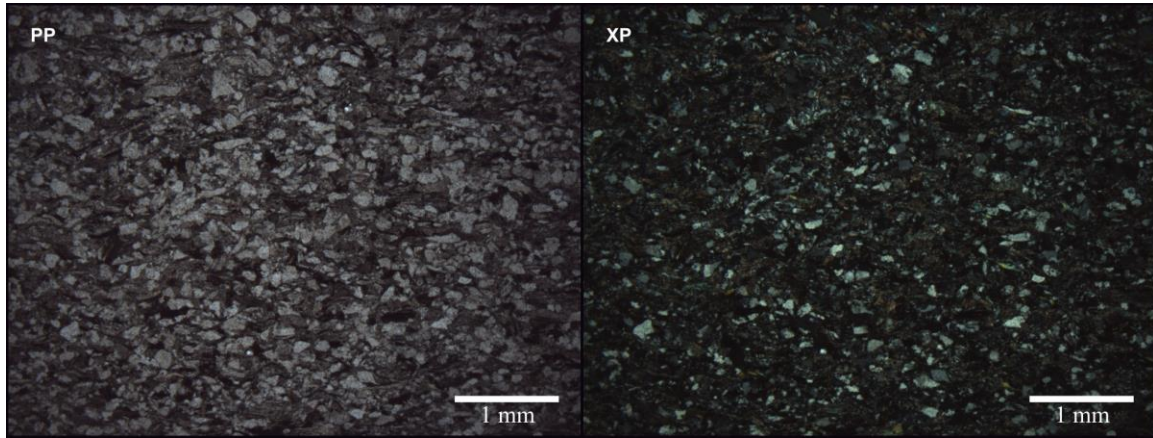


Figure A5-17. Plane and polarized light micrograph of sample R11.

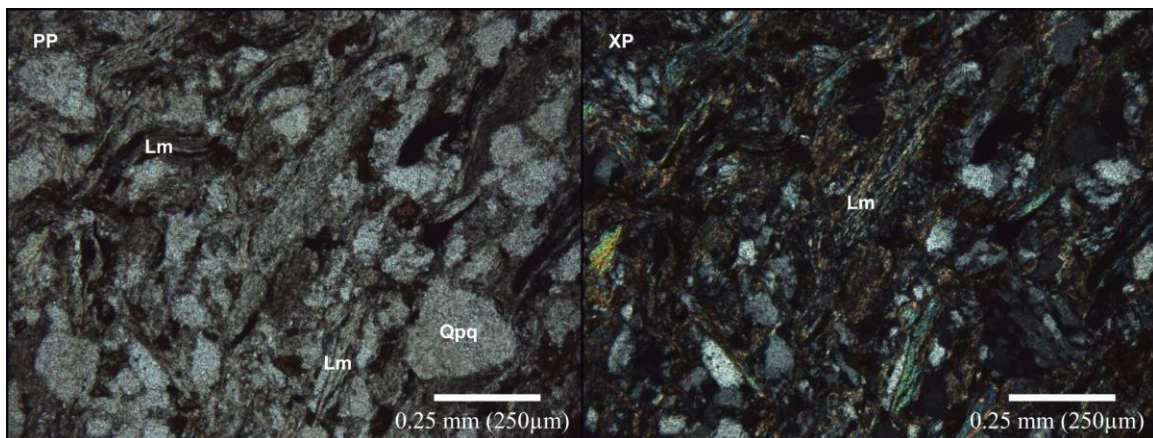


Figure A5-18. Plane and polarized light micrograph of sample R11.

R12

R12 is a fine to silty sandstone, supported by cement, with subrounded and some elongated grains. Qpq is the most abundant grain type, followed by Lm and Qm (Figure A5-18). Lm corresponds to slates, phyllites, and schists (some altered by compaction).

Loose mica and Lm are oriented making a plane parallel lamination. The calcite cement is rusty and hematite covered.

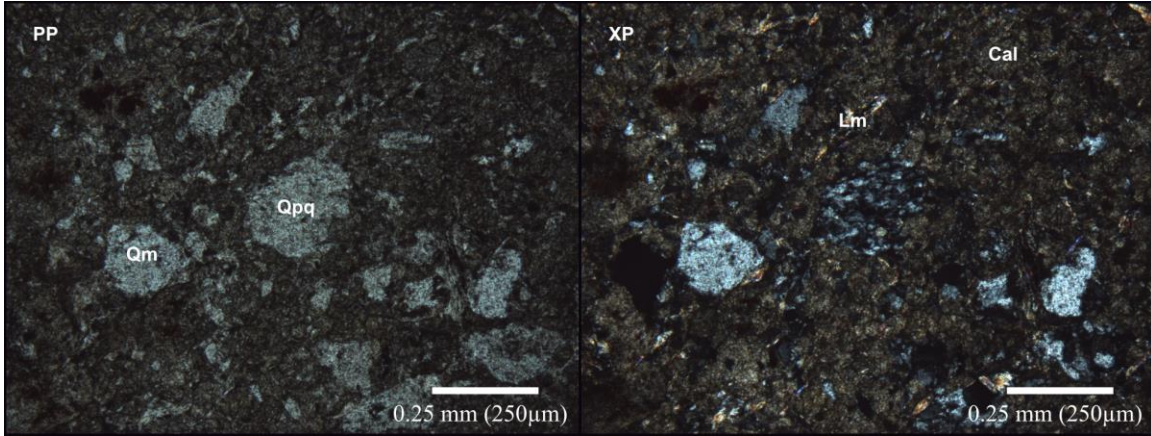


Figure A5-19. Plane and polarized light micrograph of sample R12.

R13

R13 is a very fine to silty sandstone, matrix supported, with subangular grains. Qm is the most abundant grain type. There is low Lm content. Loose mica and pseudomatrix make the matrix; the mica generates a plane-parallel lamination disrupted by folding (Figure A5-19).

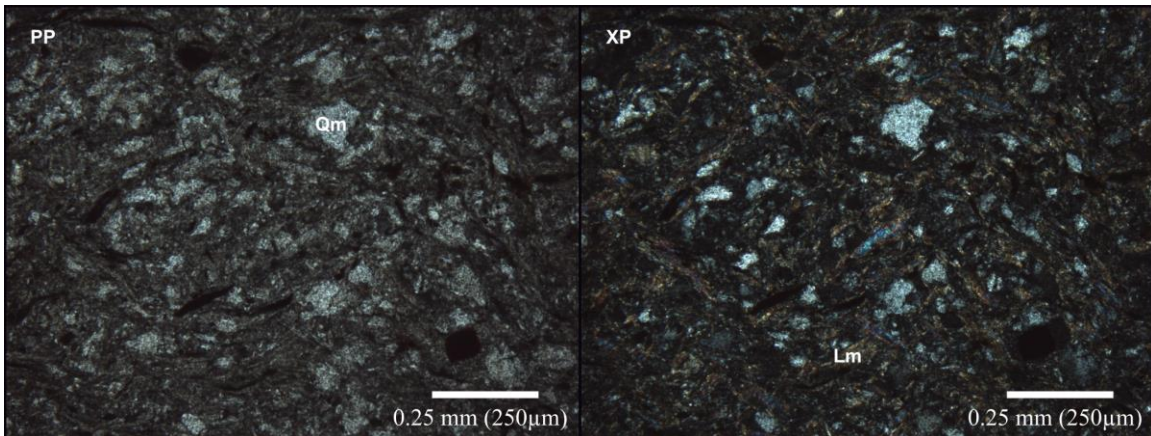


Figure A5-20. Plane and polarized light micrograph of sample R13.

R14

R14 is a clast-supported medium sand-sized sandstone. The grains are subangular to subrounded with longitudinal contacts. Qpq is predominant (Figure A5-20). Lm is the second most abundant grain class, many which corresponds to internally deformed Qpq (Figure A5-21). The slaty-phyllitic (Figure A5-22) and the schistose Lm grains are equal in proportion. Ls and Qm are the less representative types of grains. Loose mica and elongated Lm mark plane-parallel lamination.

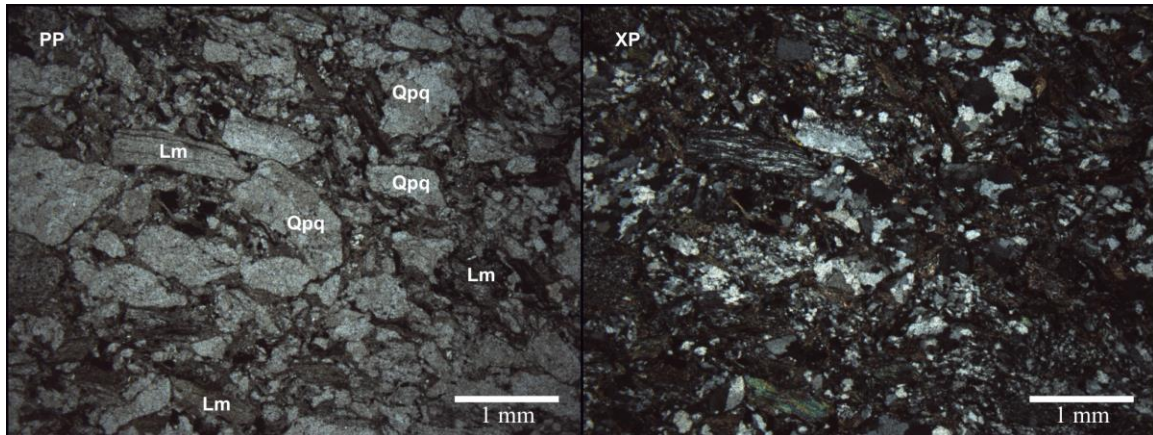


Figure A5-21. Plane and polarized light micrograph of sample R14.

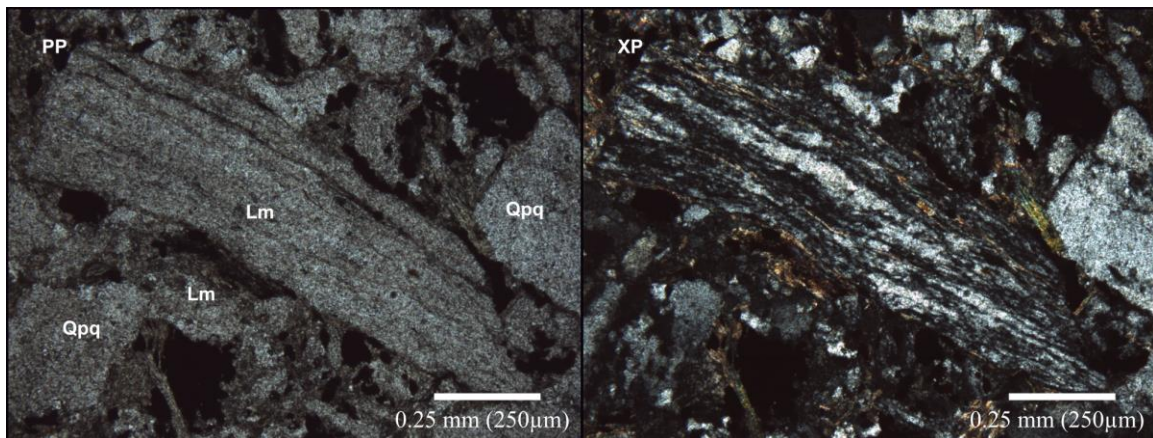


Figure A5-22. Plane and polarized light micrograph of sample R14.

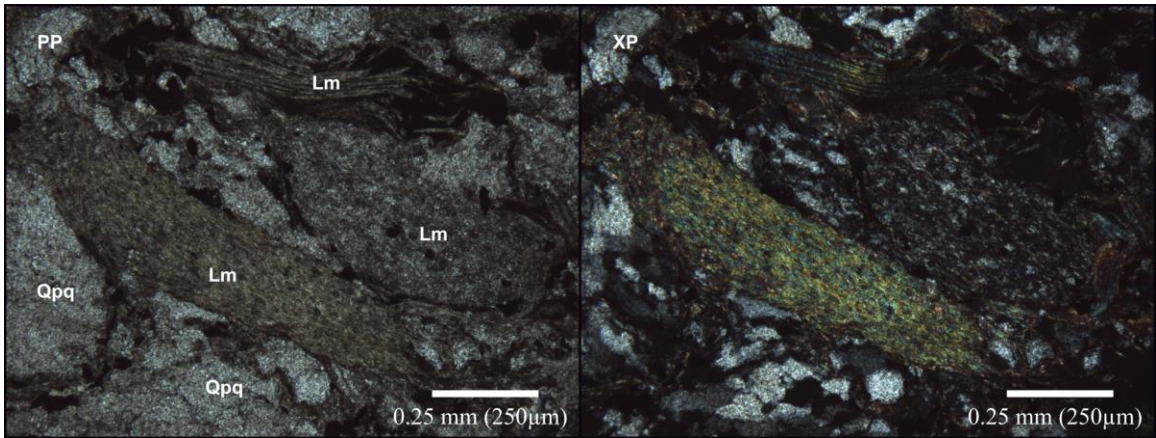


Figure A5-23. Plane and polarized light micrograph of sample R14.

R15

R15 is a clast-supported medium to coarse-grained sandstone with subangular grains and longitudinal contacts. Qpq is predominant (Figure A5-23); Lm is abundant, principally schists (Figure A5-24) and oriented Qpq (Figure A5-25), followed by phyllites and slates. Ls is present (fine sandstones) in low percentage together with Qm (Figures A5-23, A5-25).

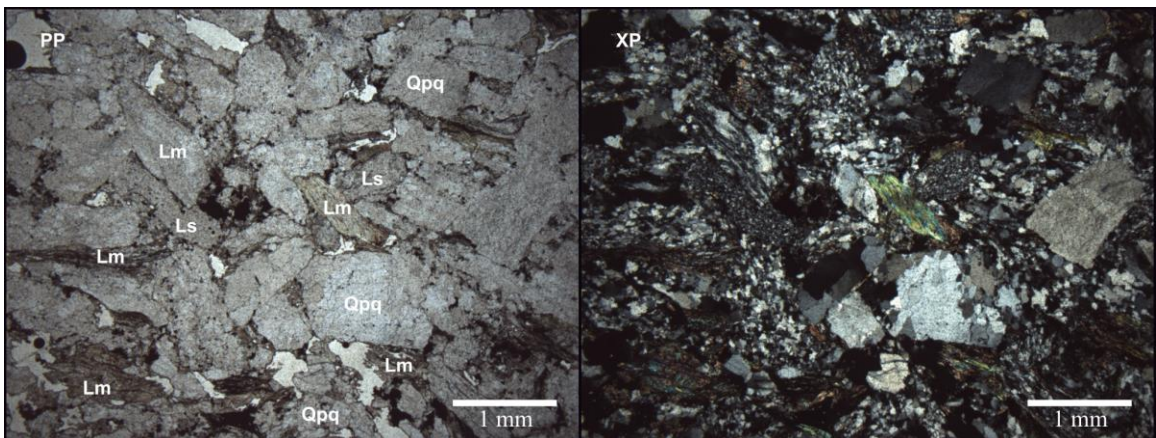


Figure A5-24. Plane and polarized light micrograph of sample R15.

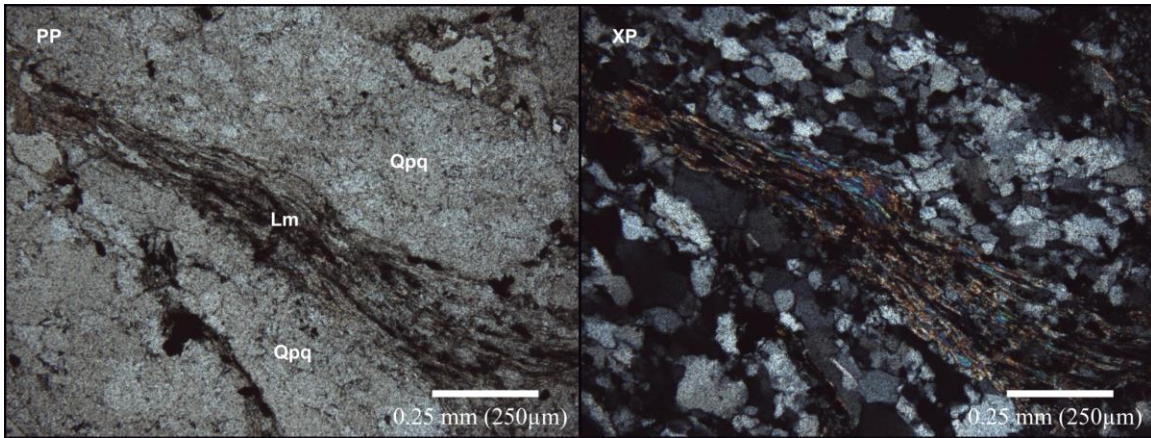


Figure A5-25. Plane and polarized light micrograph of sample R15.

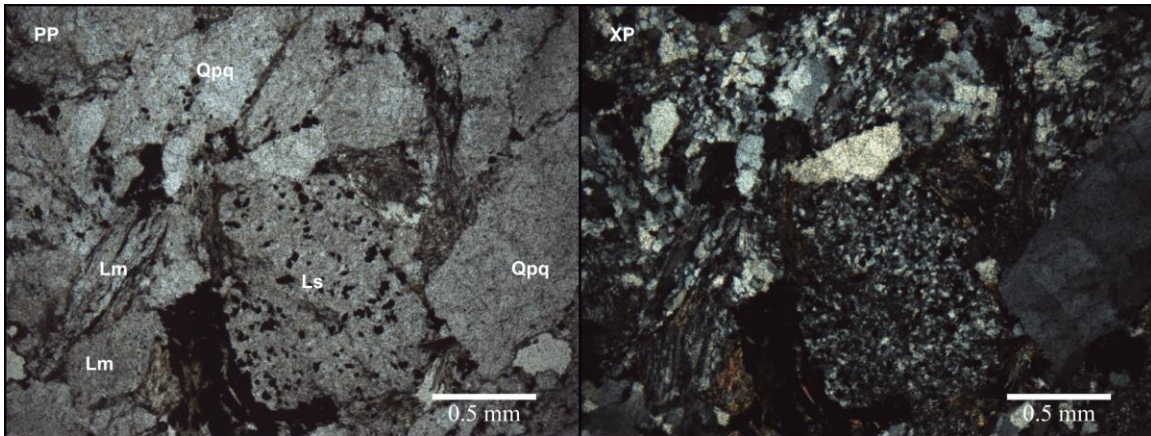


Figure A5-26. Plane and polarized light micrograph of sample R15.

R16

R16 is a clast-supported medium to coarse-grained sandstone with subrounded grains with uniaxial elongation. Qpq is overwhelmingly predominant (Figure A5-26); other compositional fractions such as Lm and Ls are present in a low percentage. Lm is schistose (Figure A5-27) and Ls sandy. Many Qpq grains are internally deformed and oriented along one axis and appear to have been subjected to pressure metamorphism (Figure A5-28). Vermicular kaolinite is filling spaces between grains.

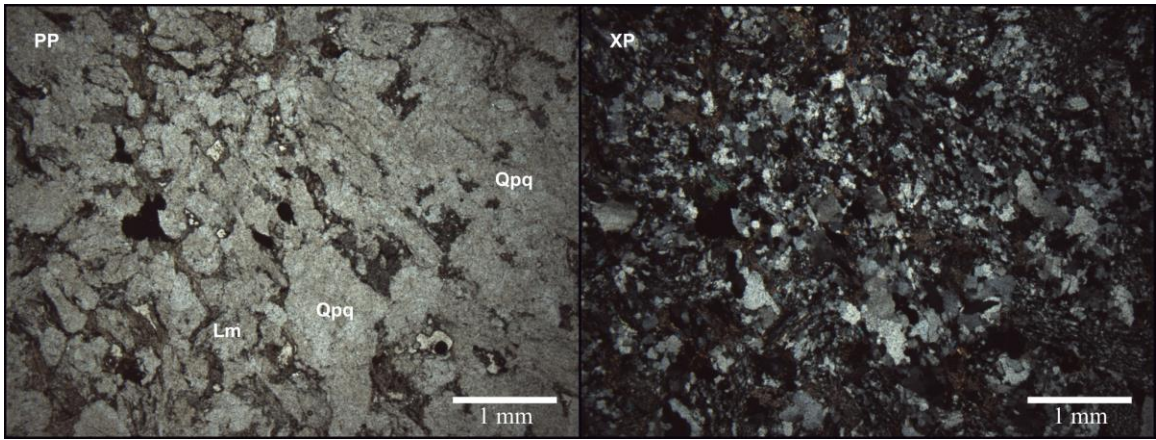


Figure A5-27. Plane and polarized light micrograph of sample R16.

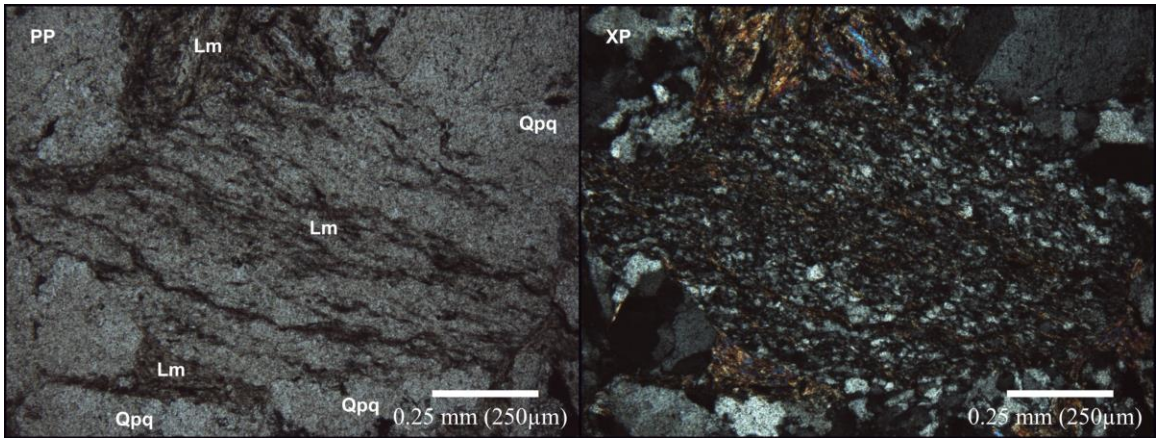


Figure A5-28. Plane and polarized light micrograph of sample R16.

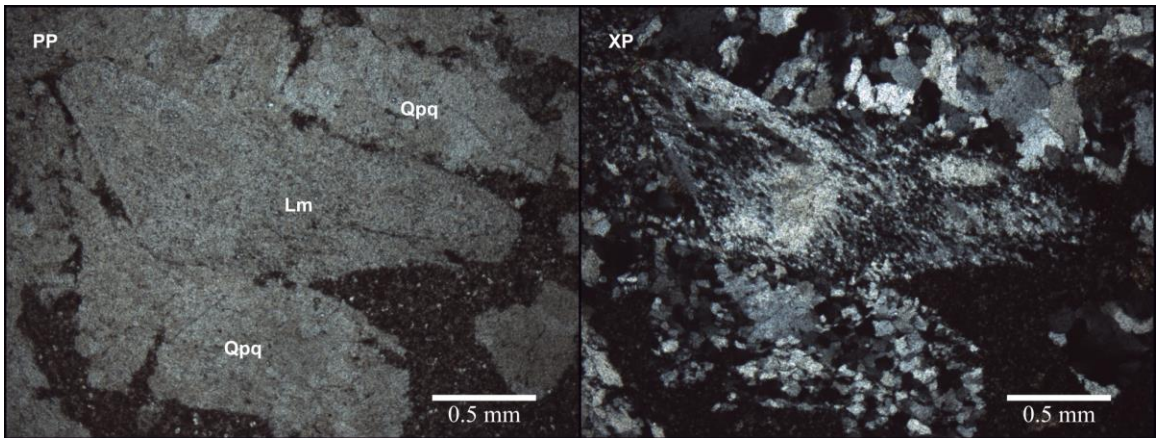


Figure A5-29. Plane and polarized light micrograph of sample R16.

R17

R17 is a cement-supported very fine to fine-sized sandstone. The majority of grains are subangular with floating contacts; some of the grains are elongated along one axis. Qm is the principal component (Figure A5-29). The second most abundant fraction is mica, some Lm grains are still preserved but in negligible quantity; either Qm and mica are interpreted as derived from bigger Qpq and Lm grains. Calcite is cementing the sample.

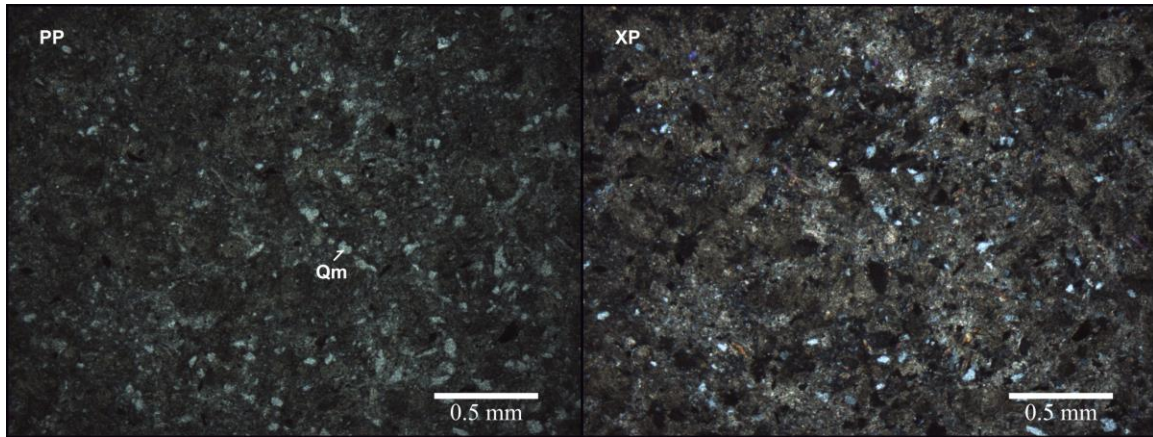


Figure A5-30. Plane and polarized light micrograph of sample R17.

R18

R18 is a clast-supported fine-sized sandstone with subangular grains. A lamination between hematite-rich and poor bands is readily distinguishable (Figure A5-30). The hematite-rich laminae have a Qm predominance over mica (Figure A5-31), in the hematite poor bands the Qm is also predominant, but some Lm grains are identified, together with loose mica; in these last bands, calcite cement is filling the spaces (Figure A5-32). The origin of hematite is secondary as void filling; nevertheless, some detritic characteristics (abraded borders) are recognized on some hematite grains (Figure A5-31, A5-32).

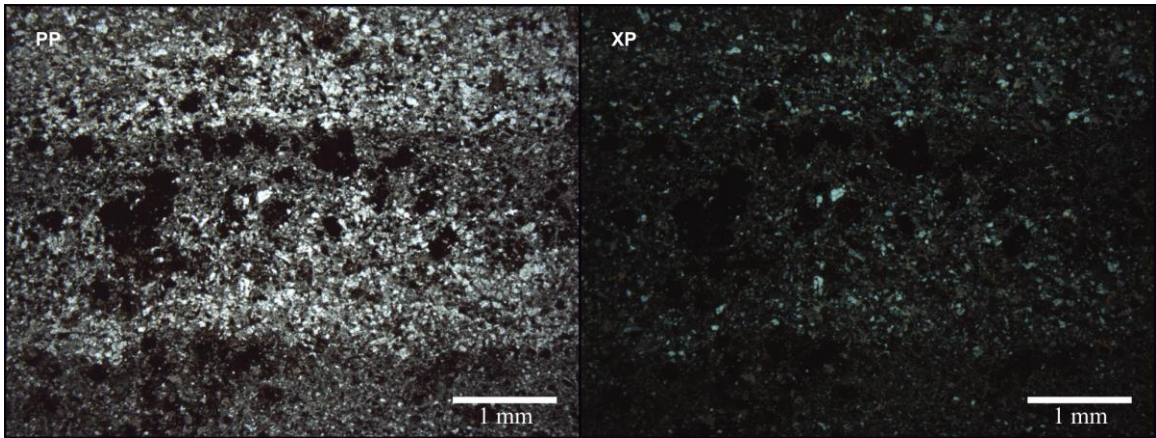


Figure A5-31. Plane and polarized light micrograph of sample R18.

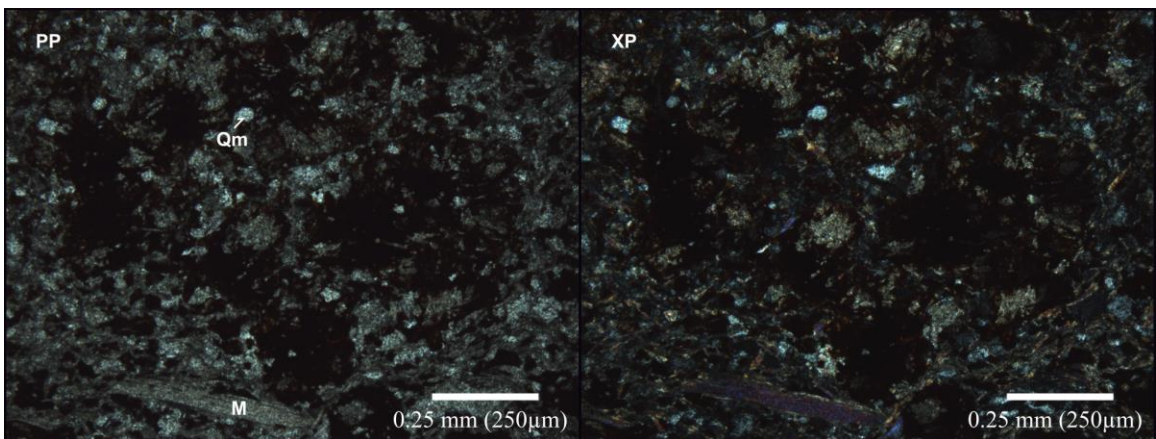


Figure A5-32. Plane and polarized light micrograph of sample R18. Zoom on dark lamina.

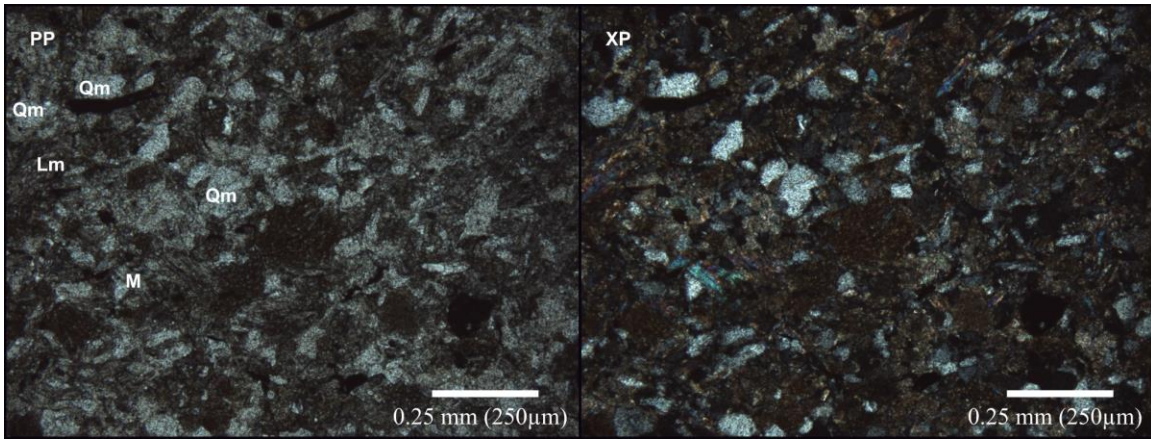


Figure A5-33. Plane and polarized light micrograph of sample R18. Zoom on light lamina.

R19

R19 is a clast-supported fine sandstone with subangular grains and longitudinal contacts. Qm and Qpq are the major components (Figure A5-33) followed by Lm and Ls (schistose and silty respectively Figure A5-34). Vermicular kaolinite fills the spaces between grains.

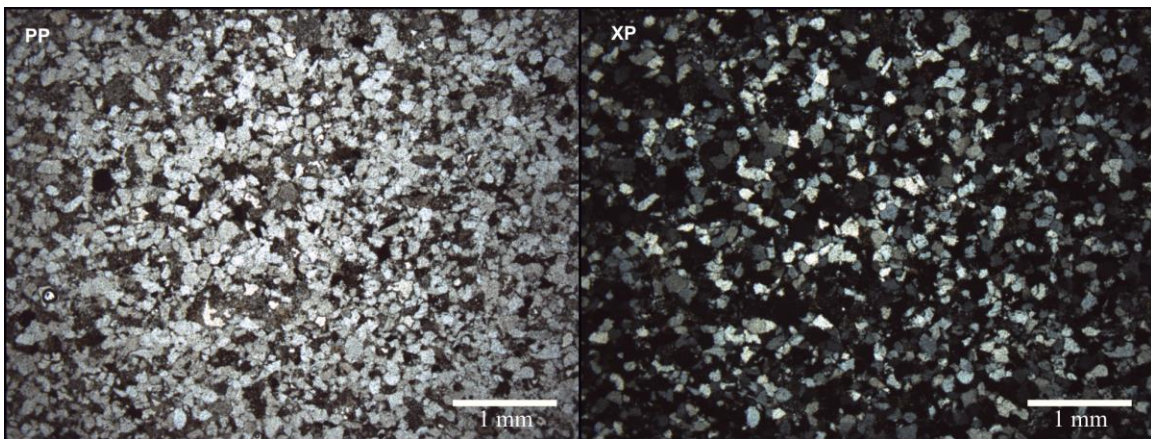


Figure A5-34. Plane and polarized light micrograph of sample R19.

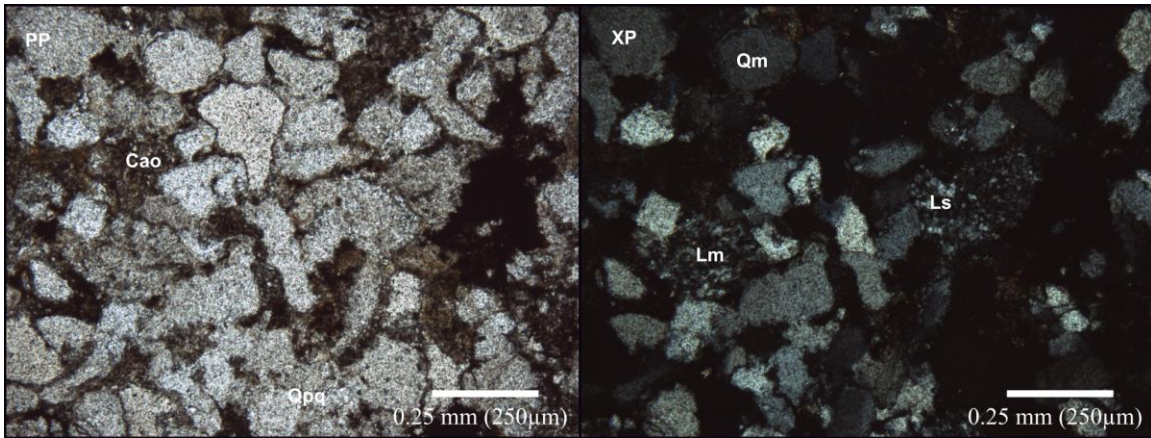


Figure A5-35. Plane and polarized light micrograph of sample R19.

R20

R20 is black in hand specimen. Microscopically is a fine to very fine sandstone composed primarily by quartz in two varieties: Qm and Qpq. Lithic components as Ls (silt, clay, Figure A5-35) are second in abundance. The sample has a high content of matrix, of silty and clayey nature with probably some organic matter.

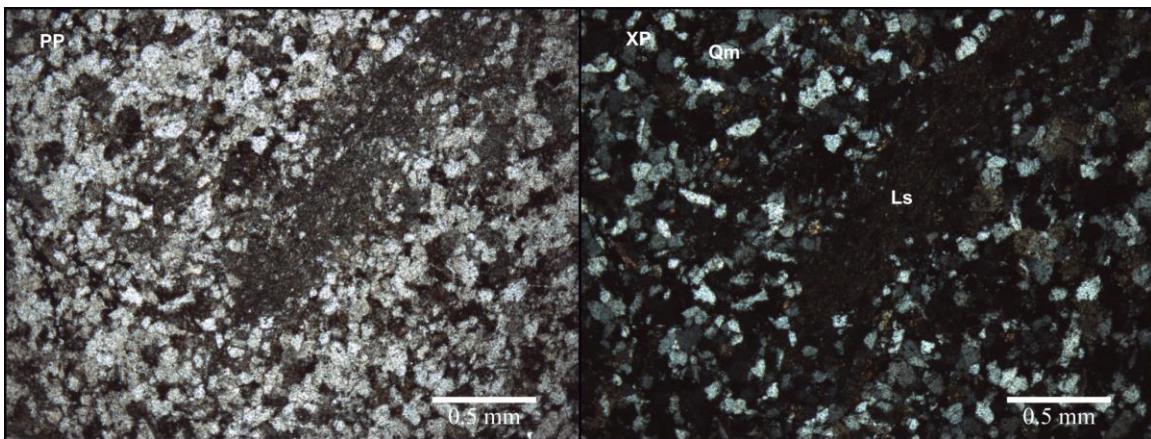


Figure A5-36. Plane and polarized light micrograph of sample R19.